



INSTITUT DE PHYSIQUE ET CHIMIE DES MATÉRIAUX DE STRASBOURG  
THÈSE DE DOCTORAT DE L'UNIVERSITÉ DE STRASBOURG

# LIGHT - TRIGGERED MOLECULAR ELECTRONICS IN THE 100 NM SIZE RANGE

par:

VINA FARAMARZI

Soutenue publiquement le 29 Novembre 2011 devant le jury composé de:

Professeur Bernard Doudin  
Dr. Ir. Sense Jan van der Molen  
Dr. Jean-François Létard  
Dr. Marc Drillon  
Dr. Jean-François Dayen

Directeur de Thèse  
Rapporteur  
Rapporteur  
Examineur  
Invité



I dedicate this thesis to my parents.



اجرام که ساکنان این ایوانند  
اسباب تردد خردمندانند  
هان تا سررشته خرد گم نکنی  
کانان که مدبرند سرگردانند

عمر خیام

The heavenly spheres which in this domain reside,  
Have bewildered the wise, thinking far and wide;  
Behold and don't lose the trail of wisdom,  
For the price of wisdom is to reel to every side.

Omar Khayyâm



# THESIS ABSTRACT

The challenge of realizing electronic devices based on organic materials started in the early 70's. The discovery and advent of conducting polymers in the 80's paved the way to new solution-based process and realization of cheap and flexible electronic devices. Mastering thin films fabrication by evaporation techniques also made possible devices realization with optimal properties and control. Organic electronics is nowadays becoming a mainstream innovative field, with perspectives in solar cells, lighting and cheap electronics. The first industrial products are emerging in our every day's life, for example in screens for portable electronics.

From another perspective, electrical transport through molecules, or entities of molecular size or thickness, created a growing interest in the research community. The development has been slower, mostly hindered by the technical issue of matching the nm molecular size with the typical 100 nm electrical interconnects sizes. This is illustrated by the scientific literature on the topic, with large fractions of the publications related to theoretical studies and nanofabrication methodologies, leaving aside only a marginal numbers of experimental results reports. The field of molecular electronics has nevertheless matured, and initial high expectations are nowadays moderated by the reality of difficulties in reuniting the molecular and macroscopic worlds. In particular, the scanning probe studies on molecules deposited on surfaces illustrated that stability usually require cryogenic temperatures, and the intrinsic conductivity of the molecules under study can be remarkably modified by the environment, the molecules conformations, and details of its interactions with the substrate. These points illustrate how difficult it is to create molecular devices of reproducible and robust properties.

Tackling molecular electronics problems through size reduction of 'standard' organic electronics systems also have stringent limits. The progress in this field cannot be compared to progress in miniaturization of inorganic silicon-based electronics. The primary technical bottleneck to miniaturization is metal-organic interfaces, which have a large importance for organic devices, and easily become predominant for sub-micrometer sizes.

A huge research effort has been dedicated to this problem in the last 15 years, aiming at better for better characterization and understanding of dielectric-organic and metal-organic interfaces joining two materials of very different electronic properties.

In the midway between bulk organic electronics and single molecule devices, are molecular electronic devices in the size range of 10-100 nm. This thesis is mostly dedicated to investigate these intermediate size devices. We envision several key advantages: (1) direct top-down nanofabrication tools can be used to fabricate reliable and reproducible interconnects in the 50 – 100 nm size range, (2) we can use bottom up fabrication methodologies to create molecular-based materials of size exceeding a few tens of nanometers, (3) by targeting devices where transport occurs through a significant number of molecules, we get access to average properties, with the advantage of studying more robust and reproducible samples, with expected environmental stability making ambient conditions measurements possible. Our ambition is to convince the reader that this mid-sized devices approach is promising, with high potentials. Our ambition is to provide a solid ground for molecular electronics devices realization, where reliability and results confidence are priorities. This explains why, all along this thesis, a large number of control experiments have been performed.

This thesis is essentially articulated in three sections. In the first section (Chapter II), we present our methodology for creating the electrodes circuit, the interconnects, the excitation and measurement environments. Light is used as a trigger or excitation source, illustrating how molecular devices can have controlled properties, making them potential candidates for devices properties beyond those of standard inorganic electronics. For this aim, the setup for electrical measurements is placed in a home built-interconnect setup over an inverted optical microscope where we can apply simultaneous optical-electrical measurements followed by temperature and magnetic field complementary studies. We report the fabrication of lateral electrodes with high aspect ratio ( $10^4$ ) separated by a 20-100 nm distance, and using simple optical lithography techniques. These ‘nanotrenches’ are our basic top-down tool for interfacing organic materials. The next section (Chapter III) is a proof-of-principle experiment, showing that we can create robust molecular electronics devices. The best experimental confirmation for the occurrence of molecular-type transport relates to the study of ‘switching’ molecules. Such systems exhibit a reversible, and possibly hysteretic, modification of their properties under external stimulus.

For experimental convenience reasons, aiming at minimizing the risks of experimental artifacts, we use a benchmark molecular system, choosing a photochromic molecular film. These molecules are known to reversibly exhibit a change of conformation (*cis*↔*trans*) under light excitations in the UV and blue ranges. We use a microsphere coated with a film of these molecules, and trapped over the nanotrench. The sphere is the intermediate size connector, closing the junction between metallic electrodes through a double molecular layer. While a light induced change of conduction has been shown in a vertical geometry in these molecules, the lateral geometry is unexplored. On-switching molecular films as check system, we provide quantitative success rate in observing electrical transport unambiguously related to molecules properties, reaching a success rate better than 90%.

The third section (chapters IV and V) presents the use of our methodology to investigate original new molecular materials. The spincrossover phenomenon, occurring as a collective transition with hysteretic behavior triggered by a change in temperature, pressure or irradiation in transition metal complexes, from paramagnetic high spin state (HS, S=2) to diamagnetic low spin state (LS, S=0) has been studied thoroughly in the literature, and well suites as switching molecular system. The transition is often accompanied by a change in color, dielectric constant and volume of the bulk material. Studies have shown that due to the collective nature of the transition, the hysteresis occurs in an ensemble of molecules and not in single molecules, thus spincrossover nanostructures are ideal candidates for observing the physical change (volume) due to the transition and we aimed to detect this change in their transport properties in chapter IV. We therefore used original spin crossover nanoparticles, of well-characterized spin transition properties, positioned over 100 nm-size gaps. The obtained results do not relate to spin transition, but to other intrinsic properties of the particles (high conductivity and photoconductivity) and confirmed that this geometry and size scale opens a view to novel properties investigation.

The other molecular system is designed for supramolecular electronics studies, where the bottom-up fabrication involves the construction of a large molecular architecture, of size matching the nanotrenches widths. We investigate a self-assembled molecular system based on a triarylamine derivative as building block. Light triggers a polymerization of these molecules, through radicals creation in the solution. When this growth procedure is probed between metallic electrodes, a surprising self-fabrication of highly conductive molecular wires parallel to the lines

of electric field in the gap is observed. The wires have an ohmic character with conductivity values of  $10^4 \text{ S.m}^{-1}$  combined with an extremely low interface resistance, typically six orders of magnitude lower than conventional polymers, samples exhibit high environmental stability persisting for a long time.

This ‘discovery’, detailed in chapter V, represents a milestone discovery for organic electronics since it describes the first molecular self-assembly having intrinsic metallic behavior in both bulk and at the metal/organic interface when lowering the temperature down to 1.5 K. Once again we emphasize the importance of the intermediate sized devices in making progress in the field of molecular electronics, by discovering materials with novel intrinsic properties and taking a great step towards lowering the parasitic interface resistance of organic materials with metals using self-fabrication procedures.

# AKNOWLEDGMENTS

Now that I have reached the closing days and hours of the preparation of my thesis, I take the opportunity to express that I'm truly and deeply indebted to many people without whose help and support I wouldn't have been able to go thus far. The years spent on the compilation and completion of the thesis comprise a unique and novel experience in my life throughout every single moment of which I learned, lived and enjoyed being involved in it. There is no way to acknowledge all this great help, support, and impacts as they deserve.

Firstly, I have to thank my dearly esteemed advisor Professor Bernard Doudin. I came to France to discover the Nano world!, and he made my dream come true by accepting me in his research group when I was a Master's student and later on, as a PhD student, I was provided with the opportunity to take part in several national and international research projects and collaborations at his discernment. I was surprised by his bright new ideas and suggestions while taking the steps gone by, and he taught me how to solve the problems by thinking in simpler ways and coming up with solutions that seemed easy but proved actually difficult to imitate. Thank you for everything Bernard.

Secondly, I am very grateful to my Thesis Committee for judging my defense and dissertation, to all the personnel and the Directorate of the Institute of Physics and Chemistry of Strasbourg (IPCMS) and Department of Magnetism of Nanostructured Objects (DMONS) where I carried on the majority of my experiments.

Thirdly, I'm indebted to all of my colleagues and friends in Professor Doudin's research group, to Jean-François Dayen for his great help in developing Nanotrenches; the ideal electrodes for molecular electronics, as well as in electrical measurements and publications and kind and caring advices.

Fourthly, thank you loads and loads, Hicham Majjad, Sabine Siegwald, Alain Carvalho, Matthieu Bailleul, Romain Bernard and Sabine Douls (STNANO nanofabrication platform) for teaching me nanofabrication with each and every detail and for your endless perseverance, patience and kind help in samples fabrication all along the years of my thesis.

Fifthly, I wonder how to deservedly thank Manuel Acosta; he was always there as a colleague and a caring friend to answer and solve my problems. I truly appreciate him for all he has done towards facilitating my experiments specially designing and developing two main sample holders for my thesis with the great help of Marc Imoff, Olivier Clauss and L. Ankenmann.

My endless thanks go to Petru Luncapopa, Guillaume Dalmas, Nabil Najjari and Jean-Baptiste Beaufrand for sharing their experiences and spending incredibly and amazingly friendly moments all filled with joy and laughter. I will always remember our office!!!

Many thanks to Fabien Chevrier, who had no hesitation in sharing his experience and being a great help and support when needed. Thanks to Neil Kemp, Venkata Kamalakar, Bohdan Kundys, Stephane Bérciaud, Nela Bejenaru and Martial Barbero.

Among all the nice people in IPCMS I would like to thank again Daniel Spor, Victor Da-Costa, Guy Schmerber, Arnaud Boulard, Nicolas Beyer, the computer department, Jose Radmacher, and our loving secretary Véronique Wernher, for whom I wish health and happiness and an amazing life.

I had the opportunity to collaborate with several research groups. Each of them opened up vistas to a new world for me. For that, I am thankful to:

- Nicolas Giuseppone, Emilie Moulin, Frederic Niess and Mounir Maaloum from SAMS group in ICS Strasbourg;
- Pierre Braunstein, Lucie Routaboul, Christophe Fliedel and Vitor Rosa from the Coordination Chemistry lab in Strasbourg;
- Paolo Samori and Corrina Raimundo from Nanochemistry group in ISIS Strasbourg;
- Marcel Mayor and Federica Reinders from Basel and Karlsruhe Universities;
- Céline Etrillard and Jean-François Létard from University of Bordeaux; and
- Sense Jan Van Der Molen and Constant Guedon from Leiden University.

Also, I appreciate a lot the guidance and help provided by my Master's advisors: Pierre Panissod, Christian Meny, Jean-Pierre Engel, and Rodolfo Jalabert.

Silvia Zanettini, thank you so much!!! Apart from being my best friend, you were and still are a great lab-mate for me. I enjoy every moment of experiments that we do together, and I wish you all the best for your PhD as you deserve it with your intelligence and patience.

I thank also all of my friends all around the world, whose friendship and love means a lot to me, including: Petru, Uliana, Alain, Celine, JB, Florence, Guillaume, Julie, Nabil, Piotrek, Marcelinka, Puja, Xi, Saqib, Alessio, Yannick, Olivier, Vincent, Marzena, Padideh, Saba, Hasti, Nazanin, Hirsra, Lionel, Negin, Paolo, Peyman, and many many more. Friends will be friends.

And finally, or at last but not the least, I am deeply indebted to my family. I have had the opportunity to enjoy of the endless ocean of love and support provided by my beautiful parents. I wouldn't have made it so far if it wasn't for your non-stop love and support. I missed you every single moment of life spent apart and I wish you a long healthy life filled with love and joy. My amazing sisters Raya and Nina, we are always there for each other; I truly appreciate your love and the meaning you give to my life. Thank you!!!

# TABLE OF CONTENTS

1. A FEW KEY CONCEPTS OF ORGANIC ELECTRONICS AND MOLECULAR ELECTRONICS .....	19
1.1. INTRODUCTION .....	19
1.2. SEMICONDUCTOR ORGANIC ELECTRONICS DEVICES (μm – mm).....	20
1.2.1. ORGANIC FIELD EFFECT TRANSISTORS.....	21
1.2.2. TRANSPORT IN ORGANIC SEMICONDUCTORS .....	27
1.2.3. HIGH MOBILITY ORGANIC SEMICONDUCTORS .....	29
1.2.4. ELECTRONIC STRUCTURE OF THE ORGANIC SEMICONDUCTOR - METAL INTERFACES .....	31
1.3. TRANSPORT THROUGH A SINGLE MOLECULE (1nm) .....	34
1.3.1. INELASTIC TUNNELING ELECTRONIC SPECTROSCOPY.....	39
1.4. MOLECULAR ELECTRONICS TESTBEDS.....	43
1.4.1. SINGLE-MOLECULE JUNCTIONS.....	43
<i>i. SCANNING TUNNELING MICROSCOPE (STM) BREAK JUNCTION.....</i>	43
<i>ii. MECHANICALLY CONTROLLABLE BREAK JUNCTIONS (MCBJ) .....</i>	44
<i>iii. SUMMARY.....</i>	46
1.4.2. MOLECULAR JUNCTIONS OF A FEW MOLECULES.....	47
<i>i. HANGING MERCURY DROP JUNCTION.....</i>	47
<i>ii. CONDUCTING PROBE ATOMIC FORCE MICROSCOPE (CP-AFM) .....</i>	48
<i>iii. NANOPARTICLE BRIDGE MOLECULAR JUNCTION.....</i>	49
1.4.3. TRANSPORT THROUGH MOLECULES IN 10-100nm SIZE RANGE, THE METHODOLOGY OF INTERMEDIATE SIZE .....	50
<i>i. WHY 10-100nm? .....</i>	50
1.4.4. SUPRAMOLECULAR ELECTRONICS .....	52
1.5. MOLECULAR ELECTRONICS SWITCHING DEVICES .....	53
<i>i. TWO-STATE SYSTEMS .....</i>	54
<i>ii. PHOTO-SWITCHABLE SYSTEMS.....</i>	55
1.5.1. SPIN TRANSITION SYSTEMS .....	56
1.6. CONCLUSION.....	57
2. STATE OF THE ART, NANOTRENCH FABRICATION .....	59
2.1. INTRODUCTION .....	59

2.2. NANOTRENCH ELECTRODE FABRICATION .....	60
2.2.1. ELECTRODE PATTERNING .....	61
2.2.2. ELECTRICAL CHARACTERIZATION OF NANOTRENCHES .....	65
2.3. MAGNETIC TRAPPING OF MICROSPHERES OVER NANOTRENCH ELECTRODES .....	68
2.4. EXPERIMENTAL SETUP, STRATEGY .....	71
2.4.1. ELECTRICAL CONNECTION SCHEMA .....	74
2.5. CONCLUSION .....	75
3. LIGHT SWITCHABLE MOLECULAR DEVICE USING MICROSPHERES CIRCUIT .....	77
3.1. TRANSPORT THROUGH MOLECULAR SWITCHES .....	77
3.2. AZOBENZENE-BASED MOLECULAR SWITCHES .....	79
3.3. CONJUGATED AZOBENZENE DERIVATIVE WITH THIOL ANCHORING GROUP .....	83
3.4. EXPERIMENTAL PROCEDURE .....	87
3.5. RESULTS AND DISCUSSION .....	89
3.6. CONCLUSION .....	95
4. SPIN CROSSOVER NANOCRYSTALS IN BISTABLE MOLECULAR DEVICES .....	97
4.1. SPIN CROSSOVER IN IRON (II) COMPLEXES .....	97
4.2. IRON (II) SPIN CROSSOVER NANOPARTICLES, BISTABLE MOLECULAR SYSTEMS .....	99
4.2.1. CHANGE OF COLOR .....	101
4.2.2. CHANGE OF THE DIELECTRIC CONSTANT .....	102
4.2.3. CHANGE OF VOLUME .....	102
4.3. MOLECULAR JUNCTIONS CREATED BY IRON (II) BASED SPIN CROSSOVER NANOPARTICLES OVER NANOTRENCHES .....	104
4.3.1. EXPERIMENTAL SETUP, STRATEGY .....	104
4.3.2. SYNTHESIS AND FABRICATION OF SCO NANOPARTICLES .....	105
4.3.3. TEMPERATURE CALIBRATION .....	109
4.3.4. PLACING THE SCO NANOPARTICLES OVER THE NANOTRENCHES .....	110
4.3.5. TRANSPORT MEASUREMENTS .....	111
4.3.6. OBSERVATION OF PHOTOVOLTAIC EFFECT .....	117
4.4. FABRICATION OF HALF METALLIC SHELLS OVER SCO NP AND TRANSPORT MEASUREMENT STRATEGY .....	119
4.4.1. TRANSPORT MEASUREMENTS .....	121
4.5. CONCLUSION .....	125

5. LIGHT TRIGGERED SELF-CONSTRUCTION OF SUPRAMOLECULAR ORGANIC NANOWIRES AS METALLIC INTERCONNECTS.....	128
5.1. INTRODUCTION .....	128
5.2. METALLIC CONDUCTIVITY IN CONJUGATED POLYMERS .....	130
5.2.1. PARASITIC CONTACT RESISTANCE .....	132
5.3. SUPRAMOLECULAR STRUCTURES .....	135
5.3.1. TRIARYLAMINE HIERARCHICAL SELF-ASSEMBLY.....	135
5.4. TRANSPORT MEASUREMENTS.....	140
5.4.1. STRATEGY.....	140
5.4.2. CONTROL MEASUREMENTS .....	141
5.4.3. FORMATION OF TRIARYLAMINE NANOWIRES BETWEEN METALLIC ELECTRODES .....	143
5.5. CHARACTERIZATION OF STANWS.....	145
5.5.1. CONDUCTIVITY VALUES.....	145
5.5.2. A CLOSER LOOK ON THE SELF-ASSEMBLY PROCESS.....	146
5.5.2.1. IMAGING THE STANWS.....	150
5.5.3. TEMPERATURE DEPENDENT MEASUREMENTS.....	153
i. TRANSPORT IN METALLIC POLYMERS.....	153
ii. RESISTANCE VERSUS TEMPERATURE MEASUREMENTS OF STANWS .....	153
5.5.4. CONDUCTIVITY AND INTERFACE RESISTANCE ESTIMATES.....	155
5.5.5. ELECTRODES MATERIAL EFFECT .....	158
5.6. EXCLUDING THE ARTIFACTS.....	159
5.6.1. SOLUTION STRESS CONDITIONS .....	159
5.6.2. BLIND TESTS.....	160
5.6.3. IMAGING NANOTRENCHES.....	162
5.6.4. ELECTRICAL PROPERTIES OF FILLED NANOTRENCHES .....	164
5.6.5. SUMMARY .....	166
5.7. CONCLUSION.....	167
6. CONCLUSIONS.....	168
7. BIBLIOGRAPHY .....	173
APPENDIX.....	195
A. MICROSPHERE FOR SURFACE BONDING STUDIES .....	196
A.1. PREPARATION OF HALF METAL COATED SILICA MICROSPHERES.....	196

A.2. MICROSPHERES SURFACE FUNCTIONALIZATION.....	197
A.3. END GROUP EFFECT IN BONDING WITH GOLD SURFACE VIA FUNCTIONALIZATION OF POLYBEAD AMINO MICROSPHERES .....	199
A.4. CONCLUSION.....	200
B. COORDINATION-DRIVEN ASSEMBLING OF MICRO-OBJECTS WITH METALLOLIGANDS .....	202
C. FABRICATION OF HALF METALLIC SHELLS ON SCO NANOPARTICLES .....	207
C.1. CHOICE OF PARTICLES .....	208
C.3. THICKNESS OF THE METALLIC FILM .....	210
D. SAMPLE HOLDERS .....	211
D.1. SAMPLE HOLDER FOR OPTICAL SETUP.....	211
D.2. SAMPLE HOLDER FOR LOW TEMPERATURE MEASUREMENTS .....	212

## CHAPTER I: A FEW KEY CONCEPTS OF ORGANIC ELECTRONICS AND MOLECULAR ELECTRONICS.

In this introductory chapter, we provide a brief review on the field of electrical transport through organic spacers. We intentionally pick a few concepts in this very broad research area, key for motivating our research, focused on robust molecular electronics approach in the 10-100 nm range.

# 1. A FEW KEY CONCEPTS OF ORGANIC ELECTRONICS AND MOLECULAR ELECTRONICS

## 1.1. INTRODUCTION

Molecular electronics, the multidisciplinary research of using molecular building blocks for fabrication of electronic components, has been studied widely through the years, from bulk organic electronics and organic thin film devices to sub-nanometer single molecule junctions [1, 2]. The intermediate size range of ten to hundred nanometers, however, has attracted less attention. The growing need for robust and reproducible molecular devices, not attainable for the moment at the nanometer scale, is nevertheless reviving the interest of studying devices of characteristic size much larger than the molecular size range. Investigating other size ranges will definitively expand our insight by providing novel information, allowing the whole body of research in this field to progress more rapidly, also revealing novel advanced materials with interesting intrinsic properties.

This thesis deals with molecular electronics in the size range of 10-100 nm under external stimuli i.e. temperature, illumination/irradiation and pressure. We will restrict our studies and discussions to lateral devices, where contacting metallic structures are laid down in the same plane (parallel to the substrate) as the active organic films or layers. This is in contrast to vertical devices, where the metallic electrodes and the organic active films are stacked over a planar substrate. While the vertical methodology has been shown to be very successful for making organic electronics devices, we picked an alternative choice for two main reasons. Firstly, the top metallic films often mix with the organic layer, making vertical devices involving very thin layers quite challenging. An intermediate film or thicker layers become then necessary. Secondly, and more importantly, a lateral geometry is ideally suited for electrical and optical access to the active molecules, which is a key criterion when aiming for building up molecular devices sensitive to multiple types of external excitations. This chapter presents a brief review on our inspiration and motivations.

The field of semiconductor organic electronics usually involves large area devices, with size range exceeding 10 microns (in the lateral geometry!). We will explain why such size is usually needed and how further miniaturization is challenging, as well as potentially bringing new understanding. Single molecule electronics, on the other side, involve interconnects at the molecule size, i.e. in the nm range, significantly below what we will focus on. We will review the motivations and potentials of single molecule studies, emphasizing why larger and more robust devices are of high interest. The advantages and motivations for studying transport in molecular devices in the tens of nm range will be detailed, while exploring the possible disadvantages/problems and solutions to them.

Even though molecular electronics is not a new area of research, the related experimental difficulties, as well as the high expectations of breakthrough discoveries have made the road to better understanding a bit bumpy. There is a strong need of benchmark simple molecular systems, and experiments providing unambiguous indications that electrical transport properties are indeed related to molecular properties. Switching molecular systems are ideal for studying the electrical response to external perturbations, as well as ideal indicators of molecular transport. This is why the last section of this chapter introduces this specific topic.

## 1.2. SEMICONDUCTOR ORGANIC ELECTRONICS DEVICES ( $\mu\text{m} - \text{mm}$ )

Along with the growth of the standard Si-based electronic industry, the search for low cost electronics with new connectivity possibilities gave rise to the field of organic electronics. A quickly developing field emerged, aiming at good performance electronic devices by fabricating low-cost, large-area electronic products on flexible substrates like paper or plastic [3]. Since 1950 with the work on crystalline organic materials, followed by breakthrough discovery of conducting polymers (resulting in the Nobel prize in chemistry for conductive polymers in 2000), a growing research effort proved spectacular improvements in semiconducting, conducting, and light emitting properties of organics (polymers, oligomers) and hybrids (organic–inorganic composites), pointing out the key contribution of chemists to optimize the

properties of such ‘active’ materials over large surfaces through novel synthesis and self-assembly techniques [4, 5, 6].

In spite of the many advantages presented by organic materials for electronics like being compatible with large-area processes at low process temperatures (low-cost), the capability of being tailored for specific electronic or optical properties and their compatibility with organic semiconductors, several improvements are still needed. Limitations of carrier mobility, the electronic and optical instability and incompatibility of processing with classical processing in semiconductor industry, leave a huge amount of work to be done in this demanding field of research.

### 1.2.1. ORGANIC FIELD EFFECT TRANSISTORS

Organic field effect transistors (OFET), the prototypical for organic electronics, are examples of devices where understanding and molecular engineering of properties have grown steadily over the past decade. This example of lateral organic electronics device is used here to show and explicit the necessary key properties of an organic semiconducting film. Field effect transistor (FET) devices dating from 1925 by Julius Edgar and Lieinfell (1930) followed by Oskar Heil in 1934, are practical tools to study the fundamental electronic structure and charge-injection physics of organic semiconductors, especially at the dielectric interface, and provide insight into the fundamental problems of explaining how microscopic molecular scale transport processes determine the electrical characteristics of macroscopic devices [7, 8]. Figure 1.1 illustrates four more common geometries of OFETs: bottom-gate and top-gate for bottom-contact and top-contact structures.

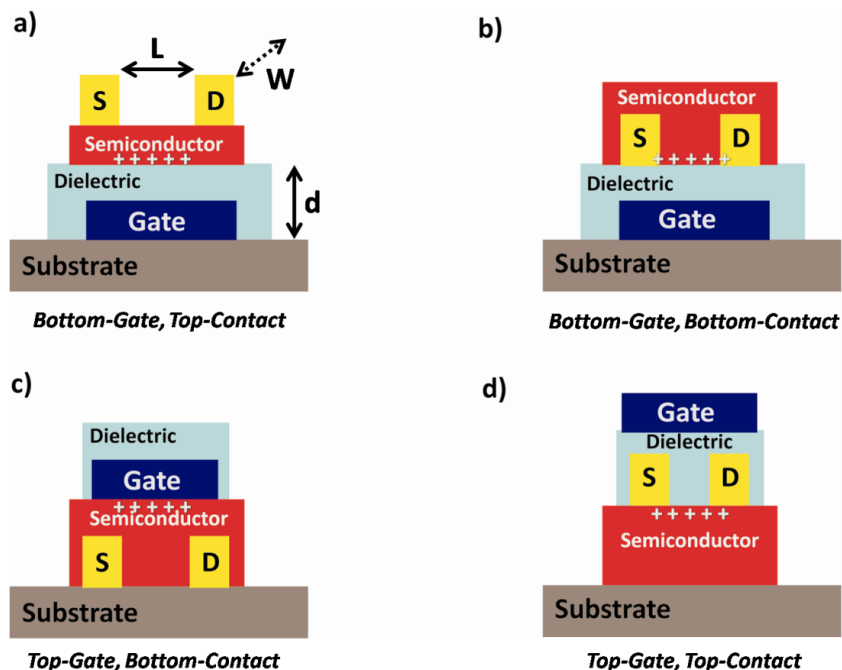


**Figure 1.1 : Schematic of bottom-gate OFETs with a) top contact (staggered), b) bottom contact (coplanar) structures. Schematic of top-gate OFETs with c) bottom contact using a standard TFT device structure and d) top contact structure. The distance between source and drain is  $L$  and the width of contacts is  $W$ ,  $d$  is the thickness of dielectric layer.**

Basically, an OFET device operates as a capacitor where one plate is a conducting channel of length  $L$  and width  $W$  between source and drain ohmic contacts and the other plate is a conducting gate electrode. By applying a voltage difference between the two plates, the density of charge carriers in the semiconducting channel can be modified. The gate electrode is separated from the organic semiconductor by a dielectric layer, providing a capacitive coupling to the organic channel. OFETs are characterized by plotting the drain current ( $I_D$ ) versus the gate electrode voltage ( $V_G$ ) (figure 1.3-b). The output plot of an OFET is the source/drain current versus source/drain voltage ( $I_{SD}(V_{SD})$ ) for different gate bias voltages (for simplicity we refer to  $I_{SD}$  or  $V_{SD}$  as  $I_D$  and  $V_D$  respectively).

Figure 1.2 presents an example of electrical properties of a state-of-the-art OFET device by measuring its' transfer curves, exposed to air and illumination right after manufacture (closed circles) and two weeks later (open circles) [1].

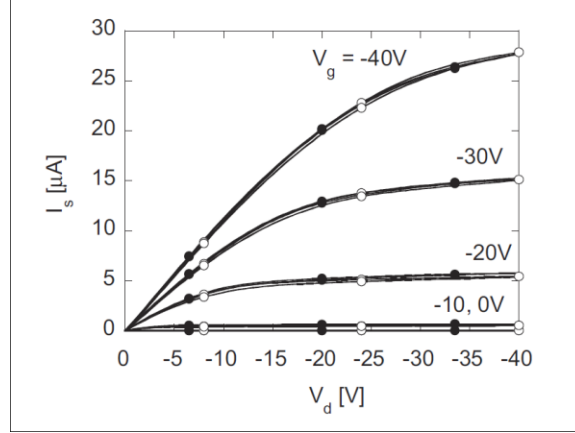


**Figure 1.2 : Output characteristics (source current  $I_s$  vs drain voltage  $V_D$ ) of a state-of-the-art unencapsulated OFET measured in air and light (closed circles: device measured after manufacture; open circles: device measured after two weeks) [1].**

The interest for designing organic semiconductors as the active layer in FETs, led to devices with high performances, which compare to the amorphous silicon thin film transistors (TFT). In recent years FETs based on organic semiconductors processed from solution have gained lots of improvement in reliability and high performance. One of the key parameters marking the performance level of a FET device is the charge mobility  $\mu$  ( $[\mu] = [\text{cm}^2\text{V}^{-1}\text{s}^{-1}]$ ), defined by the average velocity (drift velocity  $v_d$ ) of the charges in response to an applied electric field  $E$  (equation 1.1).

$$v_d = \mu E \quad \left( \mu = \frac{v_d}{E} \right) \quad (1.1)$$

The mobility is proportional to the transconductance ( $g_m$ ) of the transistor, as shown in equation 1.2, illustrating how the mobility is the key property for using OFETs as active devices. For power applications, one needs to maximize the transconductance, and therefore maximize the mobility, intrinsic to the semiconductor ( $L$  and  $W$  are the length and the width of the conduction channel,  $C$  the capacitance per unit area).

Field effect mobility in an OFET in the linear regime (low source-drain voltage) relates to  $I_D$  increasing linearly with  $V_D$  at low  $V_D$  ( $-V_D \ll -(V_G - V_T)$ ) and is approximately deduced from the transfer curve, using equation 1.3.

$$g_m = \left. \frac{\partial I_D}{\partial V_G} \right|_{V_D=\text{const.}} = \frac{WC_i}{L} \mu V_D \quad (1.2)$$

$$I_D = \mu C_i \frac{W}{L} \left( V_G - V_T - \frac{V_D}{2} \right) V_D \quad (1.3)$$

Field effect mobility in the saturated regime is obtained by increasing  $V_D$  up the saturation of  $I_D$  ( $V_G=\text{const.}$ ), and is determined from equation 1.4. In the saturation regime ( $-V_D > -(V_G - V_T)$ ), the drain current is modeled by equation 1.5 and the field effect mobility can be calculated from the slope of the plot of  $(|I_D|)^{1/2}$  versus  $V_G$  (equation 1.4). The field-effect mobilities of linear and saturated regimes are of the same order of magnitude (the latter is usually larger by 10-30%) [9, 10, 11].

$$\mu = \frac{2L}{WC_i} \left( \frac{\partial \sqrt{|I_D|}}{\partial V_G} \right)^2 \quad (1.4)$$

$$I_D = \frac{\mu C_i}{2} \frac{W}{L} (V_G - V_T)^2 \quad (1.5)$$

Apart from transconductance and field-effect mobility, the ON/OFF ratio (essential for using the FET as a switch) and threshold voltage values are deduced from  $I_D(V_G)$  and  $(|I_D|)^{1/2}(V_G)$  plots respectively. Figure 1.3 presents two sets of data for a pentacene thin film measured in a top-contact OFET, exhibiting FE mobilities of  $0.80 \text{ cm}^2\text{V}^{-1}\text{s}^{-1}$  in linear regime and  $1.23 \text{ cm}^2\text{V}^{-1}\text{s}^{-1}$  in saturation mode [8], both are very large values for organic semiconductors standards.

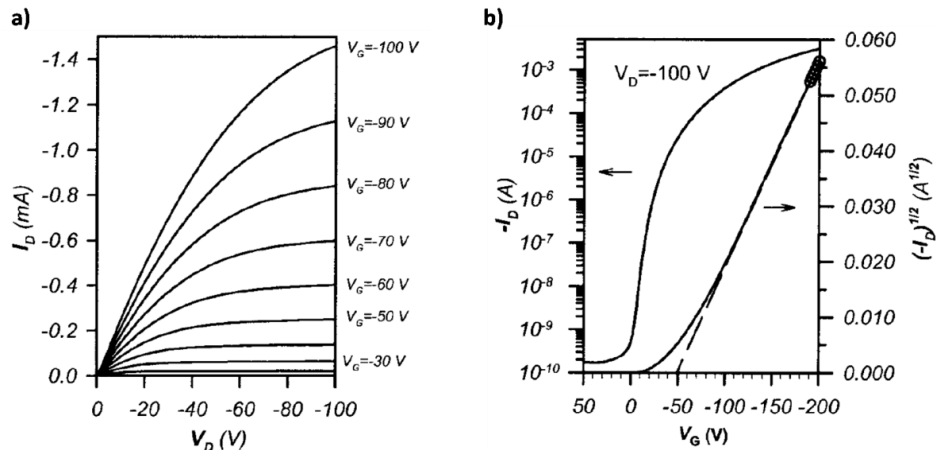


Figure 1.3 : a) Plot of a drain current  $I_D$  versus drain voltage  $V_D$  at various gate voltages  $V_G$  from a top-contact OFET comprising a polycrystalline pentacene thin film channel. The linear regime mobility is  $0.80 \text{ cm}^2\text{V}^{-1} \text{ s}^{-1}$  at  $V_D = \pm 10 \text{ V}$ , and the saturation regime mobility is  $1.03 \text{ cm}^2\text{V}^{-1} \text{ s}^{-1}$  at  $V_D = \pm 100 \text{ V}$ ,  $L = 15.4 \text{ }\mu\text{m}$  and  $W = 1 \text{ mm}$ . b) Semilogarithmic plot of  $I_D$  versus  $V_G$  (left y-axis) and plot of  $\sqrt{I_D}$  versus  $V_G$  (right axis) from a top-contact OFET comprising a polycrystalline pentacene thin film channel. The field-effect mobility  $\mu$ , calculated in the saturation regime, is  $1.23 \text{ cm}^2\text{V}^{-1} \text{ s}^{-1}$  at  $V_D = \pm 200 \text{ V}$ , ( $L = 15.4 \text{ }\mu\text{m}$  and  $W = 500 \text{ }\mu\text{m}$ ) [8].

Room-temperature mobilities of inorganic semiconductors such as single-crystal silicon can reach as high as  $10^2\text{-}10^3 \text{ cm}^2\text{V}^{-1}\text{s}^{-1}$ , and for single-walled carbon nanotubes, the mobility can surpass  $10^5 \text{ cm}^2\text{V}^{-1}\text{s}^{-1}$ . Organic materials show mobilities of around  $10^{-5} \text{ cm}^2\text{V}^{-1}\text{s}^{-1}$ . A variety of new materials have been synthesized with mobilities exceeding  $0.1 \text{ cm}^2\text{V}^{-1}\text{s}^{-1}$  in thin films and  $10 \text{ cm}^2\text{V}^{-1}\text{s}^{-1}$  in crystals (figure 1.4) [1].

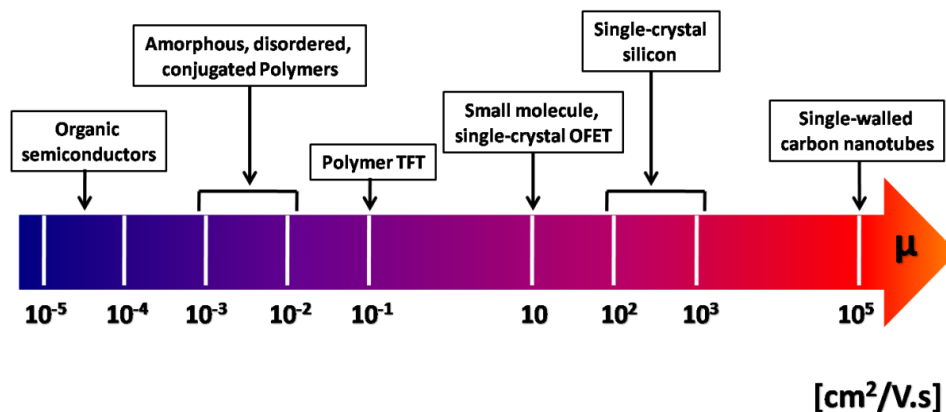


Figure 1.4 : Orders of magnitude of charge carrier mobilities for organic and inorganic semiconductors [1].

In this thesis, we deal mostly with conductivity values. The bulk drift mobility, conductivity and charge concentration are linked by equation 1.6, where  $N_m$  is the concentration of mobile charge carriers per unit volume [12]. The channel conductance for an OFET,  $\sigma$ , is determined from equation 1.7, where  $\Delta V$  is the potential drop in the SC channel [13].

$$\sigma = N_m e \mu \quad [\sigma] = [\text{S.m}^{-1}] \quad (1.6)$$

$$\sigma = \left( \frac{I_D}{\Delta V} \right) \left( \frac{L_{1-2}}{W} \right) \quad [\sigma] = [\text{S.m}^{-1}] \quad (1.7)$$

The conductivity for semiconductors and insulators varies with temperature and decreases when lowering the temperature, in opposition to temperature dependence of metallic materials [4].

As shown in figure 1.5, the conductivity values of organic materials span a very large scale. Insulator materials as Teflon or quartz have a conductivity of  $10^{-16} \text{ S.m}^{-1}$ ; conductive conjugated polymers, e.g. doped form of polyacetylene can reach conductivity values of  $10^5 \text{ S.m}^{-1}$ , only a few orders of magnitude below the  $10^8 \text{ S.m}^{-1}$  range of the best metals.

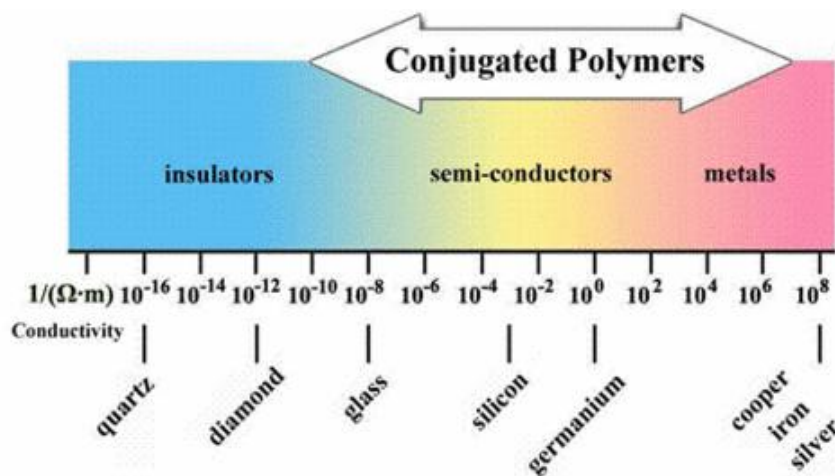


**Figure 1.5 : Conductivity of conductive polymers compared to those of other materials, from quartz (insulator) to copper (conductor). It illustrates the wide range of conductivity values shown by polymer materials.**

Metallic conductivity (and even superconductivity) exists in ionic organic systems. An example for superconductivity in organic solid state is the Bechgaard salt; an organic complex exhibiting stabilized superconductivity at low temperatures ( $\sim 1\text{-}2 \text{ K}$ ) and under pressure ( $\geq 10 \text{ kbar}$ ) [14]

with a conductivity exceeding  $10^5$  ( $\Omega\cdot\text{cm}$ )<sup>-1</sup>. Carbon materials (carbon nanotubes, graphene) can also be categorized as ‘organic’ systems, with remarkable conduction properties. We will restrict our discussion to semiconductors, emphasizing properties of small molecules and polymer materials.

## 1.2.2. TRANSPORT IN ORGANIC SEMICONDUCTORS

Organic semiconductors are organic compounds with electronic properties similar to those of inorganic semiconductors: hole and electron conduction bands and a band gap, with the key difference related to the difficulty in obtaining highly delocalized molecular states. Occurrence of current carriers originates from bonding of unhybridized p orbitals of carbon atoms in a molecular structure. Figure 1.6-a illustrates the  $sp^2$  hybridization electron configuration of carbon atom ( $C^4$ ), resulting in three  $sp^2$  orbitals equivalent in energy arranging themselves in a trigonal planar configuration ( $\theta = 120^\circ$ ) around the nucleus and one unhybridized p orbital perpendicular to the plane of  $sp^2$  orbitals (figure 1.6-b). In the molecular form, when two  $sp^2$  hybridized carbon atoms approach each other to bond, the head-to-head overlap of two  $sp^2$ -orbitals leads to a short and strong sigma ( $\sigma$ )-bond, while a pi ( $\pi$ )-bond is formed by unhybridized p orbitals approaching ‘sideways’ (figure 1.6-c, 1.6-d). The sigma electrons due to the stable and strong sigma bond are more localized and are not expected to contribute to conduction, while the pi-electrons are more mobile and can become delocalized due to the longer diffusive pi-bond. The typical few tens eV energy difference between the HOMO (Highest Occupied Molecular Orbital) and LUMO (Lowest Occupied Molecular Orbital) energy levels for the sigma bonding leads to insulating properties. The typical few eV smaller energetic difference between HOMO and LUMO in pi-bonding (figure 1.6-e), makes semiconducting properties reachable, even though these material generally exhibit low conductivity values [15, 16, 17].

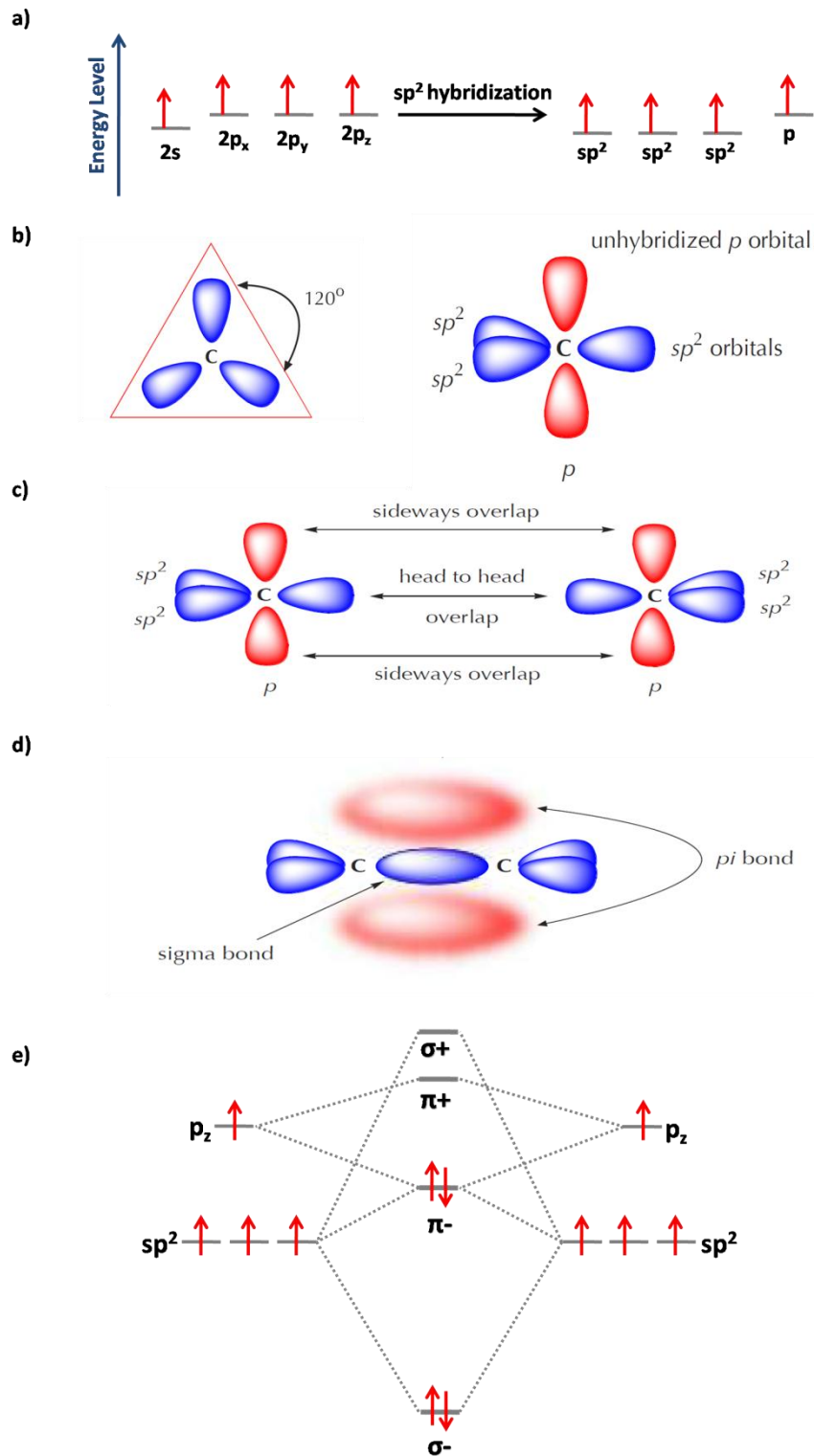


Figure 1.6 : a) electron configuration for carbon atom ( $C^4$ ) and  $sp^2$  hybridization, b) 3D illustration of triangular formation of  $sp^2$  orbitals in a plane perpendicular to unhybridized 'p' orbital, c,d) approaching of two carbon atoms and creation of sigma ( $\sigma$ )-bond by head-to-head overlap and pi ( $\pi$ )-bonds by sideways overlap, e) schematic of HOMO and LUMO energetic levels for  $C=C$  double bond.

Organic semiconductors are either long chain (polymers) like poly(p-phenylene vinylene) or short chains (oligomers, or small molecules) like pentacene and rubrene with a smaller band gap. Delocalized  $\pi$  bonds along the polymeric chain involve the formation of a conjugated backbone of continuous overlapping orbitals, extending the delocalization to several bonds length. The defects in the 1D chain also have an important role in transport properties. Charge transport in polymers occurs via two different mechanisms: transport by hopping from chain to chain and transport along the chain. Hopping consists of jumps between the localized molecular states and depends strongly on parameters like temperature, electric field, impurities in the material and charge carriers' density [18, 19, 20, 21]. This transport mechanism results in lower mobility comparing to inter bond transport via delocalized states as in crystalline organic semiconductors, making crystallinity a key parameter for understanding mobility values in polymers [22]. The inter band transport occurs in highly ordered organic materials (single organic crystals) and at low temperatures, where the mean free path of the charge carriers exceed the intramolecular distance [23, 24]. An analogy with inorganic crystals can then be developed, with a valence band arising from the overlap of HOMO states and the conduction band from the overlap of LUMO states of the molecule [25].

### 1.2.3. HIGH MOBILITY ORGANIC SEMICONDUCTORS

A large number of organic semiconductors were designed and characterized to improve the performance and quality of FETs. Field effect mobility is a key parameter for developing high performance and reliable materials, but materials with high mobilities are required to be stable in different environmental conditions like air, moisture and light exposure for application compatibility [1, 26]. Advances in organic semiconductor devices also require well-controlled manufacturing process for the gate electrode and dielectric spacer. Among high mobility materials, p-type Pentacene and n-type Fullerene are outstanding. The highest attained electron mobilities to-date are  $0.6 \text{ cm}^2\text{V}^{-1}\text{s}^{-1}$  for solution processed polymers and  $5 \text{ cm}^2\text{V}^{-1}\text{s}^{-1}$  for vacuum deposited small molecules. This last value is favorably competing with amorphous silicon (a-Si) thin film transistors (TFT) with the field effect mobility of  $0.5\text{-}1 \text{ cm}^2\text{V}^{-1}\text{s}^{-1}$  and ON/OFF ratio of  $10^6\text{-}10^8$  [1, 27].

For microcrystalline polymers, studies have shown that higher degree of crystallinity and the deposition conditions, the molecular weight of the polymer and the gate electrode manufacturing improvements, lead to higher mobility values. Designing the material to be microcrystalline, liquid crystalline or ordered through self-organization is therefore key for improving the OFET devices [26, 28]. Let us mention one example, relevant for one type of studies performed in this thesis: amorphous polymers based on triarylamine have reported to exhibit high (for disordered materials) mobilities of  $10^{-3}$ - $10^{-2}$   $\text{cm}^2\text{V}^{-1}\text{s}^{-1}$  and to be good operating with high environmental and photostability. Polytrarylamine (PTAA) derivatives were reported to have high FE mobilities up to  $6 \times 10^{-3}$   $\text{cm}^2\text{V}^{-1}\text{s}^{-1}$ , low threshold voltages, good device stabilities and continuous switching at  $120^\circ\text{C}$  without degradation [29, 30].

Recently, device operational and environmental stabilities have improved significantly as a result of availability of organic semiconductors with higher inherent oxidative stability, better understanding of the requirements for gate dielectrics, and more controlled manufacturing processes [31]. With all the improvements and progress for high performance reliable solution processed organic semiconductors, a few weak points, bottlenecks for further progress in the field, still persist:

1. Solution processed organic semiconductors cannot be fully characterized with diffraction and microscopy techniques. Their structural properties, key for transport properties, are therefore often only partly known.
2. Organic field-effect transistors are interface devices, operating typically in enhancement mode. The region where charge transport takes place, the accumulation layer, has a thickness of only a few nanometers, and is buried (therefore experimentally very difficult to characterize).
3. Due to the relatively low mobilities in organic materials the electrodes-organics interfaces are especially critical and can have a strong impact on electrical transport itself. The variation in interface properties persists despite significant optimization of material deposition techniques, e.g. solution processing, spinning, drop casting, printing, and vapor deposition.

It appears clearly that interfaces have a large importance for organic devices, and a huge research effort has been dedicated in the last 15 years to better characterize, understand and master the dielectric-organic and the metal-organic interfaces.

## 1.2.4. ELECTRONIC STRUCTURE OF THE ORGANIC SEMICONDUCTOR - METAL INTERFACES

The performance of organic field effect devices depends critically on the use of high-performance dielectrics that form active interfaces with low defect densities. Studies have shown that organic SC material achieve higher FE mobilities when in contact with dielectrics with low dielectric constants ( $\kappa$ ) rather than ones with higher  $\kappa$  [32]. This result points out the importance of elucidation of the interfacial electronic structure for organic electronic devices. The metal organic (MET/ORG) interfaces govern the charge injection at the interface between metallic electrodes and organic semiconductors and play a crucial role in the performance of organic electronic and organic opto-electronic devices. Formation of low resistance ohmic contacts with metals is always challenging for organic materials. One should combine the knowledge in the fields of surface science and electronics devices for organic molecules, to examine a MET/ORG interface, which will be extended easily to ORG/ORG or ORG/SC interfaces. The following details the interdisciplinary study on the electronic structure (energy level alignment and band bending) at MET/ORG solid interface [25].

All energy levels are referenced to the vacuum level far away from the solid ( $VL(\infty)$ ), corresponding to the energy level of an isolated electron at rest in vacuum. We simplify, for illustration convenience, the semiconducting organic thin films (or solid) as HOMO and LUMO levels, with a chemical potential within the bandgap separating these two levels (figure 1.7).

The electronic structure of an organic solid is usually mostly defined through widened energy levels of a molecule or the monomer, owing to the low density of delocalized states in the material. The gas phase ionization energy  $I_g$  in an organic solid (energy separation of the HOMO from the VL) is lower from the value for an isolated molecule, to stabilize the ions due to electronic polarization of the molecules surrounding the ions. The electron affinity of the molecules  $A_g$  (energy separation of the LUMO from the VL) is larger in the solid state than for a single molecule, due to multielectronics effect.

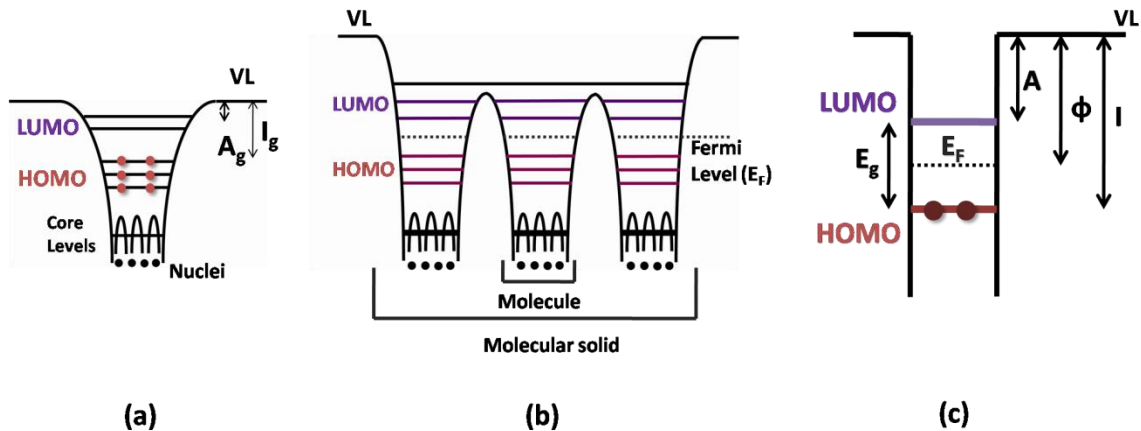


Figure 1.7 : Electronic structure with potential wells (a) a polyatomic molecule, (b) organic solid, simplified in (c).  $I_g$  : gaz phase ionization energy,  $A_g$  : gas phase electron affinity,  $I$  : solid state ionization energy,  $A$  : solid state electron affinity,  $\phi$  : work function and  $E_g$ : HOMO-LUMO band gap.

When an organic solid and a metal come into contact, the organic layer in the potential of the surface dipole of the metal has its energy levels raised for a common VL at the interface. In actual systems, due to charge transfer across the interface, redistribution of electron cloud, interfacial chemical reaction and other types of rearrangement of electronic charge a dipole layer may be formed right at the interface. With such interfacial dipole formation, there will be an abrupt shift of the potential across the dipole layer, leading to shift of virtual VL by  $\Delta$  at the interface (figure 1.8).

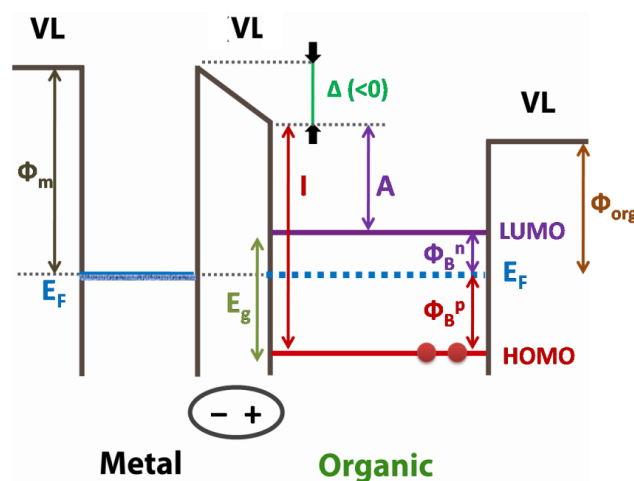


Figure 1.8 : Interfacial energy diagram related to a contact of a metal and a thin organic solid layer, with a  $\Delta$  shift of VL at the interface due to dipole layer formation.

The value of  $\Delta$  is determined by the magnitude of the dipole. More experiments are needed to investigate this effect happening at the interface thickness of few nanometers. In the field of surface science this possible shift of VL is called the change in the work function (or surface potential) of the metal.

Band bending only happens in the MET/ORG interface with thick organic layers of good semiconducting properties (with a large number of charge carriers) [33], but in general the MET/ORG interfaces do not show band bending in the tens of nm thickness range. In figure 1.8, the electronic structure at the interface for a metal and thin organic solid contact is depicted. The modification of the VL levels is important for the charge injection especially in electroluminescent devices.

The barrier heights for carrier injection at the interface for hole ( $\Phi_B^p$ ) and electron ( $\Phi_B^n$ ) can be found from figure 1.8 and are given in equations 1.8 and 1.9.

$$\Phi_B^p = I - \Delta - \Phi_m \quad (1.8)$$

$$\Phi_B^n = \Phi_m - A + \Delta = E_g - \Phi_B^p \quad (1.9)$$

If there is no VL shift at the MET/ORG interface, then  $\Delta = 0$  and barrier heights are obtained by equations 1.10 and 1.11 following the Schottky-Mott rule for simple contact MET/SC interface [34]. Values for  $\Phi_m$  and  $I$  are obtained by photoemission spectroscopy techniques and from that  $\Phi_B^p$  and  $\Phi_B^n$  are deduced.

$$\Phi_B^p = I - \Phi_m \quad (1.10)$$

$$\Phi_B^n = \Phi_m - A = E_g - \Phi_B^p \quad (1.11)$$

Barrier heights for charge injection inferior than 0.3eV ( $\Phi_B < 0.3$  eV), are similar to an optimized Schottky barrier, an example is a p-type semiconductor polymer (P3HT) on Au, where the contact resistances of source and drain are the same ( $R_S \approx R_D$ ) and depend linearly on temperature

and mobility. In high-performance OFET, contact resistance is not determined by Schottky barrier at the interface, but by bulk transport process in semiconductor near contact.

For  $\Phi_B > 0.3$  eV, the charge injection is very weak,  $R_s \gg R_D$  and the contact resistance has a very weak dependence on mobility and temperature [35].

In conclusion, the quality of charge injection at the interface depends very much on the nature of the interfaces. Vacuum depositing of organics over metals results in more suitable interface qualities, less diffusion and/or reaction, while vacuum deposition of metals over organics create a thin layer resulting from diffusion and reaction which is less suitable for charge injection. The atmosphere and chemical reactions can also affect the interfaces. Exposure to air or low vacuum or humidity results in oxidizing, adsorption or absorption of  $O_2$  or  $H_2O$ , thus increasing the contact resistance. The fabrication processes and characterizations often affect the device quality. The typical contact resistance per unit length ranges from  $10^2 \Omega.m$  to  $10^5 \Omega.m$  for conjugated polymers. Considering these values, for source/drain metallic contacts below  $1 \mu m$ , the resistance values from the equation 1.12 ( $10^8$ - $10^{11} \Omega$ ) are easily much larger than the resistance of the active channel [25, 36].

$$R = \rho \frac{L}{A} \quad [\Omega] \quad (1.12)$$

The concept of separating the active channel and MET/ORG interfaces in series resistance for explaining transport properties in a lateral device must be revisited when decreasing the length of the device. When reaching the ultimate molecular length, the two interfaces and the molecule must be treated as a single entity.

### 1.3. TRANSPORT THROUGH A SINGLE MOLECULE (1nm)

In the past few years, progress in fabrication tools and experimental techniques allowed experimental insight into electrical properties of organic materials using electrodes separation reduced down to the size of molecules, for the purpose of *Molecular Electronics* studies. Different techniques and approaches were developed and used aiming at realizing electrical contacts separated by distances not exceeding a few nanometers. The domain of research still

remains challenging, due to reaching the limits of miniaturization in fabrication and characterization and remaining control and reproducibility challenges. The previously described bulk and interface materials concepts cannot be applied in that size range. Here we review the key ingredients for understanding the transport mechanism through single molecules and present a few examples of single molecular devices experimental results.

Inserting molecules in electronic circuits was proposed for the first time in the article of Mann et al. in 1971 [37], where they studied an aliphatic organic cadmium salt with a variable chain length sandwiched between different metallic leads. They have observed the exponential decrease of conductance versus the length of aliphatic chain, as predicted by the tunneling theory (figure 1.9-left). Theory predictions for current density versus voltage characteristics were also confirmed empirically.

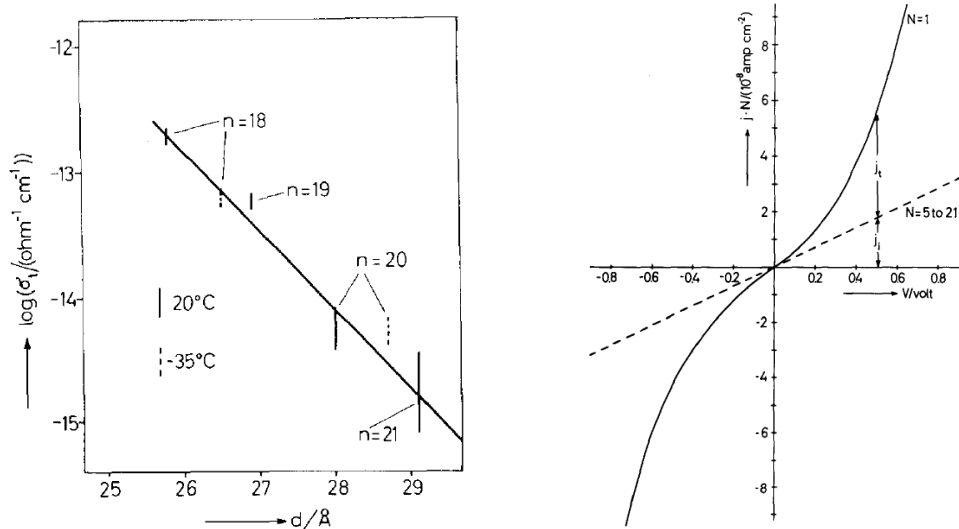


**Figure 1.9 :** Left: logarithmic plot of tunneling conductivity ( $\sigma_t$ ) vs  $d(\text{\AA})$  (distance between electrodes) for Al/S(n)/Hg. S(n) symbolizes a monolayer of the the cadmium salt of  $\text{CH}_3(\text{CH}_2)_{n-2}\text{COOH}$ . Right: Current density vs. voltage ( $j$ - $V$ ) for Al/NS(n)/Hg with 20 carbons ( $n=20$ ) and  $N$  is the number of monolayers. Solid curve ( $N=1$ ), Dashed curve ( $N=5$  to 21) [37].

The relation between the current density ( $j$ ) and applied voltage ( $V$ ) is not linear for the first monolayer ( $N=1$ ), but it becomes linear with a decreasing profile for the number of monolayers between 5 and 21. The authors concluded that the current density for  $N=5-21$  is due to impurities and for  $N=1$  is a sum of impurities and tunnel current densities (figure 1.9-right).

Following the initial work on molecular monolayers, in 1974 Aviram and Ratner described a single molecule electronic device in a theoretical study [38] proposing to use a single molecule as current rectifier. They describe simple electronic devices, diodes, based on using a single organic molecule. These molecular rectifiers are made of a  $\pi$ -donor and  $\pi$ -acceptor systems separated by  $\sigma$  barrier as in methyl ( $\text{CH}_3$ ) end group. The diode is described as the energy levels of the molecule (LUMO-acceptor, HOMO-donor) separated by tunnel barriers from the metallic electrodes, and being aligned properly for current flow for only one polarity of the applied voltage bias (figure 1.10).

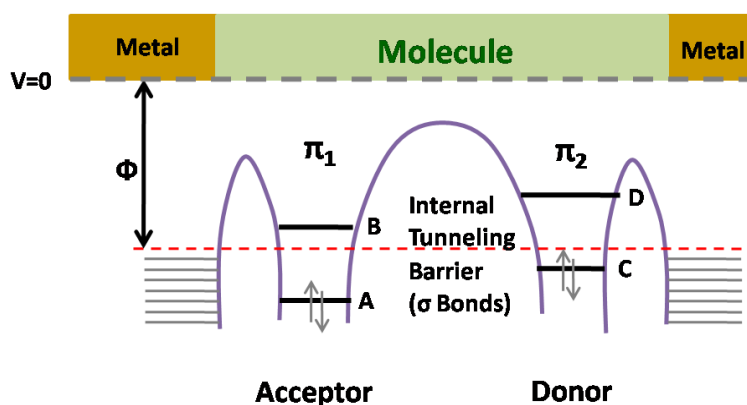


**Figure 1.10 :** Energy diagram for a molecular diode, A and C correspond to HOMO-donor and B and D correspond to LUMO-acceptor energy levels. Red dashed line presents the metals' Fermi energy level [38].

The diagram of energy levels related to a metal-molecule-metal system, and the picture of electrical transport are inspired by this model, using an electron transfer mechanism through interface tunnel barriers and intermediate energy levels related to single molecule levels (figure 1.11) [39].

As described in section 1.2., a molecule is defined by its HOMO and LUMO energy levels, the electron flow is possible if one of these levels is nearby the Fermi level ( $E_F$ ), which is in general not the case since the typical band gap ( $E_g$ ) is around few eVs. Applying a bias voltage  $V$  between the metallic leads changes their energy levels with respect to those of the molecule, thus opening the energy window making possible an electron flow through the molecule (left contact energy level rises by  $E_F + eV/2$  and the right one by  $E_F - eV/2$ , figure 1.11-b) [39]. One therefore

expects a resonance in the electronic transport related to the molecular energy states entering the voltage window imposed by the applied bias.

The tunneling rates (or escape rates)  $\Gamma_1/\hbar$  and  $\Gamma_2/\hbar$  are the typical times needed for the charge to flow between the first lead and the molecule and between the molecule and the second lead respectively. These parameters allow the quantitative characterization of current, as  $\Gamma_i/\hbar$  is the number of times an electron succeeds in being transferred through the barrier. In energy scale, the quantities  $\Gamma_1$  and  $\Gamma_2$  correspond to the coupling energy between the molecule and leads. For the case of strong coupling, the molecular orbitals overlap significantly with the electronic states of metallic electrodes, leading to a shift in molecular orbitals and a delocalized electronic wave function extended over the whole junction, with the energy levels broadened by  $\Gamma = \Gamma_1 + \Gamma_2$  (figure 1.11-d) [39].

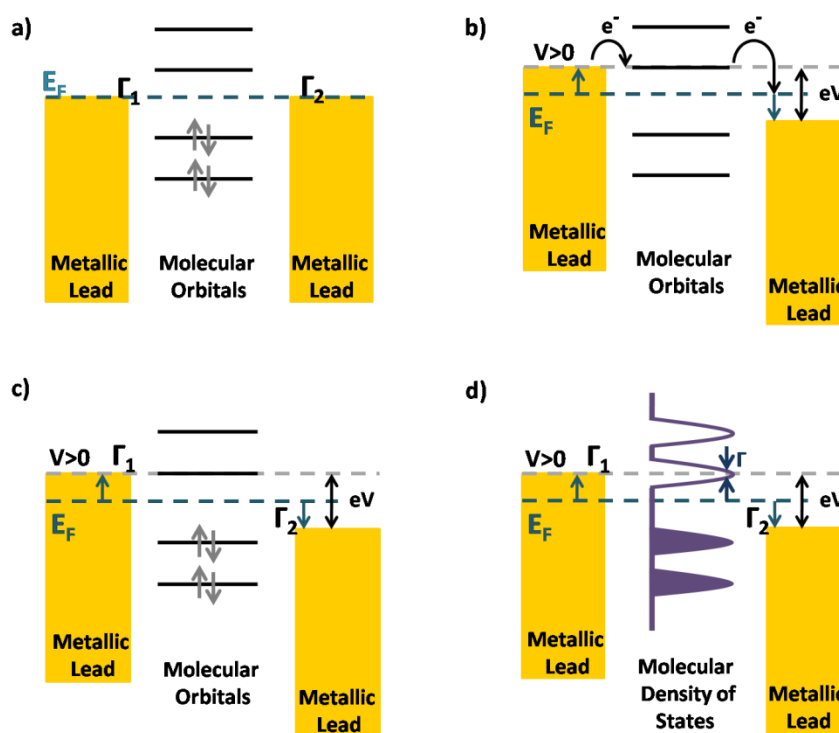


Figure 1.11 : Energy diagram of a molecule in between two metallic leads with Fermi energy  $E_F$ . a) No voltage is applied at the edges of the junction. No electron can flow as no level lies nearby the Fermi energy, b) by applying a voltage  $V$ , the leads' energies shift with respect to the Fermi energy while the molecule orbitals remain at the same position, c) Transport through a metal-molecule-metal junction, the molecule is decoupled from the leads and the levels are sharp, d) the coupling to the leads is good, hence, a broadening of the levels occurs, as well as a shift of the level, with respect to  $E_F$  [39].

A powerful method to shift the molecule energy levels with respect to the leads involve the use of an external electric field, created by a third gate electrode, in analogy with the (bottom gate) OFET described previously. This method is quite powerful for low energy coupling values and low temperatures, as it allows fine spectroscopy of the molecular states. Note however that complications, for example due to  $e-e$  interactions (e.g. Coulomb blockade effects) need to be taken into account. Owing to technical developments, for the past 15 years a significant progress has been achieved in the field of molecular electronics. Sophisticated techniques as near field microscopy and nanolithography allowed contacting single molecules to metallic leads and measuring their  $I(V)$  characteristics [40, 41, 42]. Molecular electronics nowadays has become a very exciting scientific interdisciplinary domain of research, with new challenges and directions for future.

One key question remains: are we really measuring molecules when making planar devices? This candid question has often been the source of controversies. For example, one popular method for creating planar single molecular devices involves breaking nanocontact by passing large electrical currents (electromigration technique). This method possibly creates metallic ‘debris’ or clusters that can exhibit quantized energy levels related to Coulomb blockade effects. Even though discriminating methodologies can be used, the experimentalists are still ‘shooting in the dark’ hoping for a (possibly rare) electrical behavior corresponding to the most basic theoretical models.

Scanning tunneling methods, and in particular scanning tunneling spectroscopy, can combine visualization of the molecules, with electrical spectroscopy measuring their energy spectrum properties. This tool allowed huge improvements in understanding and modeling of the metal-molecule-metal showing in particular that the model we mentioned here is very simplified [40, 43].

One of the main challenges in molecular electronics, especially when aiming at realizing devices, is to ensure that electronic response comes from the molecular property and not from a defect or contamination in the junction [44]. The ability to reliably measure the  $I-V$  characteristics of a molecular junction and relate the observed signal to the known chemical structure is a key milestone to fulfilling the promise of molecular electronics. In the next section, we present the main electrical-based method for fulfilling the task of getting a molecular fingerprint in the transport properties.

### 1.3.1. INELASTIC TUNNELING ELECTRONIC SPECTROSCOPY

Molecules are expected to be ‘soft’ materials, and exhibit low-energy excitations related to inelastic optical spectroscopy resonance. One can expect that such inelastic process can also be observed through inelastic tunneling.

A single-molecule in between metallic contacts is depicted in figure 1.12-left. For a free molecule far away from electrodes,  $\Delta E$  corresponds to the HOMO-LUMO gap and the energy difference needed for  $(N+1)^{\text{th}}$  electron regarding the  $N^{\text{th}}$  one to charge the molecule. Free molecule with  $N$  electrons has a chemical potential of  $E_i$  ( $i=1, \dots, N$ , the number of electrons), and a total electrostatic energy of  $(Ne)^2/2C$  where  $C$  is the molecules’ capacitance, and  $e$  the charge of an electron. Total energy of the molecule is thus:  $U(N) = \sum_{i=1}^N E_i + (Ne)^2/2C$  which turns into  $U(N+1) = \sum_{i=1}^{N+1} E_i + ((N+1)e)^2/2C$  after one additional electron is added to the molecule. Deducing two energies we obtain  $U(N+1) - U(N) = E_{N+1} + (2N+1)e^2/2C$  which is the electrochemical potential for charging  $N+1$  electron to the molecule ( $\mu_{N+1}$ ), thus the electrochemical potential for the charging will be:  $\mu_{N+1} - \mu_N = (E_{N+1} - E_N) + e^2/C$  where  $\Delta E = E_{N+1} - E_N$  results from the quantized-excitation spectrum of the molecule and  $E_C = e^2/C$  is the charging energy needed to overcome the Coulomb repulsion the other electrons. Once the molecule is inserted into a junction, it has a larger total capacity leading to a smaller charging energy ( $E_C$ ) due to the presence of nearby electrons [45]. The molecule, especially at cryogenic temperatures, can be treated as a quantum dot (single-electron regime:  $\Delta E + E_C \gg k_B T$ , quantum-dot regime:  $\Delta E \gg k_B T$ ,  $E_C \approx eV$ ,  $\Delta E \gg k_B T$  at 4K for a single molecule junction), where each state of the molecule can be identified and specific tunneling rates are assigned to each quantum state.

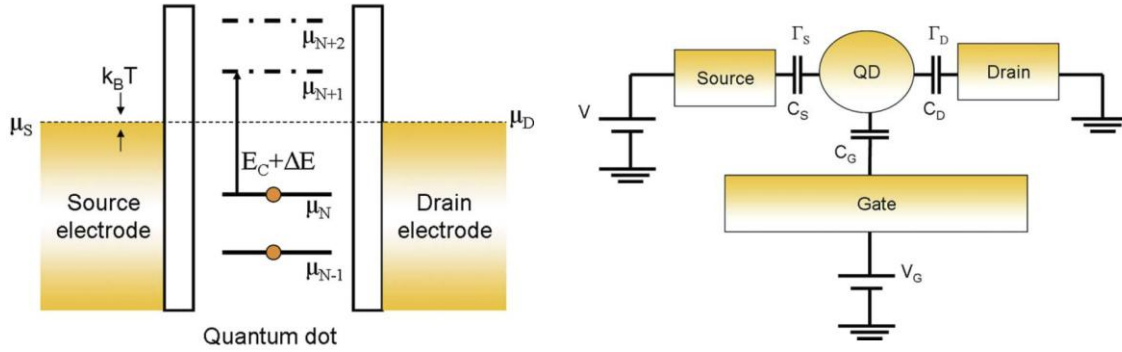


**Figure 1.12 :** Left: Energy-level alignment in a single-molecule (quantum dot) junction under equilibrium. The Fermi level (dashed line) is uniform throughout the junction. Right: A schematic of a molecule (quantum dot) in a junction. The molecule is capacitively coupled to all electrodes. Charge can tunnel into and out of the molecule only from the drain and source electrodes [45].

During the coherent tunneling transport process, electrons cross the junction via inelastic tunneling and exchange energy with the vibrational levels of the junction. At low temperatures, the vibration modes are in their ground state and the electron can only lose vibrational quanta of energy  $\hbar\omega_\alpha$  ( $\omega$  is the frequency of the vibrational mode  $\alpha$ ). When the bias  $V$  fulfills the condition:  $|V| > \hbar\omega_\alpha/e$ , then the inelastic channel causing the excitation of mode  $\alpha$  is opened. The sharp but small increase in conductance ( $dI/dV$ ) each time a new inelastic channel is opened is seen as a peak in  $d^2I/dV^2$  at  $V = \hbar\omega_\alpha/e$ . The  $d^2I/dV^2$  as a function of  $V$  is called inelastic electron tunneling spectroscopy (IETS), and therefore provides information on the vibrational levels of the junction (figure 1.13) [46]. Only a minority ( $<2\%$ ) of the electrons cross the junction inelastically and only the vibrations that modulate the tunneling probability are active in IETS, providing an active inelastic channel.

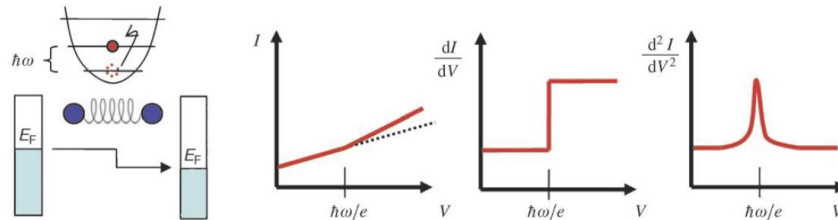


**Figure 1.13 :** Illustration of the principle of IETS: If the difference in chemical potential between the two electrodes is larger than the vibrational energy of one molecular mode, the electron can cross the junction losing one quantum of vibrational energy. This additional inelastic channel causes a small increase in conductance at  $V = \hbar\omega/e$ , better evaluated as a peak in a plot of  $d^2I/dV^2$  versus  $V$  [44].

IETS is an in situ spectroscopic measurement, unique in its ability to probe the vibrational spectrum of MET-MOL-MET junctions as well as chemical structure of incorporated molecule(s). Beyond the simple identification of molecules under study, valuable information on molecular geometry, chemical environment, the influence on the metallic electrodes and the pathways electron follow through a molecule could also be obtained by IETS, all improving our understanding of charge transport in molecular junctions incorporating complex organic systems [46].

There are several reports of studies on molecular vibronic fingerprints in junctions confirming their identity simultaneously with  $I-V$  measurements [47]. IET spectra are obtained by measuring the second derivative of the tunneling current with respect to the applied bias voltage ( $d^2I/dV^2$ ) using standard AC modulation techniques [48]. For these studies cryogenic temperatures are required to minimize the thermal broadening of electrons at Fermi level of the electrodes to enable resolution of molecular vibrations.

For example, Kushmerik et al. have reported in situ vibrational spectroscopy of MET-MOL-MET junctions containing prototypical molecular wires and determined that the tunneling charges couple strongly to longitudinal molecular vibrations [49]. Figure 1.14 shows transport properties of the molecular junction formed from a C11 molecular monolayer (C11 stands for an alkane chain with 11 carbon atoms with a thiol (SH) end, the chemical form is illustrated in figure 1.14-a top).  $I-V$  characteristics are linear over the bias range shown, steps in plots of  $dI/dV$  and peaks in  $dI^2/dV^2$  are related to molecular vibrations. The IETS spectrum is obtained by normalizing the  $dI^2/dV^2$  signal by differential conductance. Based on infrared (IR), Raman [50] and high resolution electron energy loss spectroscopy studies, the peaks in the IETS spectrum are assigned to specific molecular vibrations, i.e. C-H stretch at 362mV, CH<sub>2</sub> rocking and wagging modes at 95mV and 170mV respectively, as well as a C-C stretch at 134 mV [49, 51].

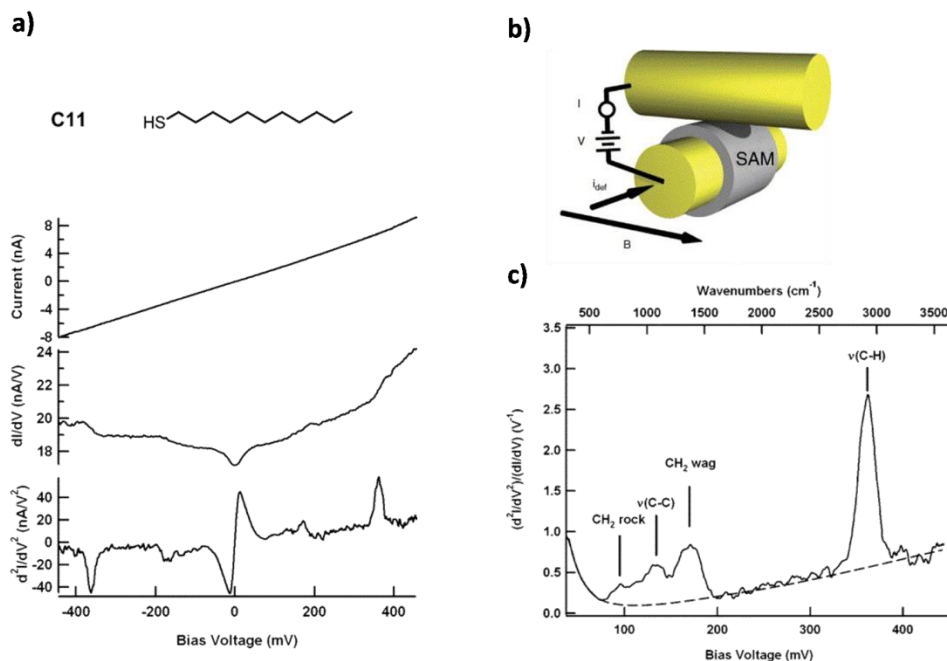


**Figure 1.14 : a) top: C11 molecule, bottom: electrical characteristics of C11 monolayer junction depicted in b) and c) IETS spectrum [52].**

Note however that these studies are rather limited to a few molecules. One can also question the adequacy of a simple quantum dot model for modeling single molecule transport. Finally, little information on the reproducibility of such measurements is indicated in the literature.

A possible methodology to circumvent the problems in measurement reproducibility of a molecule is to use statistical information, where repetitive measurements are performed, in order to extract trends or exhibit systematic intrinsic properties. The reason is mostly fundamental, as the electrical properties are very sensitive to the molecules-electrodes interactions, the position or anchoring of the molecule, its conformation, etc... Such data is obtained for example by either by opening and closing the same molecular junction in a repetitive manner, as in mechanical break junctions (MBJ) [52, 43], by investigating junctions created by scanning tunneling microscope (STM) tip [53, 54, 55], or by applying the same measurement on many samples for final statistics as in electromigration junctions (EM) [56, 57]. We present in the following section a few methods aiming at such statistical methodology.

## 1.4. MOLECULAR ELECTRONICS TESTBEDS

### 1.4.1. SINGLE-MOLECULE JUNCTIONS

#### *i. SCANNING TUNNELING MICROSCOPE (STM) BREAK JUNCTION*

Owing to the impressive technical improvements and widespread use, STM has been extensively used to study and characterize the molecular monolayers by scanning a metallic surface covered with self-assembled monolayer (SAM) of the molecule under study. The risk of this technique is the chemisorption of the SAM on the microscopes' tip. Among the many advantages of STM, one can point out the capability of measuring very low currents and the simultaneous measurement of the current and the morphology of the sample at the atomic scale. The latter allows contacting the tip to specific areas, implying the possibility of probing single molecules. Note however that a SAM is not convenient for such studies due to the large number of molecules in proximity of the tip. In typical experiments of single-molecule junctions formed by STM, the metallic tip is driven into contact with the metallic surface in a solution containing the sample molecules in rather low concentration. The junction conductance  $G$  is measured during subsequent retraction, decreasing at first with a stepwise fashion, with conductance steps values related to the conductance quanta  $G_0=2e^2/h$ , indicating a metal-metal atomic-scale contact. When breaking, one can check if preferred values of much lower conductance appear, revealing preferred conduction through molecular junctions [43, 47]. The advantage of this method lies in the statistical data obtained by re-creating new molecular junctions by a simple vertical movement of the tip. Figure 1.15 presents I-V characteristics of  $C_6$ ,  $C_8$  and  $C_{10}$  alkanethiols obtained by rapid formation of 1000 Au-MOL-Au junctions [43].

The histograms showing in the inset were made out of 1000 sets of data corresponding to conductance of the molecular junctions, for each the peaks of conductance values are marked. The I-V characteristics correspond to those peaks, and one can illustrate the decrease of current with the length of the butyl chain, confirming the idea that conduction relates to molecular interconnects [43].

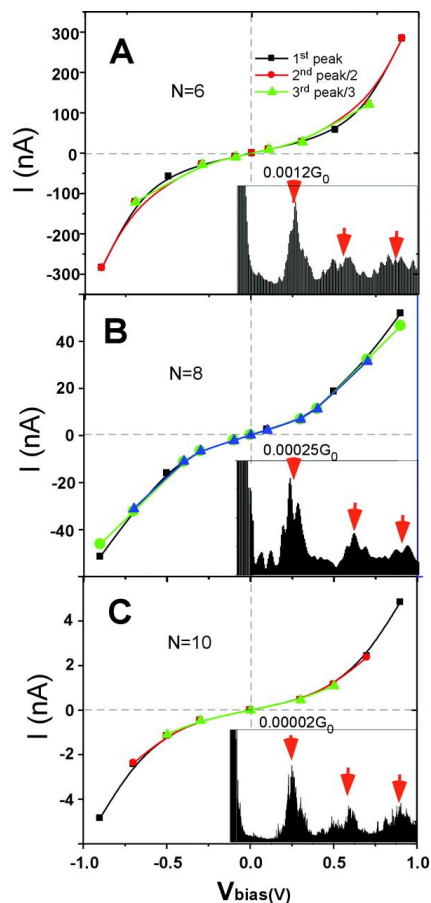


**Figure 1.15 : I-V curves for hexanedithiol (A), octanedithiol (B) and decanedithiol (C). The inset is a conductance histogram for each molecule [43].**

### *ii. MECHANICALLY CONTROLLABLE BREAK JUNCTIONS (MCBJ)*

MCBJ were developed for the first time in 1992 [58]. The technique consists of a suspended metallic bridge fabricated by lithography or a metallic wire with a narrow constriction on a gap, etched in a layer of polymer or oxide preferentially deposited on a flexible substrate. The substrate is put in a three-point bending geometry where the inter-electrodes separation can be modified in the nm range by means of micrometer displacement of a piezoelectric push rod from below by micrometric precision while the counter supports at the periphery keep the sample in a fixed position (figure 1.16) [59].

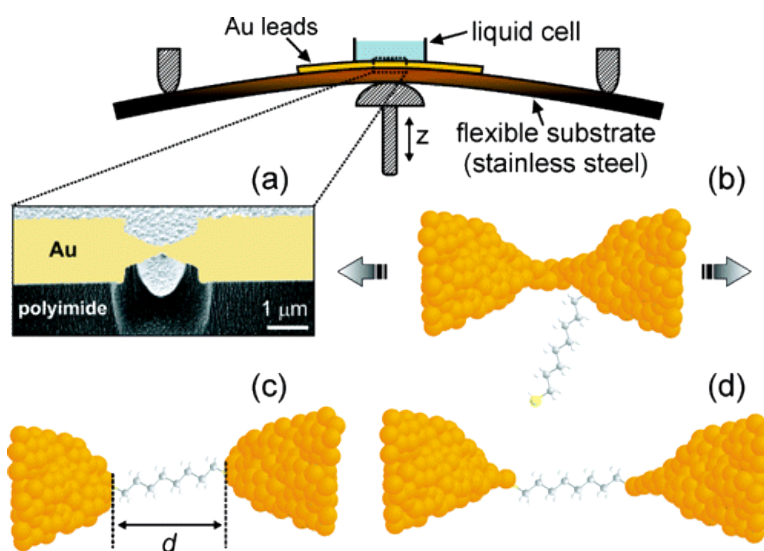


**Figure 1.16 :** (a) Schematic of the MCBJ principle with a liquid cell and SEM micrograph of the Au nanojunction. (b-d) formation of a MET-MOL-MET bridge [59].

Bending the substrate results in stretching the suspended metallic bridge, which shrinks until it breaks and a gap of size  $d$  forms (Figure 1.16). The main advantage of MCBJ is the impressive accuracy in controlling the size of the gap (subnanometric) making them perfectly suitable to ‘catch’ single molecules of given length. In addition, bending reversibility of the substrate loops gives access to repetitive measurements over a single junction. Figure 1.17 presents representative  $G(z)$  curves of 100 consecutive open-close cycles for five different samples, both in pure mesitylene and in 1mM solution of octanedithiol in mesitylene. They correspond to the variation of conductance versus piezoelectric rod displacements and indicate that preferred conductance values relate to average conduction through molecular contacts.

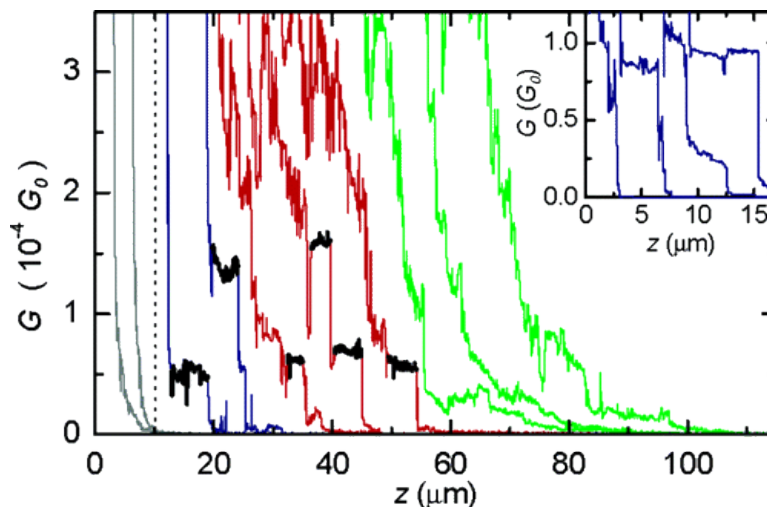


Figure 1.17 : Variation of conductance during the breaking process of a junction in pure mesitylene (left of the dotted vertical line) and in a solution of octanedithiol in mesitylene (right). Inset: examples of plateaus close to  $1G_0$ , corresponding to one atom gold contact [59].

### *iii. SUMMARY*

Despite the advantages and motivations of molecular interconnects in electronic applications, the realization of molecular devices is still limited by fundamental and technological bottlenecks:

- ❖ Strong instabilities at high temperatures are very difficult to avoid, often limiting the studies to low temperatures, especially when low molecules-electrodes interactions are expected or targeted [60].
- ❖ The devices or active molecules can suffer from solvent sensitivity. The oxygen and moisture limiting endurance of organic electronics devices are expected to be even more detrimental to molecular electronics setups.
- ❖ Single molecule electronics, with the advantage of providing precise data for transport properties of single molecules as well as less interface resistance comparing to FET devices, is still in need of large body of experiments along with developing single-molecule detection and characterization techniques. As described in 1.4.1.i for STM molecular break junctions, the single molecule transport data is presented via statistical histograms obtained by averaging over repetitive formation and measurement of molecular junctions (figure 1.15). The growing need for a robust and stable molecular device with reproducible properties not accessible via single-molecule devices points out

the importance of studying molecular devices with a few number of incorporated molecules, described in the next section.

One possible alternative to performing statistics over repetitive measurements is to perform reproducible measurements on a statistical ensemble of molecules. This compromise between single nanoscopic elements and large-scale devices is described below.

## 1.4.2. MOLECULAR JUNCTIONS OF A FEW MOLECULES

The interest towards a robust device led to transport studies over a molecular monolayer (SAMs). To this aim, several experimental techniques were designed and developed, e.g. conductive atomic force microscopy (CAFM), hanging mercury drop electrode (HMDE), 2D network of nanoparticles, nanopores and using intermediate sized particles. In the following CAFM, mercury drop and intermediate sized particle techniques are reviewed [61].

### *i. HANGING MERCURY DROP JUNCTION*

Hanging mercury drop electrodes (HMDEs), with well-defined area, were coated with molecular monolayers [62] at first to mimic biological membranes [63]. First experiments on electronic properties of molecular monolayers were performed using mercury as top contact onto a SAM [60, 64]. Formation of Hg-SAM-MET molecular junction was obtained by terminating both electrodes with Hg drops contacting in a glass capillary, or by using one Hg drop as the top electrode and a metallic layer as the bottom electrode. Due to the simplicity of the second technique the same mercury drop can be used to make several junctions on the same location of the bottom contact repeatedly, as well as forming several junctions on different parts of the substrate or other substrates, providing rapid checks and statistics over a large amount of reproducible data in a short time for different situations. Figure 1.18-b shows typical I-V curves obtained by two different experiments from Hg-C12-C12-Hg junctions (C12 is dodecanethiol) [64, 65, 66].

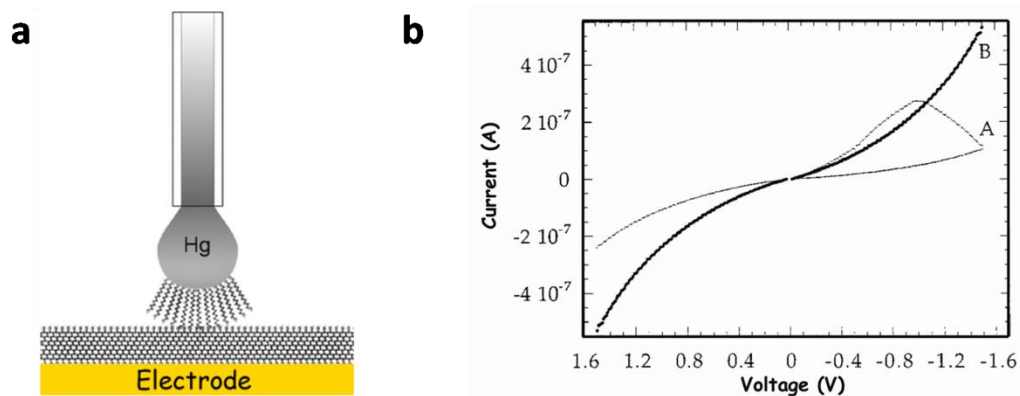


**Figure 1.18 : a) Hanging mercury drop experiment representation, b) I-V characteristics obtained from two different typical Hg-C12-C12-Hg junctions [65, 66].**

The C12 bilayer prevents Hg adsorption by Au film through a monolayer and avoids creating a short due to high affinity of Hg for Au. This explains why this type of experiments often relates to measuring a bilayer. There are other parameters affecting the results: the roughness of the bottom electrode is a critical factor, since the abrupt changes in height are not compensated by the Hg drop, the solvent for the SAM may remain partially in the junction or the contact area maybe locally distorted [66].

### *ii. CONDUCTING PROBE ATOMIC FORCE MICROSCOPE (CP-AFM)*

In a CP-AFM, a conductive probe is put directly in contact with the molecules adsorbed on a conductive substrate/electrode (figure 1.19). Applying a DC voltage between the tip and the substrate allows access to transport properties of a number (10-1000) of molecules and monitoring the tip oscillation provides a diagnostic of the tip, effectively touching the substrate. The diameter of a conductive AFM tip is significantly larger than a STM tip (a few tens of nm), thus involving electrical contacts to several molecules. This allows averaging effects, but makes the knowledge of the conductance per molecule very approximate. An example of I-V characteristics of alkanethiols with different lengths on Au substrate measured by Au coated AFM tip is presented in figure 1.19-b. The whole measurement was performed under the constant force of 2nN. The decrease of conductivity with the increase in butyl chain length is deduced from the plot (figure 1.19-b) [61, 67].

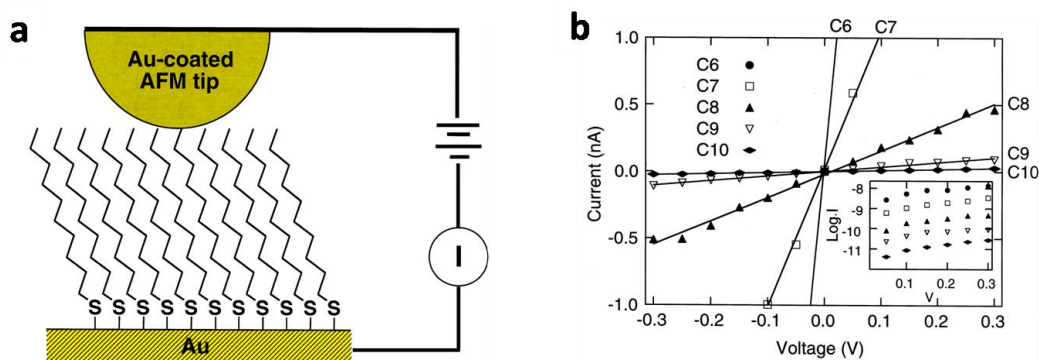


Figure 1.19 : a) Schematic of molecular junction with a CP-AFM, b) current-voltage characteristics for alkanethiols with different lengths on a Au substrate measured by a CP-AFM [67].

### iii. NANOPARTICLE BRIDGE MOLECULAR JUNCTION

A few reports of nanoparticle (NP) bridge junctions fabricated by depositing NPs over SAM-covered metallic electrodes separated by a small gap (less than the diameter of NP) [61] can be found in the literature. Studies have reported simple methods to control the formation of metallic nanowires and chains of desired length and diameter by trapping of Au NPs in between the gap by applying an alternating electric field [68].

Figure 1.20-c shows I-V characteristics of the test molecule (figure 1.20-a lower image)-nanoparticle assembly for a single nanoparticle trapped over the gap [69]. The obtained data is in qualitative agreement with previously reported data on the test molecule. This system contains two arrays of molecules connected in series. By selectively forming the SAM on only one electrode, the assembly of a single array of molecules is also possible.

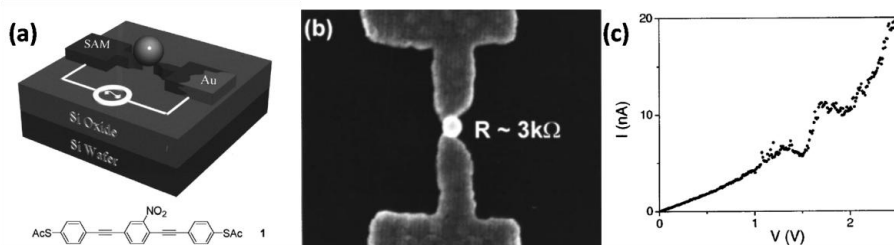


Figure 1.20 : a) Schematic of a molecular junction created by nanoparticle AC trapping, b) SEM micrograph of nanoparticle trapped in between nano-electrodes exhibiting a resistance of about 3KΩ, c) I-V characteristics of the device [69].

### 1.4.3. TRANSPORT THROUGH MOLECULES IN 10-100nm SIZE RANGE, THE METHODOLOGY OF INTERMEDIATE SIZE

The previously described molecular junctions created by NP trapping present a very interesting technique of molecular junction formation. However the nanometric gaps require sophisticated lithography and electromigration fabrication techniques and each device (MET-MOL-NP-MOL-MET) needs an electronic microscope observation for the estimation of number of incorporated NPs and connected molecules. The stability of the device, its potential breakdown during measurements and imaging reduces the efficiency of the fabrication process, usually involving a long effort for few convincing samples. This NP is nevertheless the best illustration of the strategy we will propose in this thesis: sub-100 nm size using top-down lithography should be reconciled with the 1nm molecular size range using an intermediate-size conducting medium. Increasing the gap size brings several advantages, detailed in the following section.

#### *i. WHY 10-100nm?*

Molecular junctions in the 10-100nm range have sizes midway between organic FET devices and single molecule devices. Not much research has been invested in this domain despite several advantages. Inspired from bulk organic transistors, intermediate sized molecular junctions are expected to be more robust and exhibit improved electrical and environmental stability when compared to molecular junctions. Electrodes fabrication in 100nm is simple and does not necessitate sophisticated lithography techniques, thus saving time with increasing efficiency.

The scale also makes possible the possibility of (in-situ) optical detection of the realization of molecular junctions, if intermediate size particles are large enough or allow enough contrast for detection. A well-set optical microscope can reach 200-300 nm resolutions, and objects down 30 nm size can be detected if their contrast is sufficient.

One inspiring result from the literature involves the use of micron-sized intermediate sphere for the formation of molecular junctions [70]. The authors reported transport measurements for magnetically assembled microsphere junctions (figure 1.21). IETS was performed simultaneously to electrical measurements to compare three different molecular monolayers [71] (figure 1.22). We will show our methodology reproducing their idea in more detail in a following results chapter.

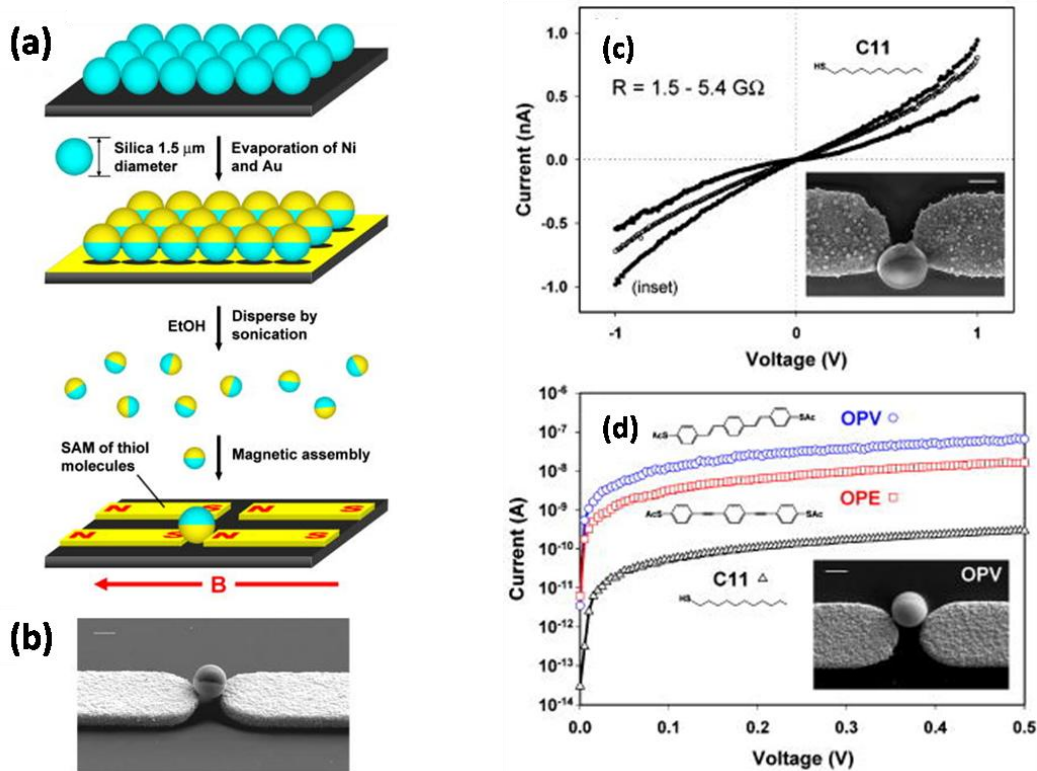


Figure 1.21 : a) formation of molecular junctions by magnetic trapping of intermediate size half metallic clusters over the SAM coated Au electrodes, b) SEM micrograph of a trapped particle over a gap (scale is 1μm), c) I-V curve related to a microsphere junction with C11 molecules, d) I-V curves for microsphere junctions for electrodes covered with SAM of C11, OPE and OPV.

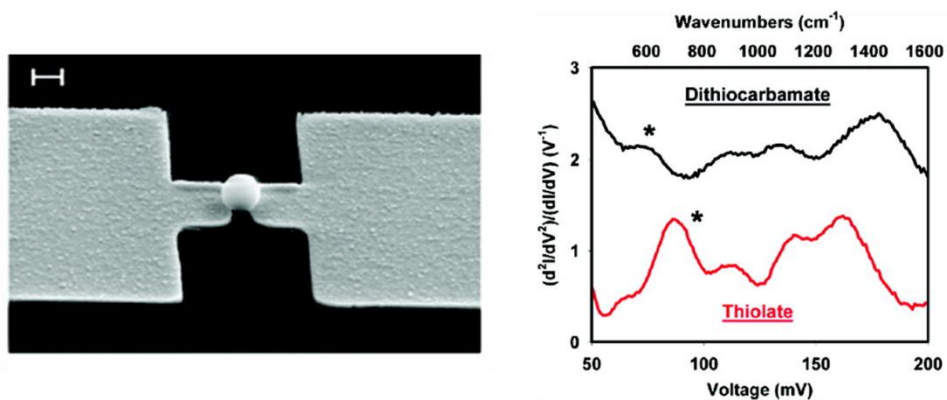


Figure 1.22 : Left: SEM micrograph of a magnetic particle trapped over nanoelectrodes covered with SAM, right: comparison of alkanethiolate and alkyl-dithiocarbamate IETS “fingerprint regions” from 50 to 200mV bias [71].

#### 1.4.4. SUPRAMOLECULAR ELECTRONICS

Another way of building molecular electronic devices using bottom-up approach in 10-100nm range is to use molecules as building blocks to construct supramolecular structures fitting in the gap size. Supramolecular chemistry, deals with developing techniques for synthesizing and characterizing ultralarge molecules and molecular assemblies (nanostructures) of different sizes and shapes in the range of 1 to 100 nm as seen in biological systems. In general, chemical synthesis of such structures follows four main strategies: (i) controlled formation of covalent bonds, (ii) covalent polymerization, (iii) self-organization, and (iv) molecular self-assembly [72]. The fourth strategy being the most relevant to nanostructure construction; molecular self-assembly is the spontaneous assembly of molecules into structured, stable, noncovalently joined aggregates.

Biological self-assembly provides striking illustrations of thermodynamically-stable architectures, including tobacco mosaic virus, DNA and numerous multimeric proteins [73]. Being inspired from biological structures, advanced materials for molecular electronics could be obtained by programming  $\pi$ -conjugated molecules into self-assembled nanowires in solution and in the solid state. An example of a supramolecular electronic device was reported on an individual self-assembled nanotube (14 nm wide) positioned across 180nm gap made by Pt nanoelectrodes on a SiO<sub>2</sub> substrate (figure 1.23) [74]. Amphiphilic hexa-peri-hexabenzocoronene, self-assembles in THF into nanotubes with aspect ratio greater than 1000. Oxidation of the tube with NOBF<sub>4</sub> changed its electrical characteristics from insulator to ohmic conductor having a resistance of 2.5 M $\Omega$  around ambient temperature, comparable to inorganic semiconductor tubes. Using the supramolecular design rules, nanowires can be created from almost any polymeric and oligomeric  $\pi$ -conjugated systems, with the controlled transfer to specific surfaces, however no methodologies have been reported to date to connect nanowires to electrodes [75].

Another key point, not discussed in the literature about supramolecular electronics, involve the key importance of the contact resistance. As previously mentioned, organic interconnects of around 100 nm length should mostly involve contact resistance. This makes, for example, the perspective of realizing a OFET-type device very challenging.

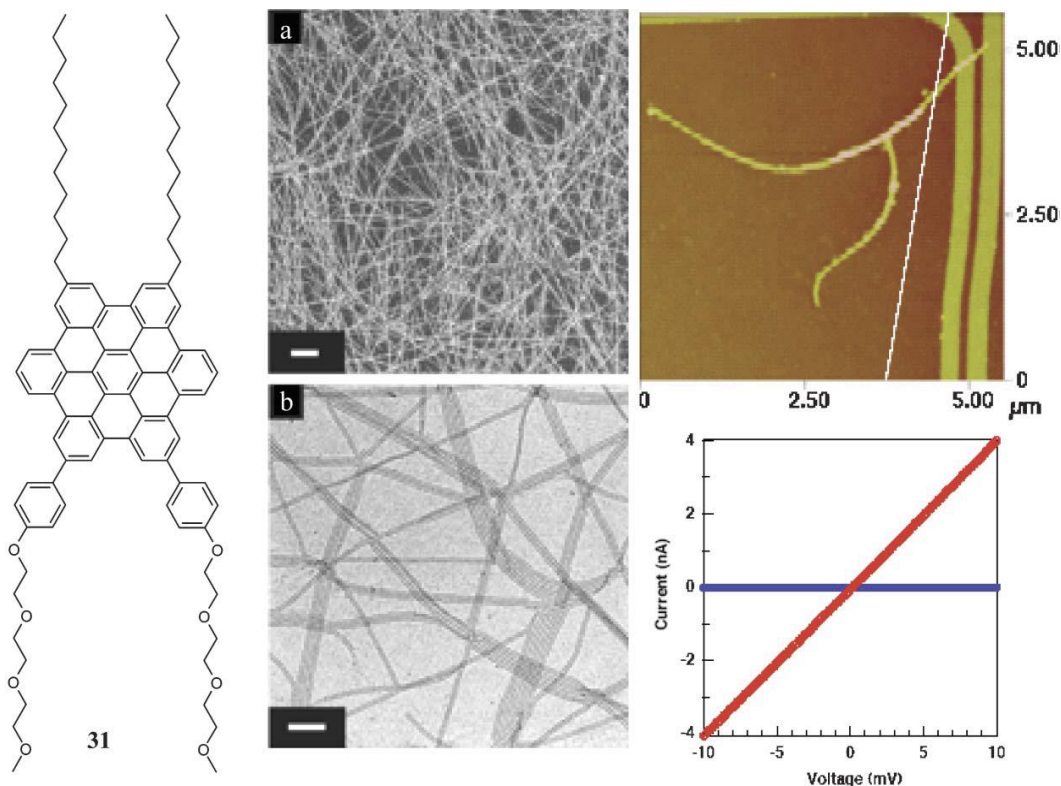


**Figure 1.23 : Amphiphilic hexa-peri-hexabenzocoronene 31 which forms tubes that can be placed between two electrodes with current voltage characteristics.**

## 1.5. MOLECULAR ELECTRONICS SWITCHING DEVICES

As previously mentioned, the unambiguous electrical information of transport properties involving molecular properties remains a challenge. The vast majority of the experimental results involves ‘boring’ molecules (alkanethiols), mostly used as dielectric spacers, and playing the role of the equivalent of a tunnel barrier, of properties modified by the choice of the length of the aliphatic chain. The simplicity of the molecules illustrates the difficulty in the experiments, often focused on series of identical molecules, with one varying parameter (the length of the chain for the alkanes example). Active or tunable molecules are highly desired, for the purpose of making a device with properties directly inspired by the intrinsic properties of the molecule. In this spirit, switching molecules are becoming of increasing interest, as unambiguous fingerprint of molecular electrical transport properties, and for creating tunable devices [76]. Molecular switches are functional molecules in which the electronic communication can be controlled by external stimuli. The possibility of designing a functional molecule using chemical expertise has made possible several type of molecular switches very interesting for applications, including

mechanically interlocked switches (rotaxanes and catenanes), redox-active molecules and photochromic switches (azobenzene and diarylethenes) [76]. A large body of ongoing research and techniques has been developed to probe these molecules both individually and in self-assembled monolayers (SAMs) [77, 78, 79]. Recognition of molecular identity in a molecular electronics device will be possible by taking advantage of switching properties of these molecules reflected in the detected signal. Devices based on switchable molecules could function as memory elements with very advantageous properties [76]. For a better understanding to basics of molecular switching, an introduction to two-state systems is given in the following.

### *i. TWO-STATE SYSTEMS*

A molecular switch has two isomeric states that can be controllably converted to each other by some external perturbations. The switching behavior is detectable in an electronic device when each isomeric state exhibits significantly different conductance properties from the other one. The generalized diagram of potential energy surfaces is depicted in figure 1.24 [76]. The reaction coordination-axis presents the physical quantity that undergoes a change during the switching process (e.g. internal torsion angle between two benzene rings). Each minima in the ground state potential energy corresponds to an isomeric state, one of them is stable while the other one is metastable. For the switching to occur, the energy barrier between the two minima  $\Delta E_{\text{act}}$  should be overcome by an external perturbation or stimulus. After stimulation, the molecule goes to its excited state, followed by relaxation and conversion to the other form, or by conversion in the ground state. Excitation can be performed in different switching mechanism, e.g. current-induced switching obtained by continuous excitation of molecular vibrations by transported electrons, field-induced switching occurs by exposing the molecule to a high electric field and non-selective switching resulting from heating the molecular system.

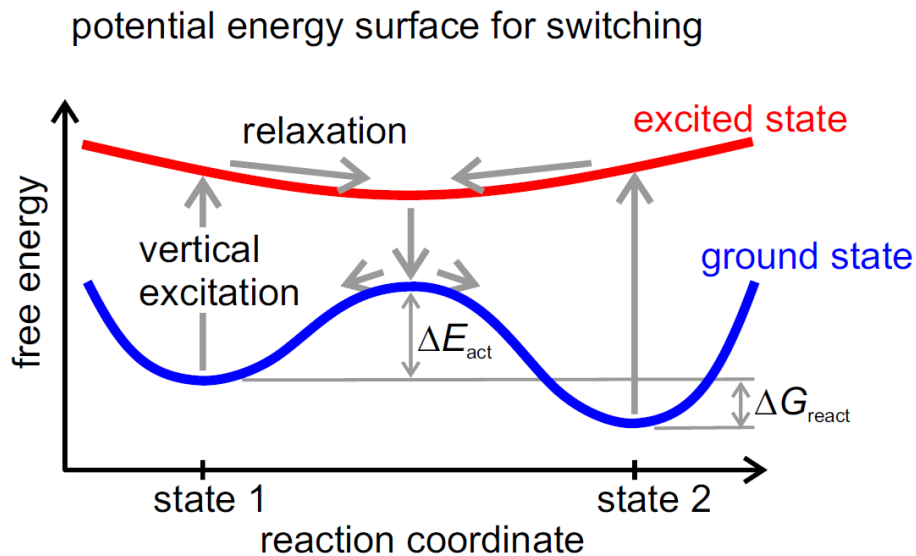


Figure 1.24 : Typical potential energy surface of a two-state molecular switch [76].

## ii. PHOTO-SWITCHABLE SYSTEMS

Photo switchable molecules are of particular interest, as they involve non-electrical method to induce the transition, limiting possible artifacts in electrical characterization experiments. The molecules undergo a procedure called photoisomerization or stereoisomerization which is a change in their three dimensional molecular structures upon photon absorption and relaxation to the other energy minimum. Regarding the potential energy state diagram of a two-state system, the reaction coordinate of the molecule in the excited state changes while the molecule goes through relaxation, followed by a transition to the ground-state where the system relaxes to one of the two minima. If the final minima state is different from the original one, then photoisomerization has occurred. The energy surface of the excited state has a strong effect on the switching rates. One of the examples of photoisomerization, is the well-known cis-trans switching in the family of azobenzene molecules [80, 81, 82, 83], which has been investigated thoroughly in solution and devices due to their potential use for applications e.g. molecular light sensors and also because they are interesting for fundamental research and understanding of molecular switching systems.

### 1.5.1. SPIN TRANSITION SYSTEMS

Spectacular example of molecular bistability, is the spin crossover (SCO) phenomenon, occurring in transition metal complexes (i.e. Iron, Nickel, Cobalt) with  $3d^n$  ( $4 \leq n \leq 7$ ) electronic configuration triggered by external stimuli as temperature, irradiation and pressure [84]. Spin crossover is a cooperative transition between the paramagnetic high spin state (HS,  $S = 2$ ) and the diamagnetic low spin state (LS,  $S = 0$ ) of the active metal ions [85, 86]. The transition is abrupt and can exhibit a thermal hysteresis, which brings a memory effect to the system.

These systems are thus ideal candidates for permanent memory elements applications [87, 88, 89]. Investigations on Iron (II) based SCO compounds imply that the collective transition is often accompanied by a change in the dielectric constant of the material, a change of color and a modification of the volume [90]. For these changes to be reflected in the electrical signal [91], the collective behavior of is essential for observing a hysteresis. Measurement on an assembly of molecules is therefore necessary, in addition to the advantages for creating a robust device with reproducible properties [92]. In chapter V we report fabrication routes of iron (II) based SCO nanoparticles with a thermal hysteresis for LS→HS transition above room temperature and their manipulation in order to position them over Au electrodes and monitor their electrical signal while the spin transition is triggered by heating [93].

## 1.6. CONCLUSION

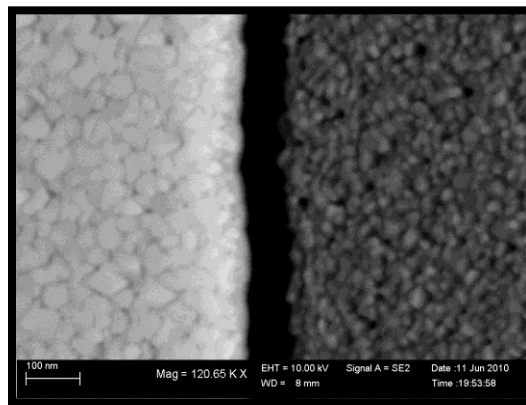
A brief review on the field of electrical transport through organic spacers has been given. Being inspired by robust device properties in bulk organic devices (FET) and the progress made in the field of single molecule electronics from device fabrication and miniaturization to simultaneous spectroscopy techniques for distinguishing the molecular identity, we focus our research on molecular electronics approach in the 10-100 nm range.

This size range is difficult to reach for organic electronics devices, mostly owing to the overwhelming interface resistance expected in this size range. This size range is not popular for molecular electronics, due to its inadequacy with the much smaller molecular size. Even though bottom up chemistry can be used to construct very large molecules, for example using supramolecular chemistry [75] or polymer synthesis can allow very long molecules to be built, the low intrinsic conductivities of these materials make the studies quite scarce.

From the series of experiments presented in this chapter, we can learn from past results, to keep in mind the key criterions for choosing and modeling the system under study:

- ❖ For molecular electronics experiments, switching molecules are ideal test systems, preferably using photochromic systems, where the light-induced change is ensuring at best the absence of artifacts.
- ❖ Quantitative information about the success rate of the experiments is key. A ‘robust’ device should involve typically better than 90% success rate.
- ❖ One should identify how to limit the interface resistance, or at least keep in mind that interfaces are the main component of the circuit we are measuring when realizing a device in the sub-100 nm size range.

## CHAPTER II: ELECTRODES PATTERNING AND EXPERIMENTAL SETUP



This chapter focuses on realizing reliable and convenient electrical interconnects capable of addressing sub-100nm nanoscale objects. We present a simple and versatile patterning procedure for the reliable and reproducible fabrication of high aspect ratio ( $>10^3$ ) “nanotrenches” separating macroscopic electrodes, with lengths down to 20nm and widths of several tens of microns. The process involves standard optical lithography techniques and allows parallel processing of many junctions, making it easily scalable and industrially relevant [136, 137]. We also present a magnetic trapping technique for positioning nanoscale objects or molecular functionalized elements over the nanotrench [93]. Finally, the optoelectronic setup where the experiments are performed is detailed.

## 2. STATE OF THE ART, NANOTRENCH FABRICATION

### 2.1. INTRODUCTION

Hereby is presented a recent developed process to design wide electrodes (potentially up to millimetre scale), separated by a short distance (down to 20 nm) corresponding to typical thickness in organic vertical structures. There is an extensive literature on nanofabrication techniques for realizing nearby electrodes, and it is clear that such size should be easily reachable by e-beam lithography tools [94]. One should however emphasize that the critical issue of obtaining high aspect ratio (HAR) gaps below 50 nm is an extremely challenging task, necessitating state-of-the-art electron beam equipment, robust e-beam photoresist process which might suffer from reliability issues when extremely high aspect ratios are desired. To this date we are not aware of reports on reliable HAR gaps ( $>10^3$ ) below 50 nm achieved by electron beam fabrication steps [95]. More importantly, the use of a sacrificial layer becomes necessary if aspect ratio exceeding 10-100 are needed. Layers made of aluminium oxide, chromium oxide, or molecular monolayers are reported in the literature [96, 97, 98, 99]. All these techniques suffer from the necessary etching process, which needs to be critically selective and critically efficient. Realizing HAR gaps devices becomes critically important when materials with intrinsic large resistivity are investigated. In the field of nanoelectronics, materials with sheet resistance of high values are commonly encountered [100]. Hopping transport makes low temperatures measurements critical and becomes a practical limitation to studies. There is therefore a need for realizing planar electrodes interconnects with large HAR, exhibiting good interface resistance, and compatible with low and high impedance systems investigations [101].

One industrially attractive approach that does not rely on electron beam lithography, maximizes the reliability for HAR trenches, and minimizes contamination, is the so-called shadow edge evaporation method. This technique has been used previously to make nanogaps of very small width (around 100 nm) to contact single entities, or to make a template for nanowires and nanochannels patterning [102, 103].

In this work a process has been developed using standard optical lithographic only to make HAR gap devices consisting in two planar electrodes separated by a “nanotrench” 20 to 100 nm wide and up to 100  $\mu\text{m}$  in length , i.e. with a ratio reaching  $5 \times 10^3$ . This ratio can be straightforwardly increased by 1-2 orders of magnitude by using an inter-digitized geometry, or by patterning longer electrodes, as the process is based on a simple geometrical effect which can be effective on theoretically infinite length, as it would be only limited by the optical lithography capability and wafers intrinsic defects. Avoiding the use of more sophisticated lithography techniques makes our fabrication strategy more relevant for industrial scaling up and it’s very practical for speeding the necessary electrodes fabrication [104, 105].

## 2.2. NANOTRENCH ELECTRODE FABRICATION

The simplicity of the geometrical effect used in this process allows us to realize nanotrenches that are reproducible, uniform all along the micrometric length of the gap, and without resist contamination into the gap area. Gaps down to 20 nm on several micrometers long length are reproducibly obtained, reaching locally distances of the order of 10 nm. Several tens of samples batch with gap sizes below 100 nm and lengths ranging from 2 to 100  $\mu\text{m}$  were routinely made mostly targeting gap values around 80nm. These nanotrench devices were obtained successfully on oxidized silicon wafers from [www.si-mat.com](http://www.si-mat.com) (originally 325-375 $\mu\text{m}$  thick silicon wafers covered on both sides with 550nm of thermal silicon oxide, cut into 25mm $\times$ 25mm squares with a diamond tip scribe), or 25mm $\times$ 25mm 130-170 $\mu\text{m}$  thick glass or quartz substrates from [www.emsdiasum.com](http://www.emsdiasum.com) compatible with optoelectronic measurements.

(The glass/quartz substrates correspond to microscope coverglass slides, for which the optical microscopy objectives correction is optimized)

## 2.2.1. ELECTRODE PATTERNING

In order to take advantage of edge-mediated shadow mask evaporation, the electrodes were patterned and fabricated in two consequent steps of optical lithography.

The micro fabrication was carried on in the class 1000 cleanroom (class 100 for the lithography section) equipped with an MJB4 (SUSS MicroTec) mask aligner, an electron beam evaporator, MEB 550S (PLASSYS), for metallic deposition and several optical microscopes for inspection.

We chose the AZ<sup>®</sup>5214E photoresist (from Microchemicals GmbH) with image reversal properties, following the standard process from the manufacturer.

The first patterned electrode will serve as a shadow mask for creating the gap. Thus straight and well defined edges are critical factors directly affecting the gap quality. The choice of photoresist was therefore motivated by its negative profile resulting in well defined and smooth edges after lift-off (figure 2.1 and figure 2.2). A step of photoresist edge bead removal was also added after the soft bake and before the first exposure to get a better sample-mask contact resulting in minimizing the outcome wavy shape of straight lines on the mask due to UV diffraction.

The optical lithography process is summarized below:

- Substrate cleaning by sonication and acetone-isopropanol standard washing.
- Oxygen plasma treatment for organic residues removal (100 Watts O<sub>2</sub> plasma for 20 minutes).
- Spin coating of the photoresist @ 4000 rpm for 30s resulting in 1.4 μm thick resist layer.
- Prebake for 2mins on a hotplate at 120°C.
- Exposure time 2.5s under 365nm UV illumination.
- Hard baking for 1.5 minutes at 120°C.
- Flood exposure for 30s, for resist image reversal.
- Development, in AZ<sup>®</sup>726 MIF photoresist developer during 25s, followed by extensive rinsing in distilled water, and nitrogen drying.

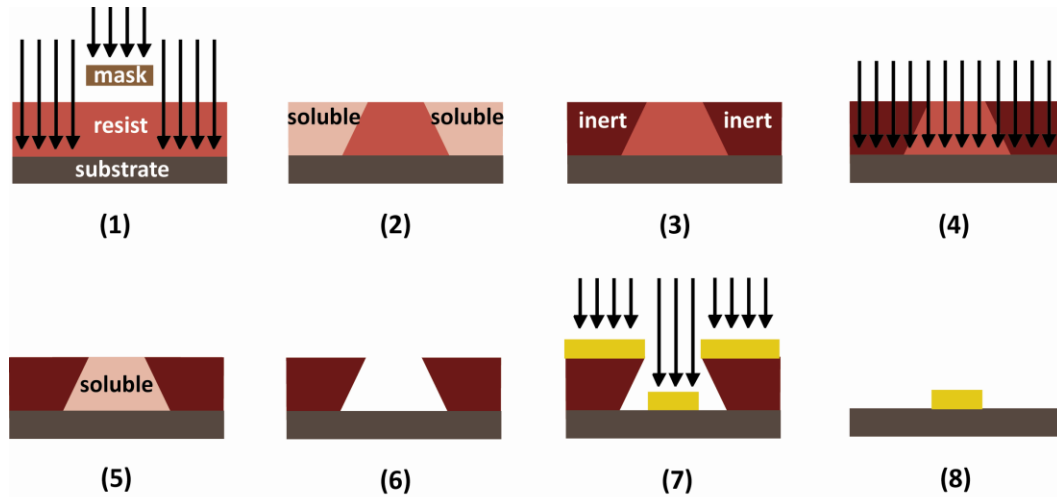


**Figure 2.1 : Microfabrication, using image reversal process followed by lift-off, (1) exposure through a positive mask, the first exposure parameters adjust the final undercut, (2) exposed areas become soluble in developer, (3) reversal bake cross-link the exposed area, the unexposed area remains photo-active, (4) The flood exposure without a mask, (5) not-exposed area becomes soluble, (6) after developing the first exposed area remains with desired undercut, (7) metallic film evaporation, (8) lift-off.**

The exposure time was calculated from the UV illumination intensity ( $\approx 14.9 \text{ mW.cm}^{-2}$ ) of the mask aligner, it varied from 2.3 to 3.6 seconds for the first exposure, in order to reach a dose of  $\approx 45 \text{ (mJ.cm}^{-2}\text{)}$ , optimum for our photoresist.

Exposure time is determined by equation 2.1:

$$\text{Exposure time (s)} = \frac{\text{Dose } \left(\frac{\text{mJ}}{\text{cm}^2}\right)}{\text{Intensity } \left(\frac{\text{mW}}{\text{cm}^2}\right)} \quad (2.1)$$

Optical microscope inspection reveals the adequacy of developing time as well as the edge line profile. The metallic deposition is performed in an electron beam evaporator. After the evaporation, the samples go through lift-off step in acetone with mild agitation for about 30minutes, then rinsed in acetone, isopropanol and dried under nitrogen flow.

The substrates with the first electrode pattern go again through oxygen plasma treatment. This step is of high importance since it removes the collar resist possibly sticking to the metallic edges due to the lift-off of the first electrode. This also ensures that during the second lithographic step, the nanotrench area is not exposed to reticulated resist. This is of critical importance if molecular

electronic studies are envisioned, as possible residue from the reticulated resist after lift-off could interfere with the molecular signature under study or behave as small current leakage path. The second electrode is patterned using the same resist process sequence, leaving a window opened on the first electrode for metal evaporation (figure 2.2-c).

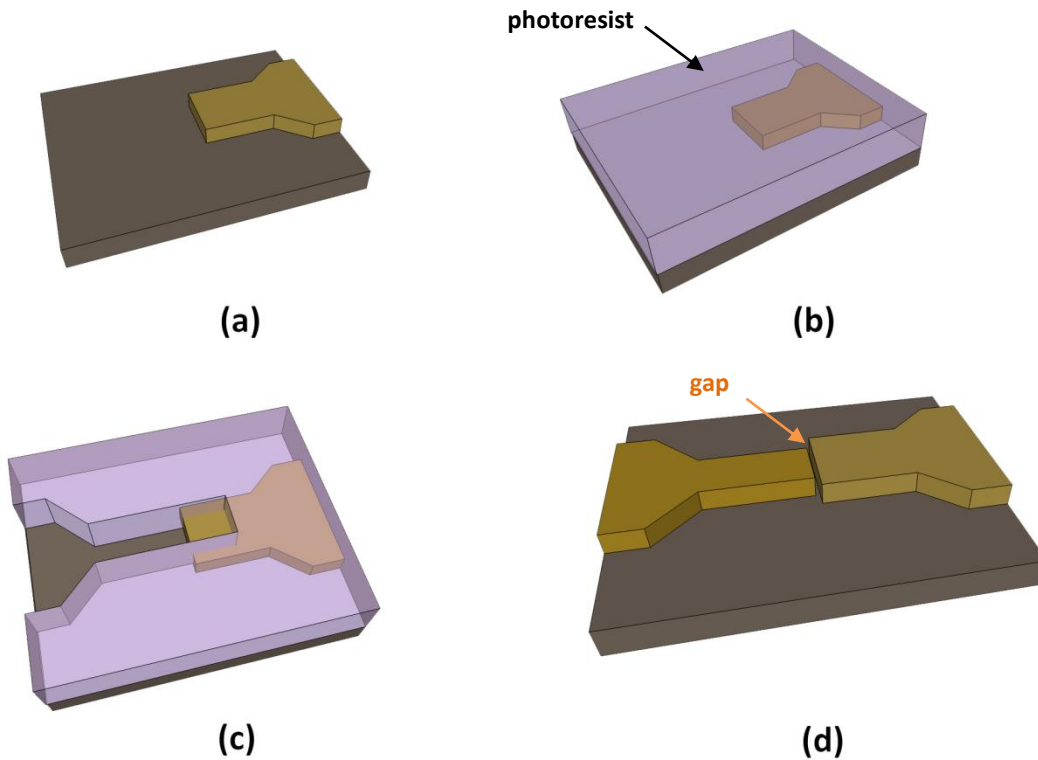


**Figure 2.2 : Schematic of the edge mediated shadow mask lithography process, (a) A first pattern is made by standard optical lithographic process, (b) and (c) The second layer is patterned by the same method over the first pattern, (d) Metal deposition with the sample tilted at a specific angle is performed to form the second metallic electrode and the nanotrench.**

The micrometer-scale electrodes are made of a titanium-gold bilayer (45 nm Au /5 nm Ti) or titanium-nickel-gold trilayer (30 nm Au/ 25 nm Ni/ 5 nmTi) deposited using the multiple-pockets electron beam evaporation followed by a standard lift-off process.

The second layer is evaporated under a tilt angle  $\theta$  (figure 2.3). The length  $L$  of the gap depends straightforwardly on the height  $h$  of the first electrode layer, and the angle  $\theta$  between the substrate normal and the source directions (equation 2.2).

$$L = h \times \tan(\theta) \quad (2.2)$$

We typically used a  $65^\circ$  deposition angle to obtain a gap of 80 nm. The thickness of H of the second electrode is  $H = T \cdot \cos(\theta)$ , where T is the thickness measured with the chamber quartz balance monitor. We typically calibrated the evaporation thickness to result in the H of values around 40 nm of composition similar to those of the first layer electrodes.

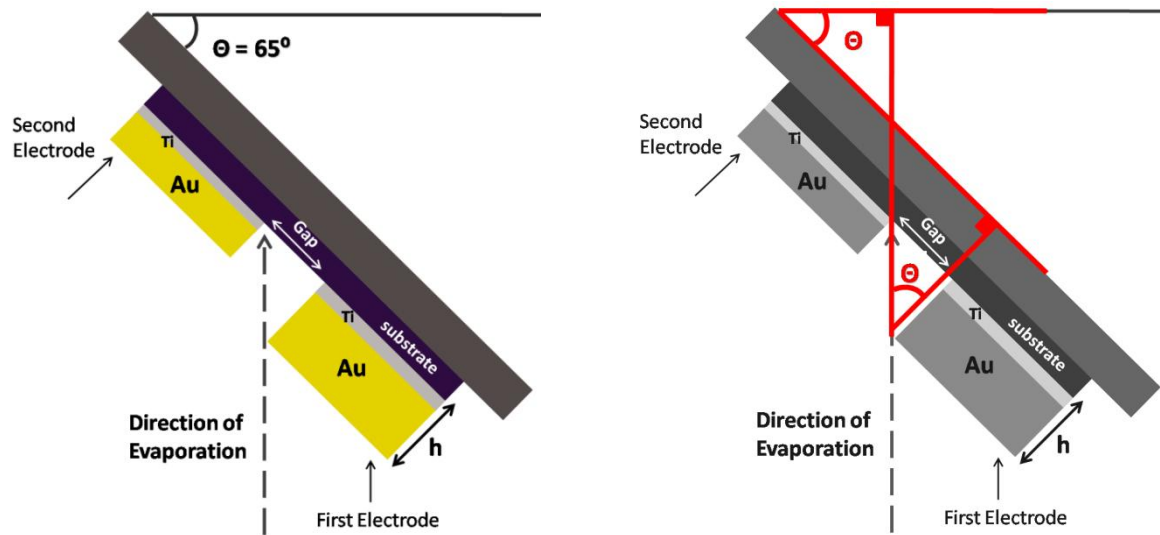


**Figure 2.3 :** Left: Schematic of the edge mediated shadow mask lithography process. Right: The length of the gap is set by the height  $h$  of the first electrode and the angle  $\theta$  of the tilted sample. In the approximation of a collimated source, the shadowing results in a gap of length “L”, determined by the equation:  $L = h \times \tan(\theta)$ .

We used scanning electron microscopy (SEM) imaging for calibrating and checking the quality and edges of the nanotrenches (figure 2.4).

Electrical characterization remained however the key characterization tool for checking the quality of the gaps, expected to exhibit minimal leakage current values. We extensively tested our structures, especially under conditions corresponding to the experimental environments of our experiments.

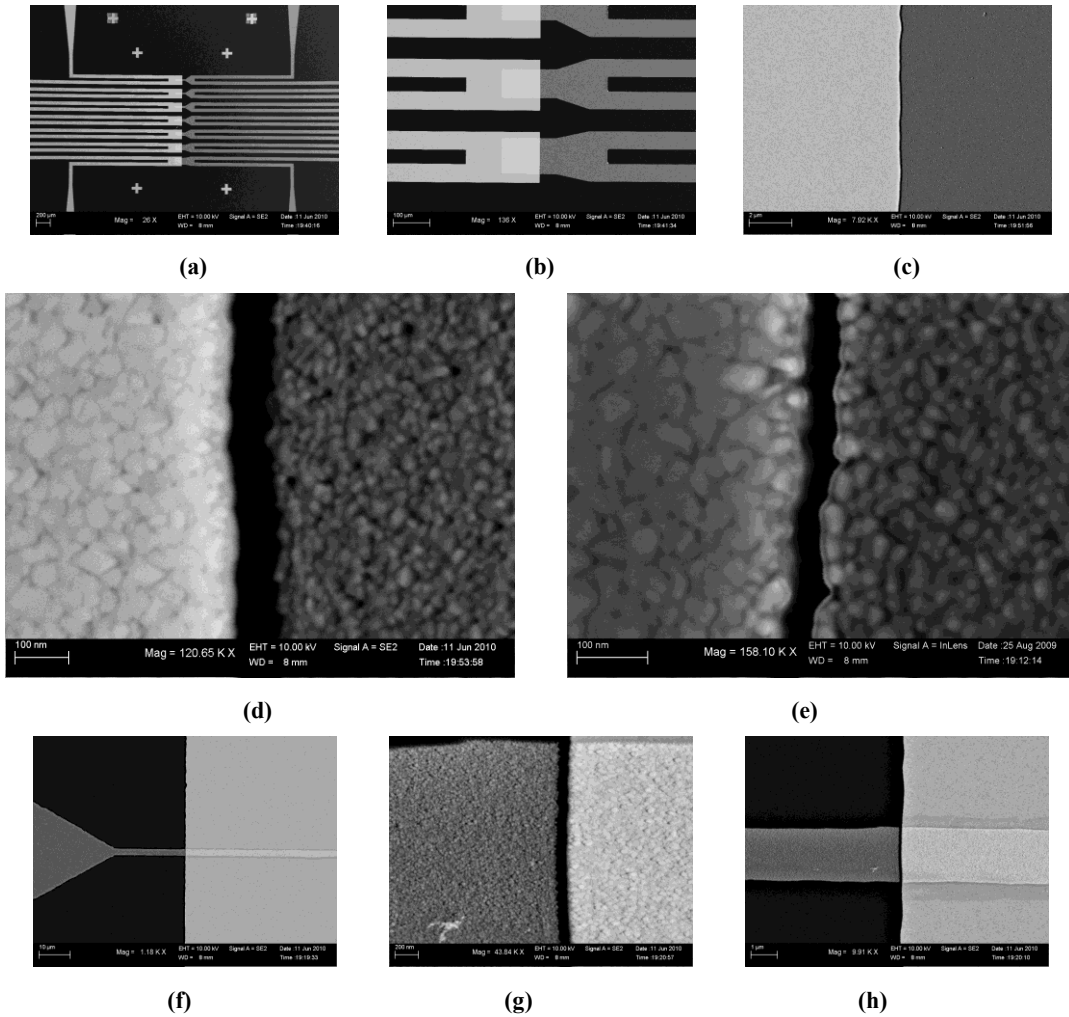


**Figure 2.4 :** SEM images of (a) and (b) nanotrenches with different length and aspect ratios in parallel , (c) and (d) 100  $\mu\text{m}$  long, 80 nm wide nanotrench electrodes, (e) 3  $\mu\text{m}$  long, 40 nm wide nanotrench electrode, (f), (g) and ( h) 3  $\mu\text{m}$  long, 80 nm wide nanotrench electrodes.

### 2.2.2. ELECTRICAL CHARACTERIZATION OF NANOTRENCHES

Nanotrenches, uniform all along the micrometric length of the gap with significantly high reproducibility and efficiency, were obtained with a high success rate, reaching more than 90% success rate for obtaining electrically open gaps. Creating nanogaps by shadow evaporation is the main reason for the absence of photoresist contamination in between the electrodes resulting in high electrical stability and reliability of the electrical contacts. For an applied bias up to 1V, sub pA leakage currents were systematically measured, the electrodes sustain high bias voltages (up to 30V, all reaching 5V under systematic testing) at room temperature and ambient conditions, immersed in water and other organic solvents without being destroyed or presenting

shorts. Trenches with widths comparing to the grain size of the deposited material, i.e. 10 nm, can be realized, but we observed a poorer reliability, as the majority of the samples with aspect ratios larger than  $10^3$  exhibit leakage currents in the nA range. Such borderline samples are therefore not considered for measurements, but reveal that critical assessment is provided by basic electrical characterization. Figures 2.5 and 2.6 present several sets of current versus voltage data in 0.5, 1, 5, 10 and 30 volts voltage sweep ranges, under ambient conditions (figure 2.5) and while electrodes are immersed in deionized ultrapure water (figure 2.6).

We observed that water immersion improved the high voltage resilience of our samples. The most obvious explanation is a larger critical electric field in a water dielectric medium. If we consider a maximum current leakage criterion, we can estimate that around 90% of our samples show leakage current below 10pA under 1V stress voltage in air, with approximately 30% inhibiting current values below 1pA.

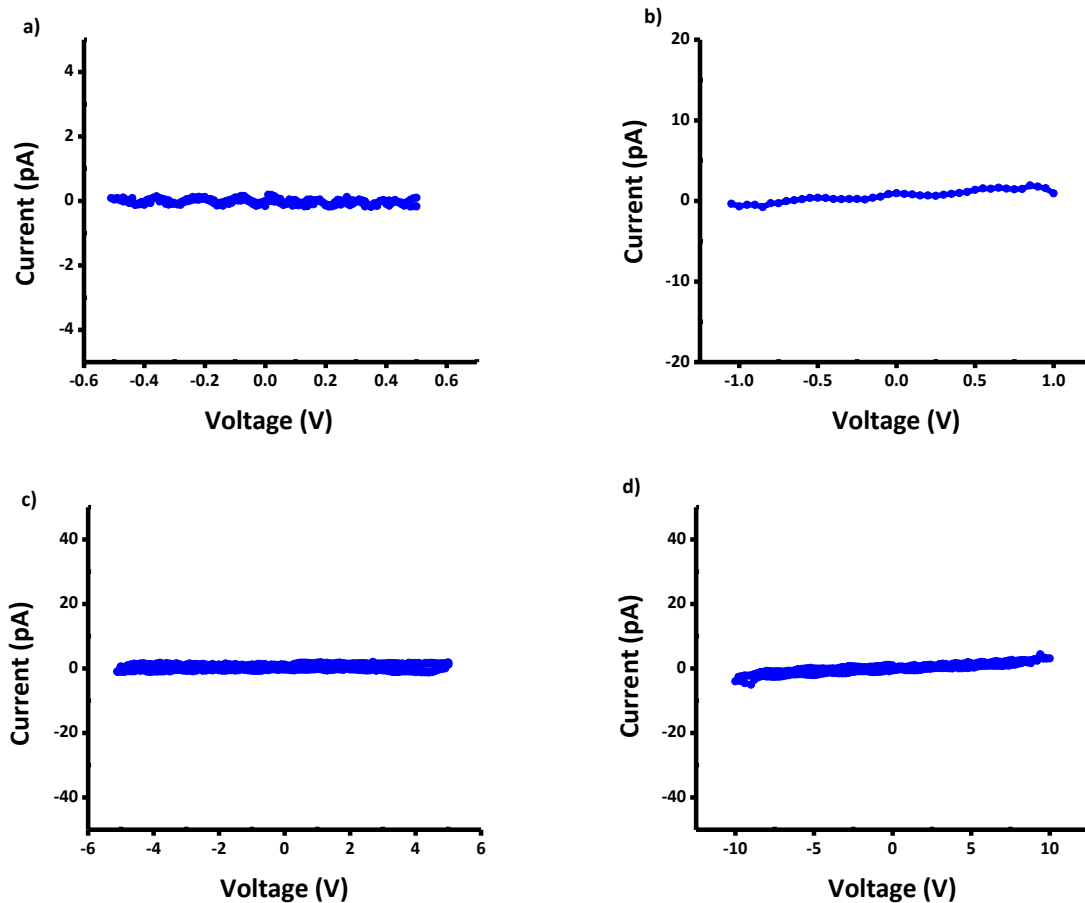


Figure 2.5 : Current-Voltage characteristics of empty nanotrench electrodes in ambient conditions, a) 500mV range, b) 1V range, c) 5V range, d) 10V range.

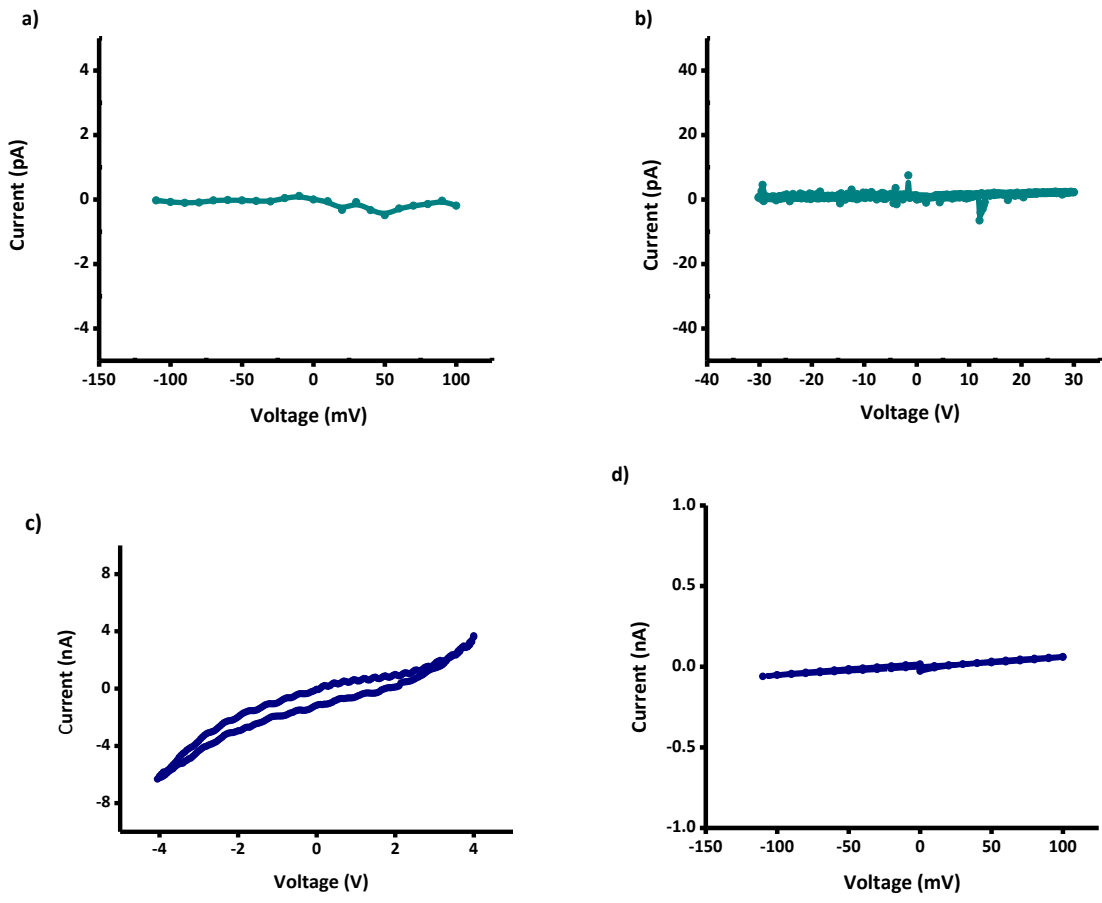


Figure 2.6 : Current-Voltage characteristics of nanotrench electrodes, a) and b) immersed in deionized ultrapure water (resistivity = 18 MΩ.cm resulting in 1.8 GΩ for a 100 nm long, 100 μm wide trench) 100 mV range (a) and 30V range (b) sweeps, c) immersed in 1,1,2,2-Tetrachloroethane (C<sub>2</sub>H<sub>2</sub>Cl<sub>4</sub>) in dark, 4V voltage sweep, the residual current is attributed to ionic impurities in solution d) immersed in Chloroform (ChCl<sub>3</sub>), 100mV voltage sweep.

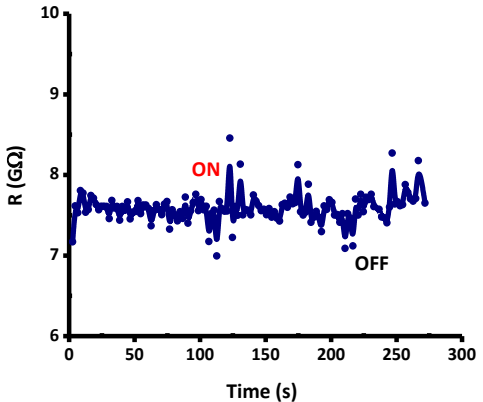


Figure 2.7 : Monitoring the leakage current of an empty trench, in the presence of 7.4 W luminous intensity and 110°C temperature. The resistance stays in the GΩ range, and there is no response to heat or illumination. Applied voltage = 1V=cte.

## 2.3. MAGNETIC TRAPPING OF MICROSPHERES OVER NANOTRENCH ELECTRODES

In this section, we present one example of particle trapping allowing us to close the circuit where the nanotrench represents the open section. The use of microparticles is developed in other chapters. We focus our presentation on this type of material, allowing us to introduce the experimental setup used for the large majority of the data presented in this thesis.

In the article entitled “*Magnetic directed assembly of molecular junctions*” in APL **86** (2005) [70], Long et al. studied molecular junction(s) by placing half metal-coated silica micron sized spheres by magnetic entrapment over microscale-contacts covered with molecular film SAM.

The electrodes were patterned by e-beam lithography on silicon substrates covered with thermal SiO<sub>2</sub> [70].

In our approach, we take advantage of the variable length of nanotrenches to trap and place several microspheres in an array over a micrometric long trench for creating molecular junctions in parallel [106]. The trench geometry is convenient for optical detection, due to the high contrast of electrodes towards each other and the substrate (see next section). The occurrence(s) of adequately positioned sphere(s) is easily detectable by optical observation means. Using high magnification objectives with high contrast microscopy techniques, spheres with the diameters superior to 100 nm are detectable. The principle of magnetic trapping is schemed in figure 2.8 [107].

With this technique, nanotrench electrodes were bridged by spheres with diameters ranging from 100 nm to 1 $\mu$ m. The smaller spheres with less mass show a higher population over the trench, while spheres of  $D \approx 1\mu\text{m}$ , had less population, but presented a better contact with the metallic electrodes due to their mass and the larger sphere-electrode contact area (figure 2.9).

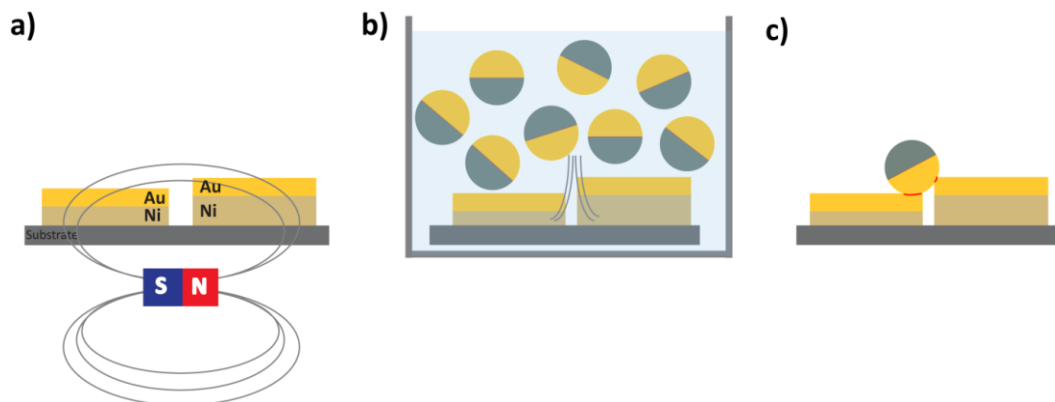


**Figure 2.8 : Microsphere junctions created by a) magnetizing the magnetic layer buried in the contacts along the long axis of the electrodes (perpendicular to the nanotrench width) for creation of a magnetic field gradient in the trench area, (magnetizing done by a permanent magnet of Ni-N52  $D = 10\text{mm}$ ,  $L=10\text{mm}$  with inside magnetic flux 1.43T and outside magnetix flux 5600 gauss) b) immersing the substrate in the solution containing metalized microsphere (with Ni layer buried under the Au film), soft agitation for about 20 minutes, c) After rinsing and drying an array of microspheres is formed on the trench area. The schema shows how the sphere is located due to the asymmetric geometry of the nanotrench. (The first layer electrode, the thicker one, contains the first electrode trilayer plus the over deposition of second electrode trilayer due to the angel evaporation, this superposition is simplified in the images in a thicker bilayer for less complexity).**

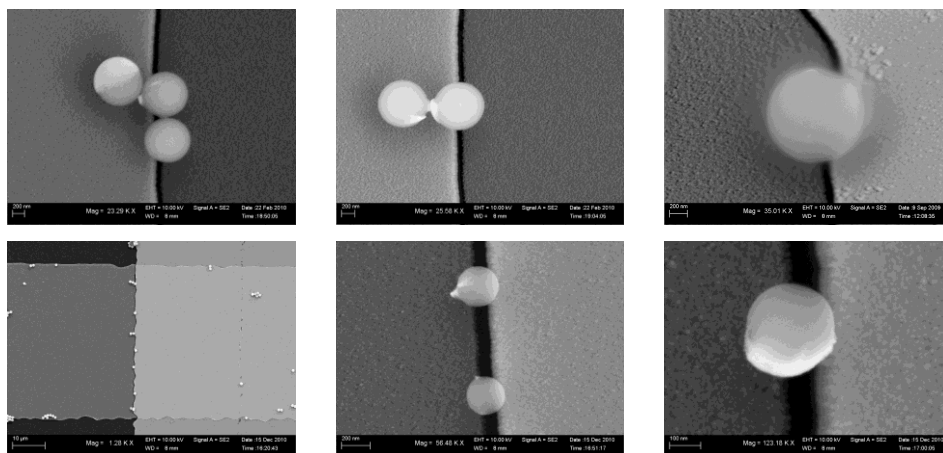


**Figure 2.9 : SEM micrographs of metalized microspheres, first row:  $D = 1\ \mu\text{m}$ , second row:  $D = 300\ \text{nm}$ , entrapped over the nanotrench electrodes. In the image with three spheres (top-left), the metallic cover on the sphere is visible, which confirms the perfect positioning of the particles towards the substrate (metallic part facing the electrodes). For particles of 300 nm diameter, the higher population of the spheres on trenches as well as less homogeneous metallic shell can be observed.**

Current-voltage data was recorded and controlled systematically before and after the magnetic entrapment of spheres. The samples with microsphere junctions showed mA currents and  $\approx 500\Omega$  resistance which will result in few ohms resistance value for the metallic particle after deducting the track resistance for two point measurements. This measurement also emphasize the wide range of current from pA to mA that can be observed, illustrating the versatility of nanotrench electrical contacts, being compatible for studying a broad variety of nanoparticles and molecular systems.

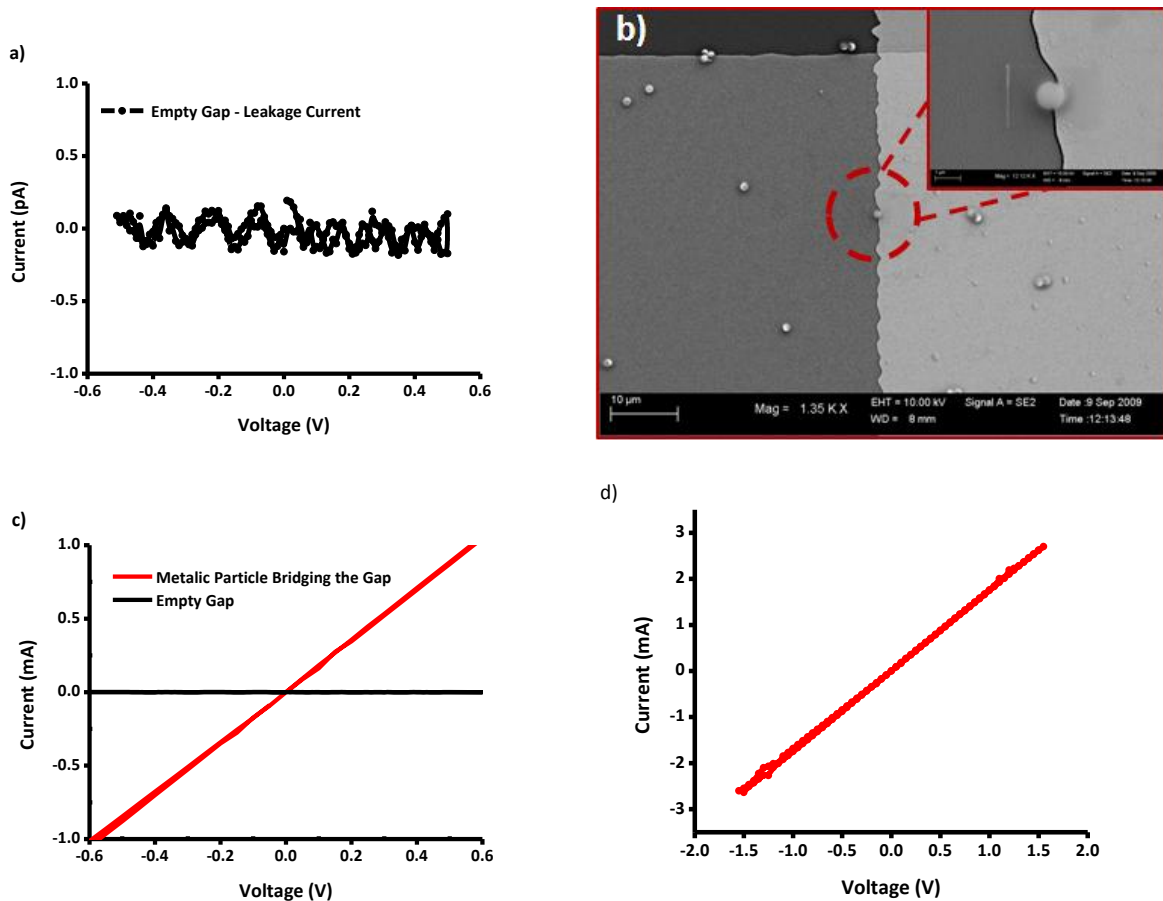


Figure 2.10 : a) I-V characteristics of an empty trench for 600mV voltage range, b) SEM micrograph of a 100µm wide nanotrench bridged by a microsphere (D = 1µm), the inset is the zoom of the trapped particle, c) superposition of I-V data for the trapped particle and the empty trench, d) I-V data of another nanotrench bridged by a microsphere (D = 300nm), 1.5 V range.

In summary, we showed that several micrometers wide electrodes separated by a sub 100 nm gap can be reproducibly produced by means of simple optical lithography techniques, with a control of the electrodes distance of the order of 10 nm accuracy. The process is simple and easily scalable for high throughput fabrication, as it uses standard optical lithography techniques and allows parallel processing of many junctions. The nanotrenches are suitable for use in micro and nano electronics where averaging measurements over several particles contacted in parallel is important, and are well adapted to nano and microparticle interconnects based strategies [108, 109]. Owing to their peculiar geometry, the nanotrench electrodes are ideally suited when high dynamic range of investigated current values is desired. This is especially useful for temperature-dependent studies on samples having resistance values strongly increasing under decreasing temperatures. Materials with large intrinsic sheet resistance value also strongly benefit from large aspect ratios of interconnects. It is interesting to note that the nature of the deposited material is not important for this process, as only the geometrical height of the electrodes is involved in the shadowing effect. Manufacturing gaps with two different electrode materials is therefore straightforward, in contrast with e-beam patterning strategies. This can be of particular interest when designing diodes or photo-active particles combined with molecular electronics systems. The process can also be straightforwardly extended to fabricate magnetic electrodes, of interest for spintronics applications, or to fabricate superconducting electrodes, relevant for mesoscopic physics and quantum effects [101].

In the following, we detail for the opto-electronic setup we built for DC electrical characterization under illumination, in combination with optical and spectroscopic observation of the samples [100].

## 2.4. EXPERIMENTAL SETUP, STRATEGY

Placing the sample with nanotrench electrodes on the stage of an inverted optical microscope allows measuring the electrical properties in the presence of external perturbations like illumination or temperature, as well as optical observation and image recording using high magnification objectives of the microscope. The sample is illuminated with tunable wavelength, intensity and polarization by transmission, through a top condenser with a 0.55 numerical

aperture, focusing the light on  $1\text{mm}^2$  area. We used a standard microscope halogen source, as well as a multiple light emitting diode (LED) microscopy illumination system, capable to combine 365, 455 and 590 nm wavelengths illuminations (Zeiss Colibri). By removing the infra red filter of the halogen illumination pathway, it is possible to heat the sample up to  $150^\circ\text{C}$ , allowing to check how temperature effects can affect the electrical properties. In the microscope reflection mode, the bottom illumination of the sample is performed through the microscope objectives. A photonic multichannel spectral analyser (PMA-11 from Hamamatsu) with an optical fiber installed on the microscope's camera output collects the spectral data, providing with the precise information about the intensity of light on the sample. Figure 2.11 illustrates how microsphere junctions could turn into molecular electronic devices, by covering the electrodes and/or the metallic part of the microsphere with SAM of molecules [111, 112].

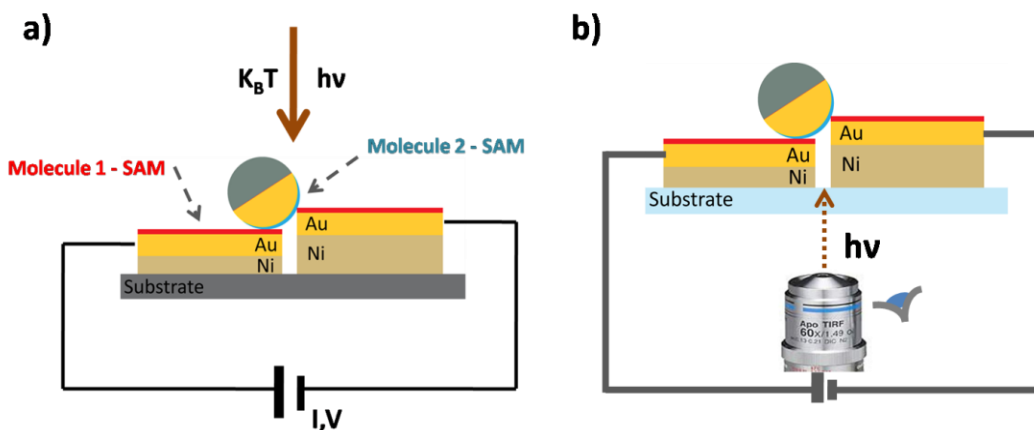


**Figure 2.11 : Microsphere molecular junctions, a) on an opaque substrate (silicon wafer covered by 550 nm thermal  $\text{SiO}_2$ ), illumination/heating by transmission through the microscope condenser, b) on a transparent substrate (130-170  $\mu\text{m}$  thick microscope coverglass/quartz) compatible with reflection microscopy.**

Inspired from the live cell imaging chambers design for inverted microscopes, a sample holder was designed and fabricated, using surface mount string connections to connect the nanotrench electrodes to measurement devices without wire bonding (figure 2.12, Appendix B).

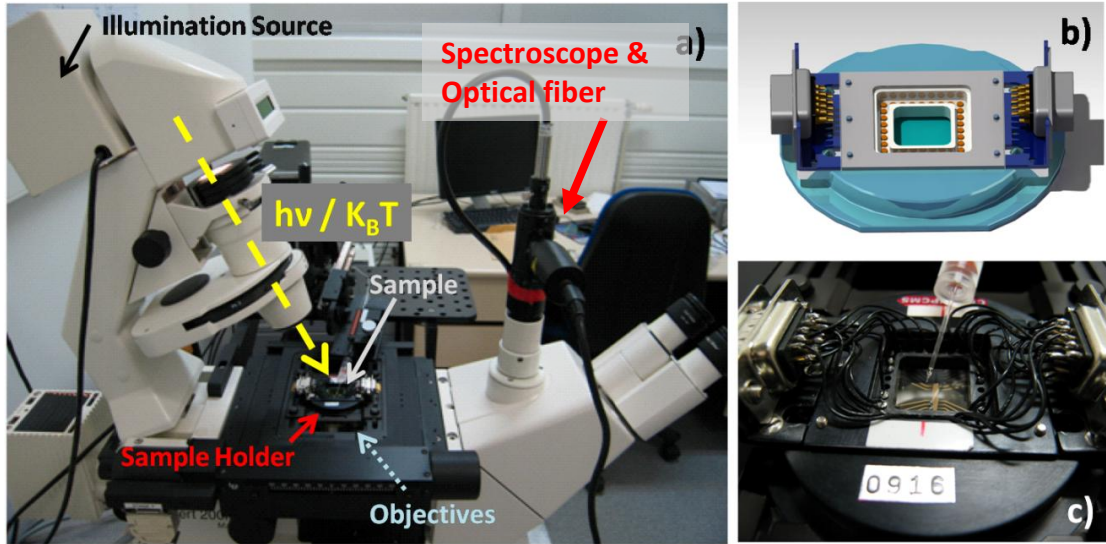


Figure 2.12 : a) Picture of the experimental setup, sample holder mounted over the microscope, b) 3D graphic of the sample holder design, c) injecting a solution of microspheres by drop casting over a sample containing 7 nanotrench electrode over a transparent substrate connected via the sample holder.

Figure 2.13 shows the optical microscope inspection images of half metalized microspheres on a substrate and trapped in between nanotrench electrodes.

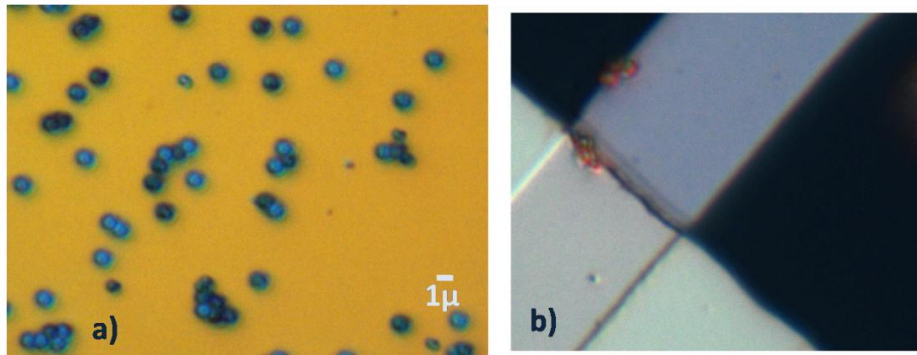
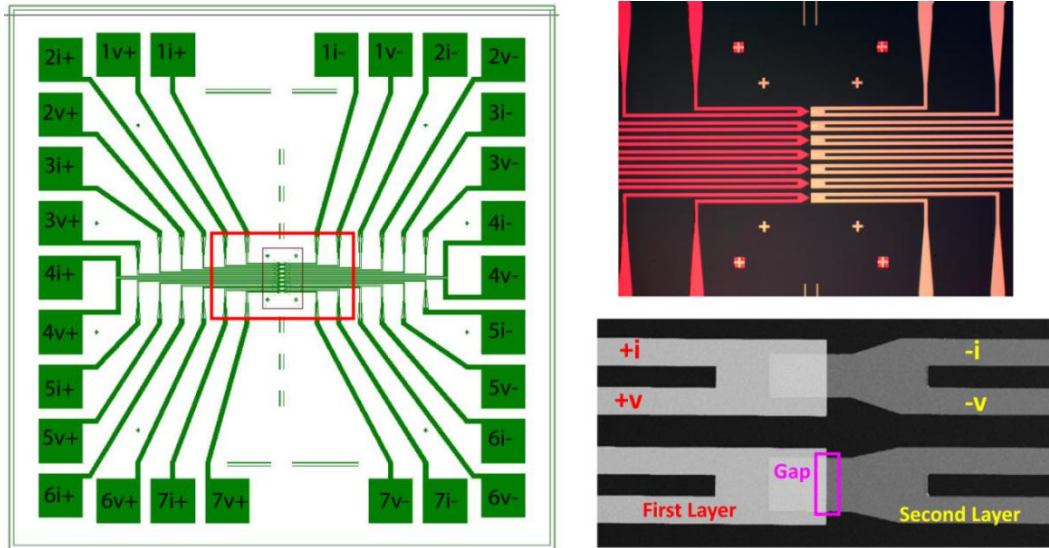


Figure 2.13 : a) Optical image of half metalized microspheres  $D = 1 \mu\text{m}$  deposited on a Si/SiO<sub>2</sub> substrate, taken by 100X magnification objective in DIC mode, the spheres are distinguishable individually, b) Optical image of two microspheres bridging the nanotrench. The high contrast in between the electrodes, spheres and the substrate provides a very clear image. The scale in image a ( $1\mu\text{m}$ ) is valid also for image b.

## 2.4.1. ELECTRICAL CONNECTION SCHEMA

The optical lithography mask designed for the fabrication of nanotrench electrodes is illustrated in figure 2.14-left), as a superposition of two layers. Each nanotrench is connected to four connection pads, compatible with applying four point measurements (figure 2.14 bottom-right).



**Figure 2.14 : Left: Optical lithography mask designed for patterning nanotrench electrodes on a  $25\text{mm}^2$  substrate. The area marked with the red rectangle is zoomed in the top-right image, containing seven nanotrenches in parallel, and showing two nanotrenches in an SEM micrograph with a more zoomed image (bottom-right image). This design with gaps in a small area at the center of the sample is compatible with our setup, when an aperture is needed from the top and at the bottom of the sample placed in the sample holder for illumination and/or for imaging.**

For the majority of our measurements, involving low current characterizations, we used a two point measurement geometry using an electrometer (Keithley 6517B). The simplified electrical circuit is shown in Figure 2.15-c. The size of the chip ( $25\times 25$  mm) is much larger than the active area ( $1\times 1$  mm) where the nanotrenches are located. This choice is driven by the convenience for optical access. It is particularly limited by the highest resolution objectives we used (63X Oil, 1.40 numerical aperture), with intrinsic large diameter and very short working distance. For such objectives, corrected with oil immersion medium and  $170\ \mu\text{m}$  glass coverslip thickness, the inverted geometry was ideally suited.

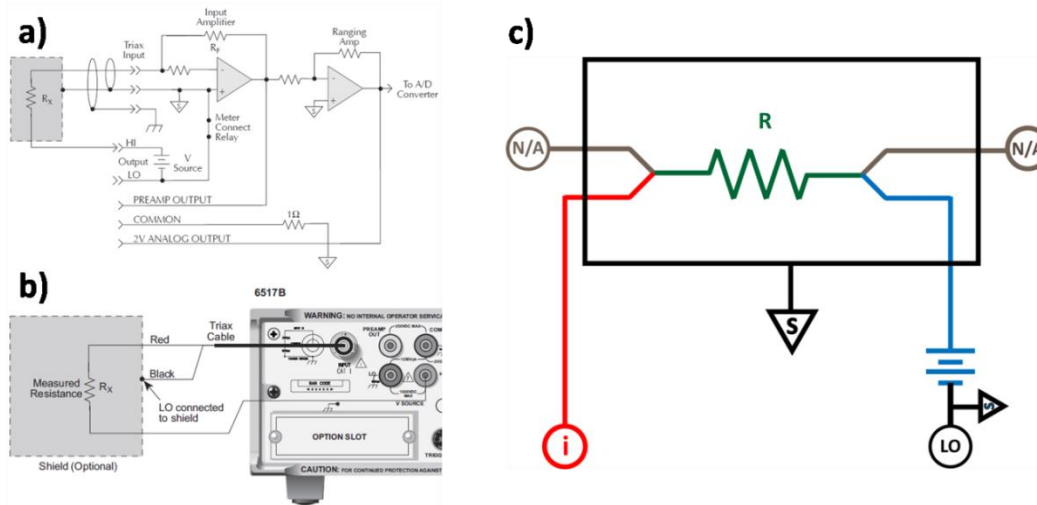
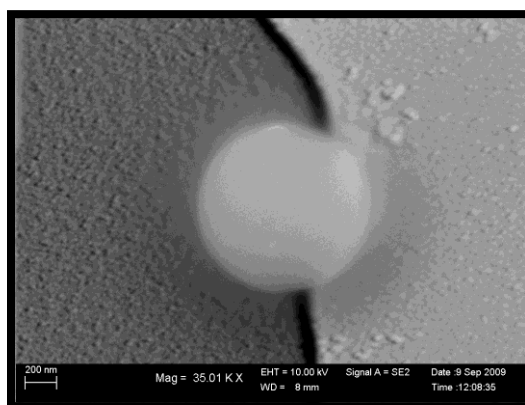


**Figure 2.15 : a) and b) electrical circuit and the connection guide for the Keithley 6517B electrometer, with floating ground system, c) our connection circuit for two point measurements. One side of the sample is connected to current reading and the other side to the voltage source, applying a voltage regarding the shield (S).**

## 2.5. CONCLUSION

We developed a dedicated setup, allowing multiple electrical interconnects with sub-100 nm separation to be exposed to variable illumination and direct microscopy observation. The on-chip electrode patterning was designed with efficiency and convenience criterions, allowing rapid scanning of samples and high degree of reliability, voltage stress test, at least a factor two more demanding than the experimental conditions presented in the following chapters, ensure that our gaps are free of current leakage paths, instabilities or electromigration pollutions, as well as substrates shorts, in more than 90% of the fabricated samples. For validating the adequacy of this approach providing access to electrical signal coming from the molecules, we identified a ‘model’ molecular system that is strongly and reversibly affected by illumination, and well documented in the literature for exhibiting a related change of electrical properties. We used this system as benchmark for showing that nanotrench gaps, and more specially microsphere junctions are well suited for molecular electronics studies [113].

## CHAPTER III: LIGHT SWITCHABLE MOLECULAR DEVICE USING MICROSPHERES CIRCUIT



We show that microsphere interconnects provide direct access to molecular transport properties. We use a benchmark molecular system that exhibits reversible conformation changes under illumination. Such photo-switching molecules show a light-induced modification of the conductance when inserted into a circuit in a vertical geometry [76]. Horizontal geometry devices are obtained using nanotrench electrodes covered with self-assembled monolayer (SAMs) of conjugated azobenzene derivatives with thiol anchoring end group (AZO), and bridged using hybrid microspheres functionalized with the same AZO SAMs. We perform reliability tests of the conductance switching by comparing these photochromic molecules to non-switching alkanethiol SAMs. The unambiguous signature of conductance switching confirms that microsphere interconnects make possible lateral molecular junction devices in the 100 nm range, opening the possibility of realizing multifunctional molecular electronics devices.

### 3. LIGHT SWITCHABLE MOLECULAR DEVICE USING MICROSPHERES CIRCUIT

#### 3.1. TRANSPORT THROUGH MOLECULAR SWITCHES

There is a large body of experiments and on-going activity for getting unambiguous access to molecular switching and study charge transport properties of switchable molecules [2, 61, 76, 77, 114]. Nevertheless, since it's impossible to connect a molecule to a metallic surface without influencing its properties, interpretation of the results can be non trivial and surprising [115].

A switchable molecule in solution may still be functional when connected to metallic interconnects (intrinsic switching), but might also lose its functionality and becomes passive in a molecular device due to strong molecule-metal electronic coupling (figure 3.1). The results interpretations can also be complicated by metallic filamentary conduction artifact [79, 116]. The re-verse phenomenon exists as well; a device may exhibit switchable properties even when a non-switchable (passive) molecule is at its core (extrinsic switching). Extrinsic switching may be the result of various phenomena related to the exact interaction between molecule and electrodes, applied voltage bias, current and local electric field [76].

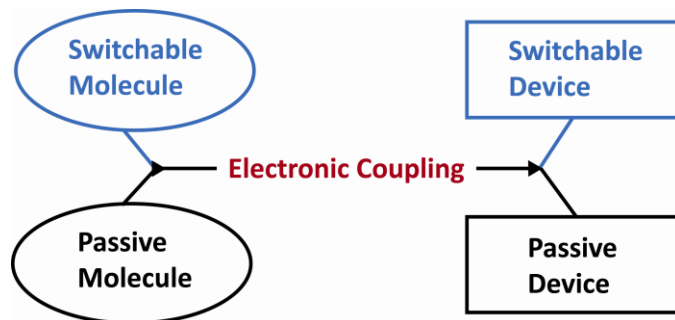


Figure 3.1 : The influence of electronic coupling on the performance of a molecular device.

The large majority of experimental data on switchable molecules are obtained in the vertical geometry. The versatility and success of scanning probe techniques [117], as well as the chemical control of surface functionalization with molecules [40], make the vertical probing rather easy and well controlled. Furthermore, the advent of soft macroscopic contacts (Hg drop technique, see section 1.4.2.i) has provided a cheap and convenient access to electrical transport through SAMs, with its ease of use making possible systematic and comparison studies [65].

Lateral planar geometries are mostly aimed at measuring single molecules properties, usually requiring challenging nm spaced electrodes (or pm-controlled elongation) and low temperatures (see section 1.4.1) [2]. The success rate for fabricating measureable and stable devices is very low, and the expected variations of conduction properties with details of the molecules and molecules-electrodes conformations drastically limit the results interpretations [135].

There is therefore a strong need for robust device construction, where the main electrical component involves molecular transport, in a planar lateral geometry. One also hopes that robustness relates to reproducibility of properties, with expectations of improving the dispersion of data typically encountered in single molecule experiments. This first step towards circuit-compatible designs should allow compatibility with developed planar (and parallel) top-down fabrication routes, and, more importantly, ensures direct access to the active channel. This provides opportunities for experimental characterization, for example by optical spectroscopy techniques. External stimuli access, for example electrical field for multi-terminals gating purposes, or illumination for optoelectronics applications, can possibly provide unique insight into multi-functional molecular properties.

The key idea is to use an intermediate circuit element, filling the size gap between the 1 nm molecule length and the 100nm top-down nanofabrication reliable separation. Reports of nanoparticles bridged devices can be found in the literature. They usually involve metallic (Au) cluster of 3-30 nm in size, trapped between electrodes [118], or self-assembled 2-dimensional (2D) networks that are macroscopically electrically addressable [119]. For this last method, we are aware of one report on photoswitchable diarylethene molecular device [100]. Electrical transport is however complicated by Coulomb blockade effects, combined with percolation in a 2D network [120]. If mechanical stability is ensured by molecular interconnects, switching molecules in networks can also introduce irreversible changes in particles arrangements, possibly complicating the interpretation and reproducibility of the experiments. Furthermore, we are not aware of light switching experiments involving single bridging nanoparticle in a lateral geometry.

A large body of literature on metal/molecule/metal devices describes the observation of switching effect of the conductance of molecular junctions, with several experimental approaches used for realizing the sandwiched junctions [76]. There is nevertheless a significant lack of control experiments for validating such observations and distinguishing the specific

results from the possible artifacts. For example Stewart et al [121] revealed that molecular switching of a Langmuir-Blodgett (LB) film sandwiched in an asymmetrical Pt/Ti vertical junction geometry was molecule-independent (figure 3.2), indicating that the electric-field driven mechanism was not related to the molecules!

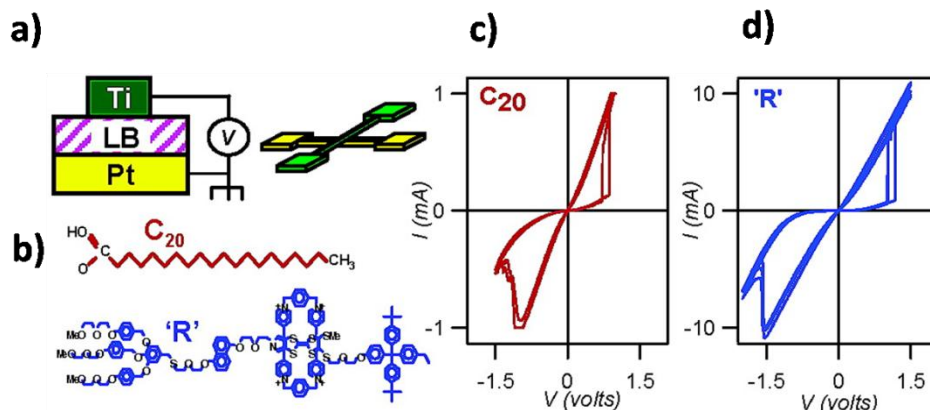


Figure 3.2 : a) A sandwich structure of 100nm-Pt/LB monolayer/5nm-Ti, b) Eicosanoic acid, C20 (top) and a rotaxane molecule (bottom), c) DC I-V measurements showing the hysteresis loops for C20 and d) DC I-V measurements showing the hysteresis loops for rotaxane molecules.

Further studies revealed that electromigration was at the origin of hot spots of filaments that can be reversibly broken by applying a significant voltage bias to the junction [122]. This model of metallic filaments that can mimic voltage switching was confirmed by others [123, 124]. These results, casting doubts on many reports of electric-field driven voltage switching [90], deliver a very important message: careful control experiments, in particular by substituting the involved molecular materials, are essential for distinguishing between molecule specific and generic behaviors.

### 3.2. AZOBENZENE-BASED MOLECULAR SWITCHES

The conversion of light to mechanical motion at the molecular level provides exciting possibilities for nanomachine control and characterization. Photoswitching is also more controllable and allows more drastic check experiments than voltage (or electric field) switching. Azobenzene-derived molecules are well-documented photochromic molecules [125] exhibiting reversible *trans*-*cis* isomerization triggered by light, with the extended *trans* configuration

switching to a compact *cis* configuration under ultra violet  $\lambda \sim 365$  nm (UV) light irradiation, with the more stable *trans* state reversibly recovered after irradiation at longer wavelength in visible range (i.e. visible blue  $\lambda \sim 450$  nm) [126]. Figure 3.3 summarizes the related energy levels schemes, where excited states can be reached under visible photon energies, with the extended *trans* state being thermodynamically preferred.

These molecules are particularly promising for nanotechnology applications and many applications profiting from the conformational rearrangement of the molecule, such as optical data storage devices, switchable supramolecular cavities and sensors, liquid–crystal alignment for displays or light-powered molecular machines delivering mechanical work [76, 127].

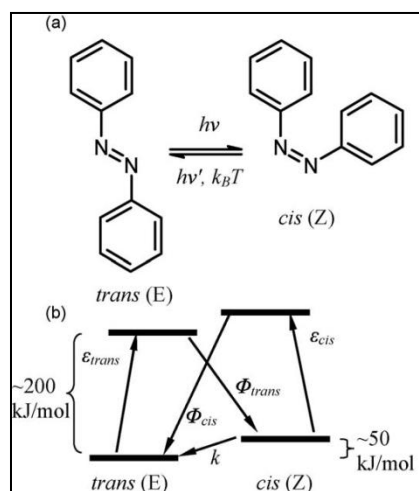


**Figure 3.3 : Simplified state model for azobenzene chromophores.  $\epsilon$  = extinction coefficients,  $\Phi$  = quantum yields for the photoisomerizations,  $k$  = rate of thermal relaxation. Competition between these pathways determines the composition of the photo-stationary state.**

The two isomeric conformations have been studied extensively in the literature showing reversible switching in solution phase upon absorption of light [76, 126]. The key question is whether the same photoisomerization processes will occur after connecting the molecules to a metal or will it be affected by factors like quenching of the excited state or steric hindrance.

Owing to the large change of molecular confirmation, one expects a related significant change of conductance properties, making transport measurements ideally suited for revealing molecular conformation changes. First experimental insight into conductivity switching were obtained by scanning tunneling microscopy (STM), which is a method highly sensitive to the height change of adsorbed molecules on surfaces.

A STM study carried in Crommie group has demonstrated that azobenzenes lying flat on the gold surface exhibited no photoswitching, owing to the large coupling between the molecule and the surface. However the photo-induced isomerization was recovered for molecules decoupled from the surface by introducing four “legs” i.e. tert-butyl side groups on the azobenzene (TTB-AZO) [128, 129].

In the experiment shown in figure 4, a single molecule is switched from *trans* to *cis* form upon UV illumination, and is going back to *trans* form after 1s of exposure to UV light. A continuous wave diode laser at an external viewport provided UV radiation at 375 nm with an average intensity of  $90 \text{ mW.cm}^{-2}$  at the surface of the sample. During UV exposures the STM tip was retracted and the sample temperature was maintained between 28 K and 2 K [128].

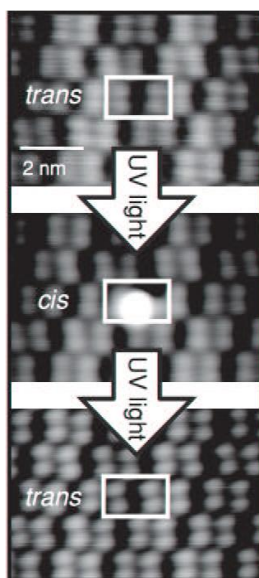


**Figure 3.4 : Reversible switching of an individual TTB-azobenzene molecule by sequential UV-illumination, from *trans* to *cis* and again to *trans* [128].**

The photomechanical switching rates for TTB-AZO molecules at the surface of gold were also measured using single molecule resolved scanning tunneling microscopy, demonstrating that visible light does not efficiently reverse the photoreaction for adsorbed molecules, contrary to what is seen for molecules in solution (figures 3.5 and 3.6) [129]. One must note that a *cis* configuration is observed for both model of full reversibility of the *cis-trans* transition is oversimplified, and one must keep in mind a thermodynamic equilibrium between the two states occupation probabilities, which is highly sensitive to details of the total free energy of molecules adsorbed on surfaces.

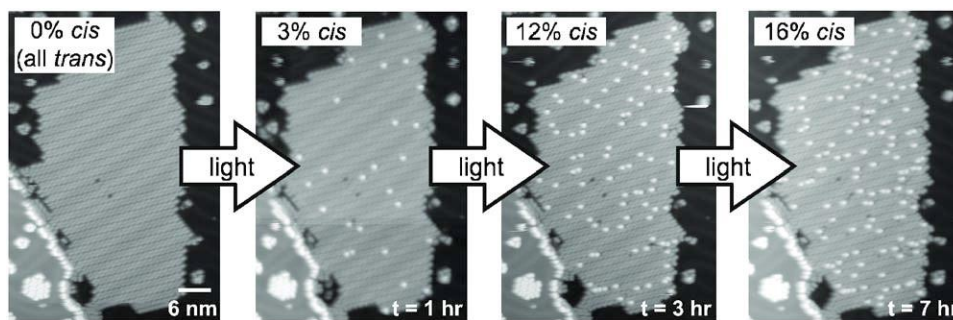


Figure 3.5 : Sequential images of a single island of TTB-AZO/Au (111) after successive exposures to 375 nm UV light. The first image is the pre exposure configuration of uniformly *trans* isomers. The three following images were acquired after 1, 3, and 7 hours total exposures to UV light [129].

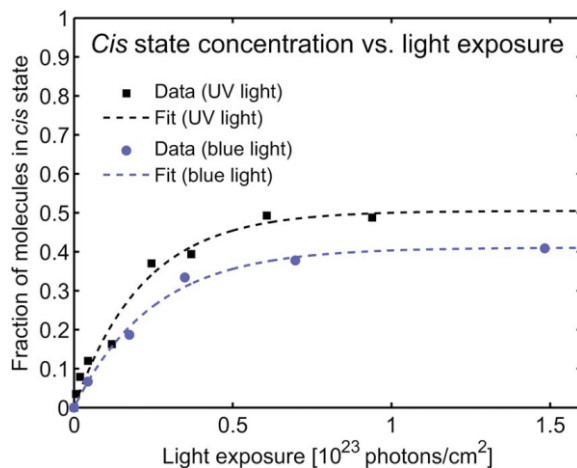
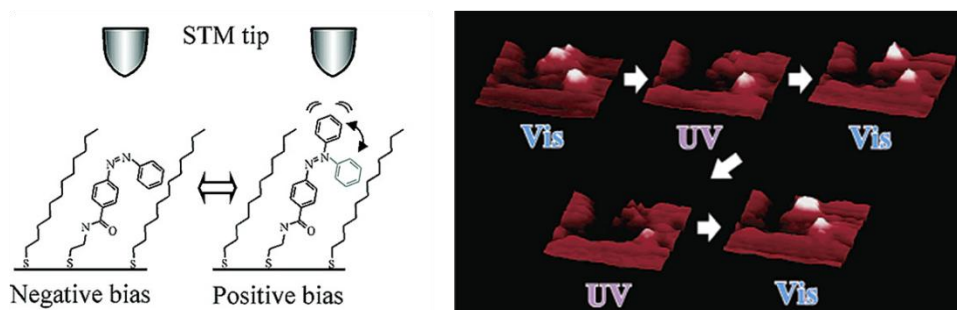


Figure 3.6 : Concentration of *cis* (TTB-AZO) molecules on Au (111) plotted vs total photon exposure for both UV (375 nm) and blue (444 nm) light, revealing photoswitching saturation behavior. The plotted fraction of *cis* TTB-AZO molecules is an average over many similar islands on the same sample. Dashed lines are fits to data [129].

Other STM studies revealed that the azobenzene isomerization can be also induced electrically, but the direction of the switching reaction could not be controlled [130].

Photoisomerization of the azobenzene was also demonstrated in STM experiments on azobenzenes embedded in alkanethiol ( $C_{12}$ ) SAMs, providing stability making room temperature experiments in  $N_2$  atmosphere feasible [131]. The bottom metallic (Au) substrate plays the role of one electrode, while the STM Pt/Ir tip acts as the second electrode (figure 3.7) [131]. Photoisomerization of the isolated azobenzene molecules was investigated by illuminating the

sample by 325 nm UV and 450 nm visible light using a He-Cd laser during STM measurements. A series of STM images represent the *cis-trans* change in the molecule [131].



**Figure 3.7 :** Left: schematic of the vertical configuration for connecting a single azobenzene to a metallic substrate as first electrode and STM tip as second electrode, Right: A series of STM images representing the *cis-trans* change in an isolated azobenzene molecule controlled by alternating 325 nm UV and 450 nm visible photoillumination (15 x 15 nm) [131].

### 3.3. CONJUGATED AZOBENZENE DERIVATIVE WITH THIOL ANCHORING GROUP

Motivated by the STM studies on single molecules, and aiming at realizing larger scale vertical molecular devices for better surface chemisorptions stability, Pace et. al, have reported the design of a rigid and fully conjugated azobenzene with a thiol anchoring group (AZO) that forms a well packed SAM on Au surface (figure 3.8), and exhibited efficient and reversible isomerization in solution (figure 3.9) [132].

Upon light irradiation of the chemisorbed SAM, a collective *cis-trans* isomerization of the entire molecular-crystalline domains of tens of nanometers in size occurred with an outstandingly high directionality. The isomerization had a cooperative character in large domains at surfaces, without perturbing the molecular lattice [132].

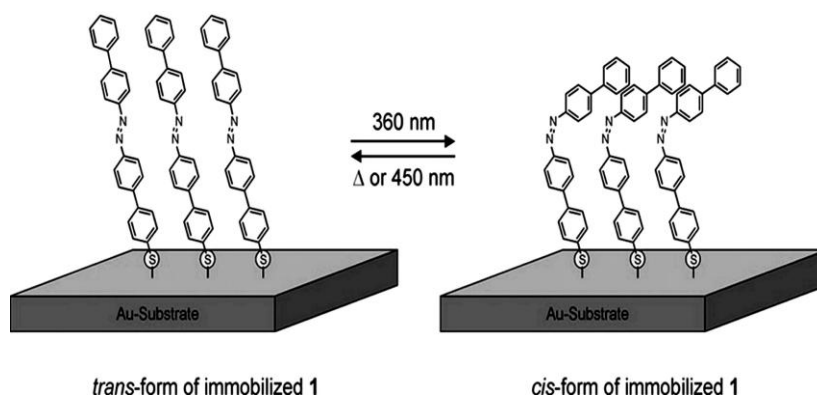


**Figure 3.8 :** Cartoon of the switching molecule on an Au surface. For the sake of example, a small domain of molecule 1 [4'-(biphenyl-4-ylazo)-biphenyl-4-thiol] immobilized on Au surface has been sketched. Intermolecular interactions between adjacent molecules stabilize the packing of domains consisting exclusively of *trans*-isomers (Left), as well as the packing of domains consisting exclusively of *cis*-isomers (Right) [132].

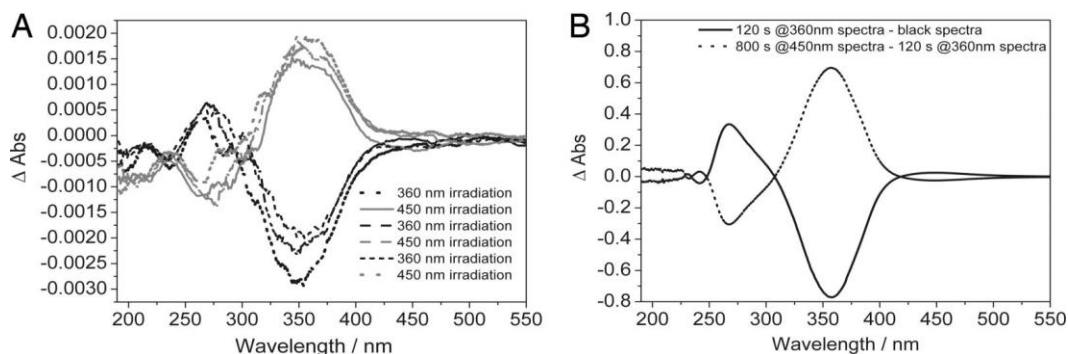


**Figure 3.9 :** Absorption spectra of the reversible switching of Thiol-AZO in a SAM on Pt and in a solution. A) UV/Vis spectral changes upon photoisomerization of Thiol-AZO arranged in SAMs on Pt surfaces. The SAM of Thiol-AZO has been switched back and forth between the *trans* and the *cis* conformer by irradiating the sample with UV light at 450 and 360 nm, respectively. B) UV/Vis spectral changes upon photoisomerization of AZO in chloroform solution [132].

Experiments related to two-terminal electrical measurements in a vertical geometry were then performed by Mativetsky et al. using a conducting AFM set-up to indicate the change of conduction on small number of connected molecules when switching from the *trans* to the *cis* state (figure 3.10). After illumination, they observed an increase of the conductance of typically a factor 25-30, which was interpreted as related to the corresponding decrease in tunnel barrier length, related to an effective change of the SAM average thickness (figure 3.11) [133].

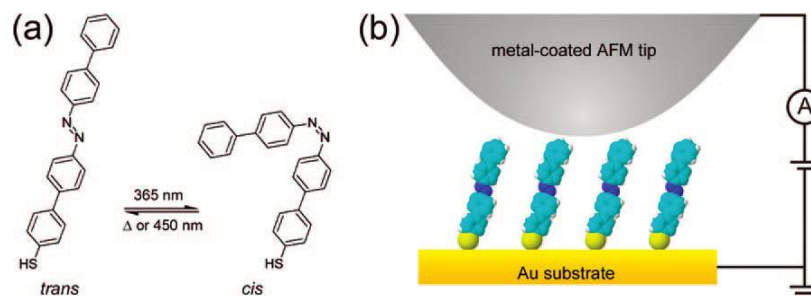


**Figure 3.10 :** (a) Structure of the *trans* and *cis* isomers of the light-switchable azobenzene derivative. (b) Schematic of the setup used for performing conductive AFM measurements on Thiol-AZO SAMs [133].

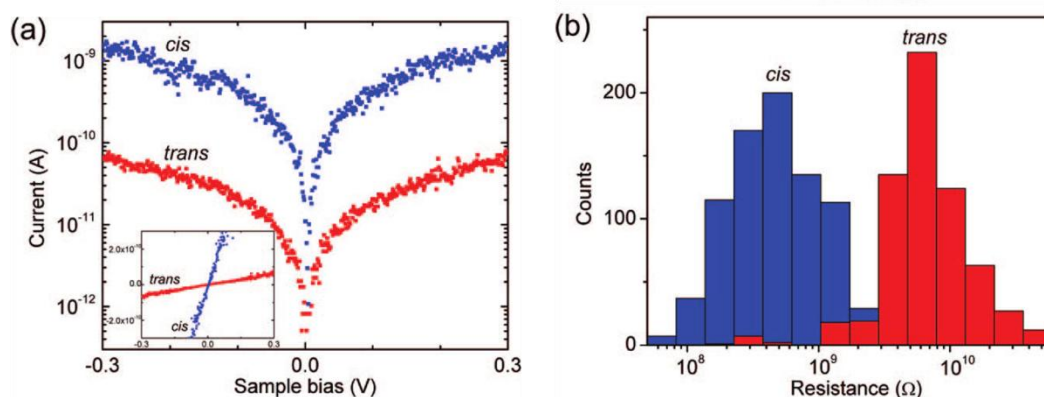


**Figure 3.11 :** (a) Representative I-V traces (semilog scale) recorded before and after UV irradiation showing larger currents following photoisomerization into the *cis* conformation (linear scale in inset). (b) Resistance histogram (based on 1484 I-V curves) exhibiting distinct peaks corresponding to the *cis* and *trans* conformations of the AZO molecules [133].

A similar result was obtained using a Hg-droplet top electrode. In this case, the authors observed reversible conductance switching with a ratio about 25 (figures 3.12 and 3.13). Interestingly, upon switching from the *cis* to the *trans* form, the azobenzene molecules were able to lift the Hg-droplet [134].

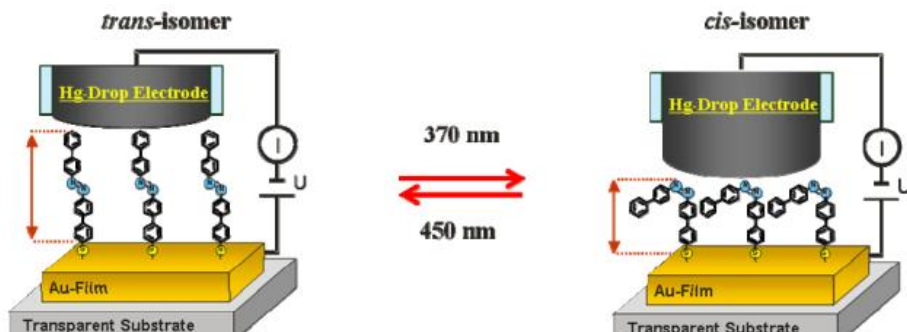


Figure 3.12 : The AZO SAM immobilized between a transparent Au surface and a Hg drop electrode. As a result of the light-triggered isomerization between the rod like *trans* isomer (left) and the more compact *cis* isomer (right), the distance between both electrodes varies, thus providing both an optoelectronic switch and an optomechanical cargo lifter. (see supporting information of [134])

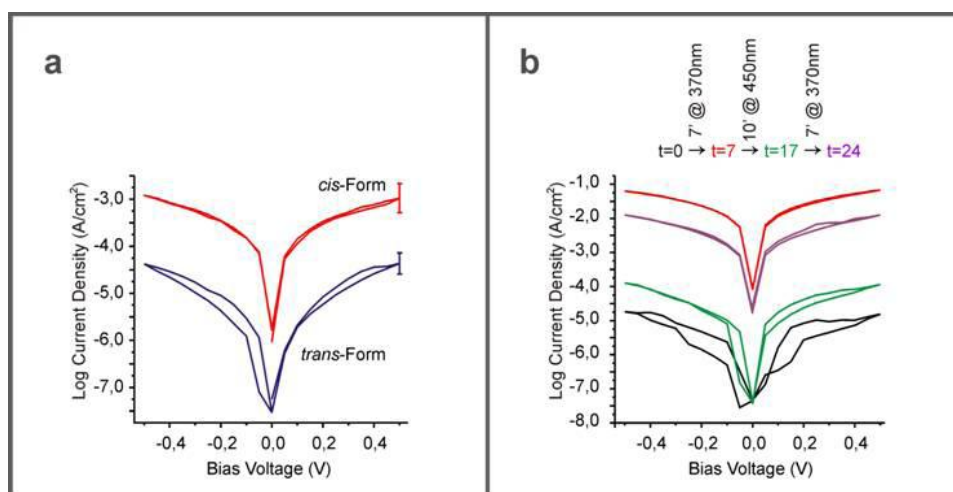


Figure 3.13 : a) I–V characteristics of Au-AZO SAM/C12 SAM-Hg junctions formed ex situ. Results for the AZO SAM in the *trans* and *cis* forms are shown as blue and red lines, respectively, b) I–V characteristics recorded in situ on an Au-AZO SAM//C12 SAM-Hg junction incorporating the *trans* isomer and subsequently irradiated with alternating wavelengths at  $\lambda = 370$  and  $450$  nm, as indicated [134].

We therefore chose this material as model photo-switchable system, where reversibility wavelength specificity, and significant conductance modification between the two conformations have been observed by several experimental techniques in the vertical geometry [133, 134].

### 3.4. EXPERIMENTAL PROCEDURE

The previously presented conjugated azobenzene derivative exposing the thiol group (AZO) was used to study light switchable microsphere molecular junctions, the choice of molecule also followed the reports of successful reversible change of conduction under illumination obtained in a vertical geometry device [133,134].

Three types of microsphere-based molecular junctions have been prepared and investigated, in order to unambiguously detect light switching by means of comparison check experiments.

1. AZO SAMs on both electrodes and on the gold surface of microsphere,
2. AZO SAMs on both electrodes and standard alkane chain of dodecanethiol (C12) SAMs on the sphere and vice versa,
3. Both electrodes and microsphere functionalized with C12 molecules.

The latest was carried out as a test to detect if there are any possible artifacts involved in microsphere circuit setup and measurement, preventing sources of switching other than intrinsic to azobenzene molecules. One can for example imagine that defects in the SiO<sub>2</sub> substrate or traces of metallic doping can result in photoconductance artifacts. C12 molecules are convenient candidates since they are well known to have high electrical resistance and are not expected to exhibit molecule-specific electronic switching via illumination in the visible spectrum.

We consider these test experiments essential for showing switching signal on AZO SAMs junctions, as discussed earlier. Despite all the activity and progress in this field, statistical information and comparison experiments are lacking. We also took advantage of a direct collaboration with the team showing photoswitching in the vertical geometry (team of Prof. Samori from ISIS, Strasbourg), providing us all necessary steps for proper fabrication and handling of azobenzene molecular films.

SAMs of azobenzene derivative with thiol anchoring group were formed on Au surface of electrodes and spheres, by exposing them to a solution of 10<sup>-5</sup>M of the molecule in degassed chloroform at room temperature for 24-48 hours ensuring a better stability of molecular coverage when trapping the microspheres. The substrates were then carefully rinsed with pure chloroform and blown dry with argon.

Nanotrench electrodes were patterned over two types of substrates, the majority over optical microscopy coverglass (0.13–0.17 mm thick), with another set of samples on standard Si/SiO<sub>2</sub> wafers with 550 nm of thermal oxide preventing electrical shorts.

Experiments were performed on an inverted optical microscope platform, with LED light source focused on the sample through the microscope objective with numerical aperture (N.A.) = 0.65 when using transparent substrates switched between 365 and 455 nm. We estimate the illumination power to be of order of 300 mW.cm<sup>-2</sup> at 365 nm and 10 W.cm<sup>-2</sup> at 455 nm. For the sake of comparison, another test batch of samples was realized on standard Si/SiO<sub>2</sub> wafers. In this case, the top illumination was brought through the illuminating condenser (N.A. = 0.55). The microscope was also a convenient observation platform allowing direct visualization of the occurrence of trapped microspheres using transparent substrates. Details on the nanotrench characteristics and the procedure for trapping of the spheres are described in chapter II. A sketch of the experimental design and electron micrograph of the resulting sample are presented in figure 3.14.

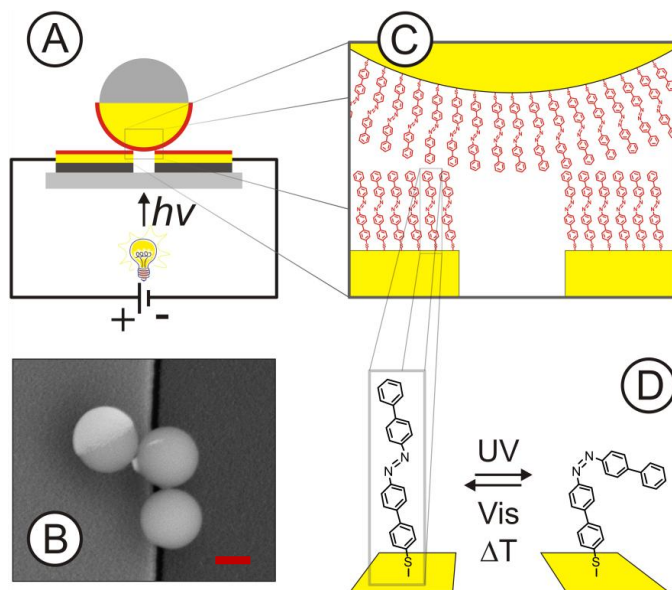


**Figure 3.14 :** (A) Schematics of the molecular circuit design. The Au hemisphere of the particle as well as the electrodes (in yellow) are coated with a chemisorbed self-assembled monolayer (in red) of either C12 or AZO. (B) scanning electron microscopy view of microsphere, of 1  $\mu\text{m}$  diameter, trapped over an 80 nm trench. The top left untrapped sphere contrast reveals the partial Ni/Au coverage of the spheres. This non-existing contrast on the trapped spheres indicates that the coating is under the sphere, bridging the two electrodes. The scale bar is 500 nm long (C) cartoon of the interaction between molecules in the specific device geometry used. (D) formula of the *cis-trans* isomerization of the photochromic thiol terminated biphenyl azobenzene molecule.

### 3.5. RESULTS AND DISCUSSION

Our strategy involved the fabrication of a significant number of devices, establishing electrical characterization criteria for realizing circuits involving trapped microspheres over the nanotrenches. After identification of devices possibly involving molecular films, we systematically tested if they were reversibly switching under illumination of adequate wavelengths.

A total of 126 nanotrench samples were made (~ 20 substrates). This number results from selecting samples with low leakage currents, using a criterion for leakage current below 10 pA under 1V bias (under illumination), with 80% of the samples exhibiting current values below 1 pA. After overnight exposure to typical 0.1mM solutions of the molecules, leakage current tests were repeated, leaving 90 available samples.

Table 1 summarizes the statistics over those samples. Their exposure to functionalized spheres resulted in only 25 samples (20%) categorized as stable closed circuits. Approximately less than 10% of the samples were categorized as ‘shorts’, with current exceeding 10  $\mu$ A under 1 V bias, which can possibly result from metal-metal interconnects due to partial coverage of the metallic surfaces with molecules. We observed that such occurrence was more likely to happen when a significant number of microspheres were bridging the gaps and one hot spot being necessary to create the short. The next tests were limited therefore to low concentration of spheres, avoiding trenches bridged by more than a few microspheres. As a result, a large fraction of the nanotrenches remained electrically open. We also used stringent stability criteria to consider candidates for molecular interconnects. We selected samples exhibiting at least two orders of magnitude current increase when comparing the initial current to post-exposure to microsphere values. We also tested the ‘connected’ samples by performing I-V curves, and kept only samples showing stable I-V curves up to 1V stress voltage (which is a test the previously mentioned high resistance samples did not pass). A typical IV curve is shown in figure 3.15.

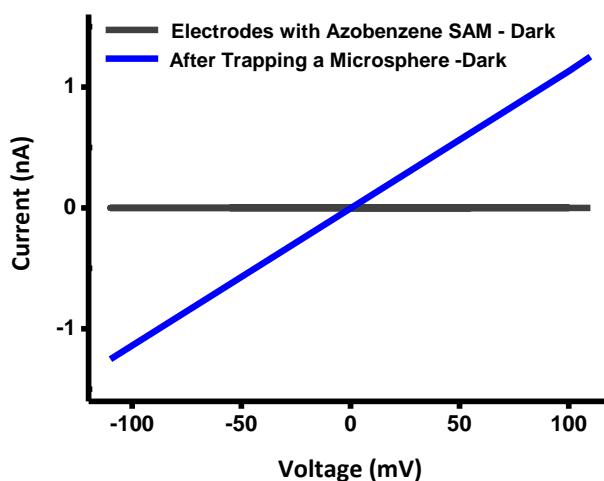


**Figure 3.15 : I-V characteristics of nanotrench electrodes before (black line) and after (blue line) microsphere trapping.**

A total of 18 samples were thus selected fulfilling these quality criteria. Samples categorized as ‘switching’ corresponded to samples where reversible changes of conductance exceeding 10% were observed. Typical observed ratio  $R_{trans}/R_{cis}$  spanned values between 1.1 and 3, significantly lower than the values reported in the literature [128, 129, 133, 134]. Example data is shown in Figure 3.16, showing successive I-V curves after illuminating the sample using 365 nm and 455 nm wavelengths. The observed I-V curves were rather linear between  $\pm 1$  V bias, similarly to previous reports [128, 129, 133, 145]. Non-linearity was observed at larger bias, poorly reproducible from sample to sample, with related large electrical instabilities.

Switching samples exhibited a sequence of conductance properties illustrated by curves 1-3 of figure 3.16 with switching ratio of around 2. The as-made junctions exhibited an initial low-conductance value (curve 1) corresponding to the thermodynamically more stable *trans* state, switching to a more conductive state under 365 nm illumination, interpreted as occurrence of *cis* configuration (curve 2). Illuminating at 455 nm revealed the reversibility of the process (curve 3, being similar to curve 1).

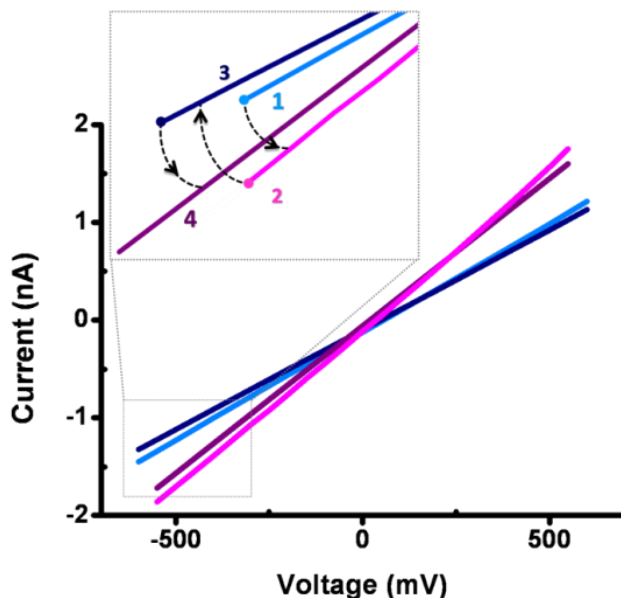


Figure 3.16 : IV curves showing one example of reversible optically modulated current switching in the junction. The curve 1 corresponds to initial junctions, expected to correspond to molecules in *trans* configuration. Curve 2 results from UV (365 nm) irradiation, of enhanced conductance due to the occurrence of *cis* configurations. Curve 3, after 455 nm illumination, illustrates the reversibility of the switching, similarly to curve 4, switching again to *cis* after re-illumination with UV.

From the 18 samples considered as representative of molecular junctions, 16 confirmed that azobenzene component of the devices resulted in reversible light-induced switching. The azobenzene sample without indication of switching was made on Si/SiO<sub>2</sub> substrate, and one could speculate that the sphere shadowing limited the light intensity on the molecular films. Si substrates showed a poor success rate, and only 2 connected devices. The unique counter-example (switching alkane connection) showed rather poor conduction ( $R \approx 3G\Omega$ ). Note that this particular sample did not exhibit reversibility in the switching, and can be categorized as accidental unstable sample that was modified under UV illumination. We nevertheless considered it, in order to show that a particular unexpected behavior can be found if enough samples are produced! A few samples were used to check that as-prepared samples (expected in the *trans* configuration) did not show significant change of conductance under excitation of wavelength exceeding 400 nm. From these experiments we can convincingly conclude that a strong statistical experimental evidence unambiguously indicate that microsphere connected devices exhibit changes of conduction related to light-induced modifications of the molecular films, confirming that the observed resistance value originates from molecular interconnects.

Type of junction	Fabricated junctions	Shorts	Connected devices	Switching	Non switching
AZO-AZO	58	2	8	7	1
C12-C12	24	3	9	1	8
C12-AZO	4	2	1	1	0

**Table 3.1 : Statistics of the number of fabricated samples. The first line corresponds to samples where electrodes and spheres are functionalized with azobenzene molecules, the second line with electrodes and spheres functionalized with alkane molecules, and the last line involving electrodes covered with alkanes and spheres with azobenzenes.**

Our devices lasted a minimum of several hours, with reproducibility and stability reaching days period under ambient atmosphere. Up to several tens of switching events can be realized, without any optimization (figure 3.17).

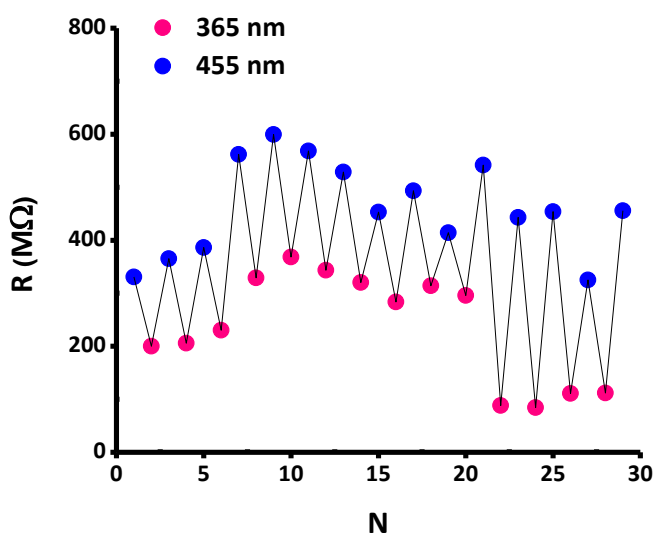


**Figure 3.17 : Evolution of the ON/OFF sample resistance after successive UV-visible light illuminations, revealing multiple possible switching events.**

Taking advantage of the time stability of devices, the time evolution of the conductance was checked and corresponding I-V curves are shown in figure 3.18, indicating a typical time scale of  $10^3$  s to reach the other conduction state value, in line with other experiments in the vertical geometry [128, 129, 133, 134]. This type of experimental insight is extremely difficult to obtain using vertical probing geometry. Switching time was observed to be of the order of a few tens of minutes, and was measured up to 30 cycles, being mostly limited by the length of the experiments (figure 3.17). One should emphasize that the observation of many switching cycles

is rather exceptional. Such number is not reported for vertical junctions, owing to the long term stability difficulties, and in general not observed for photochromic molecules, known to exhibit limited reversibility of the switching and significant fatigue effects [76].

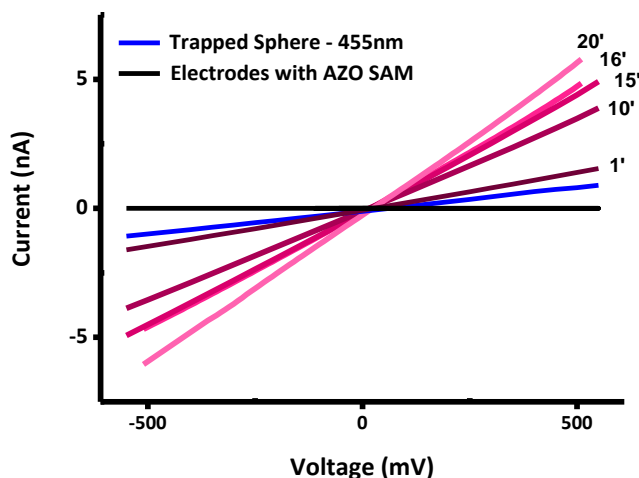


**Figure 3.18 :** Example of the time evolution of the optically tunable electrical characteristics of a junction revealing the time increase of conductance under UV illumination. The functionalized electrodes have a low-current leakage curve (black line), with significant increase after trapping functionalized spheres (blue line). The other curves show increasing conductivity under increasing indicated illumination time.

On one extensively studied sample, we observed indications of a fatigue effect, i.e. saturation of the increase of current under typically more than 10 mins UV irradiation, with and the sample partly recovering its more stable *trans* configuration, even though the excitation was still present (figure 3.19). The possible reversal of the *cis-trans* transition under UV irradiation has been reported on a previous STM data [80], motivating therefore further studies for clarifying how long-term stabilization and irreversibility of the *cis-trans* change can be optimized.

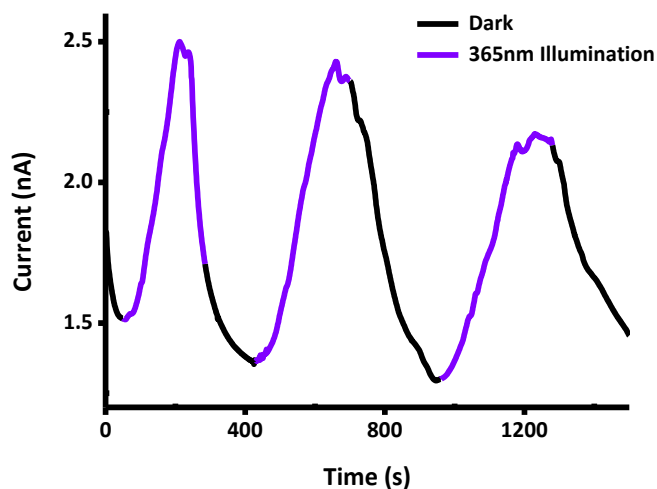


**Figure 3.19 : Observation the fatigue effect and the saturation of the increase of current under excitation and partly recovering the *trans* configuration of the sample.**

This illustration of the thermodynamical more stable *trans* state has however been observed on a single sample. Further experiments are necessary to confirm this data.

This type of observation reveals that the microsphere-bridges circuit exhibit long term stability opening relaxation, stability, and temperature studies, expected to bring new information on molecular photoswitching systems. The investigated microsphere connected devices are stable for days at ambient conditions, confirming that they can provide test bench systems of interest for performing time intensive experiments on molecular structures. Even though the trend matches, the current variation due to the photochemical response is lower than the ones observed for the vertical junctions based on Hg-drop [129, 134] or metal-coated AFM [128, 133]. However, due to the different geometry, the quantitative comparison is not straightforward.

### 3.6. CONCLUSION

Functionalized microsphere circuits confirm that the observed electrical transport originates from charges transfer through molecules. The proof-of-principle test experiments also indicate that azobenzene-type molecules can be efficiently inserted in a planar circuitry, confirming unambiguously their interest as reversible photochromic molecular electronics elements. From measurements on many samples, including dummy test comparison devices, we find electrical indications of photoswitching with a confidence ratio exceeding 90%. In layman terms, when junctions involve azobenzene molecules, they always switch; when they involve alkanethiol molecules, they never switch! The realization of stable planar molecular circuits makes also possible the realization of molecular circuits stable over several days in ambient atmosphere conditions. This unique property opens the possibility of more complete characterization of molecular circuits, in particular the variation of several external parameter, making possible the realization and investigations of multifunctional molecular materials.

## CHAPTER IV: SPIN CROSSOVER NANOCRYSTALS IN BISTABLE MOLECULAR DEVICES



This chapter focuses on positioning sub-micron-sized  $[\text{Fe}(\text{Htrz})_2(\text{trz})](\text{BF}_4)\cdot\text{H}_2\text{O}$  nanoparticles that exhibit a spin crossover transition between Au electrodes with sub-100 nm separation. We used two different approaches in order to place the SCO nanoparticles over the Au electrodes and measure their transport properties. The first one consisted of simple drop casting of particles in EtOH over the gap area while in the second one the nanoparticles were covered by very thin magnetic metallic caps, and positioned between the interconnects by magnetic trapping. After voltage poling, samples exhibit unexpected large conductivity, with photoconductance and photovoltaic behavior. The change of conduction under illumination does not require a spin transition. We observe conductivity values surprisingly high, as well as a possible photovoltaic behavior. This study also illustrates the importance of the interfaces for sub-100 nm organic interconnects [135].

## 4. SPIN CROSSOVER NANOCRYSTALS IN BISTABLE MOLECULAR DEVICES

### 4.1. SPIN CROSSOVER IN IRON (II) COMPLEXES

A paradigm example of molecular bistability [138] is the well-known spin-crossover (SCO) phenomenon, occurring in transition metal complexes, i.e. iron, cobalt and nickel [84, 85, 139]. These compounds with adequately designed ligand fields exhibit a cooperative transition between paramagnetic high spin state (HS,  $S = 2$ ) and diamagnetic low spin state (LS,  $S=0$ ), triggered by external stimuli like temperature (T), pressure (p) or light/electromagnetic radiation (hv).

SCO was first observed in 1931 by Cambi et al. [86]. Thirty years after, SCO was observed in  $\text{Fe}^{2+}$  complexes, marking the beginning of a very active research in bulk (powder or single crystal) or diluted medium (solid or liquid) materials [139].

Molecular bistability, defined as the ability of a molecular system to be observed in two different electronic states in a certain range of external perturbation, turns the SCO materials into very interesting candidates for realizing two-state molecular multi-functional permanent memory elements, attracting considerable interests in chemistry and materials fields for many years [87, 88, 89, 90]. Several hundreds of compounds exhibiting this phenomenon were synthesized and characterized, both in the solid state and in solution, using various characterization techniques: magnetic susceptibility measurements, infrared and visible UV spectrometry, NMR spectroscopy, XPS, X-ray powder diffraction [141].

For this phenomenon to occur, the metal ion needs a pseudo-octahedral coordination, with an outer electronic configuration of  $3d^n$  ( $4 \leq n \leq 7$ ). The crossover occurs when the enthalpy of the lower spin state (LS) in its equilibrium is slightly lower than the enthalpy of high spin state (HS) also in its equilibrium geometry. LS with the lowest enthalpy is thermodynamically stable at low temperatures, while at temperatures higher than  $T_{1/2}$  the HS is more stable since its associated with a larger entropy, with the product of temperature and entropy  $T \cdot \Delta S$  overcoming the enthalpy loss. (At  $T_{1/2}$  half of the molecules are in the HS and the other half in the LS).

As mentioned, the most extensively studied SCO compounds are those containing  $\text{Fe}^{2+}$  ion with the electronic configuration of  $1s^2/2s^2/2p^6/3s^2/3p^6/3d^6$ .

Electronic configurations of neutral iron, iron (II) and iron (III) ions are as follows:

([Ar] =  $1s^2/2s^2/2p^6/3s^2/3p^6$ )

Iron/Fe: [Ar] /  $3d^6/4s^2$

Iron (II) /  $\text{Fe}^{2+}$ : [Ar] /  $3d^6$

Iron (III) /  $\text{Fe}^{3+}$ : [Ar] /  $3d^5$

In  $\text{Fe}^{2+}$  pseudo-octahedral configuration, the electrons can either occupy all the lower  $t_{2g}$  level ( $^5T_2$  state) or they can occupy both  $t_{2g}$  and  $e_g$  levels ( $^1A_1$  state). The HS results from a  $t_{2g}^4 e_g^2$  electronic configuration in which the antibonding  $e_g$  orbitals are doubly occupied, leading to a  $0.15 - 0.18 \text{ \AA}$  longer Fe-ligand bonds comparing to LS with  $t_{2g}^6$  electronic configuration.

Studies have demonstrated that replacing the molecular crystals by coordination polymers in  $\text{Fe}^{2+}$  spin crossover materials gives rise to a cooperative crossover phenomenon called thermal spin transition [88, 142].

Indeed, the transition is often very abrupt occurring with a hysteresis effect with  $T_{\text{HS} \rightarrow \text{LS}} \geq T_{\text{LS} \rightarrow \text{HS}}$  providing a memory effect on the system. At a given temperature, the state of the system depends on its history and the recorded information. These systems are therefore ideal for permanent memory elements applications.

There is a vertical and horizontal shift between  $^5T_2$  and  $^1A_1$  potential wells, (figure 4.1) the horizontal shift results in greater metal-ligand distance irrespective of the ligand and the vertical one depends very much on the specific properties of the ligand. To accomplish the thermal transition, the difference of ground state energies should fall within the range of the thermal energies:  $k_B T$  [140].

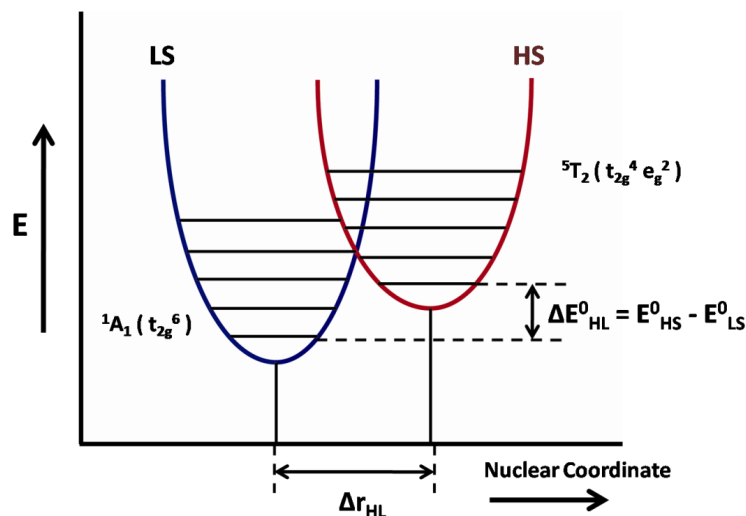


Figure 4.1 : Schematic representation of the potential wells for the  ${}^1A_1$  and the  ${}^5T_2$  states of an iron (II) SCO complex. Thermal spin transition occurs if  $\Delta E_{HL}^0$ , which is the energy difference between LS and HS ground states, fall within the range of the thermal energy  $k_B T$ .

## 4.2. IRON (II) SPIN CROSSOVER NANOPARTICLES, BISTABLE MOLECULAR SYSTEMS

The SCO complexes are ideal candidates for molecular electronics studies, mainly when aiming at realizing a chemically-engineered switching device [90, 76, 2]. Investigations on such compounds based on triazole family indicate that the spin-crossover often involves a collective behavior between the active metal ions and does not only depend on the size, but also depends on the chemical nature of the compounds and on the structural arrangement of the chains [143, 144]. Therefore, it is better to perform electrical measurements on an assembly of molecules (i.e. nanoparticles and/or nanocrystals), which are well characterized with known values of external conditions resulting into spin transition [145]. Furthermore, thermal hysteresis is not expected for single molecules, and the cooperative behavior of assembly of molecules becomes a necessary condition for permanent state realization [146]. SCO nano-objects are of high interest, since they bridge the gap of understanding the phenomenon between single molecule and bulk materials and possess unique size-related physical and chemical properties turning them into advanced materials for a wide domain of applications in current technology [87].

Spin transition nano-objects are expected to have poor conductivity values. This hypothesis points out the importance of the electrical interconnect strategy involved in their transport measurement: from one side to match the size variation of the particles and from the other side to be robust enough to keep the reproducibility of the circuit. Once again, the nanotrench geometry is well suited to investigate this family of interesting candidates for molecular electronics devices [136, 137].

SCO nanoparticles, with controlled size and shapes, were first synthesized by Létard et al. using reverse micelle (water-in-oil emulsion) technique. They observed interesting magnetic properties and a well-defined thermal hysteresis loop for the nanoparticles of  $[\text{Fe}(\text{NH}_2\text{-trz})_3]\text{Br}_2 \cdot 3\text{H}_2\text{O}$  ( $\text{NH}_2\text{-trz}$  = 2-amino1,2,4 triazole) coordination polymer at room temperature (figures 4.2 and 4.3) [147, 92, 148].

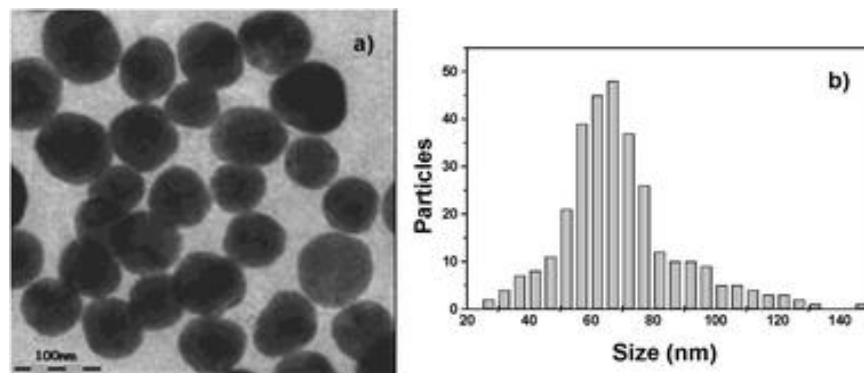


Figure 4.2 : a) TEM image of  $[\text{Fe}(\text{NH}_2\text{-trz})_3]\text{Br}_2 \cdot 3\text{H}_2\text{O}$  nanoparticles prepared by reverse micelle method, b) Statistic on particle size distribution evaluated according to TEM images on around 300 particles, average size: 69nm [92].

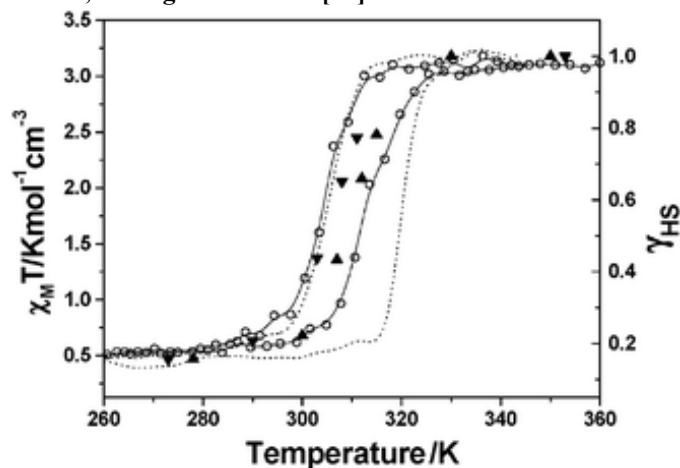


Figure 4.3 : Plot of  $\chi_M T$  vs.  $T$  of  $[\text{Fe}(\text{NH}_2\text{-trz})_3](\text{Br}_2) \cdot 3\text{H}_2\text{O}$  nanoparticles [92].

The magnetic response is expressed in the form of the  $\chi_M T$  vs.  $T$  curve, where  $\chi_M$  is the molar magnetic susceptibility and  $T$  the temperature.  $\chi_M$  is deduced from the equation 4.1, where  $\chi_V$  is the volume magnetic susceptibility,  $M$  is the molar mass and  $\rho$  the density.

$$\chi_M = \frac{M \cdot \chi_V}{\rho} \quad (4.1)$$

Building molecular devices like memory elements requires the precise information on the response of the spin crossover phenomenon to external perturbations. For applications, it is important that the spin crossover phenomenon occurs around room temperature and that the phase transition is of the first order type with a rather wide hysteresis loop ( $\Delta T = (T_{c\uparrow} - T_{c\downarrow}) \approx 30$  K,  $T_{c\uparrow}$  and  $T_{c\downarrow}$  are the LS $\rightarrow$ HS and HS $\rightarrow$ LS transition temperatures respectively).

The ligand field strength as well as short and long-range cooperative interactions in the material control the LS $\leftrightarrow$ HS transition, resulting in a hysteresis loop. Several techniques were studied to address the LS $\leftrightarrow$ HS transition: magnetic susceptibility, Mössbauer spectroscopy, optical reflectivity, vibrational spectroscopy or heat capacity measurements [149, 150, 151, 152]. Intramolecular structural changes of the iron (II) SCO complexes involving a deformation of the electronic molecular orbitals of the complex were detected, and correspond to significant variations of the Fe–N metal–ligand bond lengths (0.1–0.2 Å, i.e. 5–10%) and N–Fe–N angles (0.5–8°) [153].

#### 4.2.1. CHANGE OF COLOR

A color change from the HS pale yellow-white, to LS pink-purple reveals a spin transition of these particles. These colors may be deeper if charge-transfer bands from the associated ligands are observed, and these often mask the SCO color change.

## 4.2.2. CHANGE OF THE DIELECTRIC CONSTANT

In 2003 a study reported the change of the dielectric constant upon spin crossover for different complexes for the first time [154]. This change is due to the difference in local electrical dipoles in the material in the LS and HS state. The authors measured the thermal variation of dielectric permittivity ( $\epsilon^* = \epsilon' - i\epsilon''$ ) in isotherm frequency sweeps in the range of  $10^2 - 10^7$  Hz successively in heating and cooling modes for several compounds and compared them to results obtained by optical reflectivity or magnetic susceptibility. The imaginary part  $\epsilon''$  is related to the dissipation (or loss) of energy within the medium, the real part  $\epsilon'$  depends on time and represents the movement of the bounded charges in presence of an electric field. The results for  $[\text{Fe}(\text{NH}_2\text{-trz})_3](\text{NO}_3)_2$  are presented in the figure 4.4, similar for other complexes. This compound is of high interest since it's based on amino-triazole and is close to the compound studied in this thesis [92].

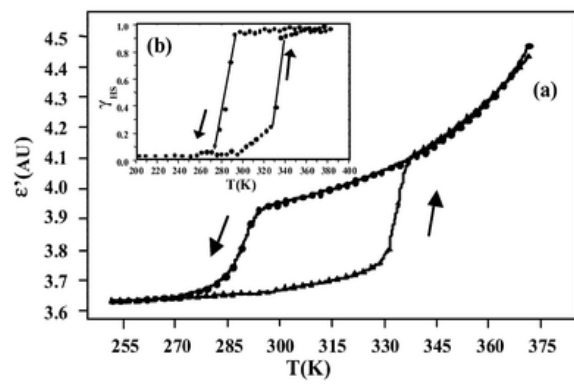


**Figure 4.4 :** (a) Thermal hysteresis of the dielectric constant associated with the spin-transition of  $[\text{Fe}(\text{NH}_2\text{-trz})_3](\text{NO}_3)_2$ . (b) Thermal variation of the proportion of high-spin molecules (HS) in  $[\text{Fe}(\text{NH}_2\text{-trz})_3](\text{NO}_3)_2$  obtained through magnetic susceptibility measurements (data points are connected to guide the eye) [154].

## 4.2.3. CHANGE OF VOLUME

As described before, due to the occupation of  $e_g$  orbitals in HS state, the average length of Fe–N ligand bond becomes larger in HS than LS.

A recent crystallographic study for  $[\text{Fe}(\text{Htrz})_2(\text{trz})](\text{BF}_4)$  compound allowed to quantify the change of volume. The LS→HS transition implies 11% change of volume due to a network

extension of 2.9%, 1.7% and 6% for the a, b and c axis respectively [155]. This change of volume could be detected in transport measurements, by increasing or decreasing the particle/electrode contact area therefore implying a change in the parasitic interface resistance reflected in the conductivity values. The changes in the volume as well as electronic polarity of the spin transition nanoparticles could eventually affect the conductivity of the particle in transition between LS and HS states, with the perspective of using the SCO NP as a switch in a circuit (figure 4.5) [90, 91, 156].

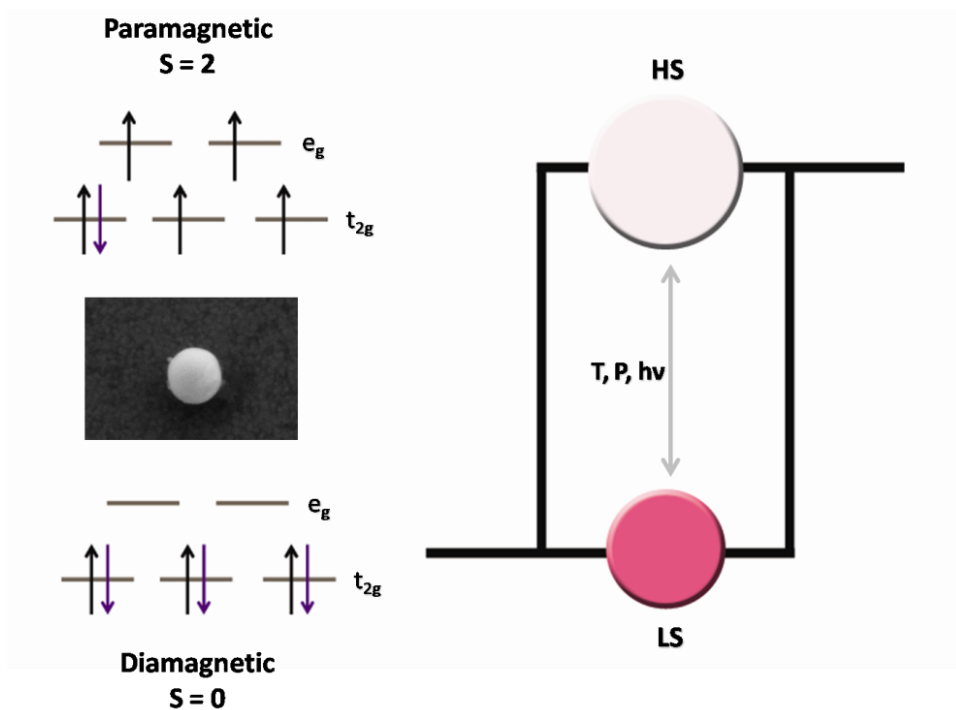


Figure 4.5 : Left: LS and HS states for an iron (II) based spin crossover nanoparticle. At the molecular state, the spin crossover corresponds to an intraionic transfer of two electrons between the  $t_{2g}$  and  $e_g$  orbitals, accompanied by a spin flip. Right: The schematic of volume and color change due to spin transition superposed on the hysteresis cycle of SCO NP.

## 4.3. MOLECULAR JUNCTIONS CREATED BY IRON (II) BASED SPIN CROSSOVER NANOPARTICLES OVER NANOTRENCHES

### 4.3.1. EXPERIMENTAL SETUP, STRATEGY

We used two different approaches in order to place the SCO nanoparticles over the nanotrench electrodes and measure their transport properties. The first one consisted of simple drop casting of particles in EtOH over the gap area while in the second one the nanoparticles were covered by very thin magnetic metallic caps, and positioned between the interconnects by magnetic trapping. Transport measurements were performed at room temperature, under ambient conditions.

The sample holder connecting the nanotrench electrodes to an electrometer (Keithley 6517b) was mounted and fixed on the observation stage of an inverted optical microscope, allowing the illumination from a 100W halogen source to be focused on the nanotrench electrodes through the microscope light condenser of 0.55 numerical aperture, providing a convenient visualization platform with precisely calibrated illumination at selected filtered wavelength as well as a heating source after removing the IR filter (figure 4.6).

One should emphasize that the type of nanoparticles presented, showing a thermal spin transition, do not exhibit a simple light-induced spin transition. It has been shown that pulsed light irradiation can lead to a spin transition only through thermal transfer effect [149, 157, 158]. In other words, light irradiation can only induce a transition through the related heating effect. Therefore, observing light induced spin transition under continuous light irradiation requires a light power density large enough to increase significantly the temperature of the sample.

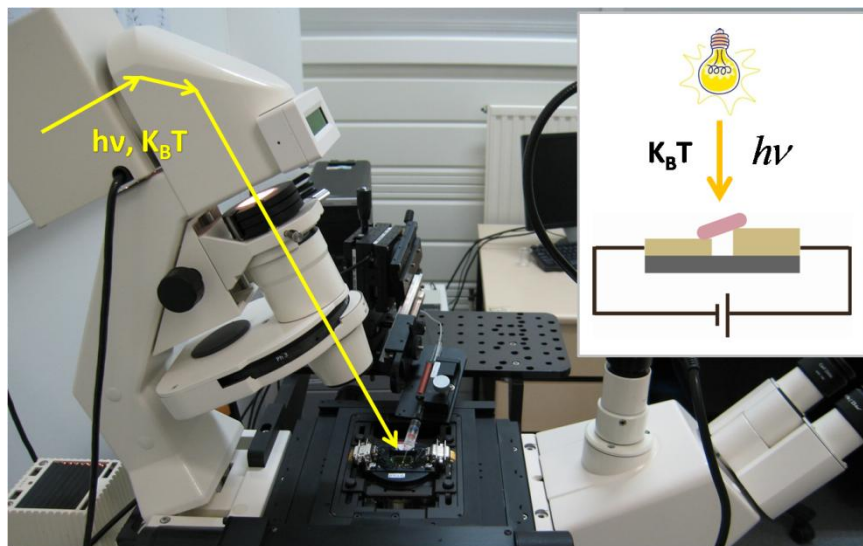


**Figure 4.6 :** Picture of the the sample mounted on an inverted optical microscope, with the light path through the condenser to the sample. Inset: schema of the experiment principle involving a nanotrench bridged by SCO NP.

#### 4.3.2. SYNTHESIS AND FABRICATION OF SCO NANOPARTICLES

The selected SCO complex in this study is a  $[\text{Fe}(\text{Htrz})_2(\text{trz})]\text{BF}_4 \cdot \text{H}_2\text{O}$  coordination polymer (with Htrz = 1,2,4-1H-triazole and trz = the deprotonated triazol) [148].

The complex was synthesized by a reverse micelle technique (figure 4.7). A reverse micelle is a dispersion of water droplets in a continuous oil phase. In the first step, two solutions were dissolved in separate flasks: 1) the iron(II) salt  $\text{Fe}(\text{BF}_4)_2$  (674mg; 2mmol) dissolved in 1.6 mL demineralized water, 2) the ligand (triazole) 1,2,4-triazole (414 mg; 6mmol) dissolved in 1.6 mL of demineralized water. Then, 6.32 gr of the surfactant (Tergitol-NP9) was added to both flasks shaken by dynamic agitation with a vortex system during 5mins in order to form thermodynamically unstable reverse micelles. The two solutions were then mixed and maintained in an ultrasonic agitation for 1 hour at  $50^\circ\text{C}$  to support the micellar exchange and the growth of well crystallized  $[\text{Fe}(\text{Htrz})_2(\text{trz})](\text{BF}_4)$  particles. Immediately after that diethyl ether solvent was added to break down the emulsion and limit the molecular diffusion degradation. Indeed, the diethyl ether solvent dissolves the surfactant without denaturizing the iron (II) coordination polymer, which finally precipitates. This was followed by a series of extraction washing steps with diethyl ether to obtain the final powder.

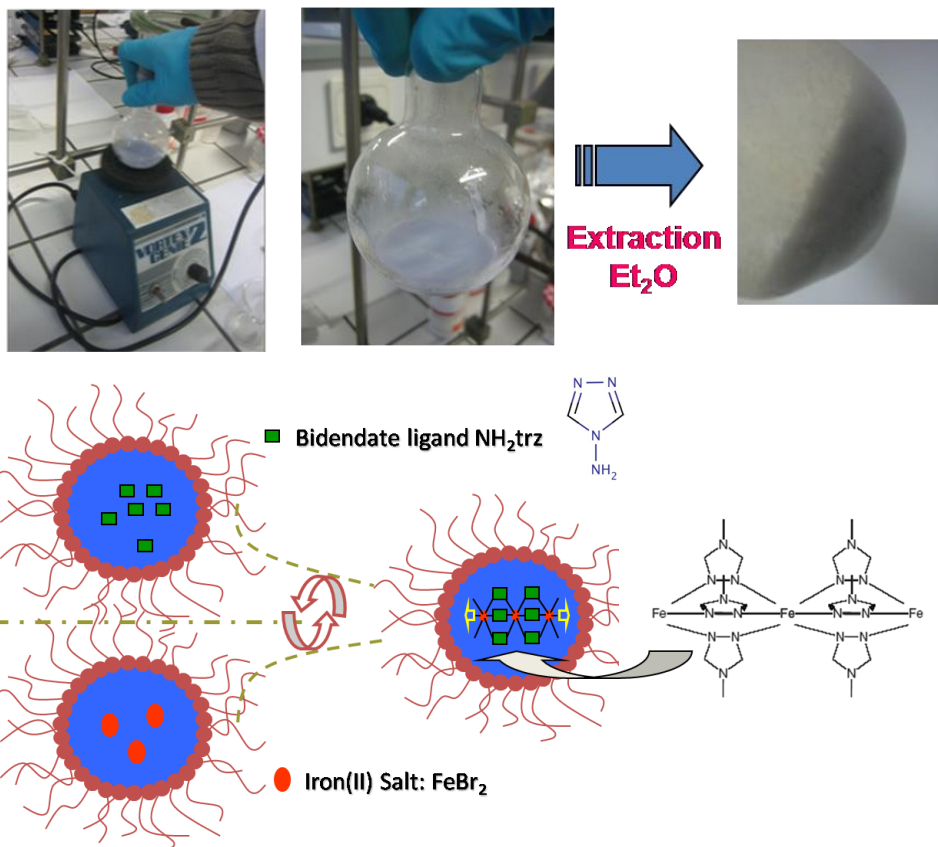


Figure 4.7 : Synthetic route and schematic representation of the  $\text{Fe}(\text{NH}_2\text{-trz})_3$  unit.

The synthesized compound called JFSD27, which is the one we studied most extensively, consists of rectangular particles of  $650 \times 200$  nm size, exhibiting a spin transition with a hysteresis of 35 K between  $T_{\downarrow}=345\text{K}$  and  $T_{\uparrow}=380\text{K}$  (figures 4.8 and 4.9).

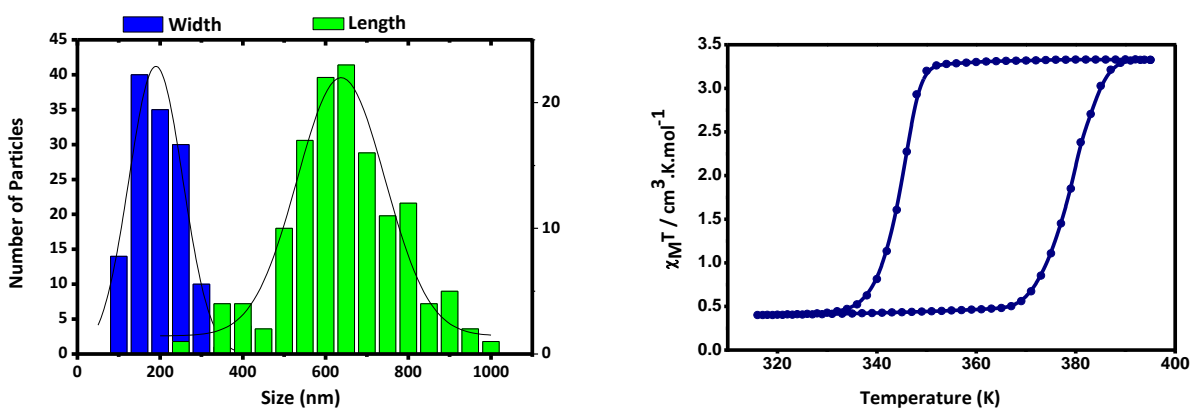
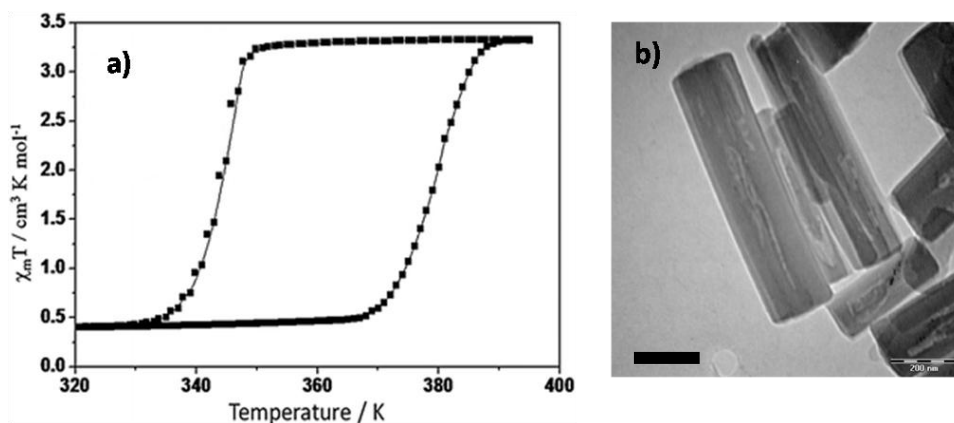


Figure 4.8 : Left: Distribution of the JFSD27 nanoparticles size, right: molar magnetic susceptibility vs.  $T$  for  $[\text{Fe}(\text{Htrz})_2(\text{trz})]\text{BF}_4 \cdot \text{H}_2\text{O}$  coordination polymer, showing a hysteresis of 35K between 354-380 K.

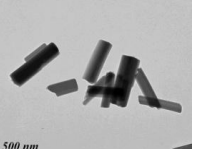
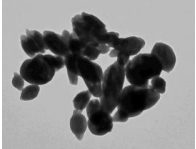
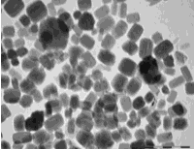
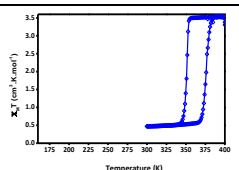
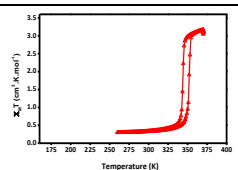
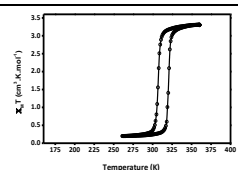
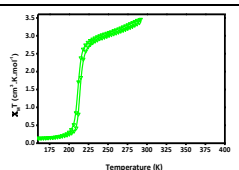
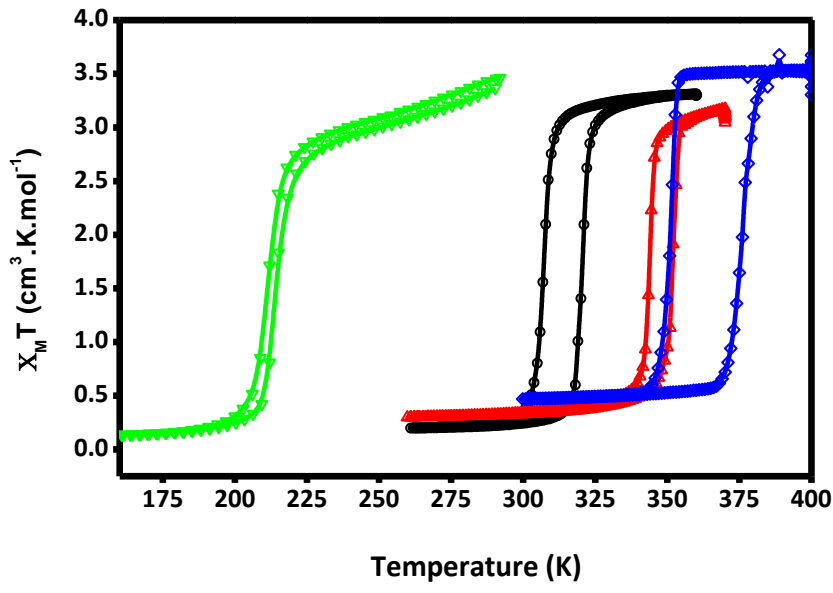


**Figure 4.9 :** a) Temperature dependence of  $\chi_M T$  product ( $\chi_M$ = molar magnetic susceptibility and T=temperature), representation of  $[\text{Fe}(\text{Htrz})_2(\text{trz})](\text{BF}_4)\bullet\text{H}_2\text{O}$  polymer, b) TEM micrograph of the nanoparticles prepared by reverse micelle method (the black bar scale is 200 nm).

This material is of high interest for room temperature studies as it exhibits a LS→HS transition at temperatures higher than ambient, with a significant thermal hysteresis [160]. Figure (4.10-b) reports Transmission Electron Microscopy (TEM) images of the particles which are rectangular with a length and width distributions of 650 nm and 180 nm, respectively.

By varying the ligand and counter ions, in conjunction with modifications in the fabrication parameters (vortex agitation time, exchange time, and temperature of the exchange step), the size and shape of the nanoparticles can be tuned. As a result, the transitions temperatures are modified. Table 4.1 summarizes the different types of nanoparticles synthesized in J-F Létard's group, and available for our studies.

**Table 4.1 : Different SCO coordination polymers synthesized and characterized.**

	JFSD27	JFCE170	JFCE128	JFCE172
Complex	[Fe(Htrz) <sub>2</sub> (trz)]BF <sub>4</sub>	[Fe(NH <sub>2</sub> trz) <sub>3</sub> ]Cl <sub>2</sub>	[Fe(NH <sub>2</sub> trz) <sub>3</sub> ]Br <sub>2</sub>	[Fe(NH <sub>2</sub> trz) <sub>3</sub> ](BF <sub>4</sub> ) <sub>2</sub>
Synthesis Conditions	5 min Vortex/ 1h US 50 °C 75 % NP9	5 min Vortex/ 7 h US 50 °C 75 % NP9	5 min Vortex 5 min Vortex 70 % Ifralan	5 min Vortex/ 1 h US 50 °C 75 % NP9
TEM Micrograph				
Shape/Size	Well defined Rods 640 (± 210) × 190(±130)	- Spheroid 290 (±1 70) - Some Rods 600 × 200	- Cube or short - Cylinder 110(±60)x170(±60)	Rods about 700 nm (±500)
Transition				
Transition T/K	351	344	307	211
Ambient T state	LS	LS	Intermediate	HS
				

### 4.3.3. TEMPERATURE CALIBRATION

The illumination source of the inverted microscope, focused through a condenser with 0.55 numerical aperture, heats significantly the sample when the IR filter removed, owing to the significant absorption of the sample and substrate at these wavelengths. Temperature calibration was performed using a Pt resistance thermometer placed at the sample position, allowing us to obtain an estimate of the sample environment temperature related to the voltage (power) setting of the illumination source power supply (figure 4.10).

(e.g. 7.4 applied volts = 61 watts power intensity heats the sample up to 110°C)

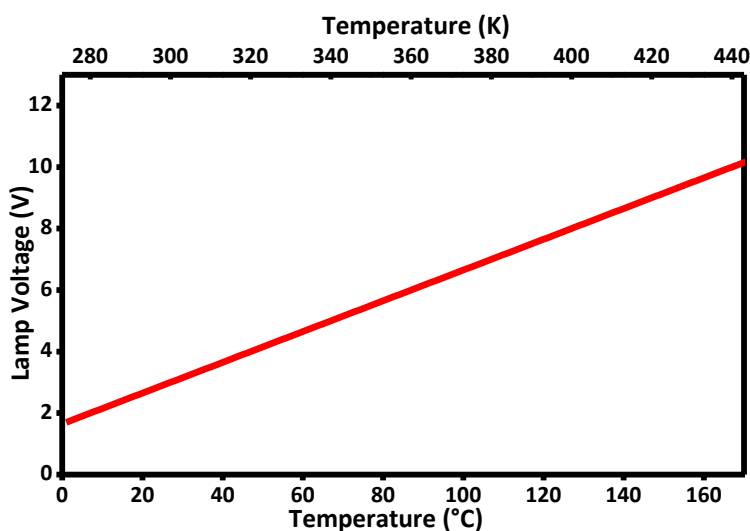


**Figure 4.10 :** The voltage applied to the halogen illumination source versus the temperature read at the sample's stage, using a PT-100 probe.

The V-T calibration data is quite precise for a probe in the position of the sample. Nevertheless the exact temperature intrinsic to the nanoparticle over the metallic nano-electrodes can be different, and the data of figure 4.10 is mostly indicative of a linearity. We have monitored the variation of the Pt probe temperature in time, for a constant voltage applied to the halogen illumination source. We observed a gradual decrease, which may be related to the temperature exchange with room and cooling mechanism of the probe.

Applying the same conditions, we monitored the variation of resistance of the metallic tracks on the sample while heating. Track resistance varies linearly versus the applied voltage to the

halogen source. The cooling effect due to heat dissipation is observed to be more progressive comparing to the probe (figure 4.11).

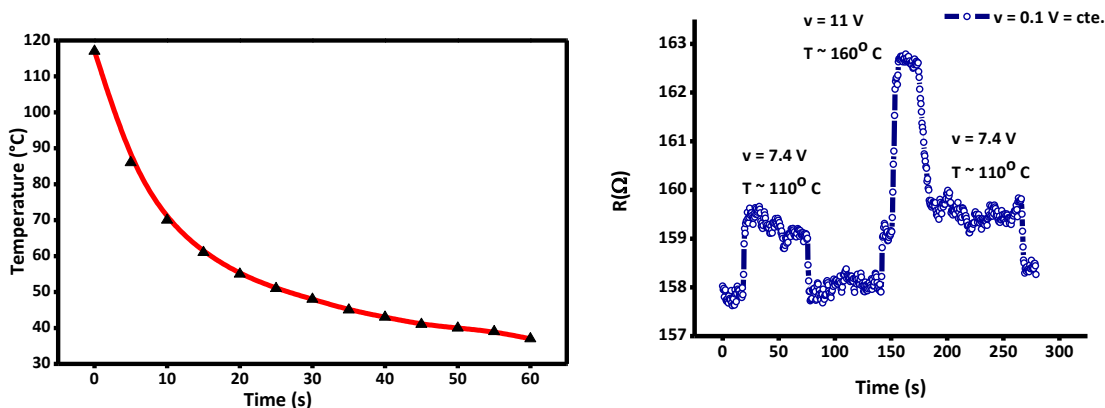
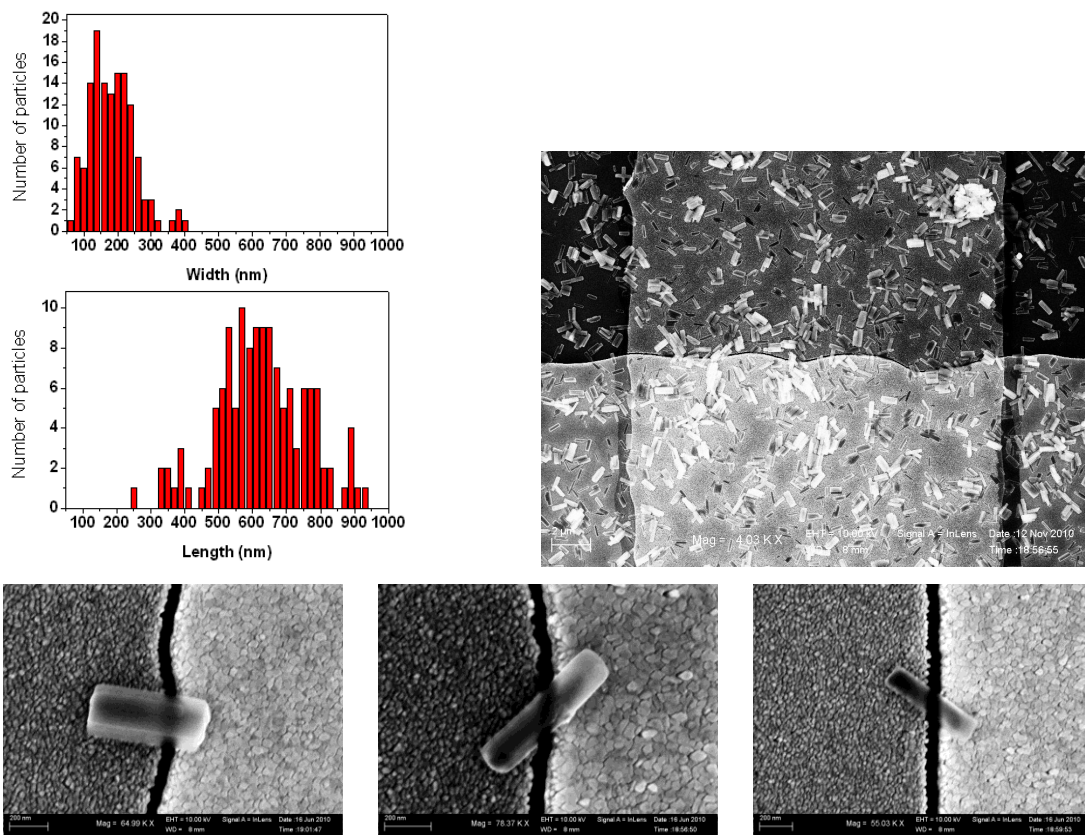


Figure 4.11 : Left: Temperature decrease versus time after turning the illumination source off at T=0 measured by a PT-100 probe glued to a microscope glass slide, Right: Evolution of the resistance of a metallic track due to heating via illumination.

#### 4.3.4. PLACING THE SCO NANOPARTICLES OVER THE NANOTRENCHES

The nanoparticles were dispersed in ethanol (typically 1mg of the compound for 2mL of ethanol), and the solution was sonicated for about 5 minutes.

In order to position the SCO NPs over a nanotrench and study their transport properties, a drop of SCO NPs in ethanol was spread over the nanotrenches by drop casting immediately after the sonication step. Owing to the high concentration of the solution, we reached 100% efficiency for obtaining nanotrenches bridged by NPs. Several current versus voltage curves were recorded before and after the deposition of the particles on trenches and current versus temperature data were taken as soon as a change in the current values was observed. We deduced from the SEM micrograph (figure 4.12), that approximately one particle per 600 nm trench width is positioned over the trench for the samples with the largest densities of trapped particles.



**Figure 4.12 : Top-right: SEM micrograph of a 20  $\mu\text{m}$  wide nanotrench covered by spin transition particles after drop casting. Top-left: Size distribution of particles of  $[\text{Fe}(\text{Htrz})_2(\text{trz})]\text{BF}_4 \cdot \text{H}_2\text{O}$  coordination polymer (with Htrz = 1,2,4-1H-triazole and trz = the deprotonated triazolato(-) ligand) used as initial powder for trapping between electrodes. Bottom: SEM micrographs examples of single  $[\text{Fe}(\text{Htrz})_2(\text{trz})]\text{BF}_4 \cdot \text{H}_2\text{O}$  nanocrystals over nanotrenches.**

#### 4.3.5. TRANSPORT MEASUREMENTS

Prior to transport measurements, several test experiments were carried out in order to check for possible artifacts of the sample and/or the setup, which may interfere with the results. Figure 4.13 presents the variation of the resistance of empty nanotrenches in the presence of illumination and heat. Even after an hour exposure, there is no significant change and the resistance value stays very high ( $\text{G}\Omega$ ), which is the typical value obtained while measuring the leakage current of nanotrench electrodes. The electrodes can sustain very high voltage bias for a relatively long time without showing modified current values due to heating or illumination (see chapter II).

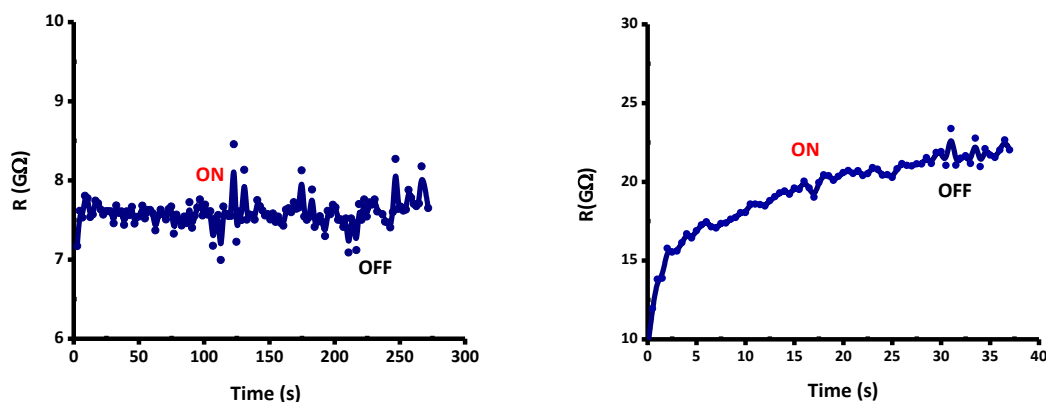


**Figure 4.13 : Monitoring the leakage current of an empty trench, in the presence of 62 Watts (2200 luminous intensity) and 110°C temperature. The resistance stays in the GΩ range, and there is no response to heat or illumination. Applied voltage = 1V=cte. The increase of the resistance in the right curve is due to the capacitive effect of the cables and/or the electrodes, as often observed in the case of leakage current measurements. The RC time constant corresponds to 0.1nF capacitance, easily reached for our setup, where triaxial shielding was not optimized.**

Current versus voltage data was recorded for nanotrench electrodes before and after deposition of  $[\text{Fe}(\text{Htrz})_2(\text{trz})]\text{BF}_4$  particles by drop casting. Very small initial currents were observed for nanotrenches bridged by several particles, with the conductance values ranging from pS to nS range. After applying a significant voltage (1-2 Volts) we observed an irreversible drastic change of conduction, decreasing the resistance of sample by typically 3 orders of magnitude (figures 4.14-a and 4.14-b). The resistance of the samples after such voltage “poling” was in the range of  $10^7$ - $10^9 \Omega$  which is a rather low value regarding the number or particles. For the samples undergoing the voltage ‘poling’, we observed a light-induced switching effect (figure 4.14-c). The amplitude of the switching varies with the light intensity and with temperature (figure 4.15) [93].

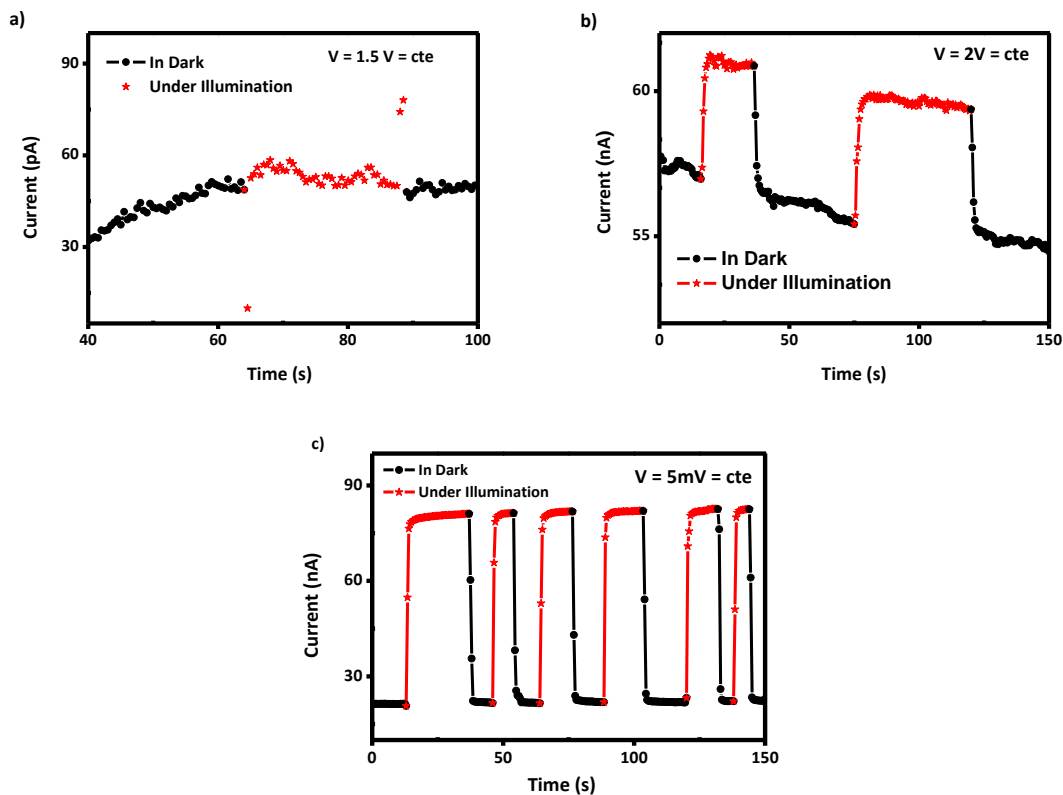


Figure 4.14 : Voltage ‘poling’ in between 1.5V and 2V for a  $[\text{Fe}(\text{Htrz})_2(\text{trz})]\text{BF}_4$  nanocrystal connecting a  $30\mu\text{m}$  long nanotrench a) showing no sensitivity to illumination/heat when 1.5 V voltage bias applied, b) resistance switching after voltage poling, the magnitude of switching effect depends on the intensity of the illumination source. c) applied voltage = 5mV, resistance switching values from  $230\text{ k}\Omega$  in dark to  $61\text{ k}\Omega$  under illumination and  $110^\circ\text{C}$  ( $61\text{ Watts}$  power and  $2200$  luminous intensity) [93].

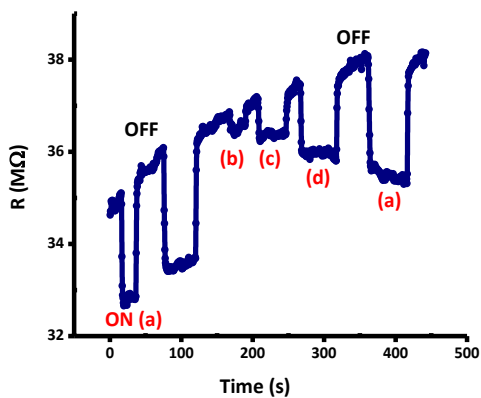
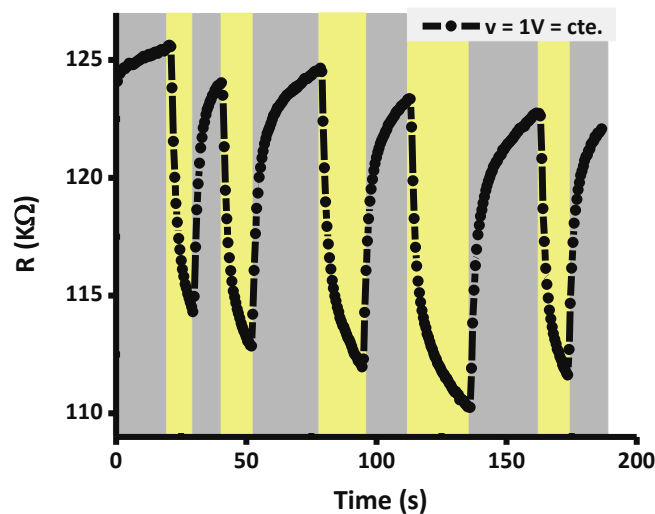


Figure 4.15 : Variation of the amplitude of switching regarding the light intensity and/or the temperature. (a)  $61\text{ watts}$  ( $7.4\text{ V}$ ) -  $110^\circ\text{C}$ , (b)  $37.5\text{ watts}$  ( $4.5\text{ V}$ ) -  $57^\circ\text{C}$ , (c)  $46\text{ watts}$  ( $5.5\text{ V}$ ) -  $77^\circ\text{C}$ , (d)  $55\text{ watts}$  ( $6.6\text{ V}$ ) -  $97^\circ\text{C}$ , ( $v = 2\text{V} = \text{const.}$ ).

Note that the hypothesis of a SiO<sub>2</sub> breakdown and possible photoconduction of Si/SiO<sub>2</sub> shorts is extremely unlikely, as the empty trenches, as well as the trenches filled with solvent only, can sustain much larger voltage stress values.

The first hypothesis for this switching behavior is the occurrence of thermal spin transition in nanocrystals by heating followed by a volume change, which eventually affects the transport parameters. There is no evidence of hysteresis behavior in the obtained data, going from LS→HS and back to LS should not result in the same resistance value for both of the LS states, which is not the case in our observations (figure 4.14-c).

The resistance drift of Au junction induced by a change of temperature from 25°C to 110 °C generated by an intense light illumination was measured with a thermocouple. The typical time scale for cooling down the sample was found to be orders of magnitudes longer than the measured switching time under similar illumination flux (less than 2 seconds) (figure 4.16).



**Figure 4.16 : Time evolution of the sample temperature revealed by the change of resistance. The yellow area corresponds to turning ON the light source without IR filter. We independently calibrated the attained temperature after 10 s illumination of about 60 °C. This figure shows that more than 10 s are needed to modify the interconnects temperature by more than 10 °C.**

We also have independently calibrated the attained temperature of the metallic interconnects, showing that it is needed more than 10 seconds to modify the temperature by more than 10°C. These typical cooling time scales cannot be reconciled with a resistance switching due to a spin

transition, as our observed switching times below less than 2 seconds do not allow a temperature change of more than a few degrees.

For another gap showing the voltage ‘poling’ on the same sample, we have applied the measurements in dark and noticed a switching effect at the presence of other external weak illumination source i.e. room light, cell phone light, residual light coming from the microscope.

We have repeated the measurements by adding an IR filter on the light pathway preventing the sample from heating and the same switching effect via illumination was observed (figure 4.17).

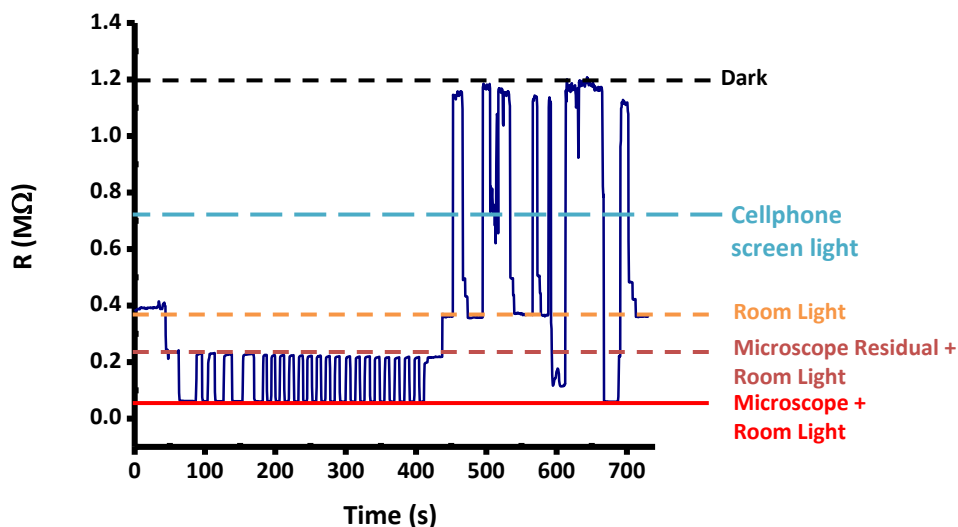


**Figure 4.17 : Resistance switching of a SCO NP over a nanotrench, showing the occurrence of switching in the presence of illumination (without heat) i.e. room light and residual light of the microscope.**

We consider therefore that we have unambiguous evidence that the observed change of conductance under illumination does not involve heating.

The same behavior was observed by placing the  $[\text{Fe}(\text{NH}_2\text{trz})_3]\text{Cl}_2$  spin crossover particles over nanotrench electrodes (figure 4.18). At ambient temperature, the spheroid-shaped particles are at the low spin state, their spin transition occurs at 344K (71°C) and 352K (79°C). We observed a current switching at 110°C. The resistance values obtained for these nanoparticles (hundreds of MΩ) are typically  $\sim 10^4$  times larger than those obtained for  $[\text{Fe}(\text{Htrz})_2(\text{trz})]\text{BF}_4$  nanoparticles (hundreds of kΩ) and the  $\frac{R_{\text{OFF}} - R_{\text{ON}}}{R_{\text{OFF}}}$  ration is typically four times smaller than what is found for  $[\text{Fe}(\text{Htrz})_2(\text{trz})]\text{BF}_4$  particles.

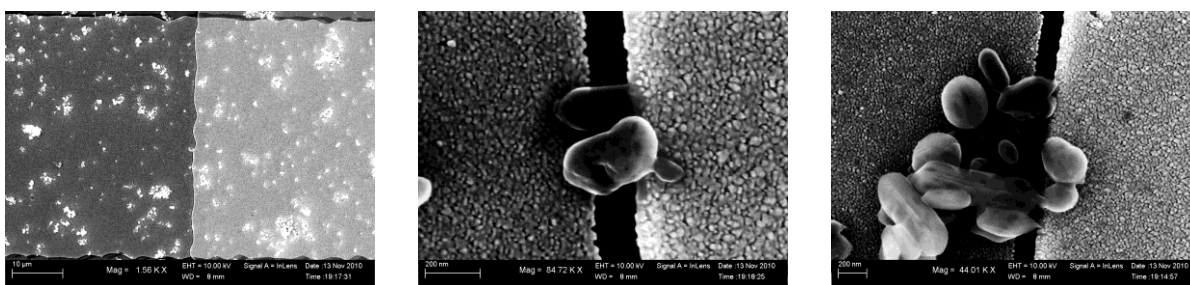
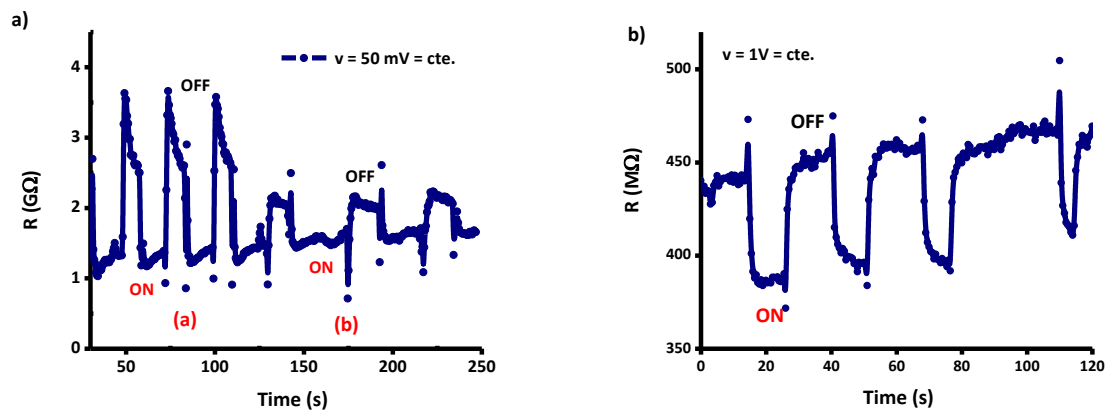


**Figure 4.18 : Top: R(time) for  $[\text{Fe}(\text{NH}_2 \text{ trz})_3]\text{Cl}_2$  spin crossover nanoparticles, a) resistance switching under (a)  $110^\circ\text{C} - 61$  watts (b)  $57^\circ\text{C} - 37.5$  Watts, Bottom: SEM micrographs of  $[\text{Fe}(\text{NH}_2 \text{ trz})_3]\text{Cl}_2\text{SCO}$  NP over nanotrench electrodes.**

The observed significant poling voltage should induce irreversible modifications near the interfaces. We envision two possibilities. First, if the nanoparticles are intrinsic good conductors, the high-developed electric field at the interfaces under voltage bias of the sample can result in breakdown of tunnel-type interface barriers. Charge diffusion is possible in an ionic-type material, and involves molecular rearrangements that drastically modify the interface resistance [1, 35]. The diffusion is self-stabilized when a better conduction through the interface is realized, as the voltage profile is more uniform over the whole sample. Second, the poling voltage magnitude can reach redox potentials of molecules of the SCO polymer, for example oxidizing  $\text{Fe}^{2+}$  to  $\text{Fe}^{3+}$ , and/or removing one electron to the  $\text{BF}_4$  counter-ion. Irreversible reactions will affect a fraction of the sample limited again to the region very near the interfaces, as the bias voltage experienced by the conducting nanoparticle varies continuously within the 0 to 1.5-2V bias window [17].

Finally, we can safely exclude that the observed photoconductions related to the substrate, defects in the  $\text{SiO}_x$ , or electromigration from the metallic electrodes. As mentioned previously,

virging samples can sustain larger voltage stress values without damages. We also often observed junctions where significant conduction and related photoconduction disappears when washing the sample, or when excessive voltage (current) stress resulted in local destruction of the nanoparticle conductive bridges.

#### 4.3.6. OBSERVATION OF PHOTOVOLTAIC EFFECT

In a few samples, exceptional occurrence of photovoltaic currents was clearly revealed at low bias. Figure 4.19 compares the most commonly observed IV curves with one sample exhibiting a flowing current at zero bias under illumination.

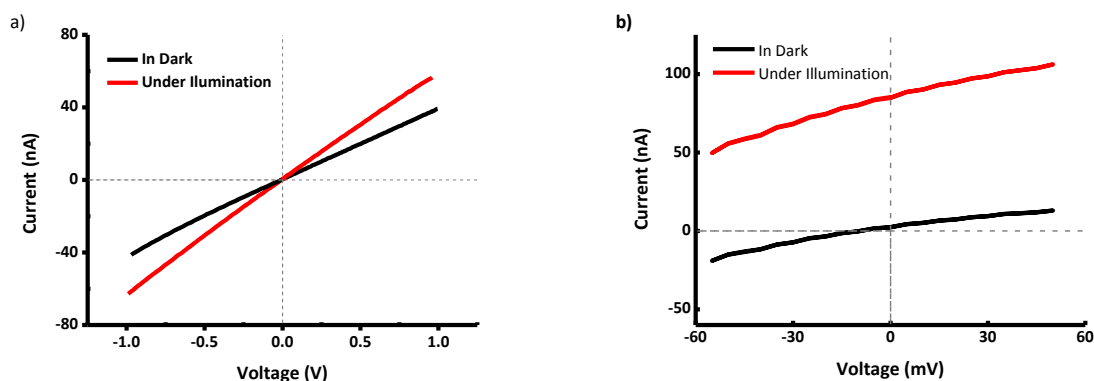


**Figure 4.19 : a) Current-voltage curve of a typical sample in dark and under illumination, b) A peculiar case exhibiting photovoltaic behavior after voltage poling of the electrodes.**

Even though the initial sample configuration involved two identical Au electrodes, the voltage poling can result in different induced effective energy barriers for the two sides of the junction, confirming therefore the key role of the interfaces [161]. We deduced from the SEM micrograph in figure 4.12 (top-right) that for a typical sample, the number of the connecting crystallites is about 30 particles for 20 $\mu$ m trench width, considering the size of the particles, the corresponding estimated width of the connected molecular assembly consequently does not exceed 10 $\mu$ m. The resistance values of the samples showing the photoconduction and ‘voltage poling’ was in the average range of 10<sup>7</sup>-10<sup>9</sup>  $\Omega$  (in the lowest case 60k $\Omega$  for one sample exhibiting a considerably high sensitivity, figure 4.17), which results in an interface resistance estimate of 10<sup>5</sup>-10<sup>8</sup>  $\Omega$ .cm. These non-negligible values are similar to quoted values for interface resistance separating semiconductor polymer thin film from metallic electrodes in thin film transistor devices (figure

4.20) [1]. Having a large number of particles connected in parallel with a negligible interface resistance will give an estimate of minimal conductivity of such crystallites. A conservative estimate leads to conductivity values larger than  $10^{-2} \Omega \text{ m}$  while there is the possibility of exceeding  $1 \Omega \text{ m}$ .

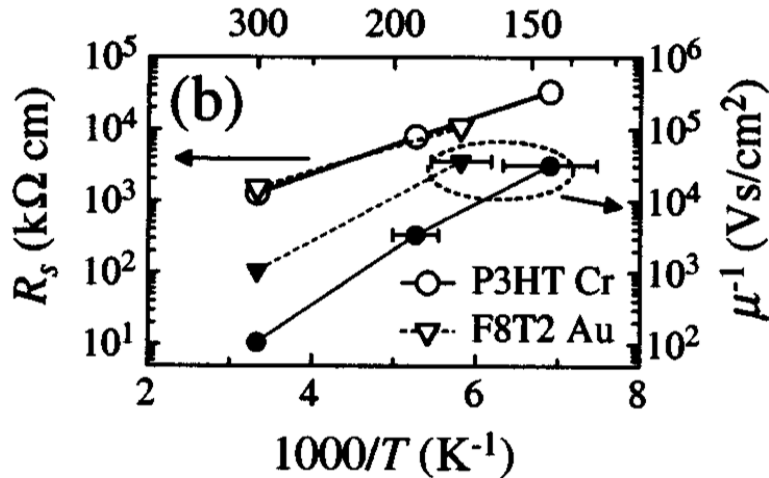


Figure 4.20 : Temperature dependence of the source contact resistance (open symbols) and inverse field effect mobility (closed symbols) as a function of the inverse temperature ( $V_G=40\text{V}$ ) for bottom-contact polymer thin film transistor device. Circles and triangles represent P3HT/Cr and F8T2/Au transistors, respectively [1, 35].

The occurrence of the SCO phenomenon assisting the photoconductance at this stage of progress is also not excluded, even though photoconductance does not require heating. One should however mention that we easily observed  $10^1$ - $10^2$  switching events, without attempts to optimize this number. This is highly unexpected for molecular switching systems, where severe limits on the number of reversible molecular modifications were generally observed [76, 90]. All these observations strongly support a simple photoconduction mechanism.

#### 4.4. FABRICATION OF HALF METALLIC SHELLS OVER SCO NP AND TRANSPORT MEASUREMENT STRATEGY.

Another set of samples were made using modified spin crossover particles. The nanoparticles were partly covered with a metallic shell using vacuum evaporation. This modification has two principal advantages:

1. By adding a thin metallic shell we may gain in conductivity value by reducing the interface resistance, resulting in transport properties more related to the particle itself (as active channel), if the metallic films is thin enough,
2. Adding the possibility of manipulation of particles, i.e. obtaining a better control of particles positioning.

Several types of particles with depositions composed of metallic bilayers and/or monolayers were prepared, and their transport properties were investigated.

For preparation of nanoparticles, 1mg of nanocrystal powder was mixed with 2mL of EtOH, sonicated for about 5 minutes in order to obtain a monodisperse solution with low agglomeration of nanocrystals.

Microscopy coverslide substrates from Electron Microscopy Sciences (0.17–0.13 mm thick) were cleaned by standard rinsing in acetone and isopropanol followed by drying under nitrogen flow. Oxygen plasma treatment (100 watts plasma power for 20 minutes) was performed for ensuring reproducible substrate quality and organic residue removal. The solution of nanocrystals in ethanol, once removed from the ultrasound bath, was left for about a minute. Then, a volume of a few hundreds of micro liters was taken from the supernatant with a micropipette and spread on the surface of the coverslides. The drop spread uniformly and after the evaporation of ethanol (few seconds) a homogenous layer of particles was formed on the substrate. The substrates were then placed in a metal evaporator where the metal deposition was performed. The substrates were then placed in ethanol and in ultrasonic bath for about 5 minutes for the particles to detach from the substrate and be dispersed in the solution. There was a decrease in the concentration of the particles, since only typically 70% of the particles were detached from the substrate.

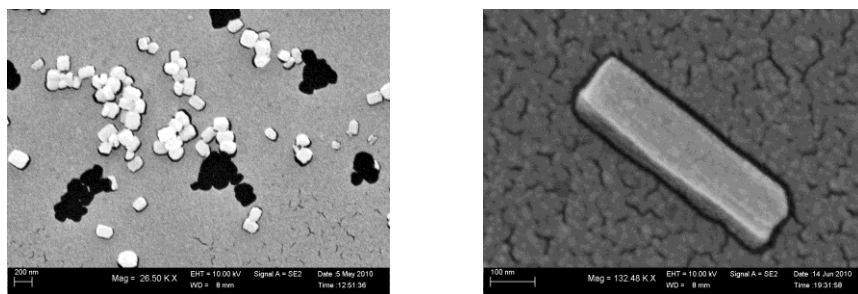


Figure 4.21 : SEM images of two different SCO-NPs covered with metallic deposition, the black holes are the particles detached from the substrate by sonication.

SCO nanoparticles were half covered with a metallic film made of Ni or Ni protected by Au layer. The same process was used as described in section 2.3 for magnetic trapping of microspheres over nanotrench electrodes (figure 4.22).

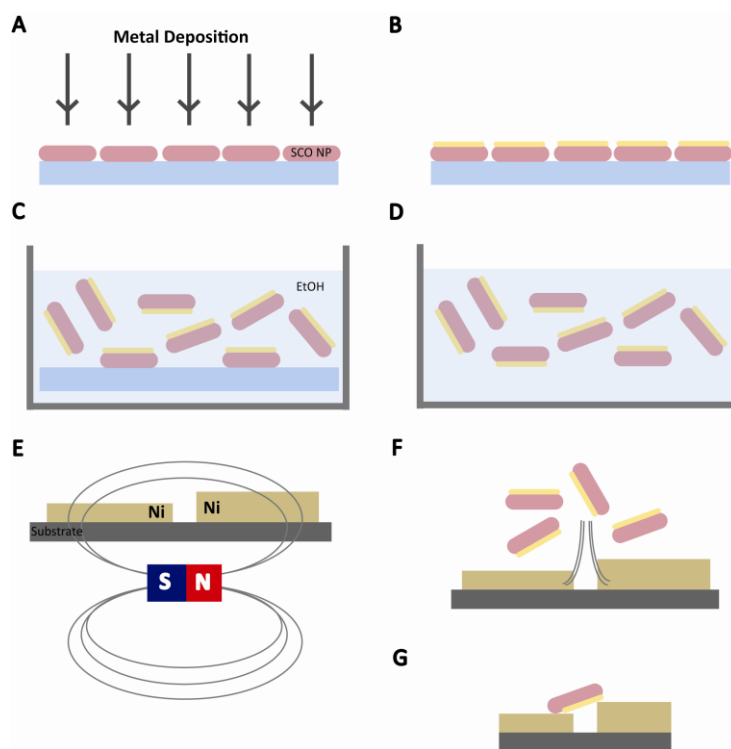
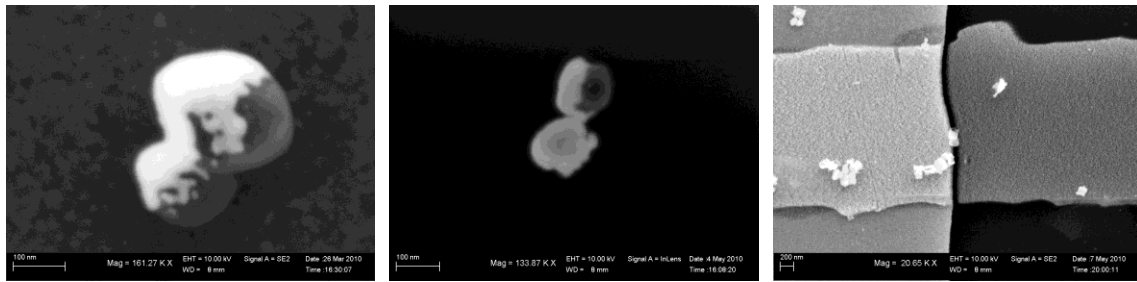


Figure 4.22 : Schematic of trapping a half metal coated SCO-NP over a nanotrench. A,B: Deposition of a Ni protected by Au layer over particles on a glass substrate, C,D: detaching the particles from the substrate and dispersing them in EtOH by sonicating, E,F: magnetizing the magnetic layer buried in the contacts along the long axis of the electrodes (perpendicular to the nanotrench) for creation of a magnetic field gradient in the trench area, (magnetizing done by a permanent magnet of Ni-N52 D = 10mm, L=10mm with inside flux 1.43T and outside flux 5600 gauss), immersing the substrate in the solution containing metalized nanoparticles (with Ni layer buried under the Au film), soft agitation for about 20 minutes, G: an array of particles entrapped and positioned over the gap. The schema shows how the particle is located due to the asymmetric geometry of the nanotrench.



**Figure 4.23 : SEM micrographs of cubic-shaped SCO NP, covered by 10nm Au over 5nm Ni, and trapped in between the nanotrench electrodes.**

#### 4.4.1. TRANSPORT MEASUREMENTS

The current-voltage characteristics after magnetic trapping depend on the number and placement of the particles on the gap, the thickness of the metallic deposition, varying from pA to  $\mu$ A for current values.

- i. As demonstrated in figures 4.24 and 4.25, particles covered with 5nm of Nickel buried under 10nm of Au had optimum response to the local magnetic field and best positioning on the nanotrench, exhibiting a resistance of  $1k\Omega$  ( $\approx 300\Omega$  after deducting the track resistance). This indicates that the conduction mostly occurs through the relatively thick and continuous metallic film on the particle. No voltage ‘poling’ and response to heat/illumination were observed.

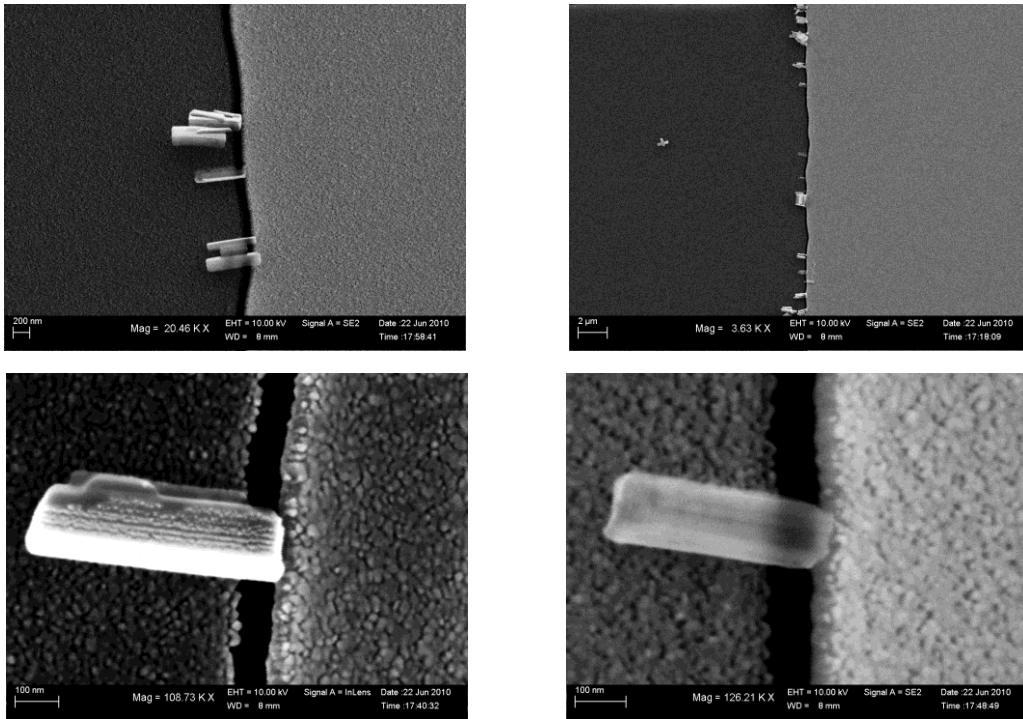


Figure 4.24 : SEM micrographs showing the positioning of SCO nanoparticles covered with 5nm of Ni protected by 10nm of Au layer over nanotrench electrodes by magnetic entrapment. The metallic deposition is quite distinguishable in down-left image.

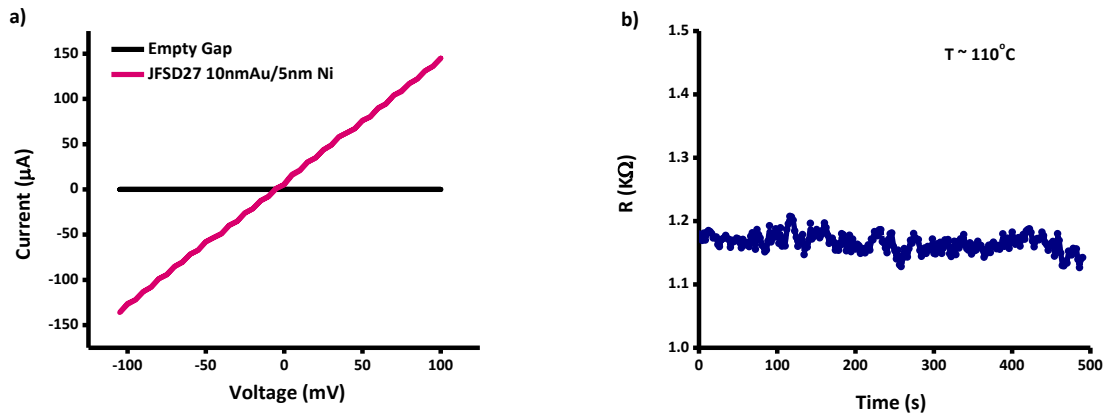


Figure 4.25 : a) I-V related to SCO nanoparticles (image in figure 4.24) with 10nm Au/5nm Ni deposition entrapped over nanotrench electrodes compared to one of an empty gap. b) Monitoring the resistance of the same particles in time, ( $T \sim 110^{\circ}\text{C}$ , 55 watts power). No response to illumination and/or heating was observed.

ii.  $[\text{Fe}(\text{Htrz})_2(\text{trz})]\text{BF}_4$  Nanocrystals covered with 2nm of Au over 4nm of Nickel and placed over the nanotrenches by magnetic trapping. They present a voltage ‘poling’ effect at 0.7 volts, with subsequent switching behavior occurring on a sample of resistance value reduced by  $10^3$ . The switching is stable and reproducible for a relatively long time (hours).

These observations confirm our findings on plain nanoparticles, identifying therefore a method to improve the trapping and the conductivity of the system by design. We cannot identify unambiguously a lower resistance value of this type of particles when compared to uncoated particles, as we lack statistical information and systematic SEM imaging over the whole trench. The data reported in figs 4.26 and 4.27 nevertheless indicate devices resistance values of ranges similar to those on virgin particles, and we can safely assume that the metallic coating did not create a significant short.

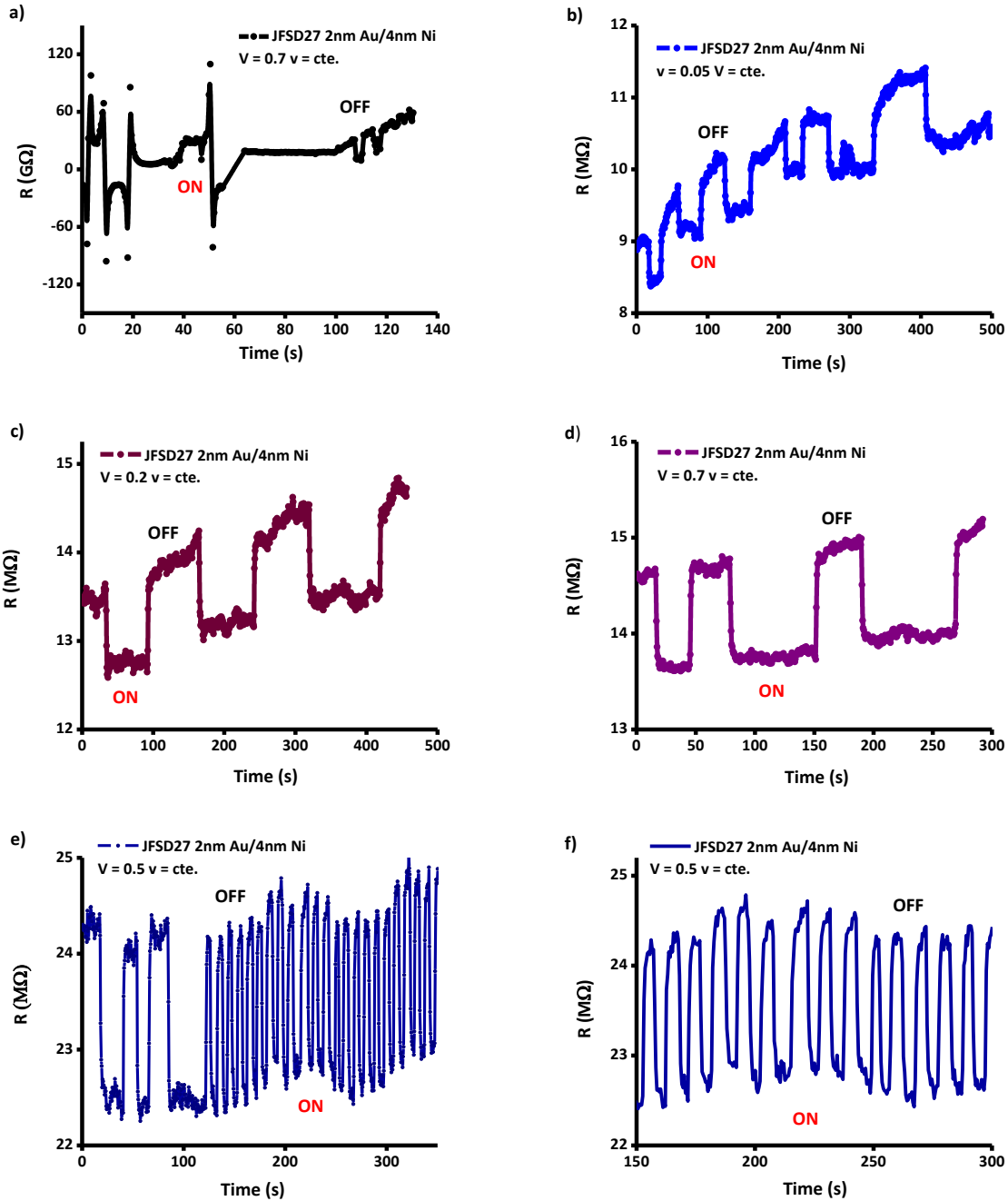
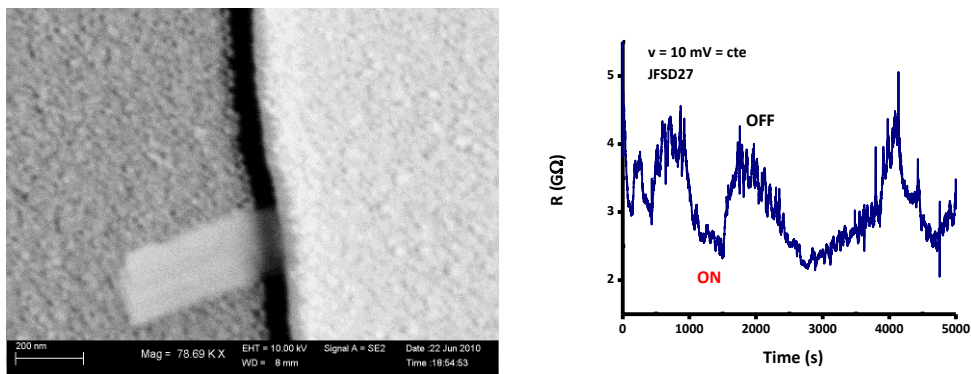


Figure 4.26 : Resistance versus time data for SCO nanoparticles covered with 4nm of Ni protected by 2nm of Au, bridging nanotrench electrodes after a magnetic trapping process, a) under 700mV constant bias voltage applied, high resistance values and no response to illumination/temperature are found, b) observation of voltage ‘poling’, i.e. a decrease of resistance by  $10^4$  and the appearance of photoconduction behavior ( $v = 0.05$  V), the same switching is observed for other voltage bias c)  $v = 0.2$  V d)  $v = 0.7$  V e), f) demonstration of multiple switching events and no fatigue effects: 50 times switching in 350 seconds time interval ( $v = 0.5$  V) .



**Figure 4.27 : SEM micrograph (left) and Resistance versus time data (right) for SCO nanoparticles covered with 4nm of Ni, trapped over nanotrench electrodes by magnetic trapping.**

## 4.5. CONCLUSION

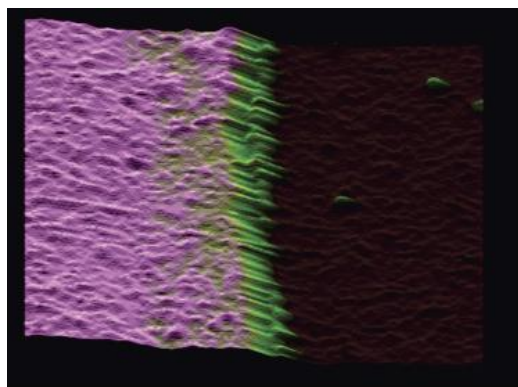
Bottom-up construction of sub micron ensemble of molecules exhibiting spin crossover transition using a reverse micelle strategy, combined with the top-down fabrication of planar electrodes with 100 nm separation, made possible to discover new and unknown properties of spin crossover nanoparticles. By careful testing on our devices, and variations in type and numbers of particles trapped in the junction, we can claim we observe the intrinsic two-points conduction properties of SCO trapped between metallic electrodes.

After a necessary voltage ‘poling’, i.e. applying a voltage stress of the order of 1V to our samples, the bridging SCO nanoparticles exhibit unexpected large conductivity, with photoconductance and photovoltaic behavior. This ‘poling’ voltage is described by irreversible changes in the molecule-metal interface and the distribution of electric field by free ions in the compound. We obtain significantly high conductivity values:  $0.01 - 1 \Omega.m$ , as well as low interface resistance values known for a polymer semiconductor/metal interface:  $10^5 - 10^8 \Omega.cm$ . By investigating SCO materials that do not make a transition under illumination (in solution), and by observing many optically-triggered switches not involving sample heating, we become confident that the change of conduction under illumination does not require a spin transition.

By adding a metallic layer on top of the SCO particles, it is possible to manipulate them. Magnetic films orient the particles along the magnetic field lines, while the field gradient allows trapping of the particles. The metallic cap screens the photoconduction effect, the thicker it gets,

the lowest the amplitude of the switching: in the case of particles covered with 5nm Ni/10nm Au the effect disappeared. For thinner metallic coverage, estimated to be below the conduction percolation thickness, the photoconduction effect is retrieved, with indications of further improvements in the system conductivity. The metallic Au coverage of the particles makes possible Au-specific surface functionalization. One can therefore envision preferential attachments of the particles to the surface, or electrical interface engineering.

# CHAPTER V: LIGHT TRIGGERED SELF-CONSTRUCTION OF SUPRAMOLECULAR ORGANIC NANOWIRES AS METALLIC INTERCONNECTS



In this chapter we present an original self-assembly approach to grow a supramolecular ensemble of nanowires between two metallic electrodes separated by 80 nm. A solution of triarylamine-type molecules exposed to illumination and electric field fills the gap between the electrodes. The resulting assembly of parallel nanowires exhibits ohmic conductivity with high conductivity and low interface resistance values. The latter is improved by six orders of magnitude when compared to organic materials, in relation with a metallic behavior observed when cooling down the system.

# 5. LIGHT TRIGGERED SELF-CONSTRUCTION OF SURPAMOLECULAR ORGANIC NANOWIRES AS METALLIC INTERCONNECTS

## 5.1. INTRODUCTION

Conjugated organic polymers have been extensively studied as active semiconducting components for more than three decades. Remarkable improvements have been attained to enhance the intrinsic charge transport along polymer chains [162]. One key methodology for performance improvements is improving the control of the molecular arrangement, aiming at diminishing the mobility bottleneck due to the interchains or inter-domains hopping. One example of such crystal engineering is a liquid-crystalline semiconducting polythiophene designed to assemble into large crystalline domains of crystallization which allows close intermolecular  $\pi$ - $\pi$  distances, facilitating high charge carrier mobility. FET with printable semiconducting polythiophene exhibited mobilities equivalent to amorphous silicon. A device with  $W = 10,000 \mu\text{m}$  and  $L = 20 \mu\text{m}$  exhibits a charge-carrier mobility of  $0.6 \text{ cm}^2\text{V}^{-1}\text{s}^{-1}$ , another device with  $W = 2,000 \mu\text{m}$  and  $L = 5 \mu\text{m}$  exhibits a charge-carrier mobility of  $0.72 \text{ cm}^2\text{V}^{-1}\text{s}^{-1}$  with field-effect mobility of  $\mu_{\text{FET}} = 0.15 \text{ cm}^2\text{V}^{-1}\text{s}^{-1}$  [163]. However, a significant problem is the device stability: I-V measurements in ambient (humidity level  $\sim 50\%$ ) were reproducible for five days, and after that the mobility decreased by a factor of two, and the ON/OFF ratio reduced by two orders of magnitude (figure 5.1). This is why a large industrial effort is aimed at finding adequate encapsulation solutions, or seeking molecules with better long-term stability.

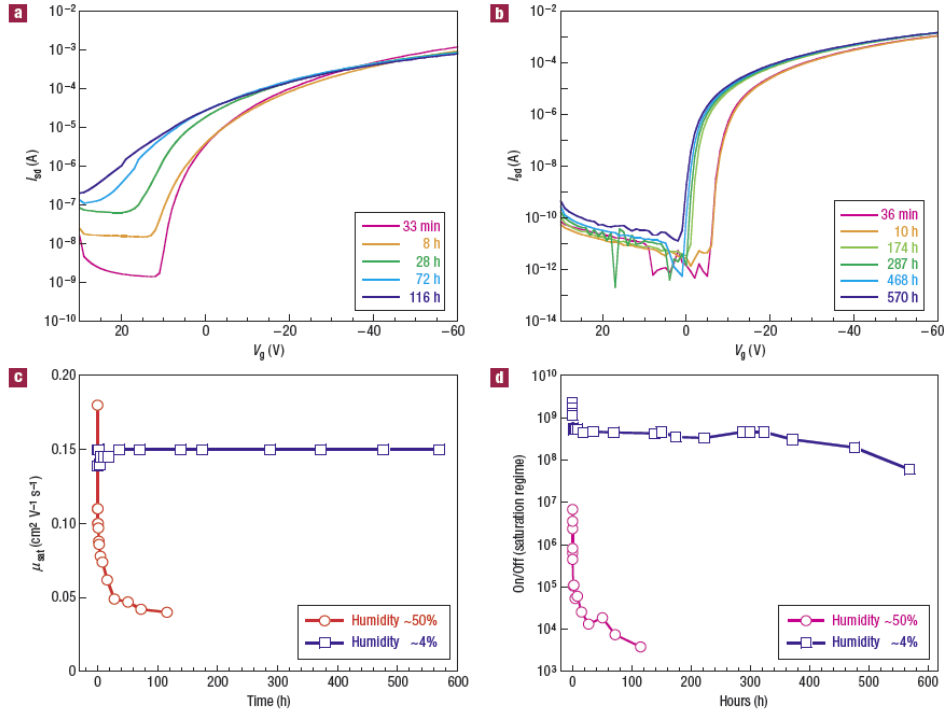


**Figure 5.1 : Transfer characteristics on prolonged exposure to a) ambient air and b) low humidity air. Change in c) mobility and d) ON/OFF ratio with time in both ambient and low-humidity air [163].**

Miniaturization is another alternative, where size reduction should mean less incoherent hopping. This route remains a challenge, in particular for realizing sub-micron devices. To our knowledge, the best results have been obtained in the vertical geometry. Figure 5.2 shows the output characteristics of a vertical-channel P3HT field effect transistor on a flexible substrate, with a channel length of 0.7- 0.9  $\mu\text{m}$  (figure 5.1-B), compared to a planar transistor with channel length  $L \approx 17\mu\text{m}$  and channel width  $W = 1\text{mm}$  (figure 5.1-A) [164]. Field-effect mobilities obtained from the saturated transfer characteristics of planar and vertical devices are reported to be on the order of  $3 \times 10^{-3} \text{ cm}^2 \text{V}^{-1} \text{s}^{-1}$ .

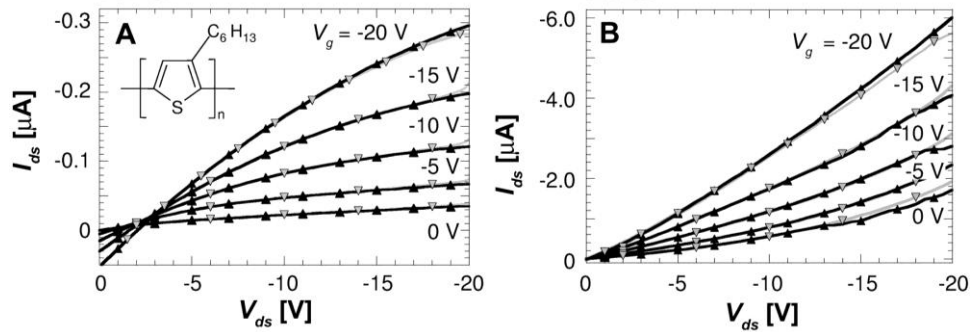


**Figure 5.2 : Output characteristics of embossed P3HT (inset in A) devices. A) Planar transistor with channel length  $L \approx 17\mu\text{m}$  and channel width  $W = 1\text{mm}$ , B) Vertical transistor with  $L \approx 900\text{nm}$ ,  $W \approx 0.5\text{mm}$  [164].**

## 5.2. METALLIC CONDUCTIVITY IN CONJUGATED POLYMERS

Semiconducting polymers can exhibit high conductivities values, reaching those of metals. They however become more insulating at low temperatures (i.e. near 0 K). The reason for an increase of resistance when decreasing the temperature mostly involve to disorder-induced localization of the charge carriers [165]. The best conducting polymers therefore exhibit first a decrease of resistance when cooling down, but always exhibit an increase of resistance at the lowest temperatures, i.e. below a few tens of K.

The first conducting polymers had modest room temperature electrical conductivity and exhibited insulating behavior at low temperatures [166, 167]. Transport in such systems is dominated only by the delocalized charge carriers and could be evaluated via determining the volume density and scattering times ( $\tau$ ) of the delocalized charge carriers [165].

The disorder in conducting polymers arises from a combination of molecular-scale disorder [16, 3] and structural inhomogeneities at mesoscopic length scales [168, 164]. Even the most highly conducting polymers have been described as disordered metals near the metal–insulator transition [16, 3]. They have a finite density of states at  $E_F$ , as verified by measurements of the Pauli spin susceptibility [169], the linear term in the temperature dependence of the thermoelectric power [170], and the linear term in the temperature dependent heat capacity [171]. Despite the finite density of states at  $E_F$ , the transport properties in the ‘metallic state’ as reported in the literature do not exhibit the traditional signatures of conventional metals. The DC conductivity ( $\sigma_{DC}$ ) is thermally activated (phonon assisted), decreasing as the temperature is

lowered [168,172, 173, 174], and  $j(q)$  is not consistent with Drude behavior in the infrared [175]. In the best cases, resistivity as a function of temperature ( $\rho(T)$ ) is nearly constant, with a weak minimum below room temperature (figure 5.3) [16, 3]. In 2006, the landmark of metallic resistivity i.e. a monotonic decrease of resistance with temperature has been reached in bulk films of doped polyaniline prepared by self-stabilized dispersion polymerization [176]. Room-temperature conductivities in excess of  $1,000 \text{ S.cm}^{-1}$  were measured and the resistivity decreases monotonically as the temperature is lowered down to 5K, with the infrared spectra characteristic of the conventional Drude model even at the lowest frequencies measured [176, 165]. As seen in figure 5.3, this occurred for two samples only (the minimum number for reproducibility check), and we are not aware of any other data on conducting polymers.

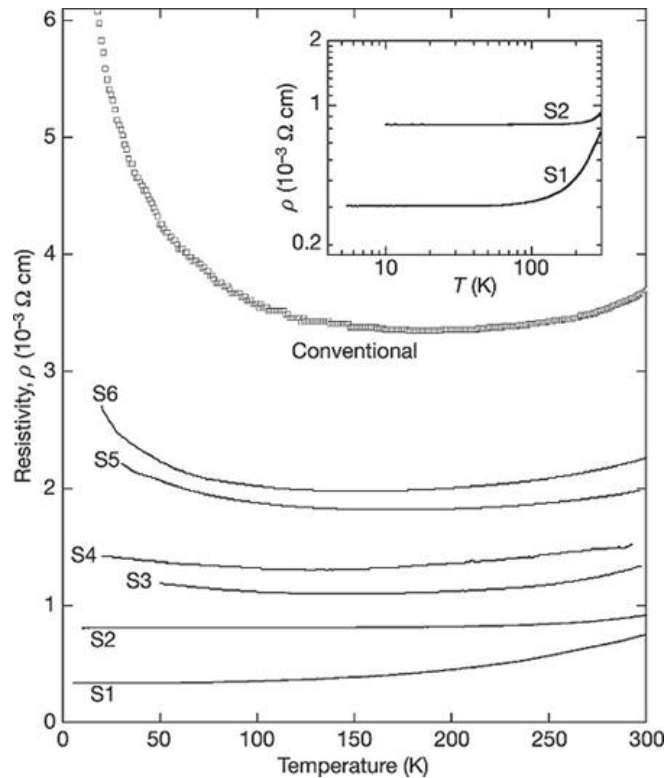


**Figure 5.3 :** Data from a conventional PANI-CSA film are shown for comparison. The SSDP PANI-CSA samples exhibit significantly enhanced conductivities compared with that obtained from the conventional sample. For more highly conducting samples (S5  $\rightarrow$  S1), the resistivity minimum weakens and shifts down to lower temperature and eventually disappears in the S1 and S2 samples (as shown more clearly in the inset) [176].

### 5.2.1. PARASITIC CONTACT RESISTANCE

For an organic channel depicted in figure 5.4, the channel resistance ( $R_{CH}$ ) is determined from equation 5.1, where the resistivity is  $\rho = \sigma^{-1}$  [ $\Omega.m$ ],  $L$  and  $W$  are the length and width of the channel respectively and the area ( $S$ ) of the contact is calculated from  $S = W \times h$ .

$$R_{CH} = \rho \frac{L}{W \times h} \quad (5.1)$$

The total resistance in such device ( $R$ ) is a sum over channel resistance ( $R_{CH}$ ) and contact resistances ( $R_{Contact}$ ) for source ( $R_S$ ) and drain ( $R_D$ ) in contact with the organic film (equations 5.2 and 5.3).

$$R = R_{Contact} + R_{CH} \quad (5.2)$$

$$R_{Contact} = R_S + R_D \quad (5.3)$$

The contact resistance relates to the charge injection/extraction of the organic layer at metal electrodes and is a key limiting factor towards performance and miniaturization. In short channels, a large fraction of applied source-drain voltage drops over the contact resistance  $R_{Contact}$  and regarding the equation 5.1, the contact resistance becomes the predominant term in  $R$ , thus limits device usefulness.

The typical values for contact resistivity for conjugated polymers in lateral devices range from  $10^2 \Omega.m$  to  $10^5 \Omega.m$ . For a channel of  $L = 1\mu m$ ,  $W = 1\mu m$  (and  $h = 100 \text{ nm}$ ) the contact resistance stays in the range of  $10^9$ - $10^{13} \Omega$  which is quite large [36, 177].

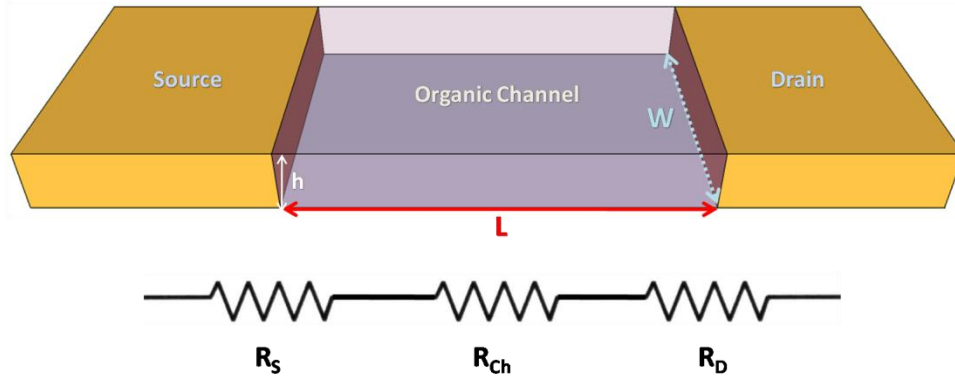


Figure 5.4 : Schematic of an organic device resulting in three series resistances as the total resistance of the device.

Figure 5.5-a shows the results of a previous study on channel length-dependent transport characteristics of a variety of solution-processed organic semiconductors. The authors argue that downsizing the geometries for higher switching speed in TFT is as important as picking high mobility materials. The results show that the source/drain current times channel length ( $I_{ds} * L$ ) decreases by a factor of about 50 when decreasing the channel length from  $40\mu\text{m}$  to  $0.75\mu\text{m}$ . The ratio of decrease is also depending on gate voltage. The current in the short channel transistor dominated by the parasitic series resistance has a lower performance than the long-channel transistor [176, 178].

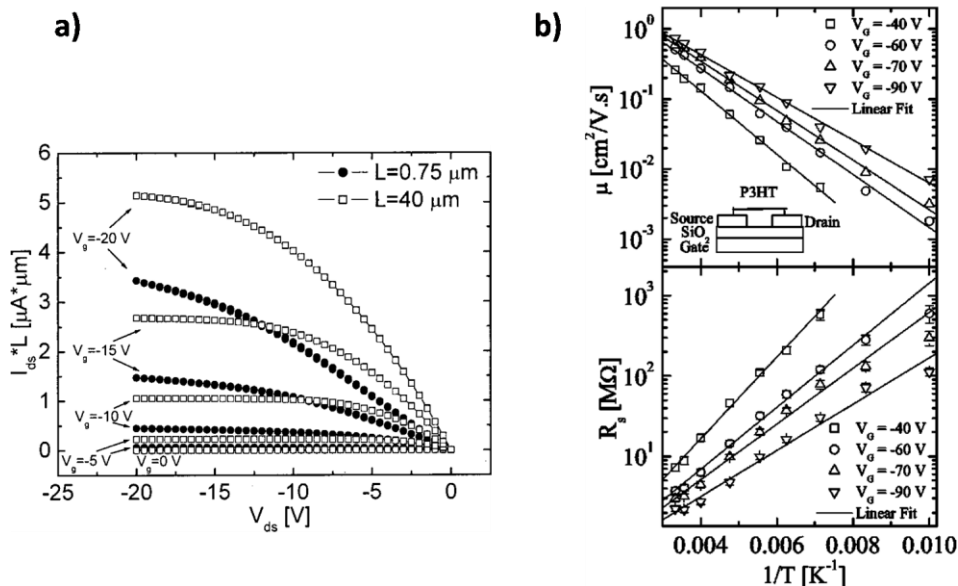


Figure 5.5 : a) Normalized output characteristics for two P3HT transistors with  $L = 0.75\mu\text{m}$  (closed circles) and  $L = 40\mu\text{m}$  (open squares) [178], b) top: mobility as a function of  $1/T$  for several gate voltages in a series of  $5\mu\text{m}$  wide devices, bottom: parasitic contact resistance as a function of  $1/T$  for the same device [169].

The metal/organic interface resistance has been observed to increase exponentially as the temperature decreases in a solution-cast P3HT transistor (figure 5-b) [169]. The authors reported that the parasitic contact resistances reduce the mobility by nearly an order of magnitude at room temperature, confirming that the performance of such polymer based devices can be limited more by metal/polymer contact physics than by the intrinsic transport physics of the polymer itself.

Low contact resistance to organic interconnects have been realized in the case of single wall carbon nanotubes (SWCNT) with Pd electrodes [170]. SWNTs with lengths of  $L \leq 1\mu\text{m}$  show  $R \approx 10 - 20 \text{ k}\Omega$  at 290 K and show half of that resistance at 4K. In this case, the contact resistance originates from quantum conductance effects, related to the size-limitation of the transmitted wave functions of the charge carriers in a one-dimensional conductor. This is why carbon nanotubes are particularly attractive for nanoelectronics realizations (among other reasons...). However, SWCNTs exhibiting low contact resistance and associated large currents remain very challenging to isolate, process, and position [171]. A huge worldwide research effort has been dedicated in the last 10 years to solve these bottlenecks, and large scale and simple solutions are still lacking.

Graphene devices are expected to bring a novel era in nanoelectronics, and the studies of contact resistance are scarce and quite recent [172, 173].

In this section, we propose an attractive alternative for carbon-based materials in the development of sub-micron organic electronics applications, using supramolecular architectures [174].

## 5.3. SUPRAMOLECULAR STRUCTURES

Supramolecular electronics is bridging the gap between single molecules and standard thin-film organic electronics, and involves the self-assembly of  $\pi$ -conjugated systems into individual nanosized wires in a solution or during a deposition [175]. By studying the intermolecular interactions and controlling the solvent evaporation process, it is possible to obtain high mobility semiconductors with a variety of shapes and properties tunable by controlling the  $\pi$ -conjugated assemblies transfer to specific surfaces [75]. Until now, metallic conductivity has never been observed in self-assemblies and, in addition, the accurate positioning of the latter between electrodes remains an enormous challenge. Furthermore, improving the intrinsic electrical properties of a material does not solve the problem of the interface resistance!

In this work we focus on the formation of highly structured supramolecular triarylamine nanowires (STANWs) between metallic interconnects exhibiting metallic conductivity and high stability [179]. The chemical structure and self-assembly route of STANWs are detailed in the following.

### 5.3.1. TRIARYLAMINE HIERARCHICAL SELF-ASSEMBLY

Triarylamine-type molecules have been incorporated in several optoelectronics applications as organic light emitting diodes (OLEDs), organic solar cells (OSCs) and OFETs for their high hole-transport mobility and photo-conducting properties. Very recently E. Moulin et al. have observed a new kind of self-assembly of triarylamine molecules, triggered by charge transfer and broken up by heating [179]. Figure 5.6-a, presents the key synthesis step of 8 triarylamine derivatives, using a modified Ullman one-pot coupling as a key process [see supporting info of 179]. The authors have observed a completely different NMR spectrum for compound **1** before and after being exposed to natural light for a couple of minutes (figure 5.6-b). The change in the properties was accompanied by a change of solutions' color from light yellow into light green after exposure to light; this change was reversible simply by heating the solution in chloroform overnight at 60°C. The solution has stable properties in every step of the process for about a week and at least three light exposure-heating cycles.

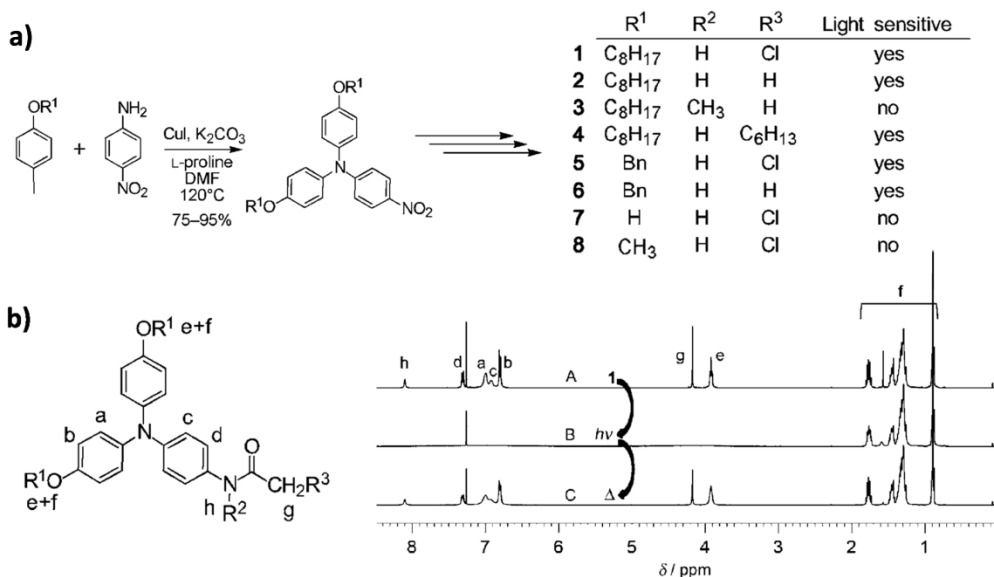


**Figure 5.6:** a) Structures and key synthetic steps to access 1-8 triarylamine derivatives, b) typical <sup>1</sup>H NMR spectra (CDCl<sub>3</sub>) of the molecular structure depicted on the left (**1**) after purification (A), after 10 min exposure to visible light (B), and after subsequent heating overnight at 60°C (C), (**1**) = 10 mM [179].

Appearance of a new absorption band at 786 nm in the UV/Vis spectra (figure 5.7) of the solution of **1** in chloroform indicates the production a small quantity of the triarylammonium radical (**1**<sup>•+</sup>). Data depicted in figure 5.7 are obtained by electron paramagnetic resonance (EPR) spectroscopy, a technique allowing the detection of free radicals of chemical species. Figure 5.7-a shows the evolution of the triarylammonium radical **1**<sup>•+</sup> over neutral **1**. Point A presents the state of the solution at room temperature without visible light excitation, upon excitation by one hour of white light exposure (A-B), the number of radicals increase to 11 per 100 molecules, and again in the absence of light at room temperature (B-C) the number of radicals smoothly decay to the horizontal dashed line: 6 radicals per 1000 molecules, stable over a week, indicating the radical-stabilization in the solution. Subsequent heating at 60°C in dark restores the solution to its original position (A).

The instability of the (B) state in comparison to the stable NMR spectra in figure 5.6-b, brings the conclusion that the disappearance of the aromatic signals is more likely caused by a self-association/delocalization process by charge transfer of these radicals when self-assembled with their neutral precursors.

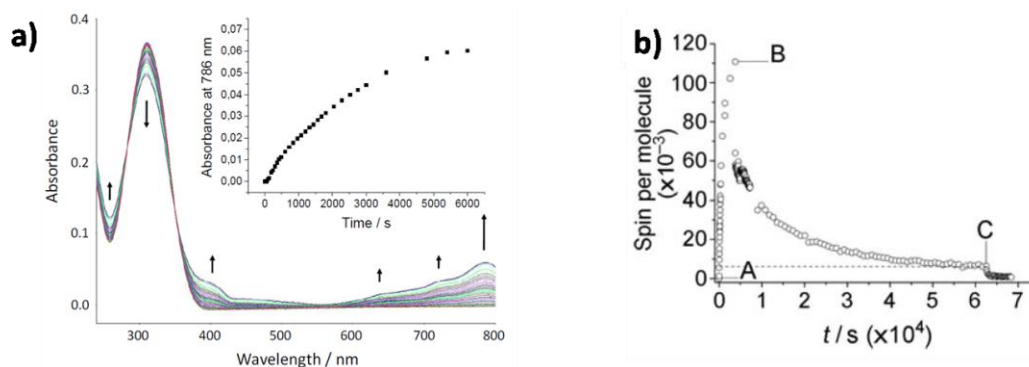


**Figure 5.7 :** a) UV-Vis-NIR spectra obtained as a function of time of irradiation for an initial 0.1 mM solution of **1** in chloroform, b) Quantitative EPR data, as a function of time, showing the evolution of the ratio of the triarylammonium radical  $1^{++}$  over neutral **1**: without visible light excitation at RT (point A); upon visible light excitation (A–B); in the absence of light at RT (B–C); and after subsequent heating (60°C) in the dark (from C;  $[1_{\text{init.}}]=10$  mM). Dotted line: y-axis value of  $6 \times 10^3$  [179].

The authors observed that the chlorinated solvents are necessary to initiate the oxidation of the triaryl amines, with the  $\text{Cl}^-$  ions expected to be the source of the radicals. The process results in unique formation of highly structured supramolecular triarylamine nanowires, which aggregate into large fibers (typically 10 – 50nm in width and 50 – 1000 nm in length). High resolution AFM imaging revealed the “corn-like” surface of the fibers, composed of bundles of individual 1D fibers strongly packed in a concentric-layer organization (figure 5.8).

For an individual 1D fiber, the separation distance between the dots ( $1.0 \pm 0.3$ ) nm in length (figure 5.9-a) corresponds to the periodic pattern of triaryl amines (figure 5.9-c) and the lateral separation distance between 1D fibers in the 3D aggregates ( $1.3 \pm 0.4$ ) nm corresponds to the dimension of individual molecular wire made from polymerization of a single row of triarylamine units. Figure 5.9 presents a minimum energy calculation of the expected stable arrangement of molecules in the supramolecular stacking.

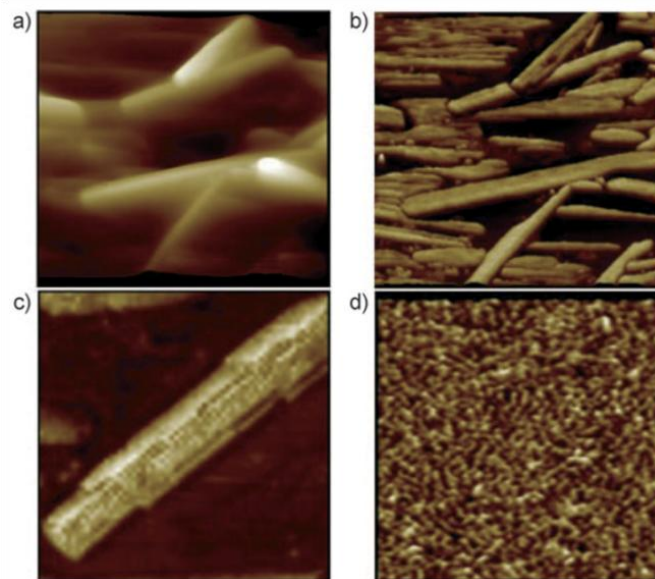


Figure 5.8 : a) AFM height and b) phase images (surface scales  $500 \times 500 \text{ nm}^2$ ) of the self-assembled structures obtained by concentration to dryness of an irradiated solution of 1 in chloroform, c) AFM high-resolution image (surface scale  $50 \times 50 \text{ nm}^2$ ) of a single self-assembled structure obtained by concentration to dryness of an irradiated solution of 1 in chloroform, d) AFM image (surface scale  $500 \times 500 \text{ nm}^2$ ) of the self-assembled structures obtained by probing a liquid film made from an irradiated solution of 1 ( $[1_{\text{init.}}]=1 \text{ mM}$  in chloroform). Evaporation of 1 without previous light irradiation showed the absence of any self-assembled structure [179].

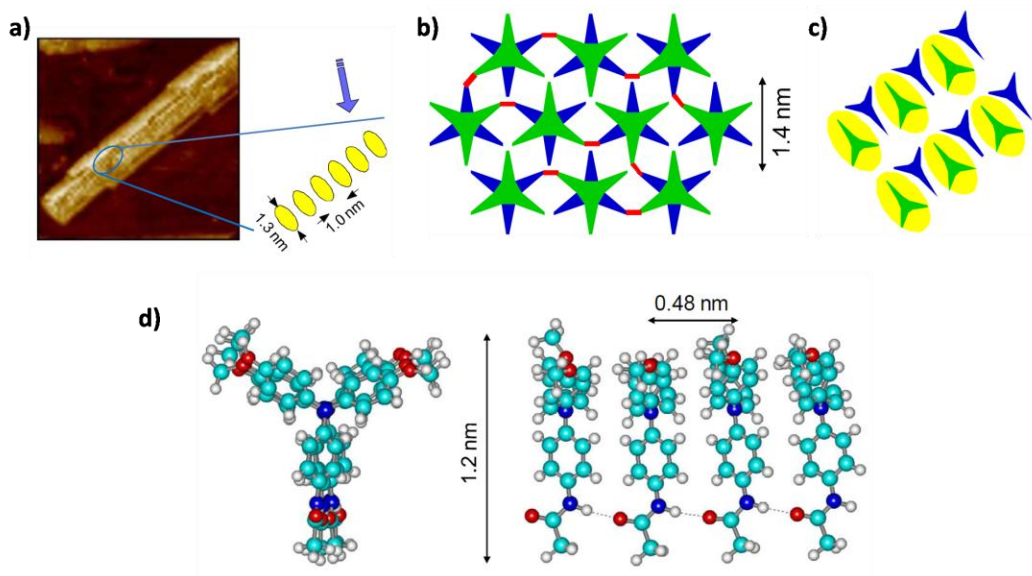
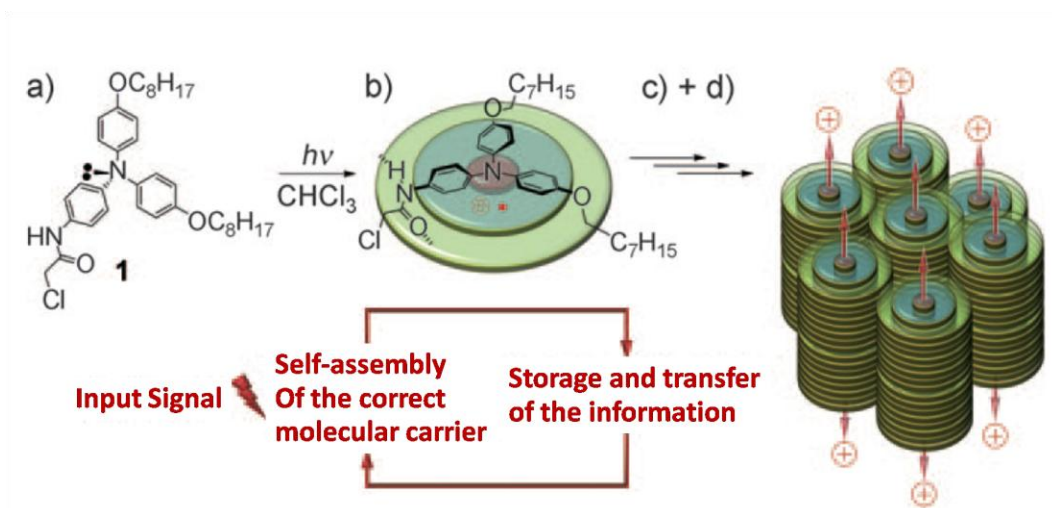


Figure 5.9 : a) Corn-like multi-stacked structure observed by AFM, b, c) Proposed molecule arrangement within the multi-stack structure made of alternating triarylamine molecules (green and blue molecules belong to neighboring layers within the stack, H-bonds can connect differently colored molecules only, the positions of H-bonds are shown by red segments), d) pattern for triarylamine molecules [supporting information of 179].

Interestingly, in a synergistic process, the STANWs permanently stabilize the charges of the initial radicals by an extended electronic delocalization within the fibers. Authors have determined a minimal ratio of 1 charge per 160 triarylaminines (but which can be higher), corresponding to an estimated “coherence” length of  $80 \pm 3$  nm. Another unique novelty of this process is the possibility to trigger the self-assembly by using visible light irradiation that results in the formation of a few cationic radicals and thus primes the self-assembly.



**Figure 5.10 :** Hierarchical self-assembly processes that occur upon irradiation of the neutral triarylamine **1**, a) The electron transfer that occurs between light-excited triarylaminines and the solvent produces a small amount of triarylammonium radical, b) In this electronic configuration, the charge transfer and various supramolecular interactions initiate the self-assembly of 1D supramolecular polymers, c) and d) which combine to produce larger 3D fibers [179].

From an electronic point-of-view, these properties mimic those of conjugated polymers, with the analogy of a delocalization over 160 ‘monomer’ units. The unique feature of these materials is the light trigger of the assembly and the reversibility of the process. This system is therefore ideally matched for attempts to create interconnects between electrodes having a separation corresponding to the 80 nm ‘coherence length’ in solution.

## 5.4. TRANSPORT MEASUREMENTS

We aim to trap the self-triggered nanowires in between metallic electrodes to probe their conductivity properties. In the following, we detail the strategy and setup designed for such measurements, followed by results and their characterizations.

### 5.4.1. STRATEGY

To investigate the transport properties of STANWs obtained as a result of self-assembly process of molecule **1** in chlorine based solvents, we immerse the nanotrench electrodes in a solution of molecule **1** in 1,1,2,2-tetrachloroethane ( $1\text{mg.mL}^{-1}$  in  $\text{C}_2\text{H}_2\text{Cl}_4$ ) by drop casting. A DC bias of few hundreds of mV is immediately applied between the electrodes (figure 5.11). Owing to the high boiling point ( $146.5\text{ }^\circ\text{C}$ ) and significantly slow evaporation of tetrachloroethane, the samples are kept in solution during a typical 1 hour time. With a single drop casting we can monitor and record the evolution of current as a function of time as well as current-voltage characteristics for each sample containing seven nanotrenches. The sample is irradiated during a few seconds under the microscope condenser illumination (numerical aperture 0.55) with a 100 W halogen light source (figure 5.11-a). Infrared filtering is used to limit the sample heating to a few degrees (see Chapter IV), resulting in irradiation of broadband visible light power density of  $10\text{ W.cm}^{-2}$ . The typical 10s irradiation time corresponds to the total number of photons used in about 30 minutes for a self-assembly made in solution using a power density of  $\approx 0.07\text{ W.cm}^{-2}$  which is more than enough to trigger the self-assembly.

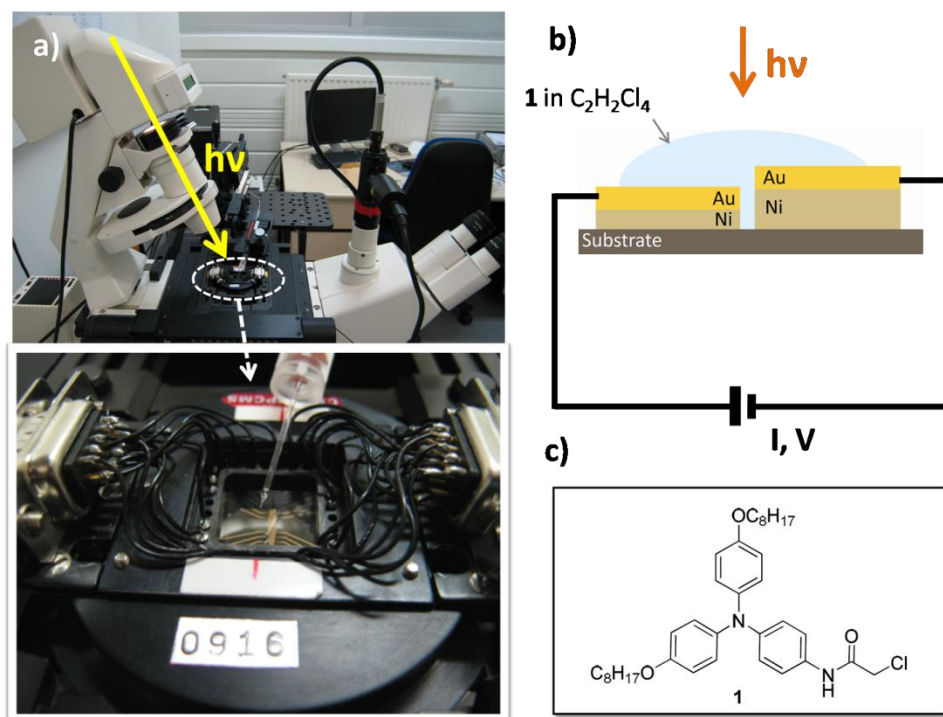


**Figure 5.11 :** a) Set-up over the inverted microscope for simultaneous electrical and optical properties probing, b) immersing the electrodes in the solution of **1** in  $C_2H_2Cl_4$  by drop casting on the sample containing nanotrench electrodes, c) chemical form of the triarylamine building block.

#### 5.4.2. CONTROL MEASUREMENTS

In the description of the electrodes fabrication process (Chapter II), we demonstrated that as-made nanotrenches can sustain a minimum of 5V bias, with typical leakage currents not exceeding a few pA (figure 2.5). When measured under vacuum conditions, bias up to 40V with pA leakage current values is observed [180]. Figures 2.6 and 2.7 of chapter II also presented the I-V characteristics of nanotrench electrodes immersed in pure deionized water, tetrachloroethane ( $C_2H_2Cl_4$ ) and chloroform ( $CHCl_3$ ) with current values not exceeding a few nA for voltage sweep ranges from 100mV to 30V.

Prior to measurements in molecular solutions, we systematically checked the circuit for the absence of leakage currents in the same conditions needed for self-assembly e.g. presence of incorporated solvents, illumination ( $10 \text{ W.cm}^{-2}$  power intensity), humidity, temperature, etc. Bare electrodes leakage current stays below nA for an applied bias of 10V, and the same value is obtained under  $10 \text{ W.cm}^{-2}$  intensity illumination (figure 5.12-a). We observe an increase of

leakage current for electrodes immersed in  $C_2H_2Cl_4$  under illumination up to 7 nA for applied bias exceeding 4 V (figures 5.12-c and 5.12-d). A possible origin for this leakage current might be the ions ( $Cl^-$ ,  $H^+$ ) created in chlorine solvent. Immersing the contacts in the solution of **1** [ $1 \text{ mg.mL}^{-1}$ ] in  $C_2H_2Cl_4$  before irradiation gives rise to a leakage current of hundreds of pA for a bias voltage below 1 V and this value can reach a few tens of nA under 4 V bias (figure 5.12-d). Samples were observed by scanning electron microscope (SEM) before and after the test measurements, no sign of electrode decomposition, deformation or corrosion was observed, all confirming the convenience of nanotrench geometry to investigate transport properties of such supramolecular systems.

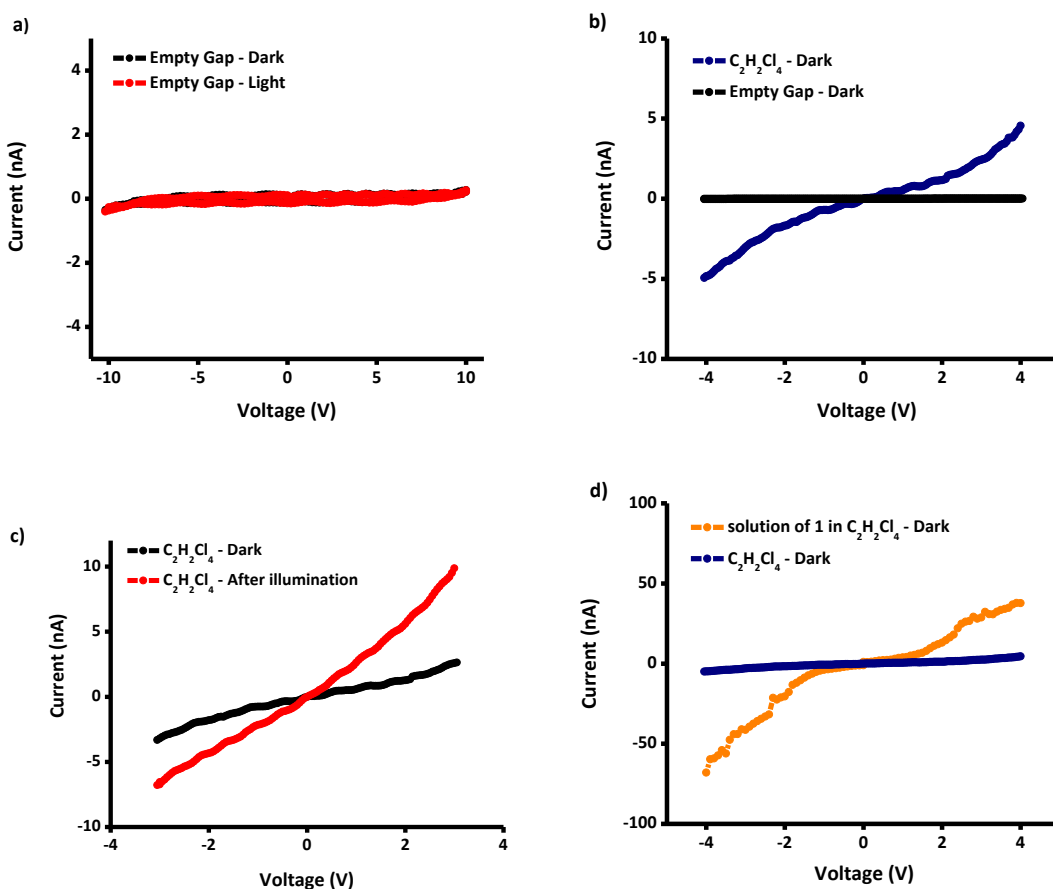


**Figure 5.12 :** Typical tests measurements of 80nm long trenches separating the electrodes, data was taken at room temperature under ambient conditions, similar to those during the self-assembly (illumination by 100W halogen lamp through 0.55 N.A. condenser) I-V characteristics of : a) empty trenches in dark and under illumination, b) electrodes immersed in  $C_2H_2Cl_4$  in dark compared to empty trenches, c) electrodes immersed in  $C_2H_2Cl_4$  in dark and under illumination, d) contacts immersed in the solution of **1** in  $C_2H_2Cl_4$  [1  $\text{mg.mL}^{-1}$ ] in dark compared to electrodes immersed in  $C_2H_2Cl_4$  in dark, the residual current is attributed to ionic impurities in the solution.

These test measurements also confirm that illumination at the same power as the one used for self-assembly does not create significant photoconduction artifacts.

### 5.4.3. FORMATION OF TRIARYLAMINE NANOWIRES BETWEEN METALLIC ELECTRODES

Electrodes immersed in the solution of **1** ( $1\text{mg.mL}^{-1}$  in  $\text{C}_2\text{H}_2\text{Cl}_4$ ) were submitted to a bias voltage of 0.1 to 0.9 V in the dark, the sample was then irradiated for 10 seconds with  $10\text{ W.cm}^{-2}$  power density white light, which produces some radicals in the solution ( $\mathbf{1}^{\bullet+}$ ) (figure 5.10-b).

The triarylammonium  $\mathbf{1}^{\bullet+}$  then induces a “supramolecular radical polymerization with neutral **1** that results in the self-assembly of triarylamine fibers aligned in the direction of the electric field in between the electrodes and strongly connecting them together. A simplified schematic of the STANWs formation is depicted in figure 5.13.

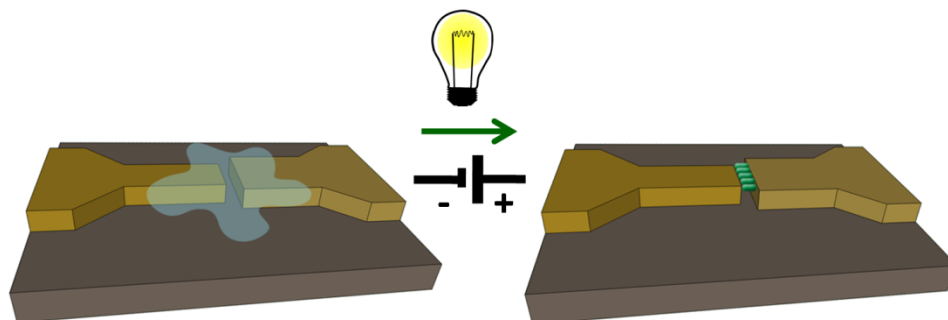


**Figure 5.13 : Schematic of nanotrench electrodes immersed in the solution of **1** in  $\text{C}_2\text{H}_2\text{Cl}_4$ , [ $1\text{ mg.mL}^{-1}$ ] exposed to electric field and illumination resulting in the formation of triarylamine based nanowires in between the electrodes along the electric field direction.**

Transport measurements reveal six orders of magnitude decrease of the samples resistance after the self-assembly process (figure 5.14)!!

The measured current at its maxima attains values in the mA range with an ohmic behavior (figure 5.15). We used a series electrometer to measure the leaking current, and avoided to change apparatus during the self-assembly process (to avoid spikes possibly damaging the sample). The huge magnitude change of sample resistance makes therefore our configuration non-adapted to low resistance samples measurements.

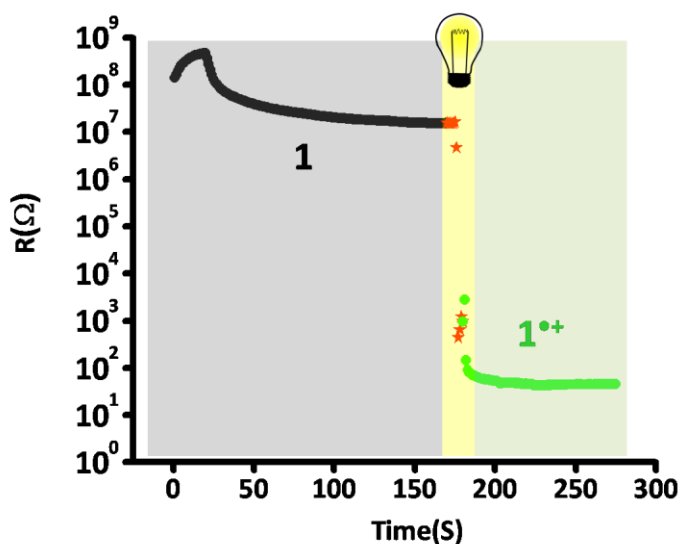


Figure 5.14 : Resistance versus time development of a nanotrench through the self-fabrication of triarylamine nanowires upon to 0.3 V bias voltage stress and  $10 \text{ W.cm}^{-2}$  white light 10 s exposure. A decrease in sample's resistance of 6 orders of magnitude occurs right after the illumination (two point measurements).

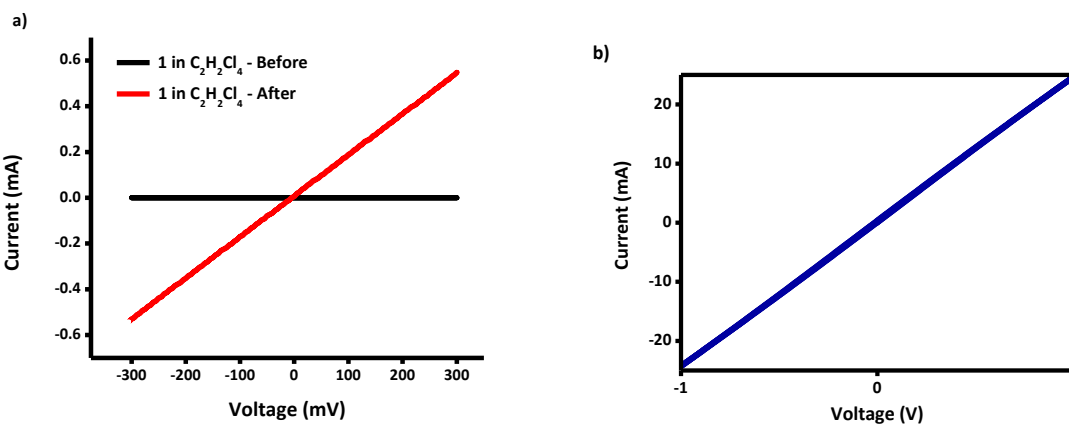


Figure 5.15 : I-V characteristics for a) nanotrench electrodes before and after the formation of STANWs related to figure 5.14,  $v = 0.3 \text{ V}$ , the two-point measurement set-up includes track resistance of typically  $600\text{-}800 \text{ } \Omega$  resulting in a sample potential drop smaller than the indicated voltage scale. b) nanotrench electrodes with STANWs measured at 200K in vacuum using four-point measurement and AC bridge technique, revealing current values of several tens of mA at higher bias.

Reference: V. Faramarzi, F. Niess, E. Moulin, M. Maaloum, J-F Dayen, J-B Beaufrand, S. Zanettini, B. Doudin and N. Giuseppone, *Triggered self-construction of supramolecular organic nanowires as metallic interconnects*, Nature Chemistry 1332 (2012).

In the following section, we present a thorough analysis, imaging and characterization of STANWs. We apply several check measurements along with AFM and SEM observation to relate the observed transport properties to the presence of STANWs between the electrodes and exclude the possibility of measuring artifacts or an electromigration process.

## 5.5. CHARACTERIZATION OF STANWS

### 5.5.1. CONDUCTIVITY VALUES

Considering the assumption that obtained resistance values are related to a nanotrench which is 100% filled with STANWs, we estimated a conductivity ( $[\sigma] = \text{S.m}^{-1}$ ) considering a resistance of  $40\Omega$  for the sample of figure 5.15 ( $R = \frac{V}{I} = \frac{1\text{V}}{25\text{mA}} = 40\Omega$ ), using equations 5.4 and 5.5, where  $L$  is the gap length (80 nm),  $W$  the gap width (100  $\mu\text{m}$ ) and  $h$  the electrodes height ( $\sim 50$  nm). Using the simplified figure 5.16 as a model, open gap ( $R \approx 10^{10}\Omega$ ) conductivity value is in the  $\text{nS.m}^{-1}$  range, while after the self-assembly ( $R \approx 40\Omega$ ) the corresponding conductivity values range from  $\sigma_{\text{low}}=400 \text{ S.m}^{-1}$  to  $\sigma_{\text{high}}=10^4 \text{ S.m}^{-1}$  (equation 5.5). Note this is a conservative estimate, where we suppose several layers of STANW's. If we recall that a typical diameter for the assembled wires is in the range of 10 nm, the estimate of (5.5), can safely be increased by a factor 5.

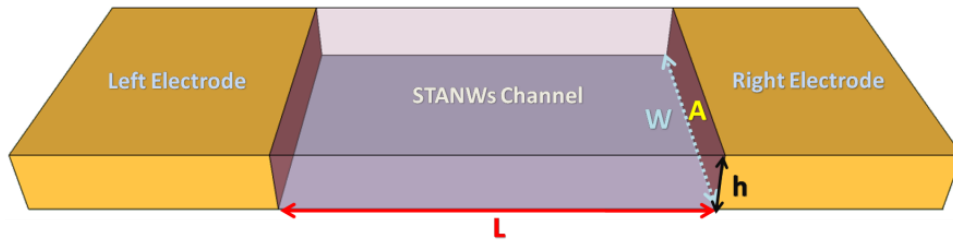


**Figure 5.16 : Geometrical characteristics of nanotrench electrodes inter-connected with triarylamine nanowires for conductance value calculation.**

$$\rho = \frac{1}{R} \times \frac{L}{W \times h} \quad (5.4)$$

$$\sigma = \frac{1}{\rho} = \frac{1}{40\Omega} \times \frac{80 \text{ nm}}{100 \mu\text{m} \times 50 \text{ nm}} = 400 \text{ S} \cdot \text{m}^{-1} \quad (5.5)$$

### 5.5.2. A CLOSER LOOK ON THE SELF-ASSEMBLY PROCESS

A key test experiment is to investigate the effects of illumination and electric field separately on the self-assembly. For this aim, we prepared two different substrates with electrodes immersed in a solution of **1** [ $1 \text{ mg} \cdot \text{mL}^{-1}$ ] in  $\text{C}_2\text{H}_2\text{Cl}_4$ , the first one was only exposed to 10s of  $10\text{W} \cdot \text{cm}^{-2}$  white light and its I (V) data was taken after few minutes: we observed that illuminating the sample gave rise to current values up to 10 nA for typical voltage of 100 mV, which is 3 orders of magnitude smaller than the current measured in the case of self-assembled nanowires (figure 5.17-a). The second sample was submitted to different bias voltage values in the dark, and no change in current/resistance values was observed in time (figure 5.17-b). By simultaneous exposure to electric field ( $v = 100 \text{ mV}$ ) and illumination we recreated the self assembly with the  $\mu\text{A}$  range current values. We therefore conclude that applying an initial voltage threshold through the gap previous to the light irradiation is a necessary condition for an efficient and stable formation of the STANWs.

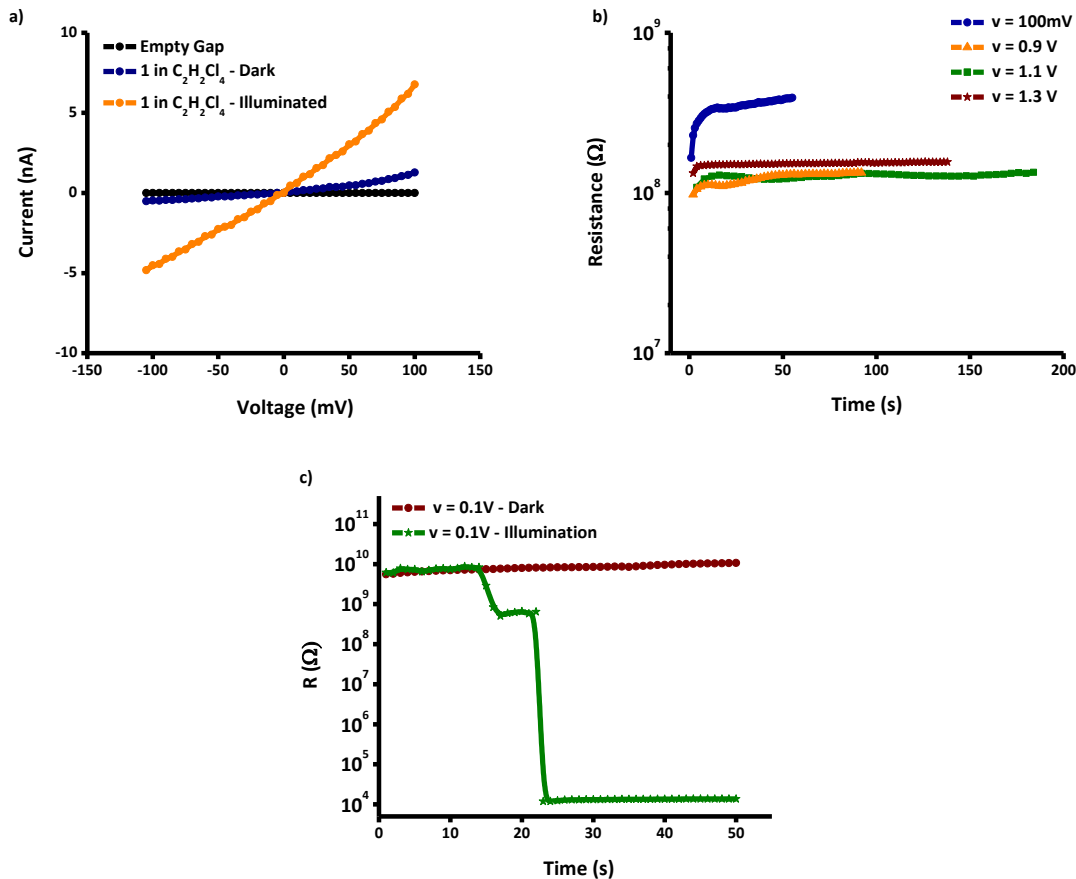


**Figure 5.17 :** a) I-V characteristics of an empty trench exhibiting pA leakage current, reaching nA range when immersed in the solution of 1 in  $C_2H_2Cl_4$  in dark and after 10s of  $10 W.cm^{-2}$  white light illumination b) Monitoring of the resistance versus time of a solution of 1 in  $C_2H_2Cl_4$  in dark ,c) monitoring the resistance versus time of a solution of 1 in  $C_2H_2Cl_4$  under illumination compared to its behavior in the dark. Interconnect process requires both the presence of the electric field and the illumination.

The necessity of a minimum voltage bias suggests the hypothesis that a localized assembly starts at the electrode that attracts a positively charged radical, which shares its electronic wave function with the metallic substrate, and then primes the next molecules stacking over it. The elongation process is polarized along the electric field and is self-limiting when the other electrode is reached, with its electron reservoir providing the neutralization path for stopping the growth. This scenario is also supported by the fact that a shorter exposure time to white light is able to prime the interconnect construction, with a resistance closure occurring afterwards in the dark (figure 5.18)!

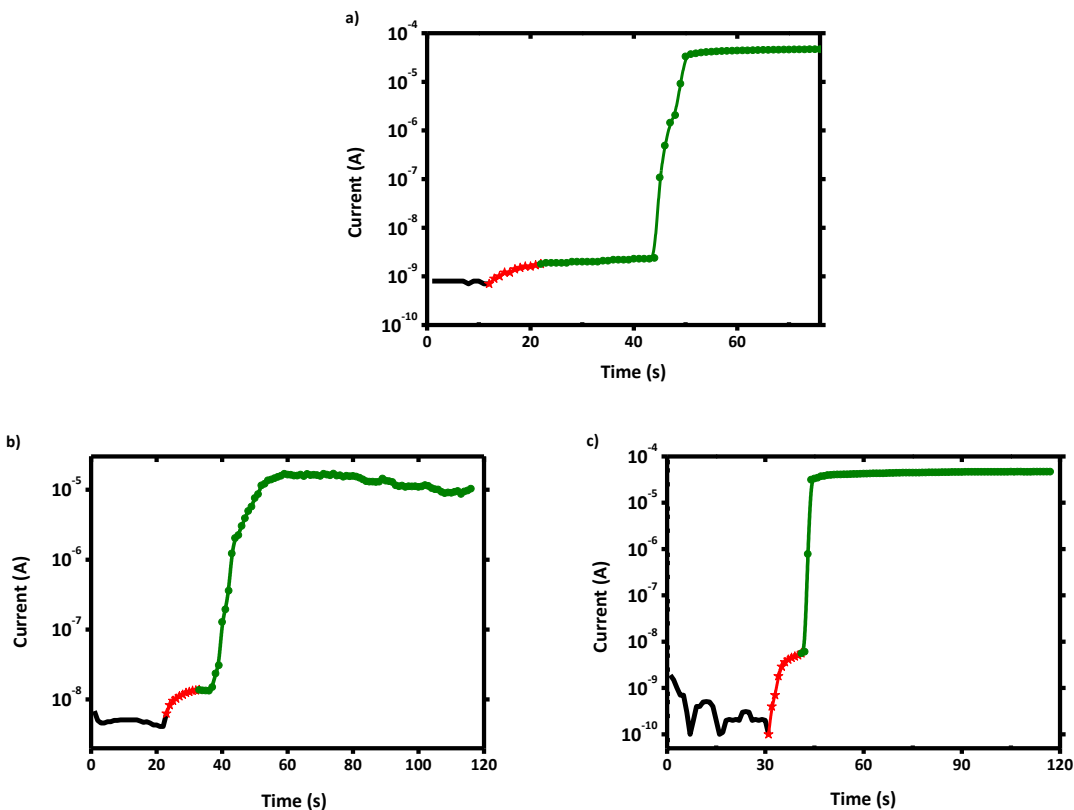


**Figure 5.18 : Three different self assembly processes, under 0.1 V bias. The red part of the curve sample was measured during exposure to light, the data in green and black are recorded in dark, the green is an indication of activated solution a) we observe that the closing of the gap by self assembly occurs around 20 seconds after stopping the illumination, b),c) these 2 sets of data have been taken from one single gap, being opened after washing away the STANWS using extensive ethanol-acetone rinsing. B) is the second closure, c) is the third closure.**

Data presented in figure 5.18 illustrates the concept of self-fabrication, which results from a “directional supramolecular living radical polymerization”, as described in solution [179]. Here, in addition, we witness the perfect voltage-casting that enforces the orientation in the device for an electrode separation around 100nm, which corresponds to the estimated length for the stacking ‘coherence length’ in solution [179]. This is supported by the facts that currents measured using more distant electrodes (500 nm and 5 $\mu$ m) increase by only 1-2 orders of magnitude compared to the immersed empty gap and nanowires fully disassemble and wash away by extensive solvent rinsing (figure 5.19). This enables to correlate the mechanical stability

with the low resistance values, suggesting that efficient sharing of conduction charges between electrodes and nanowires improves the mechanical stability of the device.

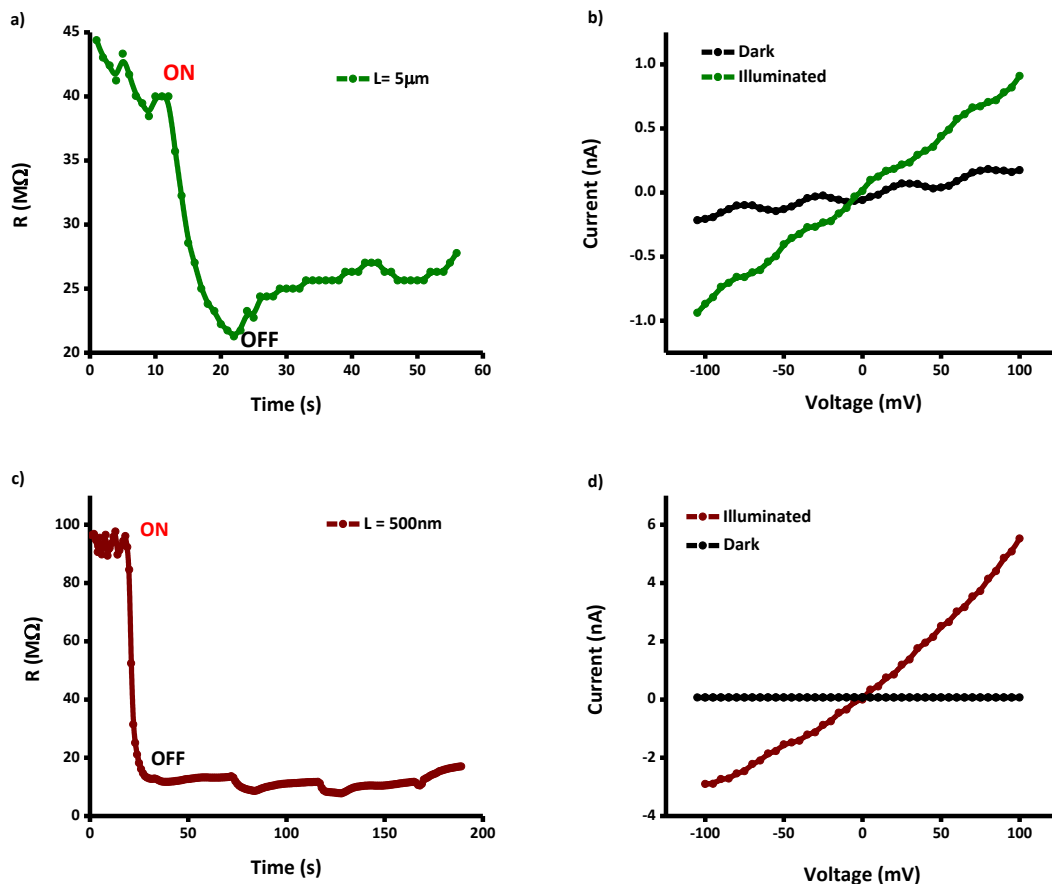


**Figure 5.19 :** a) Resistance versus time for metallic contacts separated by 5  $\mu\text{m}$  distance, b) related I(V) characteristics, c) Resistance versus time for metallic contacts separated by 500 nm distance, d) related I (V) characteristics

We also observe a reversibility of the process when heating connected STANWs in  $\text{C}_2\text{H}_2\text{Cl}_4$  at  $100^\circ\text{C}$  overnight, after which the non-covalent structure collapses and the wires dissolve (figure 5.20), as it happens in the solution [179]. We find no significant differences when repeating the self-assembly process between the electrodes (up to six times), indicating that the metallic interconnects are not significantly harmed during the self-assembly and heating process (figure 5.18-b,c). Furthermore, after solvent drying, the structures become stable and provide reproducible results after overnight heating at  $100^\circ\text{C}$ .

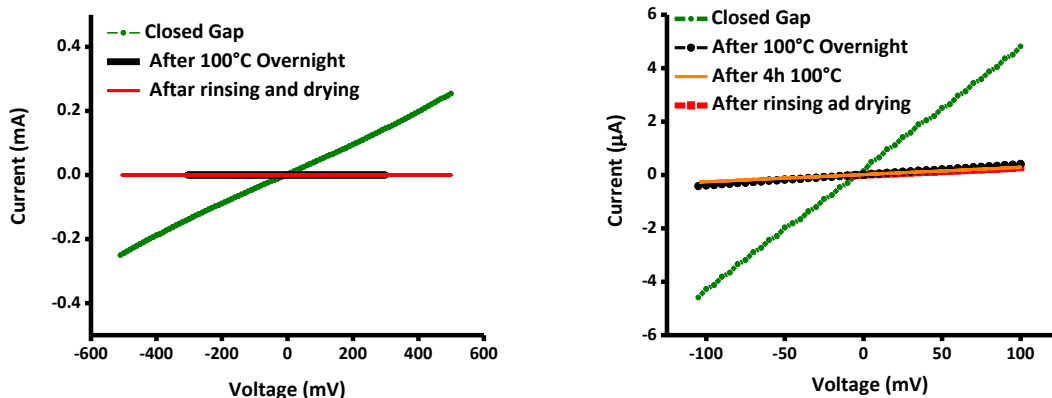
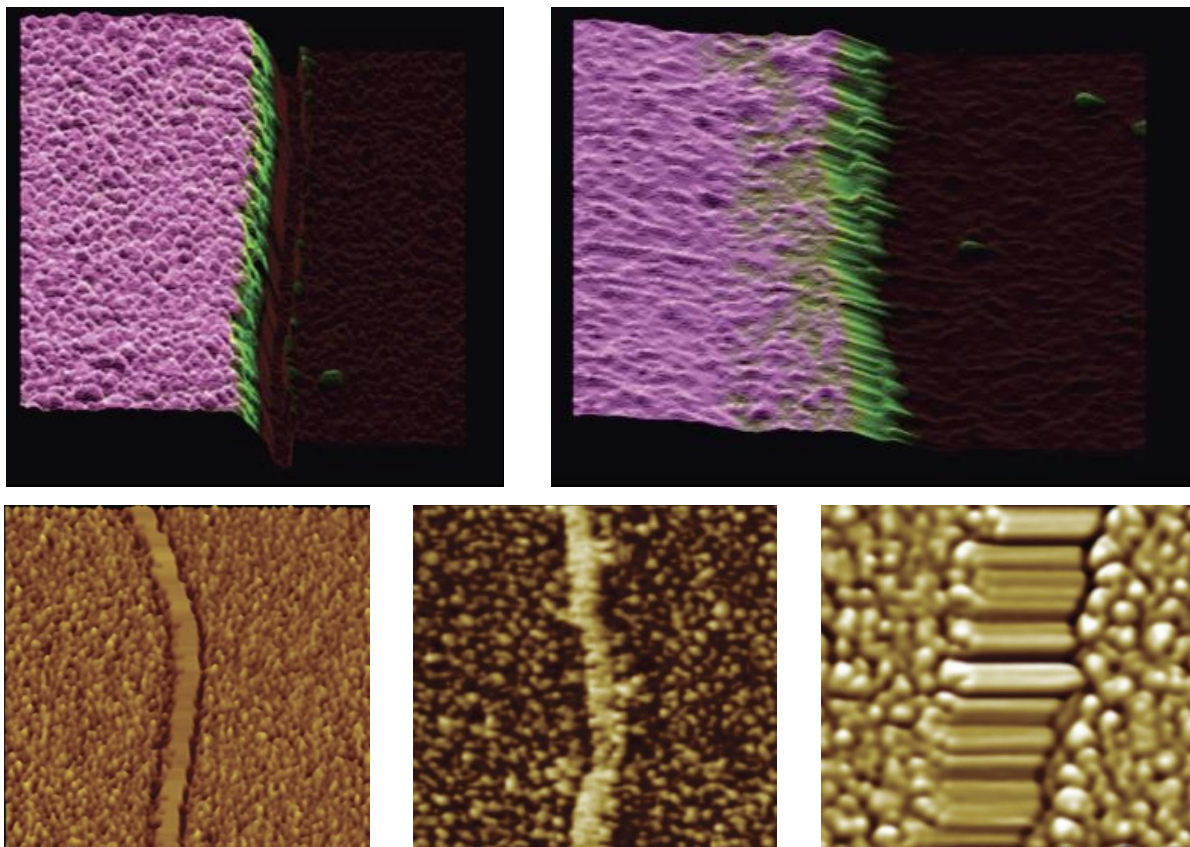


Figure 5.20 : Two sets of current voltage characteristics showing opening of the closed gap by self-assembled triarylamine blocks after overnight on the hotplate at 100°C and after 4 more hours at 100°C and after excessive rinsing with organic solvents. The gaps were opened and closed again by self-assembly!

### 5.5.2.1. IMAGING THE STANWS

After extensive rinsing of the sample i.e. washing in Cl based solvents (e.g.  $C_2H_2Cl_4$ , chloroform- $CHCl_3$ , and dichloromethane- $CH_2Cl_2$ ), rinsing in acetone followed by ethanol or isopropanol, samples are imaged. Let us emphasize that the cleaning process is quite aggressive, and mimics our cleanroom process for cleaning substrates with organic residues. We find that atomic force microscope (AFM) imaging was the best-suited method for imaging our samples since the SEM shows no contrast revealing material trapped between the electrodes. This is not fully surprising, since the SEM is not optimized for revealing light atoms structures. AFM images are shown in figure 5.21).



**Figure 5.21 :** Top left) topography of the open gap seen by AFM before light irradiation, Top right) topography of the closed gap filled with STANWs after light irradiation. Bottom) left: AFM phase image of a fiber-free gap (surface scale  $1500 \times 1500 \text{ nm}^2$ ) before light irradiation, middle: AFM phase image of a STANWs-filled gap (surface scale  $1500 \times 1500 \text{ nm}^2$ ) after light irradiation, right: Zoom in the STANWs-filled gap after light irradiation (surface scale  $250 \times 250 \text{ nm}^2$ ), after image processing.

AFM images reveal that the wires length exactly matches the electrode gap, with orientations following the electric field applied during the assembly and with homogeneous diameters of  $12 \pm 2 \text{ nm}$  (figure 5.22).

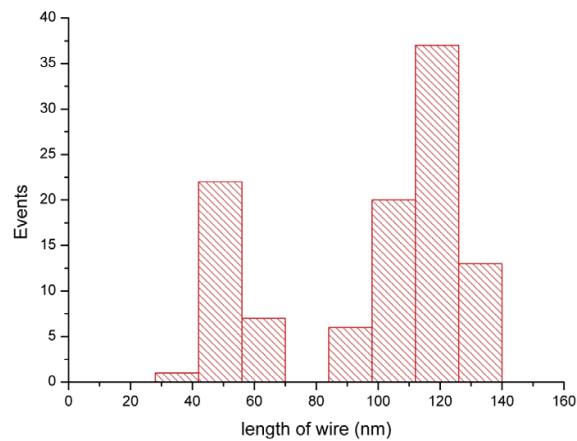
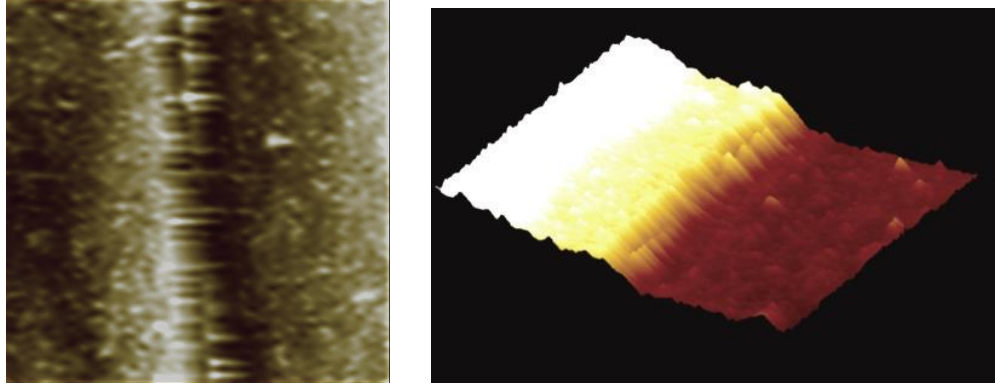


**Figure 5.22 : Size distribution of STANWs in the gap. (A) AFM image of the closed gap with STANWs (surface scale  $500 \times 500$  nm<sup>2</sup>). (B) Topography extracted from image (A). (C) Length distribution of STANWs observed from a typical gap and obtained from a series of AFM phase image as shown in (A and B). The short length average distribution is due to residual non-connecting wires at the surface and that survive the washing of the device. The resolution of the AFM images of the STANWs cannot be as good as the one obtained in [22]. Indeed, here the fibers make a high angle with the surface because of the presence of a step between the two electrodes. The presence of this height decreases considerably the resolution. The AFM cantilevers used here are Arrow probe (from NanoAndMore). These probes are very sharp ( $<10$  nm of curvature radius) and made from monolithic silicon which is highly doped to dissipate static charge. The STANWs diameters were measured taking into account the convolution of the image by the AFM tip during the imaging process ( $12 \pm 2$  nm). Here, we measured a portion where a bimodal distribution can be found, although several domains only present the longest population.**

### 5.5.3. TEMPERATURE DEPENDENT MEASUREMENTS

#### i. TRANSPORT IN METALLIC POLYMERS

The model for the intrinsic temperature dependent resistance of a quasi-1D polymer along a defect free chain was proposed by Kivelson and Heeger in 1989. This model can be expressed as in equation 5.6 where  $\hbar\omega_0$  is the energy of the phonons that backscatter electrons and  $k_B$  the Boltzman constant ( $0.087 \text{ meVK}^{-1}$ ), for temperatures such that  $k_B T$  is much less than energy  $\hbar\omega_0$  of the backscattering phonons, the resistivity would be expected to vary as the number of these phonons thermally excited [181, 182]. Resistance of conducting polymers increases by lowering the temperature. In late 1990s, Kaiser and Graham proposed a “heterogeneous” model on where they added separated thin barrier regions to the Kivelson and Heegers’ model [182].

$$R(T) = R_0 \exp\left(\frac{-\hbar\omega_0}{k_B T}\right) + R_{(T=0)} \quad (5.6)$$

#### ii. RESISTANCE VERSUS TEMPERATURE MEASUREMENTS OF STANWS

After STANWs formation, for washed samples, low temperature electrical measurements are carried out inside a vacuum-pumped cryostat ( $P < 10^{-6}$  mbar) or in a Helium flow system going down to 1.5 K. Measurements of electrical properties are performed using an Agilent E5270B semiconductor parameter analyzer (DC properties), and a SRS 830 lock-in amplifier (AC properties, 4 mV rms excitation). For this set of measurements, we use a pseudo-four points technique, where the electrodes have two patterned lines nearby the trench, limiting the circuit series resistance below  $2 \Omega$  (see chapter II).

Temperature-dependent studies confirmed the high conductivity of our samples, because they reveal sample resistance systematically and reproducibly diminishing when decreasing temperatures down to 1.5 K (figure 5.22). We find that these data can be satisfactorily fitted

using predictive models established for quasi-1D polymer metallic conduction [27, 32], equation 5.8, and one may correlate these fits with the unidirectional supramolecular shape of the wires that we initially described (see supporting information of [179]).

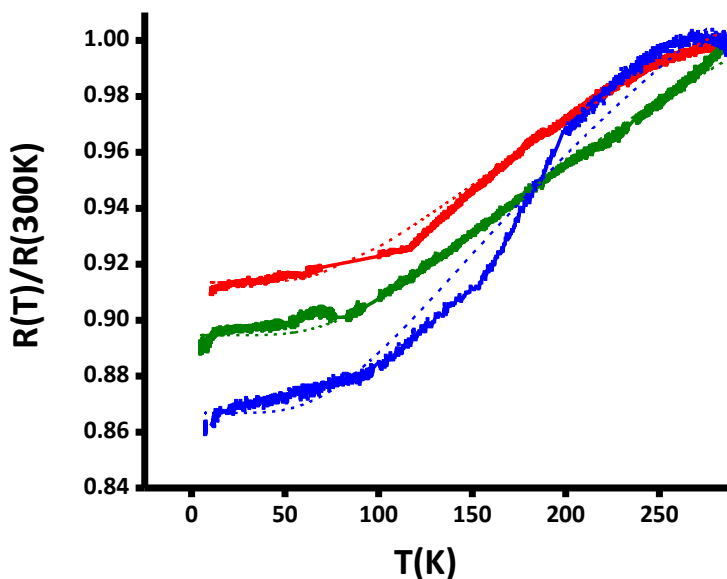


**Figure 5.23: Ohmic behavior and conductivity characteristic of the STANWs as a function of temperature. Normalized  $R(T)$  measurements of three independently prepared STANWs functionalized devices, between room temperature and 1.5 K. The initial resistances for each sample at 300 K are the following: 22  $\Omega$  (RED), 45  $\Omega$  (GREEN), 360  $\Omega$  (BLUE). Each set of data is fitted (dashed lines) using the equation 5.8 [181, 182].**

This result is astounding, as it indicates a metallic behavior or a purely organic material. As mentioned previously, the examples are extremely seldom in nature, and essentially limited to carbon structures. In fact, the numerous check plots presented previously were motivated by the necessary checks to confirm the reality of the conductivity findings. We must also emphasize that the measured sample resistance does not simply probe the fibers intrinsic properties, but also includes the interface series resistance.

### 5.5.4. CONDUCTIVITY AND INTERFACE RESISTANCE ESTIMATES

Current-voltage characteristics in low temperature reveal very high conductivity values for nanowires. As mentioned in Fig. 5.23, the sample shave intrinsic resistance values as small as a few tens of  $\Omega$ , however lacking sample-to-sample reproducibility. A sample presented in figure 5.23, measured using a pseudo 4-point contact technique at 1.5 K, shows a resistance below  $20\Omega$ . Each nanowire has a channel resistance and two contact resistances in series. If we consider that the measured resistance value originates from the bulk STANWs only, considering the device geometry illustrated in figure 5.16, and estimating the density of nanowires per unit length from AFM images (a trench width of  $100\mu\text{m}$  could be fully filled with  $\sim 10^4$  nanowires with 12 nm diameter), we obtain a channel conductivity exceeding  $5 \times 10^3 \text{ S.m}^{-1}$  which is a minimum value, supposing that the resistance originates from the STANWs bulk only. Alternatively, we estimate that interface resistance per unit length is below  $2 \times 10^{-4} \Omega.\text{m}$  which is a maximum limit under the hypothesis that the resistance of the sample originates from the interface only. One should recall that polymer devices exhibit interface resistance values of the order or  $10^2\Omega.\text{m}$  to  $10^5\Omega.\text{m}$ , orders of magnitude larger than the upper limit we estimate in our samples! Our value is still 4 orders of magnitude lower than the best interface resistance values reported for organic materials, found on single crystals of rubrene [183], and below what is observed for graphene interface resistance values [172] (figure 5.24)!

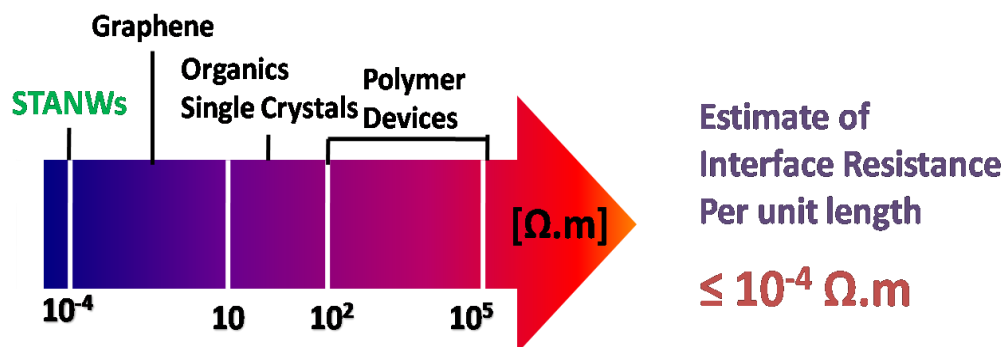


Figure 5.24: Diagram of Interface resistance per unit length of organic materials.

From the  $R(T)$  measurements, we can therefore infer that the sum of ohmic contact resistance and intrinsic conductivity of STANWs has a metallic character. To date, only ballistic carbon nanotubes with highly transparent resistance contacts showed such a characteristic [170]. In addition similar  $k\Omega$  range of resistance per fiber is estimated by counting their number through AFM imaging. Note that our sample conductivity is of the same order of magnitude than the best conductivity we found reported in the literature for ensemble of parallel high-purity and well-connected metallic carbon nanotubes, exhibiting optimized conductivity reaching  $10^4$  to  $10^5$   $S.m^{-1}$  [184]. We find that ohmic behavior persists up to high bias at low temperatures (figure 5.26).

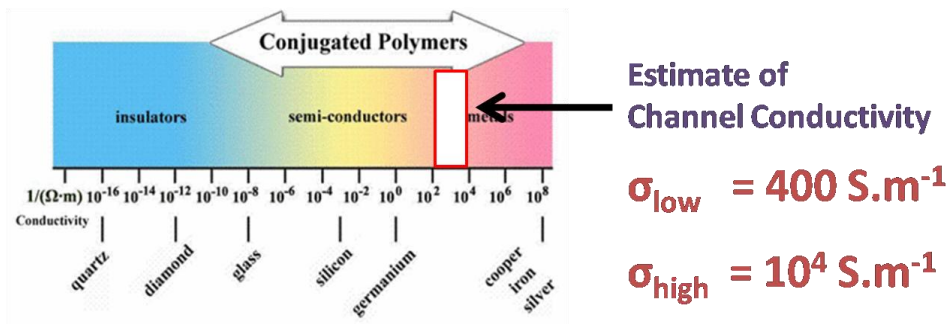


Figure 5.25 : Conductivity of conductive polymers compared to those of other materials, from quartz (insulator) to copper (conductor). Polymers may also have conductivities corresponding to those of semiconductors [4].

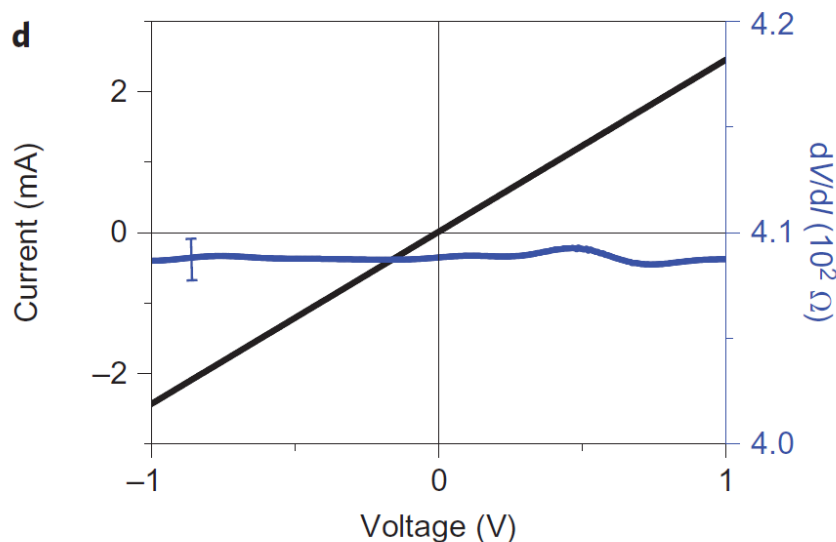
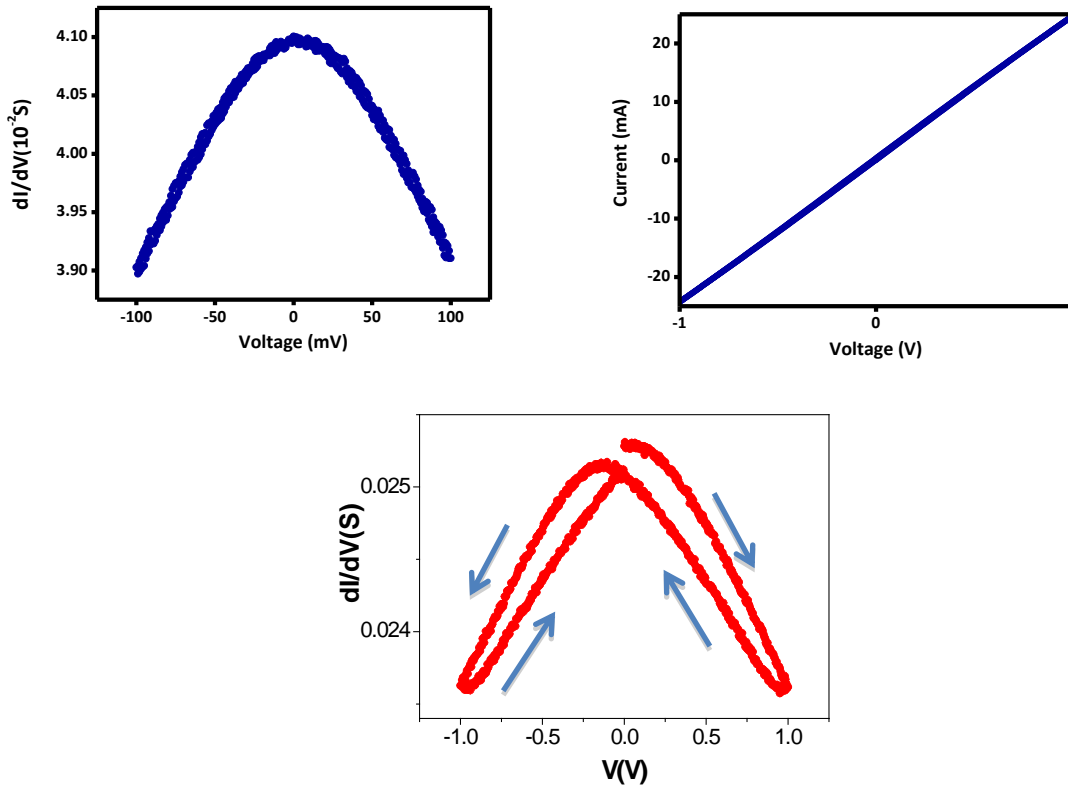


Figure 5.26:  $I(V)$  curve measured after self-assembly, rinsing and drying of the device. The pseudo four-point measurement, performed at 4K and under atmospheric pressure, shows a perfectly linear character up to 1V bias, as confirmed by the calculated differential resistance  $dV/dI$  including error bar.

When large current stress is applied, small deviations from perfectly linear I/V curves can be attributed to sample heating (figure 5.27-a). We nevertheless observe very large current values, up to 25 mA for the lowest resistance samples submitted to a 1V bias, at 200 K, under vacuum conditions which severely limit the heat diffusion with our suspended samples (figure 5.27-b). The corresponding current density is thus estimated in the order of  $10^7$  A.cm<sup>-2</sup>, which is remarkably large for organic films and corresponds to the onset current density value for electromigration in metallic circuits. The technologically relevant value is the Blech length [185], the product of the current density by the channel's length. In our case the estimate of 100 A.cm<sup>-1</sup> is only 15 to 50 times below the so called 'immortal interconnect' conditions [186].



**Figure 5.27 :** Two examples of differential conductance of STNWs, measured at 200 K in vacuum using an AC bridge technique (4 mV rms excitation). The decrease of conductance with bias is interpreted as heating, confirmed by the hysteresis in the bottom curve, disappearing when slowing down the bias voltage sweep.

### 5.5.5. ELECTRODES MATERIAL EFFECT

A transition metal component in the electrode material (Nickel, Cobalt, Fe and Permalloy) was a necessary condition for successful interconnects self-assembly. Self-assembly with better than 90% success rate were obtained between Ni and Fe electrodes. No reliable and stable self-assembly occurred between electrodes made of Au or Pt only (with Ti adhesion layer). We found that covering the electrodes with Au provided better similar than 90% success rate, with long-term sample stability. The samples can then survive the extensive cleaning procedure, and show reproducible resistance value, even after 2 months storage under ambient atmosphere. The dependence of the electrodes composition is surprising, and might cast the doubt that an electrode dissolution process can occur, and that we would measure metallic nanostructures or filaments due to dissolution/electromigration during the self-assembly process. We tested the chemical stability of the electrodes, and found that exposition to light-induced radical in triarylamine solutions can indeed result in electrodes corrosion (Figure 5.26).

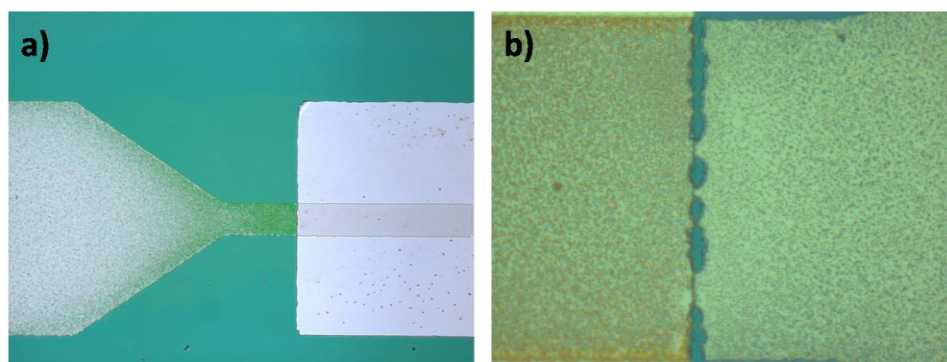


**Figure 5.28 : Optical images of the nanotrench electrodes composed of Au/Ni/Ti after being immersed in the solution of 1 in  $C_2H_2Cl_4$  and exposed to pen lamp UV for 10 minutes. Image b) is the zoom on the trench area of image a).**

Increasing the light exposure time by two orders of magnitude result in indications of chemical reactivity of the radicals possibly slowly damaging the electrodes (figure 5.26). We therefore performed extensive test and check experiments. Several tests, already shown in section 5.4.2., performed on empty trenches with solvents, molecules, and under illumination, clearly indicate that very low currents limit the hypothesis of spontaneous electrodes metallic shorts, but other check are needed, and presented below.

## 5.6. EXCLUDING THE ARTIFACTS

### 5.6.1. SOLUTION STRESS CONDITIONS

We tested that exposures of the electrodes to the radicals did not prohibit the STANWs growth. First, we found that multiple construction/dissolution process was possible. We realized up to ten successive STANWs growth between the same electrodes, using mild heating to re-open the gap. After cleaning open nanotrenches, we found no indications of Au/Ni electrodes dissolution using SEM inspection.

We checked how the self assembly process depends on the molecules concentration. Our initial value ( $1\text{mg.mL}^{-1}$ ) was chosen in analogy with the experimental conditions of paper [179]. We observed that increasing this concentration was detrimental to the self-assembly ( $5$  and  $10\text{mg.mL}^{-1}$ ), with no interconnects realized under larger concentrations. This corresponds to the observation in solution, where an excessive concentration of radicals is found to impede the self assembly. Even if this effect remains a bit mysterious, one should recall that the thermodynamics of the construction of the supramolecular assembly can easily be perturbed and made unstable, for example when varying the pending groups of the triarylamine molecules [179]. Nevertheless, larger concentrations relates to more reactive solutions, and therefore should favor dissolution artifacts. Our experiments shows the contrary.

For further testing the hypothesis of transition metal ions in solution promoting the STANWs growth, we performed the self-assembly experiment with Au electrodes (with no success of interconnects growth under standard conditions), in the presence of a piece of Ni metal in the solution of **1**. The lack of success of self assembly, makes the scenario of dissolution of the  $\text{Ni}^{(0)}$  and generation of concomitant STANWs and Ni very unlikely.

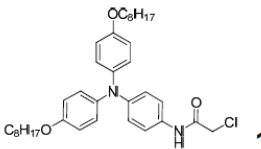
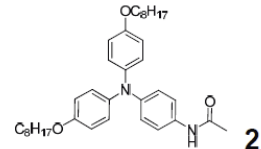
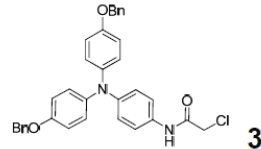
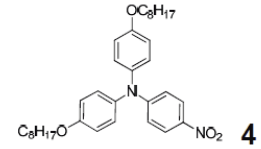
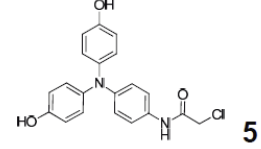
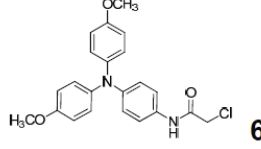
## 5.6.2. BLIND TESTS

As mentioned previously, some triarylamine compounds self-assemble, some others don't. Triarylamine analogues 1-6 (see Table 5.1) behave differently upon light stimulation in chlorinated solvents. <sup>1</sup>H NMR experiments have shown that compounds 1-3 self-assemble in CDCl<sub>3</sub> solutions upon light stimulation, while compounds 4-6 do not produce stacks. This structure-property relationship highlights that several features should be simultaneously operating to produce STANWs: a) a triarylamine core, b) an amide group for hydrogen bondings (the chlorine having no role in the self-assembly); and c) alkyl chains or benzylic groups on the phenols for hydrophobic or stacking secondary interactions.

In the series 1-6, redox behaviors are however similar and our control experiment can discriminate between parasitic electrochemical processes that would be initiated by the production of triarylammonium species, and the conductivity related to the subsequent formation of self-assembled STANWs.

The control experiments were performed using a blind test protocol: the person who prepared the solutions did not perform the conductivity experiments and the labels on each vials was kept coded until the measurements were performed and analyzed. Each sample was measured under the same conditions: we applied a voltage of 1 V to solutions of triarylamine 1-6 (1 mg.mL<sup>-1</sup>), together with a 100 W irradiation at constant distance ( $\approx 10 \text{ W.cm}^{-2}$ ) for a period of 10 seconds; then, I/V dependence was measured for each gap. Results are summarized in Table 5.1 for each derivative and by comparison to the expected behavior determined in solution. The correlations clearly show that the conductivity is self-assembly dependent. When the gaps were closed, the resistance values were measured in the same range for the various derivatives.

Solutions of triarylamine molecules that do not self-assemble because of a chemical modification (molecule 4 of table 5.1), under illumination, showed leakage currents in the nA range (3 V bias) (figure 5.29) Typically up to seven orders of magnitude smaller than those obtained on successfully self-assembled systems.

Molecule	Behavior in solution determined by $^1\text{H}$ NMR (1)	State of the gap
 <b>1</b>	Self-assembled	Closed
 <b>2</b>	Self-assembled	Closed
 <b>3</b>	Self-assembled	Closed
 <b>4</b>	Non self-assembled	Open
 <b>5</b>	Non self-assembled	Open
 <b>6</b>	Non self-assembled	Closed <sup>a</sup>

<sup>a</sup> The gap was however opened after rinsing with solvent under conditions where STANWs derivatives 1-3 remain stable; this shows the weakened mechanical properties of STANWs starting from 6. The fact that we don't observe the self-assembly in solution for 6 is thus certainly related to the time delay between the irradiation and the NMR measurement which is sufficient to "disassemble" the system.

**Table 5.1: Summary of the control experiments – performed in blind test conditions – to determine the influence of the self-assembly on the conductivity starting from derivatives 1-6.**

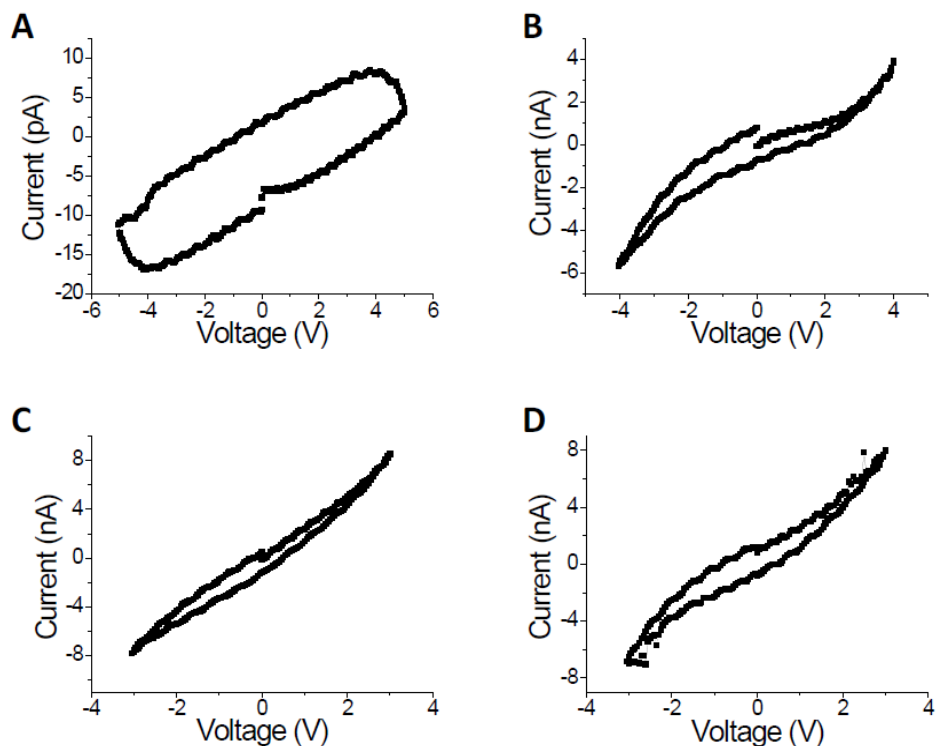


**Figure 5.29: Intensity/voltage measurements of the empty gap at high voltages. (A) I/(V) of an empty reference nanotrench (width = 100  $\mu\text{m}$ ; length = 0.08  $\mu\text{m}$ ) without any solvent. (B) I/(V) of the reference nanotrench (width = 100  $\mu\text{m}$ ; length = 0.08  $\mu\text{m}$ ) and before light irradiation. The residual current is attributed to ionic impurities in solution. (C) I/(V) measurements of the nanotrench (width = 100  $\mu\text{m}$ ; length = 0.08  $\mu\text{m}$ ) immersed in  $\text{C}_2\text{H}_2\text{Cl}_4$ , and upon white light irradiation (density 10  $\text{W}\cdot\text{cm}^{-2}$ ). (D) I/(V) curve of a reference nanotrench (width = 100  $\mu\text{m}$ ; length = 0.08  $\mu\text{m}$ ) covered by a solution of molecule 4 (1  $\text{mg}\cdot\text{mL}^{-1}$  in  $\text{C}_2\text{H}_2\text{Cl}_4$ ), after white light illumination, characteristic of a chemically and redox related sample, but without self-assembly properties**

### 5.6.3. IMAGING NANOTRENCHES

Systematic imaging of the gaps, including those which experienced several self-assembly processes, did not reveal the presence of metallic bridging structures [79, 187], or extensive degradation of the metal. We present a series of measurements, mostly aimed at checking that the observed remarkable conductivity of our samples does not rely on metallic shorts originating from the electrodes interconnects.

We extensively checked the morphology and the difference of the electrodes before and after self-assembly. We used scanning electron microscopy (SEM) and atomic force microscopy

(AFM) to obtain qualitative and quantitative information on the nanotrenches. Figure 5.30-b and figure 5.30-d show the appearance of the nanotrenches prior to self-assembly, and Figure 5.30-a and figure 5.28-c provide SEM and AFM imaging information after self-assembly. SEM imaging of the filled trenches provide limited contrast from the organic spacer. Figure 5.30-a and figure 5.30-b illustrate a series of systematic SEM micrographs along the whole length of a filled trench of 50  $\Omega$  resistance value. Even by exaggerating the contrast to image better the interconnects, it was not possible to visualize them.

The information given by SEM is however important because we cannot detect the presence of large metallic bridges that would explain the observed conductivity. Even under the hypothesis that small metallic residues would exist, they could not sustain the current and voltage applied to the sample (see discussion in the next section). In contrast, AFM provides clear indication of fiber-like structures filling the trenches, with diameters expected from self-assembly morphology observed in solution. In addition, by increasing the force on the AFM tip for imaging, the fibers appeared very brittle. Figures 5.30-c and 5.30-d reveal that the fibers can be easily broken, thus illustrating the organic nature of the STANWs and their tight attachment at each electrode, as well as their suspension over the trench.

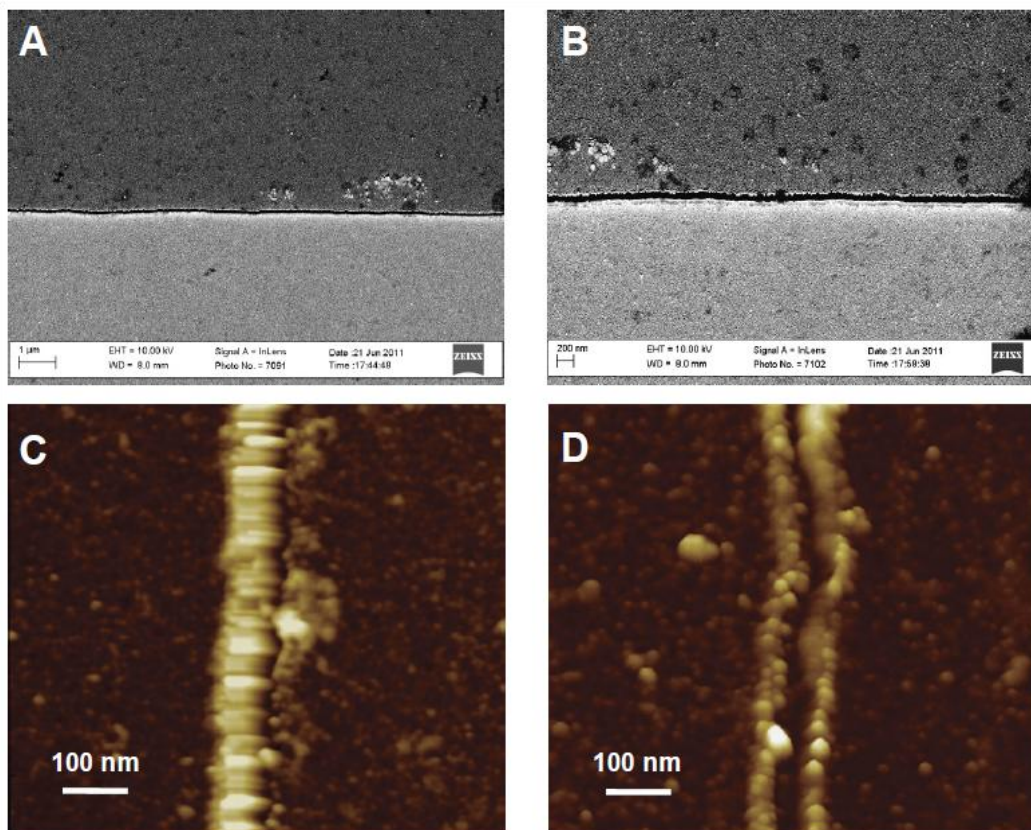


**Figure 5.30 : SEM and AFM imaging of a nanotrench filled with STANWs, after rinsing, of 50  $\Omega$  resistance. (A) One typical region of the trench is shown, where no high-contrast bridges can be seen. The dark spots on the electrodes are solvent or solution residues. (B) Zoomed image of the nanotrench, without indication of continuous electrical interconnects. (C) Corresponding AFM imaging indicates that the trench imaged by SEM is indeed fully filled with STANWs. Some non-oriented remaining material can be seen close to the gap. (D) The AFM imaging is very sensitive to the applied force value, which has to be maintained in a very narrow interval to preserve the STANWs; a slight increase in the applied force causes destruction of the organic suspended fibers bridging the two electrodes.**

#### 5.6.4. ELECTRICAL PROPERTIES OF FILLED NANOTRENCHES

Stress voltage experiments were performed on self-assembled and cleaned samples, at lower temperatures (200 K) and vacuum environment. Currents of a few tens of mA and bias of 1 V were reproducibly observed on several samples (figure 5.26 and 5.27). The observed currents and voltages of the samples provide more arguments against the hypothesis of electrodes metallic ‘debris’ bridging the nanotrench. On a separate set of experiments using a similar setup, the electromigration of Au and Ni nanoscale constrictions was investigated for the purpose of

studying electrical properties of ultra-small metallic bridges [188]. In these experiments, metallic constrictions of typically 50 nm width patterned by e-beam were exposed to stress of a few mA and pulses of a few hundreds of mV. Such values were large enough to initiate electromigration, ultimately resulting in breaking of the nanocontact. If we recall that the bridging particles should be more electrically fragile than patterned continuous metallic lines, we would need several tens of such small structures to sustain the high current shown in figure 5.27. If we suppose that the current is involving nanoparticle hot points, the related current density that can be estimated is in the range  $10^9$ - $10^{11}$  A.cm<sup>-2</sup>, and cannot lead to resistance values with long-term stability as observed in figure 5.27.

Finally, if metallic residues take place, we expect that the electrodes would exhibit a corresponding loss of material. When performing experiments involving successive self-assembly, no morphological difference within the SEM resolution was found, confirming that the metallic electrodes were left essentially undamaged by the self-assembly.

### 5.6.5. SUMMARY

All our test experiments confirm the hypothesis that the low resistance values we observe is related to the filling of the void between two electrodes by a pure organic material:

- a full correlation between self-assembly in solution and success in creating low resistance interconnects is found
- no significant indication of inorganic debris filling the trenches are found by SEM and AFM imaging
- if small metallic (buried) particles exist, the large current values they can sustain implies a very large number of metallic shorts between the electrodes. There are no related morphological indications that the width of the nanotrench is increased, even after ten successive interconnects growth.

There are several possible possibilities for explaining the electrodes composition dependence of the STANWS growth

- this is a nucleation problem, expected to be surface dependent
- the initial stage of the fiber growth is an electrochemical redox process, requesting a radical reduction potential that might depend on the electrodes composition
- the radical chemisorptions on the surface requires limited charge transfer to the substrate, in order to keep possible the fiber growth, in a process analogous to the one in solution.
- the charge transfer depends on the substrate, and it might be possible that a native oxide (expected for transition metals) is necessary to limit the transfer.

**Reference:** V. Faramarzi, F. Niess, E. Moulin, M. Maaloum, J-F Dayen, J-B Beaufrand, S. Zanettini, B. Doudin and N. Giuseppone, *Triggered self-construction of supramolecular organic nanowires as metallic interconnects*, Nature Chemistry 1332 (2012).

## 5.7. CONCLUSION

In conclusion, by matching bottom-up self-assembly strategy of supramolecular systems with the top-down methodology of patterning metallic circuitry, a unique class of conducting metallic soft organic materials was discovered, that can be easily processed from solutions, and which exhibit conduction behavior matching metallic interconnects properties. The necessary light-trigger and the intrinsic self-limiting supramolecular process enable to insert organic interconnects in pre-determined positions in a circuit, making possible lateral control of nanoscale organic devices. The performance of obtained samples is not noticeably sensitive to moisture and oxygen, which constitutes a strong asset for organic electronic devices. No inert atmosphere conditions were used during the self-assembly, and the samples left on the bench for one month (for example after AFM measurements) showed reproducible transport properties.

The share of the electronic wave function of the STANWs with the metallic substrate is likely the fundamental reason explaining the low interface resistance values, coherent with the metallic character of the organic spacer. The interface resistance per unit length value is six orders of magnitude smaller than the measured for conducting polymers [169, 178] in lateral devices, four orders of magnitude lower than those of the best contacts on organic single crystals [183] and below what is achieved on highly mobility graphene flakes [172]. Such impressive improvement is coherent with the occurrence of a metallic-type spacer, where less interface resistance is expected, owing to the better-matching of the transport properties of the spacer and the electrodes. Only single wall metallic CNT can exhibit better interfaces, being bound by the quantum interface resistance value resulting from relaxation in the metallic terminal.

The first generation of STANWs already presents tremendous potential for making novel processable electronic nano-devices, which will require enhanced conductivity values, both in the bulk and at the metal/organic interface. Furthermore, the versatile chemical structure of STANWs offers numerous opportunities for tuning their electrical properties by straightforward variations using classical organic synthesis. Finally, the self-fabrication methodology, which can in principle be coupled to additional top-down engineering such as high resolution ink-jet printing, is opening new research avenues for light-directed patterning lithography methods or soldering of (bio)electronic circuits, with expectations of long term reliability.

## CHAPTER VI: CONCLUSIONS

### 6. CONCLUSIONS

During this dissertation, we focused on establishing a setup and procedure for creating reliable and robust molecular electronics devices. The motivation was the necessity to obtain solid and unambiguous experimental grounds for investigating electrical circuits involving molecular entities as key element. From a nanofabrication point of view, it is clear that top down tools cannot fulfill reliability criteria when molecular size spacing (1 nm) are targeted. This is why we restricted ourselves to more conservative length scale (a few tens of nanometers), with emphasis on simplicity and reproducibility of the process. We therefore elaborated and developed high aspect ratio interconnects with sub 100-nm separation, using simple shadowing techniques to create ‘nanotrenches’, stable, free of current leakage paths, electromigration pollution and substrate shorts [136, 137]. A significant time and effort had to be spent for implementing the nanofabrication process and building up the electrical characterization and light-excitation setup. This involved sample holder design and fabrication, as well as building-up from an empty room to a well-equipped laboratory with cables connected to the right places, capable of recording adequate measurement data.

The closure of the circuit over a typical 80 nm nanotrench width was achieved by several methods. The first experiment aimed at showing the proposed methodology can efficiently provide access to molecular properties. For this purpose, we relied on the extensive literature on self-assembled monolayers, where investigations of the electrical properties of compact organic thin films are normally performed in a vertical geometry, typically using a small tip to touch a large surface fully covered with molecules. We investigated an alternative approach, using the lateral geometry, where one can expect more stable interconnects, opening the possibility to study them under changes of external parameters, with expectation of long term stability. The first experimental element is the identification of the methodology for bridging the size gap separating the nanotrenches length and the thickness of molecular films. For this purpose, microspheres, partly coated with a Au/Ni bilayer, were successfully controlled and positioned by

magnetic trapping for creating metallic junctions over the Au/Ni electrodes with few ohms resistance [190]. Coating these spheres with SAMs of molecules allowed us to create double molecular junctions [70]. The second ingredient is the adequate choice of the molecules to study. We proposed to investigate bistable molecular systems, where two molecular configurations can be thermodynamically stable at a given temperature. We focused on reversible photoswitching molecules, where light excitation can reversibly be used as energy trigger for modifying the molecular configuration. We validated the adequacy of this approach by proof-of-principle test experiments on azobenzene derivatives used as benchmark molecules. Conduction properties modifications triggered by light were previously reported for this family of molecules, but no experiments previously performed in the lateral geometry. In chapter 3, our results indicated that these photochromic molecules films exhibit electrical fingerprint of photoswitching with 90% confidence rate! This quantitative estimate was possible by performing experiments on a significant number of samples, and using non-switching molecules as tests for checking the absence of artifacts.

Having gained confidence in the experimental approach, we proposed to investigate more original molecular materials. Investigations of the intrinsic conduction properties of spin crossover (SCO) nanocrystals are of high interest, as we could expect to take advantage of the hysteresis in the bistability of these materials to obtain unambiguous interpretation of the expected bistability of the electrical properties. We successfully used SCO particles a few hundreds of nanometers long to bridge the electrodes separated by a nanotrench. The SCO nanoparticles exhibited unexpected large conductivity (0.01–1  $\Omega\cdot\text{m}$ ), and we found that a voltage ‘poling’ was necessary to limit the polymer semiconductor-metal interface. We observed photoconductance and photovoltaic behavior as well, confirmed not to be spin transition originated after several supplementary control experiments [92, 93]. The seeded bistability was not found, possibly due to our lack control of the particle temperature. While the interpretation of the results and properties remain to be further developed, one lesson we can learn from this experiment is that the proposed 10-100 nm size range was ideal for revealing unexpected or enhanced properties of the material, opening novel application for this rich family of bistable molecules.

The last experiment relied on a chemical approach. We took advantage of the impressive and rich possibilities of realizing molecular architectures reaching the 100 nm size range, making the ‘molecules’ size-compatible with the nanotrenches. We therefore used a supramolecular chemistry approach, where molecular self-assembly can result in stable large molecular entities. The field of ‘supramolecular electronics’ is younger than molecular electronics, and is driven by the perspective of realizing well-controlled  $\pi$ -stacked architectures, of expected significant conductivity values. There are however two bottlenecks: the positioning of the assemblies between electrodes is difficult to control, and the organic-metal interfaces are expected to govern the total resistance of the device. We proposed a very original route, where the molecular self-assembly was triggered by light, and where the molecular assembly was expected to grow between the electrodes. We discovered a unique class of conducting soft organic materials, processed from solution, forming nanowires exhibiting metallic conductivities. Metallic organics are extremely seldom, being mostly limited to organic salts (where ionic conduction allows metallicity) and one specific conducting polymer sample. Our observed long lasting stability and the remarkable low interface resistance (6 orders of magnitudes lower than measured for conducting polymers), are expected to open new possibilities for realizing hybrid organic-inorganic electrical systems.

This thesis work started from scratch, in the framework of a novel activity and a laboratory creation. This is essentially why we focused on the principle of realizing molecular electronics circuitry at the 10-100 nm size scale, and chose to investigate several types of materials and experimental strategies. The three types of experiments performed can now become three PhD projects, aiming at full characterization and insight into the presented three chapters! As short-term perspectives of this work, I propose to emphasize how the presented experiments could be further developed.

Microsphere molecular junctions exhibit long-term stability of high interest, allowing for example temperature-dependent studies. For bistable systems, this could for example provide unique insight into the energy barrier separating the two states. As mentioned in Chapter 4, long-term studies can also be used to investigate further relaxation effects, or test the fatigue of switching events. This fundamental knowledge need to be gained if we want to assess the applicability of molecular switching circuits, or if we need to find methodologies or routes to improve the switching properties. The insertion of a magnetic layer, used for magnetic trapping,

was also initially designed for testing the magnetic response of the samples. If the microsphere can be displaced under external large field, this should result in changes in electrical properties. The related mechanical strains on the molecules or the strain-induced molecular reorganization can also result in a very original topic in the field of molecular electronics.

Spin crossover nanoparticles are synthesized in versatile variety of sizes and shapes, with different transition temperatures. We limited our investigations to two materials, aiming at studying transition temperatures slightly larger than ambient. One interesting approach to these samples would be the addition of an electrostatic gate, for the purpose of mimicking the OFETs devices. As an approximate rule of thumb, efficient bottom gate requires a dielectric thickness half the distance between metallic leads, i.e. a few tens of nm for nanotrench devices. Our samples suspended over at least 50nm high electrodes are therefore challenging to gate efficiently, especially when one realizes that the spacer would involve a bad dielectric like air or vacuum. This is in particular why we did not enter into this field during the thesis. Electrical gating solutions (for example using top gating through electrochemical methodologies) remain nevertheless an interesting avenue for checking if the studied nanocrystals can be used as semiconducting materials of significant mobilities. A significant effort is also needed to check if the spin transition can be obtained, and a related change of conductance observed. For this purpose, a better thermal environment should be used, and an optical diagnostic tool should be used to check if the particles experience a spin transition. Again, this involves a significant effort, with apparatus acquisition and buildup.

The remarkable results on the metallic properties of STANWs are evidently motivating further research. For example, we also propose to check if these materials can be electrostatically gated. This appears at first sight surprising for metallic systems, known to screen the electric field very efficiently. More specifically, the electric field goes to zero within a length scale related to the

Thomas-Fermi screening length, of the order of  $\lambda_{TF} = \frac{1}{2} \sqrt{\frac{a_0}{n^{\frac{1}{3}}}}$ , which depends on the density

of charge carriers ( $n$ ) ( $a_0$  is the Bohr radius). For example in OFETs, this length can be limited to a few nm only, which is the active thickness for gating the carriers channel. If the current is carried in molecular-size filaments with dielectric spacings, it is not unreasonable to consider that transport in these materials can be affected by an external electric field. Alternatively, chemical engineering, and the variety of possible self-assembling structures might make possible

the realization of high-mobility semiconducting STANWs channels. Another application relates to spintronics, where organic spin valves realization suffer from the same limits as spin valves involving inorganic semiconductor spacers. The resistance mismatch between ferromagnetic metals and semiconductors can possibly be lifted if the organic spacer is metallic. We tried to self-assemble between pure transition metal electrodes, with limited success. The structure lacked time stability, and transition metals electrodes suffered from the exposure to radicals. For convincing spintronics devices fabrication, working in more inert environments, and lowering the density of radicals should be systematically tested for samples reliability issues.

We should restate that the large majority of the experiments involve control and check experiments. The key result is the realization of a setup where we can unambiguously distinguish electrical signal originated from molecules from artifacts and defects in the system. Much has been learned about the fundamental charge transport in single molecules, which plays a key role in both basic science and technological applications. Although it is still difficult to fabricate reliable and robust electronic devices made with single molecules, the beauty of 100nm size approach lies in its novelty and ability of revealing the intrinsic properties and/or discovering new class of materials, from one part for bringing information for single molecule studies and from the other part helping with downscaling of OFETs.

We believe that a not-too-far reachable goal of the proposed approach is to realize multifunctional devices, taking advantage of bottom-up molecular engineering. One can for example envision the self-assembly of molecules involving transition metal centers, with ligand environments making spin crossover transition possible. The potential realization of light-tunable OFETs, of good mobility and with significant magnetoresistance properties, having hysteretic bistability properties, can open the way to electrical circuits tunable and/or programmable using (for example) light, electric field, magnetic field, temperature as multiple external stimuli. Such realization would fully exploit the intrinsic properties of molecular engineering, making possible realizations beyond what can be attained with current Si-based technologies. We hope that this thesis convinced the reader that lateral structures at the 10-100 nm length scale are optimally suited for this ambitious goal.

## 7. BIBLIOGRAPHY

- [1] H. Sirringhaus, *Device physics of solution-processed organic field-effect transistors*, Adv. Mater. **17** (2005) 2411.
- [2] N.J. Tao, *Electron transport in molecular junctions*, Nat. Nanotech. **1** (2006) 173-181.
- [3] S. R. Forrest, *The path to ubiquitous and low-cost organic electronic appliances on plastic*, Nature **428** (2004).
- [4] A. J. Heeger, A. G. MacDiarmid and H. Shirakawa, *Conductive polymers*, The Nobel Prize in Chemistry (**2000**).
- [5] I. McCulloch, *Organic electronics – from materials to applications*, Adv. Mater. **22** (2010) 3760-3761.
- [6] D. Tobjörk and R. Österbacka, *Paper electronics*, Adv. Mater. **23** (2011) 1935-1961.
- [7] H. Klauk (Ed.), *Organic electronics. Materials, manufacturing and applications*, Wiley-VCH (**2006**).
- [8] C. D. Dimitrakopoulos and P. R. L. Malenfant, *Organic thin film transistors for large area electronics*, Adv. Mater. **14** (2002) 99-117.
- [9] V. C. Sundar, J. Zaumseil, V. Podzorov, E. Menard, R. L. Willett, T. Someya, M. E. Gerhenson and J. A. Rogers, *Elastomeric transistor stamps: reversible probing of charge transport in organic crystals*, Science **303** (2004) 1644.
- [10] D. Braga and G. Horowitz, *High-performance organic field-effect transistors*, Adv. Mater. **21** (2009) 1473-1486.
- [11] Y. Yamashita, *Organic semiconductors for organic field-effect transistors*, Sci. Technol. Adv. Mater. **10** (2009) 024313.

- [12] A. R. Brown, D. M. de Leeuw, E. E. Havinga and A. Pomp, *A universal relation between conductivity and field-effect mobility in doped amorphous organic semiconductors*, Synth. Met. **68** (1994) 65-70.
- [13] V. Podzorov, *Charge carrier transport in single-crystal organic field-effect transistors*, Ed. Z. Bao and J. Locklin, (2007) 27-72.
- [14] D. Jérôme, A. Mazaud, M. Ribault and K. Bechgaard, *Superconductivity in a synthetic organic conductor (TMTSF)<sub>2</sub>PF<sub>6</sub>*, J. Physique LETTRES **41** (1980) 95-98.
- [15] S. Thomposon and J. Staley, *Orbitals and molecular representations*, National Small-Scale Chemistry Center, Colorado State University.
- [16] A. J. Heeger, *Semiconducting and Metallic Polymers: The Fourth Generation of Polymeric Materials (Nobel Lecture)*, Angew. Chem. Int. Ed. **40** (2001) 2591–2611.
- [17] A. J. Heeger, *Handbook of conducting polymers (ed. Skotheim TA)*, **2** (1986) 729-756 (New York, Marcel Dekker).
- [18] L. Zupproli, M. N. Bussac, S. Paschen, O. Chauvet and L. Forro, *Hopping in disordered conducting polymers*, Phys. Rev. B **50** (1994) 8.
- [19] R. W. I. De Boer, *Organic single-crystal field-effect transistors*, PhD thesis, Technische Universiteit Delft (2005).
- [20] M. C. J. M. Vissenberg and M. Matters, *Theory of the field-effect mobility in amorphous organic transistors*, Phys. Rev. B **57** (1998) 20.
- [21] S. F. Nelson, Y. Y. Lin, D. J. Gundlach and T. N. Jackson, *Temperature-independent transport in high-mobility pentacene transistors*, Appl. Phys. Lett. **72** (1998) 1854.
- [22] R. Corehoorn, W. F. Pasveer, P. A. Bobbert and M. A. J. Michels, *Charge-carrier concentration dependence of the hopping mobility in organic materials with Gaussian disorder*, Phys. Rev. B. **72** (2005) 155206.

- [23] K. Hannewald, V. M. Stojanović, J. M. T. Schellekens and P. A. Bobbert, *Theory of polaron bandwidth narrowing in organic molecular crystals*, Phys. Rev. B. **69** (2004) 075211.
- [24] E. A. Silinsh and V. Capek, *Organic molecular crystals: interaction, localization and transport phenomena*, AIP New York (1994).
- [25] R. Farchioni and G. Grosso, *Organic electronic materials*, Springer Berlin (2001).
- [26] A. A. Virkar, S. Mannsfeld, Z. Bao and N. Stingelin, *Organic Semiconductor Growth and Morphology Considerations for Organic Thin-Film Transistors*, Adv. Mater. **22** (2010) 3857–3875.
- [27] P. F. Baude, D. A. Ender, M. A. Haase, T. W. Kelley, D. V. Muyres and S. D. Theiss, *Pentacene-based radio-frequency identification circuitry*, Appl. Phys. Lett. **82** (2003) 22.
- [28] R. Kline, M. McGehee, E. Kadnikova, J. Lui and J. Fréchet, *Controlling the field-effect mobility of regioregular polythiophene by changing the molecular weight*, Adv. Mater. **15** (2003) 18.
- [29] J. Veres, S. Ogier and G. Lloyd, *Gate insulators in organic field-effect transistors*, Chem. Mater. **16** (2004) 4543-4555.
- [30] J. Veres, S.D. Ogier, S.W. Leeming, D.C. Cupertino and S. M. Khaffaf, *Low- $\kappa$  insulators as the choice of dielectrics in organic field-effect transistors*, Adv. Func. Mater. **13** (2003) 199-204.
- [31] h. B. Singh and N. S. Sariciftci, *Progress in plastic electronics devices*, Annu. Rev. Mater. Res. **36** (2006) 199-230.
- [32] S. Braun, W. R. Salaneck and M. Fahlman, *Energy-level alignment at organic/metal and organic/organic interfaces*, Adv. Mater. **21** (2009) 1450-1472.

- [33] S. M. Sze, *Physics of semiconductor devices*, 2<sup>nd</sup> ed., Wiley, New York (1981).
- [34] W. Mönch, *Metal-semiconductor contacts: electronic properties*, Surf. Sci. **299/300** (1994) 928-944.
- [35] L. Büergi, T. J. Richards, R. H. Friend and H. Sirringhaus, *Close look at charge carrier injection in polymer field-effect transistors*, J. Appl. Phys. **94** (2003) 6129.
- [36] X. Crispin, V. Geskin, A. Crispin, J. Cornil, R. Lazzaroni, W. R. Salaneck and J. L. Brédas, *Characterization of the interface dipole at organic/metal interface*, J. Am. Chem. Soc. **124** (2002) 8131-8141.
- [37] B. Mann and H. Kuhn, *Tunneling through fatty acid salt monolayers*, J. Appl. Phys. **42** (1971) 11.
- [38] A. Aviram and M. A. Ratner, *Molecular rectifiers*, Chem. Phys. Lett. **29** (1974) 277-283.
- [39] L. Bernard, *Expanding the horizon of molecular electronics via nanoparticle assemblies*, PhD Thesis (2006) University of Basel.
- [40] H. Haick and D. Cahen, *Making contact: Connecting molecules electrically to the macroscopic world*, Progress in Surface Science **83** (2008) 217-261.
- [41] N. Prokopuk and K-A Son, *Alligator clips to molecular dimensions*, J. Phys. Condens. Matter **20** (2008) 374116.
- [42] D. K. James and J. M. Tour, *Electrical measurement in molecular electronics*, Chem. Mater. **16** (2004), 4423-4435.
- [43] B.Q. Xu and N.J.J. Tao, *Measurement of single-molecule resistance by repeated formation of molecular junctions*, Science **301** (2003) 5637 1221-1223.

- [44] A. Troisi and M. A. Ratner, *Molecular signatures in the transport properties of molecular wire junctions: what makes a junction “molecular”?*, *Small* **2** (2006) 2 172-181.
- [45] Y. Selzer and D. L. Allara, *Single-molecule electrical junctions*, *Annu. Rev. Phys. Chem.* **57** (2006) 593-623.
- [46] K. W. Hipps and U. Mazur, *Inelastic electron tunneling spectroscopy*, *Handbook of vibrational spectroscopy* J. M. Chalmers and P. R. Griffiths (ed.), John Wiley & Sons Ltd, Chechester (**2002**).
- [47] J. G. Kushmerick, A. S. Blum and D. P. Long, *Metrology for molecular electronics*, *Analyt. Chim. Act.* **568** (2006) 20-27.
- [48] R. C. Jaklevic and J. Lambe, *Molecular vibration spectra by electron tunneling*, *Phys. Rev. Lett.* **17** (1966) 22.
- [49] J. G. Kushmerick, J. Lazorcik, Ch. H. Patterson and R. Shashidhar, *Vibronic contrinutions to charge transport across molecular junctions*, *Nano Lett.* **4** (2004) 639-642.
- [50] D. R. Ward, N. J. Halas, J. W. Ciszek, J. M. Tour, Y. Wu, P. Nordlander and D. Natelson, *Simultaneous measurements of electronic conduction and raman response in molecular junctions*, *Nano Lett.* **8** (2008) 919-924.
- [51] A. Troisi, J. M. Beebe, L. B. Picraux, R. D. van Zee, D. R. Stewart, M. A. Ratner and J. G. Kushmerick, *Tracing electronic pathways in molecules by using inelastic tunneling spectroscopy*, *PNAS* **104** (2007) 36 14255-14259.
- [52] M.A. Reed, C. Zhou, C.J. Muller, T.P. Burgin, and J.M. Tour, *Conductance of a molecular junction*, *Science* **278** (1997), 252-254.
- [53] J.K. Gimzewski, E. Stoll, and R.R. Schlittler, *Scanning tunneling microscopy of individual molecules of copper phthalocyanine adsorbed on polycrystalline silver surfaces*, *Surf. Sci.* **181** (1987) 267-277.

- [54] P.S. Weiss, L.A. Bumm, T.D. Dunbar, T.P. Burgin, J.M. Tour and D.L. Allara, *Probing electronic properties of conjugated and saturated molecules in self-assembled monolayers*, Ann. N.Y. Acad. Sci. **852** (1998) 145.
- [55] W. Haiss, C. Wang, I. Grace, A.S. Batsanov, D.J. Schiffrin, S.J. Higgins, M.R. Bryce, C.J. Lambert, and R.J. Nichols, *Precision control of single-molecule electrical junctions*, Nat. Mater. **5** (2006), 995-1002.
- [56] W. Liang, M.P. Shores, M. Bockrath, J.R. Long, and H. Park, *Kondo resonance in a single-molecule transistor*, Nature **417** (2002), 725-729.
- [57] J. Park, A. N. Pasupathy, J. I. Goldsmith, C. Chang, Y. Yaish, J. R. Petta, M. Rinkoski, J. P. Sethna, H. D. Abruja, P. L. McEuen, and D. C. Ralph, *Coulomb blockade and the Kondo effect in single-atom transistors*, Nature **417** (2002), 722-725.
- [58] C. J. Muller, J. M. van Ruitenbeek and L. J. de Jongh, *Experimental observation of the transition from weak link to tunnel junction*, Physica C: Superconductivity **191** (1992) 485-504.
- [59] M. T. González, S. Wu, R. Huber, S. J. van der Molen, Ch. Shönenberger and M. Calame, *Electrical conductance of molecular junctions by a robust statistical analysis*, Nano Lett. **6** (2006) 10 2238-2242.
- [60] J. R. Heath, *Molecular electronics*, Physics Today (**2003**) May issue.
- [61] H. B. Akkerman and B. de Boer, *Electrical conduction through single molecules and self-assembled monolayers*, J. Phys.: Condens. Matt. **20** (2008) 013001.
- [62] A. Ulman, *Formation and structure of self-assembled monolayer*, Chem. Rev. **96** (1996) 1533-1554.
- [63] L. Becucci, M. R. Moncelli and R. Guidelli, *Surface charge density measurements on mercury electrodes phspholippid monolayers*, J. Electroanalytic. Chem. **413** (1996) 187-193.

- [64] K. Slowinski, R. V. Chamberlain, C. J. Miller and M. Majda, *Through-bond and chain-to-chain coupling. Two pathways in electron tunneling through liquid alkanethiol monolayers on mercury electrodes*, J. Am. Chem. Soc. **119** (1997) 11910-11919.
- [65] M. A. Rampi, O. J. A. Schuller and G. M. Whitesides, *Alkanethiol self-assembled monolayers as the dielectric of capacitors with nanoscale thickness*, Appl. Phys. Lett. **72** (1998) 1781.
- [66] K. Slowinski, H. K. U. Fon and M. Majda, *Mercury-mercury tunneling junctions. I. Electron tunneling across symmetric and asymmetric alkanethiolate bilayers*, J. Am. Chem. Soc. **121** (1999) 7257-7261.
- [67] D. J. Wold, C. D. Frisbie, *Formation of metal-molecule-metal tunnel junctions: microcontacts to alkanethiol monolayers with a conducting AFM tip*, J. Am. Chem. Soc. **122** (2000) 12 2970-2971.
- [68] L. Bernard, M. Calame, S.J. van der Molen, J. Liao and C. Schönenberger, *Controlled formation of metallic nanowires via Au nanoparticle ac trapping*, Nanotech. **18** (2007) 235202.
- [69] I. Amlani, A. M. Rawlett, L. A. Nagahara and R. K. Tsui, *An approach to transport measurements of electronic molecules*, Appl. Phys. Lett. **80** (2002) 15.
- [70] D. P. Long, C. H. Patterson, M. H. Moore, D. S. Seferos, G. C. Bazan and J. G. Kushmerick, *Magnetic directed assembly of molecular junctions*, Appl. Phys. Lett. **86** (2005), 153105.
- [71] D. P. Long and A. Troisi, *Inelastic electron tunneling spectroscopy of alkane monolayers with dissimilar attachment chemistry to gold*, J. Am. Chem. Soc. **129** **49** (2007) 15303-15310.
- [72] G. M. Whitesides, J. P. Mathias and Ch. T. Seto, *Molecular self-assembly and nanochemistry: a chemical strategy for the synthesis of nanostructures*, Science **254** (1991) 1312-1319.

- [73] J. S. Lindsey, *Self-assembly in synthetic routes to molecular devices. Biological principles and chemical perspectives: A review*, New J. Chem. **15** (1991) 153-180.
- [74] J. P. Hill, W. Jin, A. Kosaka, T. Fukushima, H. Ichihara, T. Shimamura, K. Ito, T. Hashizume, N. Ishii and T. Aida, *Self-assembled hexa-peri-hexabenzocoronene graphitic nanotube*, Science **304** (2004) 1481-1483.
- [75] A. P. H. J. Shenning and E. W. Meijer, *Supramolecular electronic; nanowires from self-assembled  $\pi$ -conjugated systems*, Chem. Comm. (**2005**) 3245-3258.
- [76] S. J. van der Molen and P. Liljeroth, *Charge transport through molecular switches*, J. Phys.: Condens. Matter **22** (2010) 133001.
- [77] W. R. Browne and B. L. Feringa, *Making molecular machines work*, Nat, Nanotech. **1** (2006) 25-35.
- [78] D. Dulić, S. J. van der Molen, T. Kudernac, H. T. Jonkman, J. J. D. de Jong, T. N. Bowden, J. can Esch, B. L. Feringa and B. J. van Wees, *One-way optoelectronic switching of photochromic molecules on gold*, Phys. Rev. Lett. **91** (2003) 207402.
- [79] C. N. Lau, D. R. Stewart, R. S. Williams and M. Bockrath, *Direct observation of nanoscale switching centers in metal/molecule/metal structures*, Nano Lett. **4** (2004) 4 569-572.
- [80] M. J. Comstock, N. Levy, A. Kirakosian, J. Cho, F. Lauterwasser, J. H. Harvey, D. A. Strubble, J. M. J. Fréchet, D. Trauner, S. G. Louie and M. F. Crommie, *Reversible photomechanical switching of individual engineered molecules at a metallic surface*, Phys. Rev. Lett. **99** (2007) 038301.
- [81] M. J. Comstock, N. Levy, J. Cho, L. Berbil-Bautista, M. F. Crommie, D. A. Poulsen and J. M. J. Fréchet, *Measuring reversible photomechanical switching rates for a molecule at a surface*, Appl. Phys. Lett. **92** (2008) 123107.

- [82] M. Alemani, M. V. Peters, S. Hecht, K. H. Reider, F. Moresco and L. Grill, *Electric field-induced isomerization of azobenzene by STM*, J. Am. Chem. Soc. **128** (2006) 45 14446-14447.
- [83] B. Y. Choi, S. Kahng, S. Kim, H. Kim, H. W. Kim, Y. J. Song, J. Ihm and Y. Kuk, *Conformational molecular switch of the azobenzene molecule: a scanning tunneling microscopy study*, Phys. Rev. Lett. **96** (2006) 156106.
- [84] Eds. P. Gütllich and H.A. Goodwin, *Spin crossover in transition metal compounds*, Top. Curr. Chem. **233-235** (2004).
- [85] Ph. Gütllich, H. A. Goodwin, *Spin Crossover – An overall perspective*, Top. Curr. Chem. **233** (2004), 1-47.
- [86] L. Cambi and L. Szegő, *Über die magnetische Suszeptibilität der komplexen Verbindungen*, Ber. Dtsch. Chem. Ges. **64** (1931) 2591–2598.
- [87] J.-F. Létard, P. Guionneau and L. Goux-Capes, *towards spin crossover applications*, Top. Curr. Chem. **235** (2004) 221-249.
- [88] O. Kahn and C.J. Martinez, *Spin-transition polymers: from molecular materials toward memory devices*, Science **279** (1998) 44.
- [89] O. Kahn, J. Kröber and C. Jay, *Spin Transition Molecular Materials for displays and data recording*, Adv. Mater. **11** (1992) 718.
- [90] A. S. Blum, J. G. Kushmerick, D. P. Long, Ch. H. Patterson, J. C. Yang, J. C. Henderson, Y. Yao, J. M. Tour, R. Shashidhar and B. R. Ratna, *Molecularly inherent voltage-controlled conductance switching*, Nat. Mater. **4** (2005) 167-172.
- [91] F. Prins, M. Monrabal-Capilla, E. A. Osorio, E. Coronado and H. S. J. van der Zant, *Room-temperature electrical addressing of a bistable spin-crossover molecular system*, Adv. Mater. **23** (2011) 1545-1549.

- [92] T. Forestier, S. Mornet, N. Daro, T. Nishihara, S.-I. Mouri, K. Tanaka, O. Fouché, E. Freysz and J.-F. Létard, *Nanoparticles of iron (II) spin-crossover*, Chem. Comm. **4327** (2008).
- [93] C. Etrillard, V. Faramarzi, J. F. Dayen, J. F. Létard and B. Doudin, *Photoconduction in [Fe(Htrz)<sub>2</sub>(trz)](BF<sub>4</sub>)•H<sub>2</sub>O nanocrystals*, Chem. Comm. (2011) Advanced article.
- [94] T. Li, W. Hu and D. Zhu, *Nanogap Electrodes*, *Adv. Mater.* **22** (2010), 286–300.
- [95] A. Javey, P. Qi, Q. Wang, and H. Dai, *Ten- to 50-nm-long quasi-ballistic carbon nanotube devices obtained without complex lithography*, PNAS **101** (2004), 13408-13410.
- [96] L. F. Sun, S. N. Chin, E. Marx, K. S. Curtis, N. C. Greenham and C. J. B. Ford, *Shadow-evaporated nanometer-sized gaps and their use in electrical studies of nanocrystals*, Nanotechnology **16** (2005), 631.
- [97] A. Fursina, S. Lee, R. G. S. Sofin, I. V. Shvets, D. Natelson, *Nanogaps with very large aspect ratios for electrical measurements*, Appl. Phys. Lett. **92** (2008), 113102.
- [98] J. Tang, Y. Wang, C. Nuckolls, S. J. Wind, *Chemically responsive molecular transistors fabricated by self-aligned lithography and chemical self-assembly*, J. Vac. Sci. Technol. B **24** (2006), 3227-3229.
- [99] R. Negishi, T. Hasegawa, K. Terabe, M. Aono, T. Ebihara, H. Tanaka and T. Ogawa, *Fabrication of nanoscale gaps using a combination of self-assembled molecular and electron beam lithographic techniques*, Appl. Phys. Lett. **88** (2006), 223111.
- [100] S. van der Molen, J. Liao, T. Kudernac, J. Agustsson, L. Bernard, M. Calame, B. van Wees, B. Feringa and C. Schönenberger, *Light-controlled conductance switching of ordered metal–molecule–metal devices*, Nano Lett. **9** (2009), 76-80.
- [101] S. M. Lubber, F. Zhang, S. Lingitz, A. G. Hansen, F. Scheliga, E. Thorn-Csanyi, M. Bichler, M. Tornow, *High-Aspect-Ratio Nanogap Electrodes for Averaging Molecular Conductance Measurements*, Small. **3** (2007), 285-289.

- [102] John G Bai, Cheng-Ling Chang, Jae-Hyun Chung, and Kyong-Hoon Lee, *Shadow edge lithography for nanoscale patterning and manufacturing*, *Nanotechnology* **18** (2007), 405307.
- [103] **John G. Bai, Woon-Hong Yeo and Jae-Hyun Chung**, *Nanostructured biosensing platform-shadow edge lithography for high-throughput nanofabrication*, *Lab on Chip* **9** (2009), 449 – 455.
- [104] J. M. Tour, *Molecular electronics: commercial insights, chemistry, devices, architecture and programming*, World Scientific, River Edge, (2003).
- [105] K. S. Kwok, J. C. Ellenbogen, *Molecular electronics: future electronics*, *Materials Today* **5** (2002), 28.
- [106] D. Long, J. Lazorcik, and R. Shashidhar, *Magnetically directed self-assembly of carbon nanotube devices*, *Adv. Mat.* **16** (2004), 814–819.
- [107] A. Hirohata, C.C. Yao, H.T. Leung, Y.B. Xu, C.M. Guertler, and J.A.C. Bland, *Magnetic domain studies of permalloy wire-based structures with junctions*, *IEEE Transactions on Magnetism* **36** (2000), 3068-3070.
- [108] I. Amlani, A. M. Rawlett, L. A. Nagahara, and R. K. Tsui, *An approach to transport measurements of electronic molecules*, *Appl. Phys. Lett.* **80, 15** (2002).
- [109] C. Chu, J. S. Na and G. N. Parsons, *Conductivity in alkylamine-gold and alkanethiol-gold molecular junctions measured in molecule-nanoparticle-molecule bridges and conducting probe structures*, *J. AM. CHEM. SOC.* **9 129** (2007), 2289.
- [110] S. Niyogi, C. Hangarter, R. M. Thamankar, Y.F. Chiang, R. Kawakami, N. V. Myung and R.C. Haddon, *Magnetically assembled multiwalled carbon nanotubes on ferromagnetic contacts*, *J. Phys. Chem. B* **108** (2004), 19818-19824.

- [111] Y. Selzer, L. T. Cai, M.A. Cabassi, Y. X. Yao, J. M. Tour, T. S. Mayer, D. L. Allara, *Effect of local environment on molecular conduction: isolated molecule versus self-assembled monolayer*, Nano Lett. **5** (2005), 61-65.
- [112] H. B. Akkerman, P. W. M. Blom, D. M. de Leeuw, B. de Boer, *Towards molecular electronics with large-area molecular junctions*, Nature. **441** (2006), 69-72.
- [113] B. C. Haynie, A. V. Walker, T. B. Tighe, D. L. Allara, N. Winograd, *Adventures in molecular electronics: how to attach wires to molecules*, Appl. Surf. Sci. **203** (2003), 433-436.
- [114] A. Nitzan and M. A. Ratner, *Electron transport in molecular wire junction*, Science **300** (2003) 1384-1389.
- [115] D. Dulić, S. J. van der Molen, T. Kundernac, H. T. Jonkman, J. J. D. de Jong, T. N. Bowden, J. van Esch, B. L. Fergina and B. J. van Wees, *One-way optoelectronic switching of photochromic molecules on gold*, Phys. Rev. Lett. **91** (2003) 207402.
- [116] J. M. Beebe and J. G. Kushmerick, *Nanoscale switch elements from self-assembled monolayers on silver*, Appl. Phys. Lett. **90** (2007) 083117.
- [117] J. M. Beebe, V. B. Engelkes, L. L. Miller and C. D. Frisbie, *Contact resistance in metal-molecule-metal junctions based on aliphatic SAMs: effects of surface linker and metal work function*, J. Am. Chem. Soc. **124** (2002) 11268.
- [118] T. Dadosh, Y. Gordin, R. Krahn, I. Khivrich, D. Mahalu, V. Frydman, J. Sperling, A. Yacoby and I. Bar-Joseph, *measurement of the conductance of single conjugated molecules*, Nature **436** (2005) 677.
- [119] J. Liao, L. Bernard, M. Langer, C. Schönenberger and M. Calame, *Reversible formation of molecular junctions in 2D nanoparticle arrays*, Adv. Mat. **18** (2006) 2444.
- [120] H. Nakanishi, K. J. M. Bishop, B. Kowalczyk, A. Nitzan, E. A. Weiss, K. V. Tretyakov, M. M. Apodaca, R. Klajn, J. F. Stoddart and B. A. Grzybowski, *Photoconductance and*

- inverse photoconductance in films of functionalized metal nanoparticles*, Nature **460** (2009) 371.
- [121] D. R. Stewart, D. A. A. Ohlberg, P. A. Beck, Y. Chen, R. S. Williams, J. O Jeppesen, K. A. Nielsen and J. F. Stoddart, *Molecule-independent electrical switching in Pt/organic monolayer/Ti devices*, Nano Lett. **4** (2004) 133-136.
- [122] N. R. Couch, B. Movaghar, I. R. Girling, *Electromigration failure in filaments through Langmuir-Blodgett films*, Solid State Communications **59** (1986) 1 7-9.
- [123] A. M. Bratkovsky, *Theory of electron current rectification, switching, and a role of defects in molecular devices*, Appl. Phys. A, Materials science & processing **80** (2005) 1363-1372.
- [124] B. Larade and A. M. Bratkovsky, *Effect of impurities on transport through organic self-assembled molecular films from first principles*, Phys. Rev. B. **72** (2005) 3.
- [125] H. Rau, *in Photochromism: Molecules and Systems*, edited by H. Durr and H. Bouas-Laurent, Elsevier, Amsterdam (**1990**).
- [126] N. Tamai and H. Miyasaka, *Ultrafast dynamics of photochromic systems*, Chem. Rev. **100** (2000) 5 1875-1890.
- [127] W. E. Browne and B. L. Fergina, *Making molecular machines work*, Nature Nanotech. **1** (2006) 25.
- [128] M. J. Comstock, N. Levy, A. Kirakosian, J. Cho, F. Lauterwasser, J. H. Harvey, D. A. Strubbe, J. M. J. Fréchet, D. Traunder, S. G. Louie and M. F. Crommie, *Reversible photomechanical switching of individual engineered molecules at a metallic surface*, Phys. Rev. Lett. **99** (2007) 038301.
- [129] M. J. Comstock, N. Levy, J. Cho, L. Berbil-Bautista, M. F. Crommie, D. A. Poulsen and J. M. J. Fréchet, *Measuring reversible photomechanical switching rates for a molecule at a surface*, Appl. Phys. Lett. **92** (2008) 12107.

- [130] M. Alemani, M. V. Peters, S. Hecht, K-H Rieder, F. Moresco and L. Grill, *Electric field-induced isomerization of azobenzene by STM*, J. Am. Chem. Soc. **128** (2006) 45 14446-14447.
- [131] S. Yasuda, T. Nakamura, M. Matsumoto and H. Shigekawa, *Phase switching of a single isomeric molecule and associated characteristic rectification*, J. Am. Chem. Soc. **125** (2003) 52 16430-16433.
- [132] G. Pace, V. Ferri, C. Grave, M. Elbing, C. Von Hänisch, M. Zharnikov, M. Mayor, M. A. Rampi and P. Samori, *Cooperative light-induced molecular movements of highly ordered azobenzene self-assembled monolayers*, Proc. Natl. Acad. Sci. USA **104** (2007) 9937.
- [133] J. M. Mativetsky, G. Pace, M. Elbing, M. A. Rampi, M. Mayor and P. Samori, *Azobenzene as light-controlled molecular electronics switches in nanoscale metal-molecule-metal junctions*, J. Am. Chem. Soc. **130** (2008) 9192-9193.
- [134] V. Ferri, M. Elbing, G. Pace, M. D. Dickey, M. Zharnikov, P. Samori, M. Mayor and M. A. Rampi, *Light-powered electrical switch based on cargo-lifting azobenzene monolayers*, Angew. Chem. Int. Ed. **47** (2008) 407-3409.
- [135] J. M. Seminario, C. E. De la Cruz and P. A. Derosa, *A Theoretical analysis of metal-molecule contacts*, J. Am. Chem. Soc. **123** (2001) 5616-5617.
- [136] J-F Dayen, V. Faramarzi, M. Pauly, N. T. Kemp, M. Barbero, B. P. Pichon, H. Majjad, S. Begin-Colin and B. Doudin, *Nanotrench for nano and microparticle electrical interconnects*, Nanotechnology **21** (2010), 335303.
- [137] J. F. Dayen, V. Faramarzi and B. Doudin, *Nanotrenches: a full optical lithography process for high aspect ratio nanogaps in micro and nanofabrication technologies, in vistas in nanofabrication*, Ed. F. Rahman, Pan Stanford Publications, Singapore (**2011**).
- [138] O. Kahn and J. P. Launay, *Molecular bistability; an overview*, Chemtronics **3** (1988) 140.
- [139] K. Ono, M. Yoshizawa, M. Akita, T. Kato, Y. Tsunobuchi, Sh. Ohkoshi and M. Fujita, *Spin crossover by encapsulation*, J. Am. Chem. Soc. **131** 8 (**2009**) 2782-2783.

- [140] P. Gütllich, A. Hauser and H. Spiering, *Thermal and optical switching of Iron (II) complexes*, Angew. Chem. Int. Ed. En. **33** (1994) 2024–2054.
- [141] A. Bousseksou, G. Molnár, L. Salmon and W. Nicolazzi, *Molecular spin crossover phenomenon: recent achievements and prospects*, Chem. Soc. Rev. **40** (2011) 3313-3335.
- [142] A. Bousseksou, G. Molnár, *The spin-crossover phenomenon: towards molecular memories*, C. R. Chimie **6** (2003) 1175-1183.
- [143] N. Willenbacher and H. Spiering, *The elastic interaction of high-spin and low-spin complex molecules in spin-crossover compounds*, J. Phys. C. Solid State Phys. **21** (1998) 1423-1439.
- [144] H. Spiering, E. Meissner, H. Köppen, E. W. Müller, P. Gütllich, *The effect of the lattice expansion on high spin ↔ low spin transitions*, Chem. Phys. **68** (1982) 65.
- [145] C. Janiak, *Engineering coordination polymers towards application*, Dalton Trans. (**2003**) 2781-2804.
- [146] J. Larionova, L. Salmon, Y. Guari, A. Tokarev, K. Molvinger, G. Molnár and A. Bousseksou, *Towards the ultimate size limit of the memory effect in spin-crossover solids*, Angew. Chem. Int. Ed. **47** (2008) 8236.
- [147] J.-F. Létard, N. Daro and O. Nguyen, *Nanoparticles of a spin transition compound*, Patent FR **0512476** (2005-08-12), Patent WO **065996** (2007-06-14). (<http://www.sumobrain.com/patents/wipo/Nanoparticles-spin-transition-compound/WO2007065996.html>)
- [148] T. Forestier, A. Kaiba, S. Pechev, D. Denux, P. Guionneau, C. Etrillard, N. Daro, E. Freysz and J.-F. Létard, *Nanoparticles of [Fe(NH<sub>2</sub>-trz)<sub>3</sub>]Br<sub>2</sub>•3H<sub>2</sub>O (NH<sub>2</sub>-trz=2-Amino-1,2,4-triazole) prepared by the reverse micelle technique: Influence of particle and coherent domain sizes on spin-crossover properties*, Chem. Eur. J. **15** (2009) 6122.
- [149] G. Galle, J. Degert, C. Mauriac, C. Etrillard, J.-F. Létard and E. Freysz, *Nanosecond study of spin state transition induced by a single nanosecond laser shot on [Fe(NH<sub>2</sub>trz)<sub>3</sub>]*

- compounds inside and outside their thermal hysteresis loops*, Chem. Phys. Lett, **500** (2010) 18.
- [150] J. Kröber, J-P. Audière, R. Claude, E. Codjovi, O. Kahn, J.G. Haasnoot, F. Grolière, C. Jay, A. Bousseksou, J. Linares, F. Varret and A. Gonthier-Vassal, *Spin transitions and thermal hystereses in the molecular-based materials [Fe(Htrz)<sub>2</sub>(trz)](BF<sub>4</sub>) and [Fe(Htrz)<sub>3</sub>](BF<sub>4</sub>)<sub>2</sub>•H<sub>2</sub>O (Htrz = 1,2,4-4H-triazole; trz = 1,2,4-triazolato)*, Chem. Mater. **6** (1994) 1404-1412.
- [151] A. Bousseksou, K. Boukheddaden, M. Goiran, C. Consejo, M. L. Boillot and J. P. Tuchagues, *Dynamic response of the spin-crossover solid Co(H<sub>2</sub>(fpa)<sub>2</sub>en)(py)<sub>2</sub> to a pulsed magnetic field*, Phys. Rev. B **65** (2002), 172412.
- [152] V. A. Varnek and L. G. Lavrenova, *Mössbauer studies of Fe<sub>x</sub>Zn<sub>1-x</sub>(4-amino-1,2,4-triazole)<sub>3</sub>(NO<sub>3</sub>)<sub>2</sub> complexes possessing the <sup>1</sup>A<sub>1</sub>↔<sup>5</sup>T<sub>2</sub> spin transition*, J. Struct. Chem. **35** (1994) 842.
- [153] B. Gallois, J. A. Real, Ch. Hauw, J. Zarembowitch, *Structural changes associated with the spin transition in Fe(phen)<sub>2</sub>(NCS)<sub>2</sub>: A single-crystal x-ray investigation*, Inorganic Chemistry **6** (1990) 29 1152-1158.
- [154] A. Bousseksou, G. Molnár, Ph. Demont and J. Menegotto, *Observation of a thermal hysteresis loop in the dielectric constant of spin crossover complexes: towards molecular memory devices*, J. Mater. Chem. **13** (2003) 2069-2071.
- [155] I. Boldog, A. B. Gaspar, V. Martinez, P. Pardo-Ibáñez, V. Ksenofontov, P. Bhattacharjee and J. A. Real, *Spin-crossover nanocrystals with magnetic, optical, and structural bistability near room temperature*, Angew. Chem. Int. Ed. **47** (2008) 6433.
- [156] F. Volatron, L. Catala, E. Rivière, A. Gloter, O. Stéphan and T. Mallah, *Spin-crossover coordination nanoparticles*, Inorg. Chem. **47** (2008) 6584.
- [157] A. Hauser, *Light-induced spin crossover and the high-spin→low-spin relaxation*, Top. Curr. Chem. **234** (2004) 155-198.

- [158] S. Decurtins, P. Gülich, C.P. Köhler, H. Spiering, *Light-induced excited spin state trapping in a transition-metal complex: the hexa-1-propyltetrazole-iron(II) tetrafluoroborate spin-crossover system*, Chem. Phys. Lett. **105** 1 (1984) 1-4.
- [159] T. Forestiere, *Synthèse de nanoparticules à transition de spin en milieu confiné*, PhD Thesis, (2008). ([http://ori-oai.u-bordeaux1.fr/pdf/2008/FORESTIER\\_THIBAUT\\_2008.pdf](http://ori-oai.u-bordeaux1.fr/pdf/2008/FORESTIER_THIBAUT_2008.pdf))
- [160] E. Coronado, J.R. Galán-Mascarós, M. Monrabal-Capilla, J. García-Martínez and P. Pardo-Ibáñez, *Bistable spin-crossover nanoparticles showing magnetic thermal hysteresis near room temperature*, Adv. Mater. **19** (2007) 1359.
- [161] S. W. Rhee and D. J. Yun, *Metal–semiconductor contact in organic thin film transistors*, J. Mater. Chem. **18** (2008), 5437–5444.
- [162] J. L. Bredas, in *Handbook of conducting polymers vol II*, (ed. Skotheim TA), New York, Marcel Dekker (1986) 859-913.
- [163] I. McCulloch, M. Heeney, C. Bailey, K. Genevicius, I. MacDonald, M. Shkunov, D. Sparrowe, S. Tierney, R. Wagner, W. Zhang, M. L. Chabinyc, R. J. Kline, M. D. McGehee and M. F. Toney, *Liquid-crystalline semiconducting polymers with high charge-carrier mobility*, Nature Mater. **5** (2006) 328-333.
- [164] N. Stutzmann, R. H. Friend and H. Sirringhaus, *Self-aligned, vertical-channel, polymer field-effect transistors*, Science **299** (2003) 1881-1884.
- [165] R. S. Kohlman, A. Zibold, D. B. Tanner, G. G. Ihas, T. Ishiguro, Y. G. Min, A. G. MacDiarmid and A. J. Epstein, *Limits for metallic conductivity in conducting polymers*, Phys. Rev. Lett. **78** (1997) 20.
- [166] C. K. Chiang, C. R. Fincher Jr., Y. W. Park, A. J. Heeger, H. Shirakawa, E. J. Louis, S. C. Gau, and A. G. MacDiarmid, *Electrical Conductivity in Doped Polyacetylene*, Phys. Rev. Lett. **39** (1977) 1098.

- [167] A.J. Epstein, J. Joo, R.S. Kohlman, G. Du, A.G. MacDiarmid, E.J. Oh, Y. Min, J. Tsukamoto, H. Kaneko and J.P. Pouget, *Inhomogeneous disorder and the modified Drude metallic state of conducting polymers*, Synth. Met. **65** (1994) 149-157.
- [168] *Materials for electronics*, Chem. Rev. **110** (2010) 1-574.
- [169] B. H. Hamadani and D. Natelson, *Temperature-dependent contact resistances in high-quality polymer field-effect transistors*, Appl. Phys. Lett. **84** (2004) 3.
- [170] D. Mann, A. Javey, J. Kong, Q. Wang and H. Dai, *Ballistic transport in metallic nanotubes with reliable Pd ohmic contacts*, Nano Lett. **3** (2003) 1541-1544.
- [171] A. R. Harutyunyan, G. Chen, T. M. Paranyan, E. M. Pigos, O. A. Kuznetsov, K. Hewaparakrama, S. M. Kim, D. Zakharov, E. A. Stach and G. U. Sumanasekera, *Preferential growth of single-walled carbon nanotubes with metallic conductivity*, Science **326** (2009) 5949 116-120.
- [172] K. Nagashio, T. Nishimura, K. Kita and A. Toriumi, *Contact resistivity and current flow path at metal/grapheme contact*, Appl. Phys. Lett. **97** (2010) 143514.
- [173] S. Bae, H. Kim, Y. Lee, X. Xy, J. S. Park, Y. Zheng, J. Balakrishnan, T. Lei, H. R. Kim, Y. I. Song, Y. J. Kim, K. S. Kim, B. Özyilmaz, J. H. Ahn, B. H. Hong and S. Lijima, *Roll-to-roll production of 30-inch grapheme films for transparent electrodes*, Nat. Nanotech. **5** (2010) 574-578.
- [174] V. Percec, M. Glodde, T. K. Bera, Y. Miura, I. Shiyanovskaya, K. D. Singer, V. S. K. Balagurusamy, P. A. Heiney, I. Schnell, A. Rapp, H. W. Spiess, S. D. Hudson and H. Duan, *Self-organization of supramolecular helical dendrimers into complex electronic materials*, Nature **417** (2002) 384-387.
- [175] L. Welte, A. Calzolari, R. D. Felice, F. Zamora and j. Gómez-Herrero, *Highly conductive self-assembled nanoribbons of coordination polymers*, Nature **5** (2010) 110-115.
- [176] K. Lee, Sh. Cho, S. H. Park, A. J. Heeger, Ch. W. Lee and S. H. Lee, *Metallic transport in polyaniline*, Nature **441** (2006) 04705.

- [177] H. Ishii, K. Sugiyama, E. Ito and K. Seki, *Energy Level Alignment and Interfacial Electronic Structures at Organic/Metal and Organic/Organic Interfaces*. Adv. Mater. **11** (1999) 605–625.
- [178] E. J. Meijer, *Scaling behavior and parasitic series resistance in disordered organic field-effect transistors*, Appl. Phys. Lett. **82** (2003) 25.
- [179] E. Moulin, F. Niess, M. Maaloum, E. Buhler, I. Nyrkova and N. Giuseppone, *The hierarchical self-assembly of charge nanocarriers: a highly cooperative process promoted by visible light*, Angewan. Chem. Int. Ed. **49** (2010) 6974-6978.
- [180] G. Dalmas, *Nouvelles molécules pour l'électronique moléculaire et leurs applications en électronique de spin*, PhD Thesis (2010). ([http://scd-theses.u-strasbg.fr/1934/01/DALMAS\\_Guillaume\\_2f010.pdf](http://scd-theses.u-strasbg.fr/1934/01/DALMAS_Guillaume_2f010.pdf))
- [181] A. B. Kaiser, G. U. Flanagan, D. M. Stewart and D. Beaglehole, *Heterogeneous model for conduction in conducting polymers and carbon nanotubes*, Synth. Met. **117** (2001) 67-73.
- [182] S. Kivelson and A. J. Heeger, *Intrinsic conductivity of conducting polymers*, Synth. Met. **22** (1988) 371-384.
- [183] I.N. Hulea, S. Russo, A. Molinari, A.F. Morpurgo, *Reproducible low contact resistance in rubrene single-crystal field-effect transistors with nickel electrodes*, Appl. Phys. Lett. **88** (2006) 113512.
- [184] S. Tawfick, K. O'Brien, and A. J. Hart, *Flexible high-conductivity carbon-nanotube interconnects made by rolling and printing*, Small **5** (2009) 2467–2473.
- [185] I. A. Blech, *Electromigration in thin aluminum films on titanium nitride*, J. Appl. Phys. **47** (1976) 1203-1208.
- [186] *International technology roadmap for semiconductors, Roadmap information on interconnects, (2009)*.

- [187] J. Borghetti, D. B. Strukov, M. D. Pickett, J. J. Yang, D. R. Stewart and R. S. Williams, *Electrical transport and thermometry of electroformed titanium dioxide memristive switches*, J. Appl. Phys. **106** (2009) 124504.
- [188] J.-B. Beaufrand, J.-F. Dayen, N. T. Kemp, A. Sokolov, and B. Doudin, *Magnetoresistance signature of resonant states in electromigrated Ni nanocontacts*, Appl. Phys. Lett. **98** (2011) 142504.
- [189] *International technology roadmap for semiconductors, Roadmap information on interconnects, (2009)*.
- [190] J. Ch. Love, B. D. Gates, G. B. Wolfe, K. E. Paul and G. M. Whitesides, *Fabrication and wetting properties of metallic half-shells with submicron diameters*, Nano Lett. **2** (2002) 891-894.
- [191] A.L. Eckermann, D. J. Feld, J. A. Shaw, T. J. Meade, *Electrochemistry of redox-active self-assembled monolayers*, Coord. Chem. R. **254** (2010) 1769-1802.
- [192] N. M. Esfandiari, Y. Wang, J. Y. Bass, T. P. Cornell, D. A. L. Otte, M. H. Cheng, J. C. Hemminger, T. M. Mcintire, V. A. Mandelshtam and S. A. Blum, *Single-Molecule Imaging of Platinum Ligand Exchange Reaction Reveals Reactivity Distribution*, J. Am. Chem. Soc. **132** (2010) 15167-15169.
- [193] D. P. Cormode, A. J. Evans, J. J. Davis and P. D. Beer, *Amplification of anion sensing by disulfide functionalized ferrocene and ferrocene-calixarene receptors adsorbed onto gold surfaces*, Dalton Trans. **39** (2010) 6532-6541.
- [194] M. Mannini, F. Pineider, C. Danieli, F. Totti, L. Sorace, Ph. Sainctavit, M-A Arrio, E. Otero, L. Joly, J. C. Cesar, A. Cornia and R. Sessoli, *Quantum tunneling of the magnetization in a monolayer of oriented single molecule magnets*, Nature **468** (2010) 417-421.
- [195] L. Bogani and W. Wensdorfer, Nature Mater. **7** (2008) 179-186.

- [196] J-M Basset, A. Baudouin, F. Bayard, J-P Candy, C. Coperet, A. De Mallmann, G. Godard, E. Kuntz, F. Lefebvre, C. Lucas, S. Norcis, K. Pelzer, A. Quadrelli, C. Santini, D. Soulivong, F. Stoffelbach, M. Taoufik, C. Thieuleux, J. Thiyolle-Cazatand and L. Veyre, *Modern surface organometallic chemistry*, Wiley-VCH Weinheim (2009) 23-135.
- [197] A.J. Ward, A. F. Masters and T. MAschmeyer, *Modern surface organometallic chemistry*, Wiley-VCH Weinheim (2009) 167-237.
- [198] J. M. Fraile, J. I. García, J. A. Mayoral and E. Pires, *Catalysis by metal complexes (Series Eds. C. Bianchini, D. J. Cole-Hamilton and P. W. N. M. van Leeuwen)*, Springer New York **33** (2010) 65-121.
- [199] F. Schweyer-Tihay, P. Braunstein, C. Estournès, J-L Guille, B. Lebeau, J-L Paillaud, M. Richard-Plouet and J. Rosé, *Synthesis and characterization of supported Co<sub>2</sub>P nanoparticles by grafting of molecular clusters into mesoporous silica matrixes*, Chem. Mater. **15** (2003) 57-62.
- [200] P. Braunstein, H-P Kormann, W. Meyer-Zaika, R. Pugin and G. Schmid, *Strategies for the anchoring of metal complexes, clusters and colloids inside nanoporous Alumina membranes*, Chem. Eur. J. **6** (2000) 4637-4646.
- [201] J. C. Love, L. A. Estroff, J. K. Kriebel, R. G. Nuzzo and G. M. Whitesides, *Self-assembled monolayers of thiolates on metals as a form of nanotechnology*, Chem. Rev. **105** (2005) 1103-1170.
- [202] H. Ma, H-L Yop, F. Huang and A. K-Y Jen, *Interface engineering for organic electronics*, Adv. Func. Mater. **20** (2010) 1371-1388.
- [203] G. Rogez, B. Donnio, E. Terrazi, J-L Gallani, J-P Kappler, J-P Bucher and M. Drillon, *The quest for nanoscale magnets: the example of [Mn12] single molecule magnets*, Adv. Mater. **21** (2009) 4323-4333.
- [204] R. H. Ismayilov, W. Z. Wang, G. H. Lee, C. Y. Yeh, S. H. Hua, Y. Song, M. M. Rohmer, M. Bénard and S. M. Peng, *Two linear undecanickel mixed-valence complexes: Increasing the size and the scope of the electronic properties of nickel metal strings*, Angew. Chem. Int. Ed. **50** (2011) 2054-2048.

- [205] G. Ch. Huang, Sh-A Hua, I. P-C Liu, Ch. H. Chien, J. H. Kuo, G. H. Lee and Sh. M. Peng, *Further studies of  $[Ni_4(DAniDANy)_4](DAniDANy^{2-}=N,N'$ -bis-*p*-anisyl-2,7-diamido-1,8-naphthyridine) and its one-electron oxidation product: metal-metal sigma bonding in  $Ni_4^{9+}$  complex*, C. R. Chimie **15** (2012) 159.
- [206] L. Zhou, Sh. W. Yang, M. F. Ng, M. B. Sullivan, V. B. C. Tan and L. Shen, *One dimensional iron-cyclopentadienyl sandwich molecular wire with half metallic negative differential resistance and high-spin filter efficiency properties*, J. A. Chem. Soc. **130** (2008) 4023-4027.
- [207] N. Tuccitto, V. Ferri, M. Cavazzini, S. Quici, G. Zhavnerko, A. Licciardello and M. A. Rampi, *Highly conductive ~40nm long molecular wires assembled by stepwise incorporation of metal centres*, Nature. Mater. **8** (2009) 41-46.
- [208] A. Nait abdi, O. Toulemonde, J-P Bucher, J. Rosé, P. Braunstein, R. Welter and M. Drillon, *Grafting and thermal stripping of organo-bimetallic clusters on Au surfaces, toward controlled Co/Ru aggregates*, Chem. Eur. J. **14** (2008) 2355-2362.
- [209] W. F. Egelhoff Jr., *Core-level binding-energy shifts at surfaces and in solids*, Surf. Sci. Rep. **6** (1987) 253-415.
- [210] S. Ye and R. L. Carroll, *Design and fabrication of bimetallic colloidal 'Janus Particles'*, ACS Appl. Materials and Interfaces **2** (2010) 616-620.
- [211] V. Faramarzi, F. Niess, E. Moulin, M. Maaloum, J-F Dayen, J-B Beaufrand, S. Zanettini, B. Doudin and N. Giuseppone, *Light-triggered self-construction of supramolecular organic nanowires as metallic interconnects*, Nature Chemistry **1332** (2012).

# APPENDIX

## A. MICROSPHERE FOR SURFACE BONDING STUDIES

The aim of this study is to use microspheres as a mediator tool for validating several chemical reactions of a group of molecular wires interesting for molecular electronics studies [191].

The series of experiments have been carried out to study the behavior of different organic molecules towards different metallic surfaces and also visualizing coordination chemistry with the use of microspheres. These micrometric particles can carry a group of organic molecules and are detectable by optical means, which make them a clever tool of evidence for several studies [192].

### A.1. PREPARATION OF HALF METAL COATED SILICA MICROSPHERES

Sicastar<sup>®</sup> Monodisperse silica Microspheres with mean diameter ranging from 100nm to 1.00 $\mu$ m (Micromod) and Polystyrene monodisperse microspheres (Polysciences) mean diameter 1.00  $\mu$ m, were diluted and washed in distilled water by several centrifuging steps. Microscope glass slides were cleaned in acetone then ethanol and dried by nitrogen flow. The glass slides then go through oxygen plasma surface treatment in order to have a hydrophilic surface [193]. Microspheres in aqueous solution are spread on the slides using drop casting. They disperse almost uniformly after the solvent evaporation on the glass surface.

These substrates are then metal coated using an e-beam evaporator, depositing a trilayer of Au(20 nm)/Ni(30 nm)/Ti(5 nm). The spheres are then detached from the surface by soft sonication in ethanol, washed, collected by centrifuging, dispersed in ethanol for further modifications (figure A.1) [190]

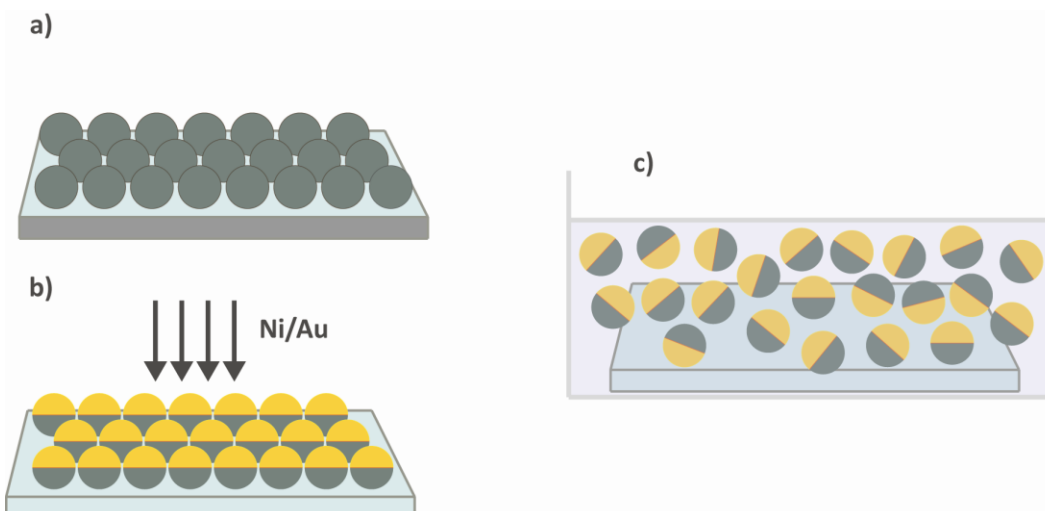


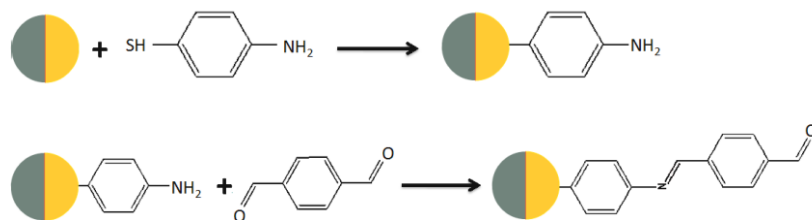
**Figure A.1 : Fabrication of half-metal coated microspheres: a) formation of monolayer islands of microspheres on glass slide, b) Au/Ni deposition on one half of the spheres, c) detaching the spheres from the substrate and dispersing in ethanol by soft sonication.**

## A.2. MICROSPHERES SURFACE FUNCTIONALIZATION

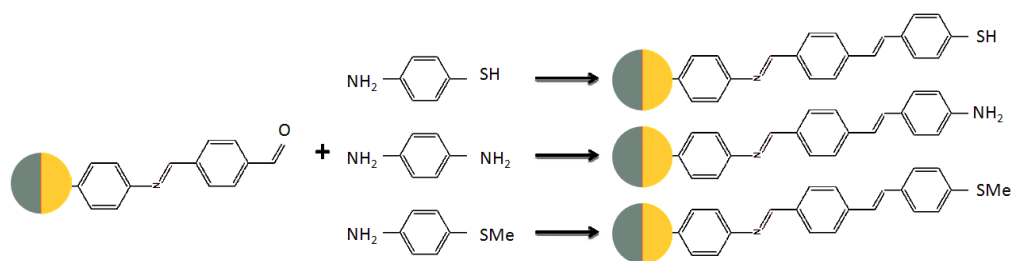
Molecular wires interesting for this study are attached to microspheres in three steps using a sequence of the self-assembly process in solution (figure A.2) [194].

Half metal coated microspheres dispersed in ethanol are added to a solution of 10mM of 4-Aminothiophenol (4-ATP – Aldrich 96%) in ethanol. The thiol group of 4-ATP bonds covalently to the gold surface of the sphere which results in the formation of a self-assembled monolayer (SAM) on the gold surface. After overnight agitation which ensures a well packed SAM, the spheres are separated from the rest of the solution during centrifuging steps in ethanol.

a)

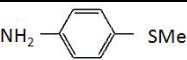
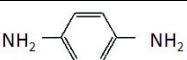


b)



**Figure A.2: a) First and second step of functionalization, b) Attaching different molecular chains to the aldehyde group via step by step functionalization of half-coated silica microspheres, using sequel deposition in the solution.**

The next molecular chain to be attached to the 4-ATP is the terephthalaldehyde (TDA - Aldrich, 99%) molecule. One of the aldehyde groups of TDA reacts with the amine group of 4-ATP by forming a  $\pi$ -conjugated imine bond. The last step consists of adding a molecule by forming the imine bond with the free aldehyde group of the TDA. Several molecules with different end groups were chosen and used in order to compare their behavior facing a metallic surface (table A.1).

Name	Molecular Structure	Chemical Formula	Concentration Used
4-Aminothiobanisole / 4-Methylmercapto Aniline		CH <sub>3</sub> SC <sub>6</sub> H <sub>4</sub> NH <sub>2</sub>	50mg in 5mlit EtOH 71.82mM
4-Aminothiophenol		H <sub>2</sub> NC <sub>6</sub> H <sub>4</sub> SH	50mg in 5mlit EtOH 79.87mM
p-Phenylenediamine		C <sub>6</sub> H <sub>4</sub> (NH <sub>2</sub> ) <sub>2</sub>	50mg in 5mlit EtOH 92.47mM

**Table A. 1 : Different molecules determining the end group of the long molecular chain.**

### A.3. END GROUP EFFECT IN BONDING WITH GOLD SURFACE VIA FUNCTIONALIZATION OF POLYBEAD AMINO MICROSPHERES

Polybead amino monodisperse polystyrene microspheres from Polysciences, mean diameter 1 $\mu$ m, containing surface primary amine groups are diluted and washed in ethanol by centrifuging steps.

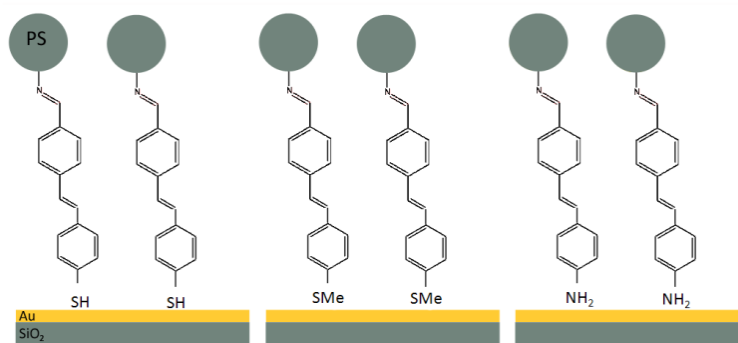
These particles only go through the 2nd and 3rd steps of functionalization, since their surface is originally covered with primary amine group that forms an imine bond with the aldehyde group. Polystyrene microspheres were used in the first experiments, since they don't resist to several organic solvents, were replaced by silica microspheres.

Gold substrates were prepared by evaporation of 45nm of Gold over 5nm of Ti (as adhesion layer). Substrates consist of 320-375  $\mu$ m thick silicon wafers covered with 550nm silicon oxide on both sides, scribed to 1cm<sup>2</sup> squares, cleaned in acetone, ethanol and dried under nitrogen flow.

The substrates were immersed in solutions containing the amino polystyrene microspheres with molecular chains attached, after few hours over soft agitation they were rinsed in ethanol to remove the excess non-absorbed particles and molecules, and dried gently with nitrogen flow.

Optical observation of the samples was carried on under a direct optical microscope, which could determine the distribution and population of the spheres on the substrate. It is possible to detect the spheres individually and count them using the high magnifying objectives. (Zeiss Microscope, 100X objective)

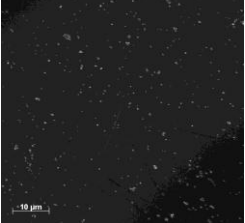
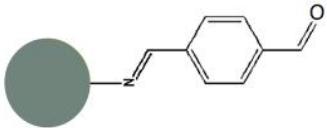
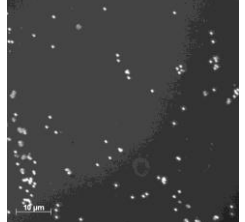
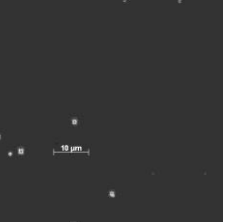
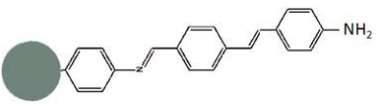
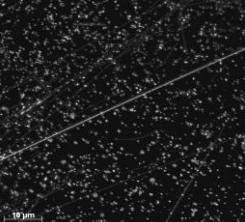
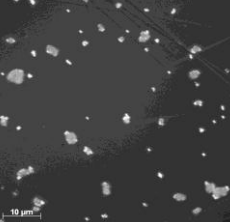
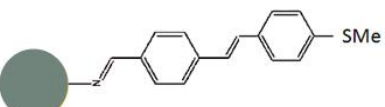
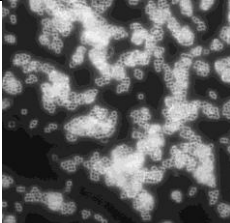
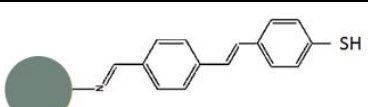
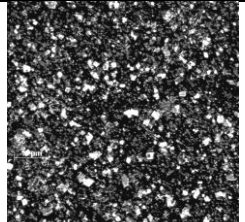
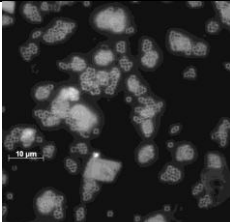
By Comparing the average density of population of the spheres on the surface, the preference of each end-group to create a bond with the gold surface is deduced.



**Figure A.3 : Functionalized polystyrene microspheres with different end groups on gold surfaces**

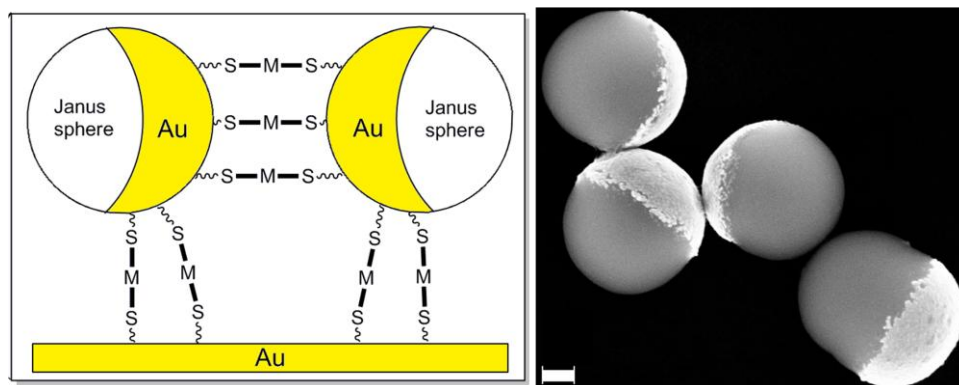
#### A.4. CONCLUSION

The optical observation presents the number of the spheres per  $\mu\text{m}^2$  from which the tendency of the each end group of each molecular chain towards bonding with the gold surface is deduced. The average density of population of the spheres on the gold surface in increasing order starts from the lowest for particles having an aldehyde end group, then primary amine group of the polystyrene particle, amine group of the diamine molecule, methyl group and the highest for the thiol group.

Amino Polybead with a molecular chain	Microspheres on the Gold Surface (Optical Microscope Image)	Microspheres on the Gold Surface (Optical Microscope Image) Zoomed
		
		
		
		
		

**Table A.2 : Images taken by optical microscope showing the distribution and the density of population of the spheres with different molecular chains on the gold substrate.**

## B. COORDINATION-DRIVEN ASSEMBLING OF MICRO-OBJECTS WITH METALLOLIGANDS



Straightforward assessment of molecular anchoring on metallic surfaces is obtained by optical microscopy imaging of functionalized Janus gold-coated silica microspheres. This simple visualization methodology is applied on a rigid thioether-functionalized bis(diphenylphosphino) amine-based metalloligand linker. This represents an unprecedented application of coordination complexes.

## B.1. INTRODUCTION

Chemical grafting of organometallic or coordination complexes on metallic surfaces or into mesoporous materials is often oriented toward the formation of modified electrodes sensors, molecular spintronic devices or heterogeneous catalysts [191, 192, 193, 194, 195, 196, 197]. These molecules are based on a metallic core, which can be mono- or polynuclear, homo- or heterometallic, and an organic ligand acting as linker to the inorganic support. Such a ligand must be at least bifunctional, with a donor end group suitable to coordinate the metal and a reactive anchoring group adapted to the desired support, these two functions being connected by a spacer [198]. This is illustrated e.g. by the successful anchoring of molecular clusters into mesoporous materials using alkoxysilyl-functionalized bis(diphenylphosphino)amine ligands [199, 200].

The growing interest for molecular anchoring on conducting substrates is inspired by the success of self-assembled monolayers (SAMs), with applications e.g. in the fields of molecular electronics interfaces and molecular magnetism [201, 202, 203]. Linear metal chain complexes have potential for spintronics applications, following the experimental indications of longrange electronic transport in organometallic wires [204, 205, 206, 207]. Substrate binding stability remains a key issue. Although recently our chemist collaborators succeeded in anchoring a heterometallic Ru/Co molecular cluster to a gold surface through a phosphino-thiol ligand, limitations of the thiol anchoring group were noted since it is easily converted into a disulfide bridge, even though all experiments were carried out under inert atmosphere [208].

Straightforward experimental insight into successful and stable molecular anchoring on a metallic surface is challenging. Surface spectroscopy techniques (in particular XPS) are necessary to identify surface chemical bonding, and imaging techniques like scanning electron microscopy (SEM), or surface scanning microscopy (AFM, STM) provide insight into the thin films morphology and structures. These methods, however, require adequate substrate flatness (AFM, STM), involve energetic particles irradiation (XPS, SEM), and thus necessitate care in time-consuming experiments [209].

Here we report the use of silica microspheres partly coated with a thin layer (*ca.* 45 nm) of Au or Janus spheres, for the rapid and convenient optical microscopy assessment of successful molecular bonding to a metal surface, illustrated with a new ditopic metalloligand (Figure B.1) [210].

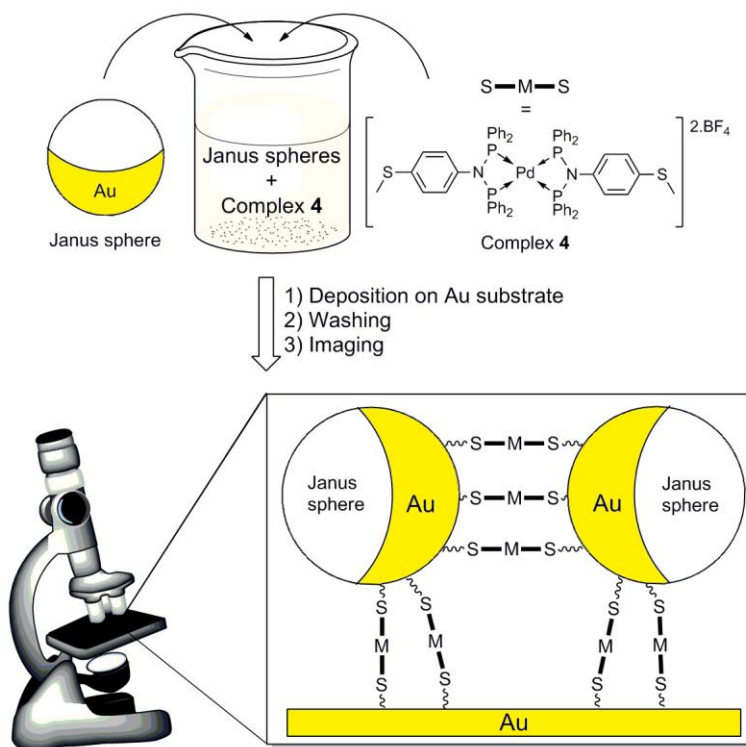


**Figure B.1 : Protocol for the functionalization of partially gold-coated silica microspheres and irreversible linkage seen under an optical microscope.**

Our purpose here is to describe a proof-of-concept experiment. Ideally, one would like to have at our disposal rigid molecules, with two opposite functional end groups at fixed distance with affinity for a Au surface, that could act as linkers between two Au-coated microspheres and/or a microsphere and the substrate onto which they will be deposited. We have therefore considered a square-planar metal complex containing two strong chelates bearing each a thioether donor group pointing as much as possible away from each other. A dppa-type ligand (dppa = HN(PPh<sub>2</sub>)<sub>2</sub>) was chosen for the ease of formation of *N*-functionalized derivatives and the rigidity of its bis-chelated metal complexes.

## B.2. EXPERIMENTAL PROCEDURE

Metalloligands were synthesized and characterized in the Coordination Chemistry Lab under the supervision of Pierre Braunstein in Strasbourg. The solid-state structure of complex **4** (Figure B.1) confirmed the bis10 chelation of the Pd(II) centre and the desired disposition of the thioether groups, pointing in opposite directions to each other. The S donor atoms, separated by 17.85 Å, are sterically readily accessible, which should facilitate assembling interactions between this metalloligand and an Au surface.

Janus microspheres were obtained with Sicastar silica beads (White-Silica sicastar® spheres from Micromod GMBH) deposited on a glass substrate, subsequently vacuum coated with 5 nm of Ti as adhesion layer followed by 45 nm of Au. A typical batch involves processing  $10^6$  microspheres deposited on a microscope slide. Ultrasonic detachment of the spheres from the substrate was achieved in more than 95% yield. They are 900 nm in diameter, which is large enough to allow optical observations but small enough to avoid rapid sedimentation. A solution of complex **4** ( $0.01 \text{ mmol}\cdot\text{L}^{-1}$  in  $\text{CH}_2\text{Cl}_2$ ) was added to a suspension of the partially gold-coated silica spheres (approximately  $10^4$  microspheres per  $\mu\text{L}$  of  $\text{CH}_2\text{Cl}_2$ ) with the objective to link the latter to the Au surface through the thioether functions of the metalloligand. The resulting mixture was gently stirred overnight, and after a few centrifugation steps, the functionalized spheres were decanted, washed with  $\text{CH}_2\text{Cl}_2$  and deposited on a Au or  $\text{SiO}_2$  substrate for imaging, after the surface has been rinsed with ethanol (Figure B.1). Optical microscopy (Figure B.2) shows that a significant number of spheres remained on the surface, isolated spheres being very seldom, in contrast to spheres processed without exposure to complex **4**. Similar optical microscopy images (Figure B.2) were found for  $\text{SiO}_2$  and Au substrates.

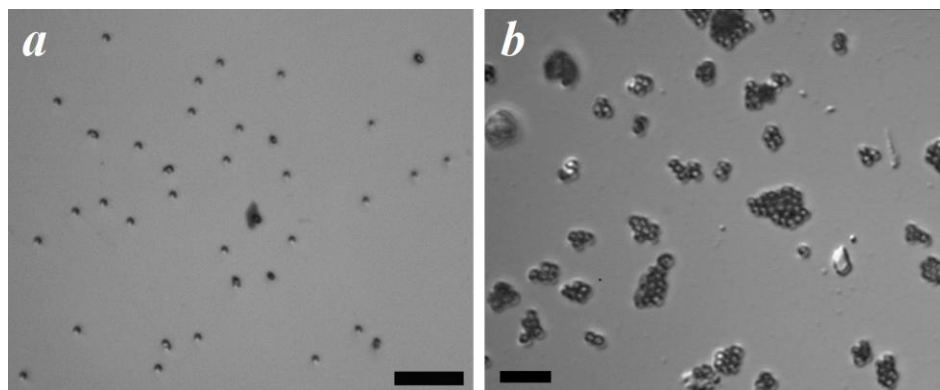


**Figure B.2 : Differential interference contrast optical micrographs of partially gold-covered microspheres over a gold surface, after ethanol washing. (a) Individual microspheres on the surface, with more than 90% of the spheres gone after washing (b) Janus spheres functionalized with **4**, after ethanol washing, showing agglomerates of microspheres. The scale bar is 10µm long.**

The SEM images (Figure B.3) on Au substrates reveal that the spheres are mutually connected when linking molecules are present. Blurring of high-magnification SEM imaging on SiO<sub>2</sub> substrates was caused by charging the insulating substrate, but unambiguous metal-interconnected spheres can be nevertheless assessed. This strongly suggests that molecules of **4** act as linkers between the spheres and the surface and between the spheres (Figure B.3 (b)). In contrast, when non-functionalized spheres were deposited (blank experiment), and the latter analyzed after rinsing, only very few spheres remained on the surface (Figures B.2 (a)), without images indications of interconnected spheres. These results validate the strategy presented in Figure B.1. These simple experiments show that silica microspheres partly coated with Au exhibit inter-spheres attachments when exposed to a solution of a suitable metalloligand as revealed by unambiguous optical microscopy imaging signature (Figure B.3). SEM clearly confirms the irreversible chemical adsorption of the thioether-functionalized complexes to the Au surfaces (Figure B.3).

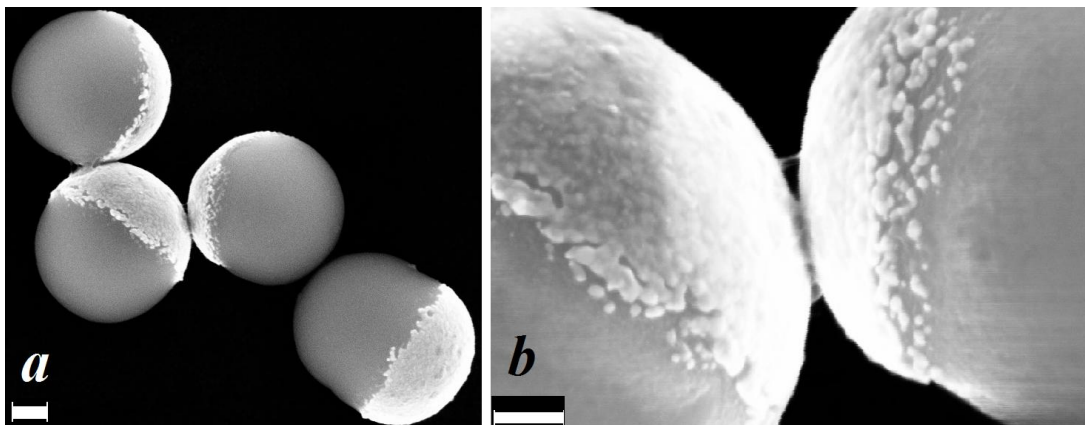


**Figure B.3 : SEM micrographs of partially gold-coated microspheres treated with a solution of 4. The scale bar is 200nm (a) and 100nm (b) long. In (a,b) the spheres are mutually connected through their Au hemispheres, with a zoomed image in (c). In (b) the Au hemispheres are oriented toward the Au substrate, as expected for their preferential linkage to the substrate via the metalloligand molecules.**

Our results demonstrate the potential of Janus microspheres as easy-to-use tools for validation and rapid screening of surface anchoring processes. These results open the possibility of a stepwise approach, by decorating first the microspheres with a suitable difunctional ligand, and then coordinating the dangling donor groups to a diversity of metal cations, using optical visualization to validate the process. The presented proof-of-concept experiments show that a marker methodology based on microspheres requires no heavy experimental tools and can be potentially applied on a wide variety of experiments studying occurrence and stabilization of molecular films on metallic substrates.

## C. FABRICATION OF HALF METALLIC SHELLS ON SCO NANOPARTICLES

The spin crossover nanoparticles have well defined shapes and sizes, with corresponding transition temperature for each, some with hysteresis effect and some without.

To select the best group of particles of this study, we covered them with metallic shells. It helps to better understanding the size and morphology of the particle using SEM imaging. We have observed that depending on the thickness of the metallic film, some particles could not be detached from the substrate.

## C.1. CHOICE OF PARTICLES

We have chosen the particles larger than the trench width (80nm), so they will be placed “over” the trenches and not “in” them.

Nanoparticles in the form of spheres, cubes, disks (170 nm diameter, 50nm thickness) and anisotropic rod shaped ( $300 \times 60$  nm,  $100 \times 40$  nm) were covered with a gold film of 25 nm thickness. The substrates were imaged before and after sonication. The particles detached from sonication also were collected and imaged separately. The related SEM micrographs are presented in figure C.1.

For the substrate with JFCE128 particles, we observed a good dispersion of particles and limited agglomerations. After 15 minutes of ultrasound bath, we observed that almost 50% of the particles have been detached.

For JFCE148 substrate, before sonication, we observed a good dispersion of the particles. After ultrasonic bath, 75% of the particles were detached from the surface.

For JFCE149 substrate, before sonication, we observed more agglomerations and less mono disperse distribution. After ultrasonic bath we observed significant residual agglomerations, with a non-uniform gold film. Disk-shaped nanoparticles were mostly buried under the gold film and couldn't detach from the substrate even after staying a long time in ultrasonic bath, while the agglomerates were more easily detached from the substrate.

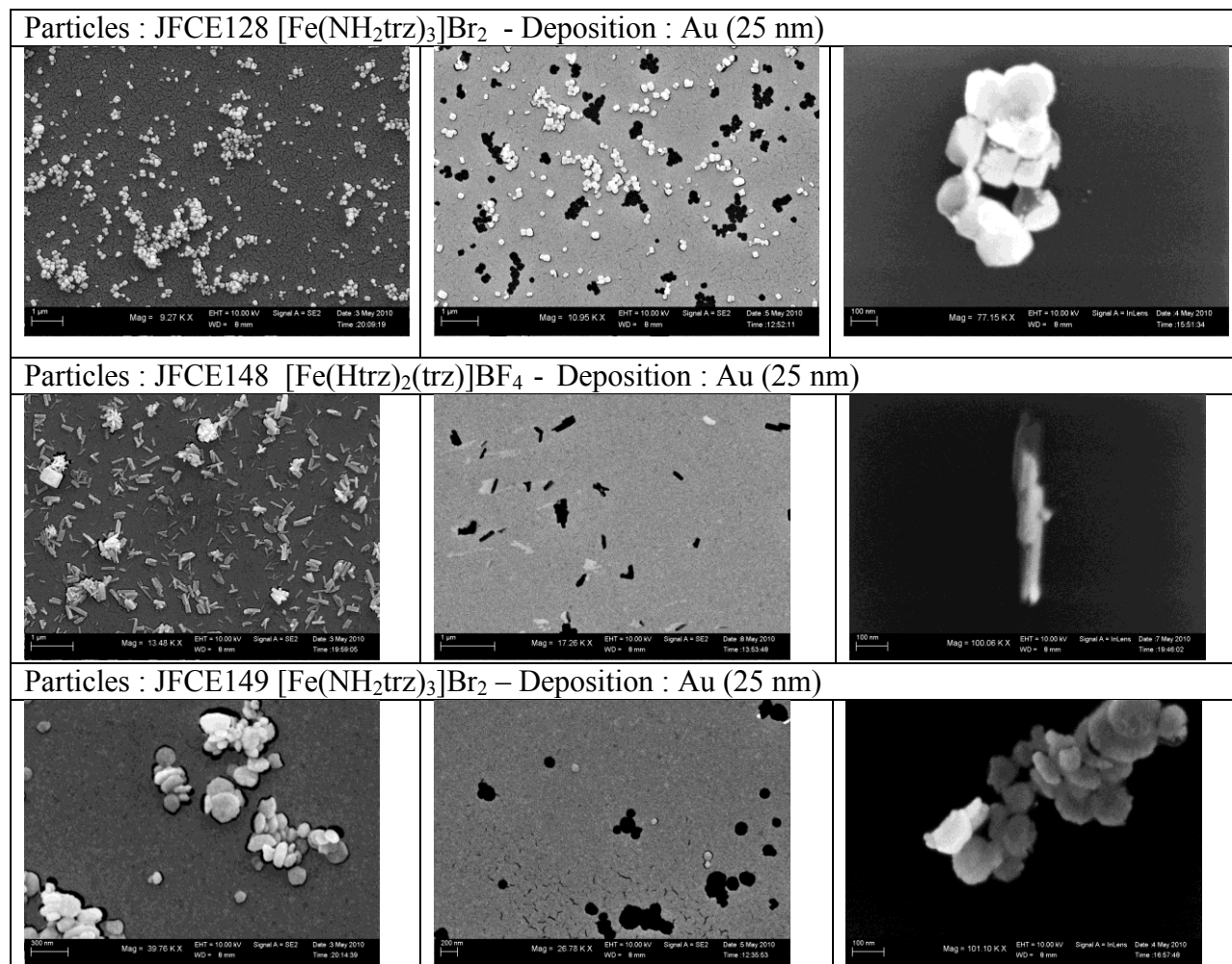


**Figure C.1 : SEM micrographs of metallic deposition and characterization of JFCE128 (top row), JFCE148 (middle row), JFCE149 (bottom row) SCO nanoparticles.**

From this study we can conclude that the particles with more volume like JFCE128 or JFCE148 present a better dispersion on the substrate, and their metallization is more uniform.

As a basic intuitive rule of thumb, larger particles are easier to detach, which follows simple intuition.

As a result we have chosen the largest particles and avoided flat disk shaped ones.

### C.3. THICKNESS OF THE METALLIC FILM

Gold films with three different thicknesses (15 nm, 25 nm and 45 nm) were deposited over rod shaped particles. For the three thicknesses, we have observed a granular continuous film. We have observed that the 15 nm thick film completely covers the particle surface. Films thinner than 15 nm were not continuous and could not cover the particle. A thicker 45 nm film was found too thick to form a homogeneous layer on the particle.

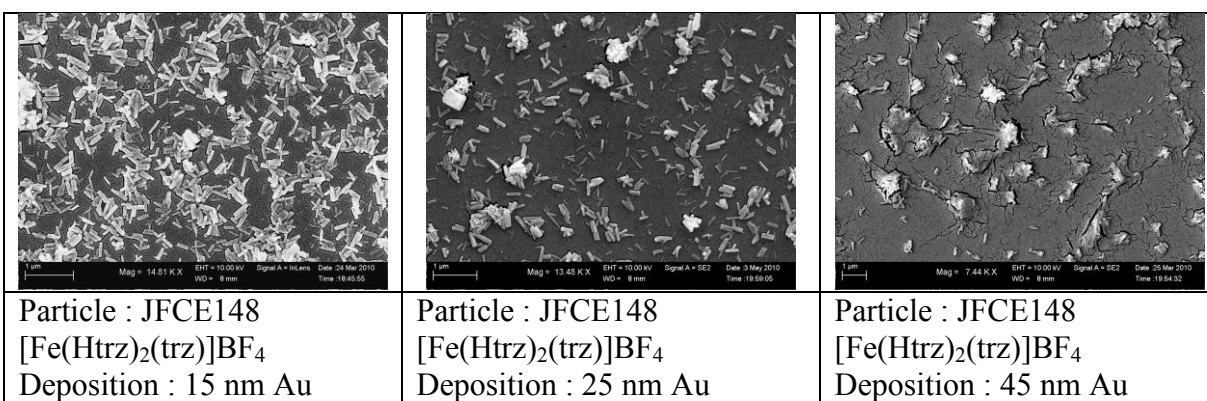


Figure C.2 : SEM micrographs of metallic deposition of 15 nm Au over JFCE148 (left), 25 nm Au over JFCE148 (middle), 45 nm Au over JFCE148 (right) SCO nanoparticles.

Following these morphological studies, we have chosen four different compounds with different properties, identified as best-suited for subsequent manipulations:

1.  $[\text{Fe}(\text{Htrz})_2(\text{trz})]\text{BF}_4$  (*JFSD27*) well defined rod-shaped (640 nm length and 190 nm width). The particles are in low spin state at room temperature and the LS→HS transition occurs at high temperatures.
2.  $[\text{Fe}(\text{NH}_2\text{trz})_3]\text{Cl}_2$  (*JFCE170*) spheroidal particles (300 nm diameter), they are in LS state at room temperature and their transition occurs at 352K (79°C).
3.  $[\text{Fe}(\text{NH}_2\text{trz})_3]\text{Br}_2$  particles (100nm × 170nm), their transition temperature is close to ambient. (*JFCE128*)
4.  $[\text{Fe}(\text{NH}_2\text{trz})_3](\text{BF}_4)_2$  (*JFCE172*) needle shaped (700 nm average length), these particles are at high spin state at ambient temperature.

## D. SAMPLE HOLDERS

### D.1. SAMPLE HOLDER FOR OPTICAL SETUP

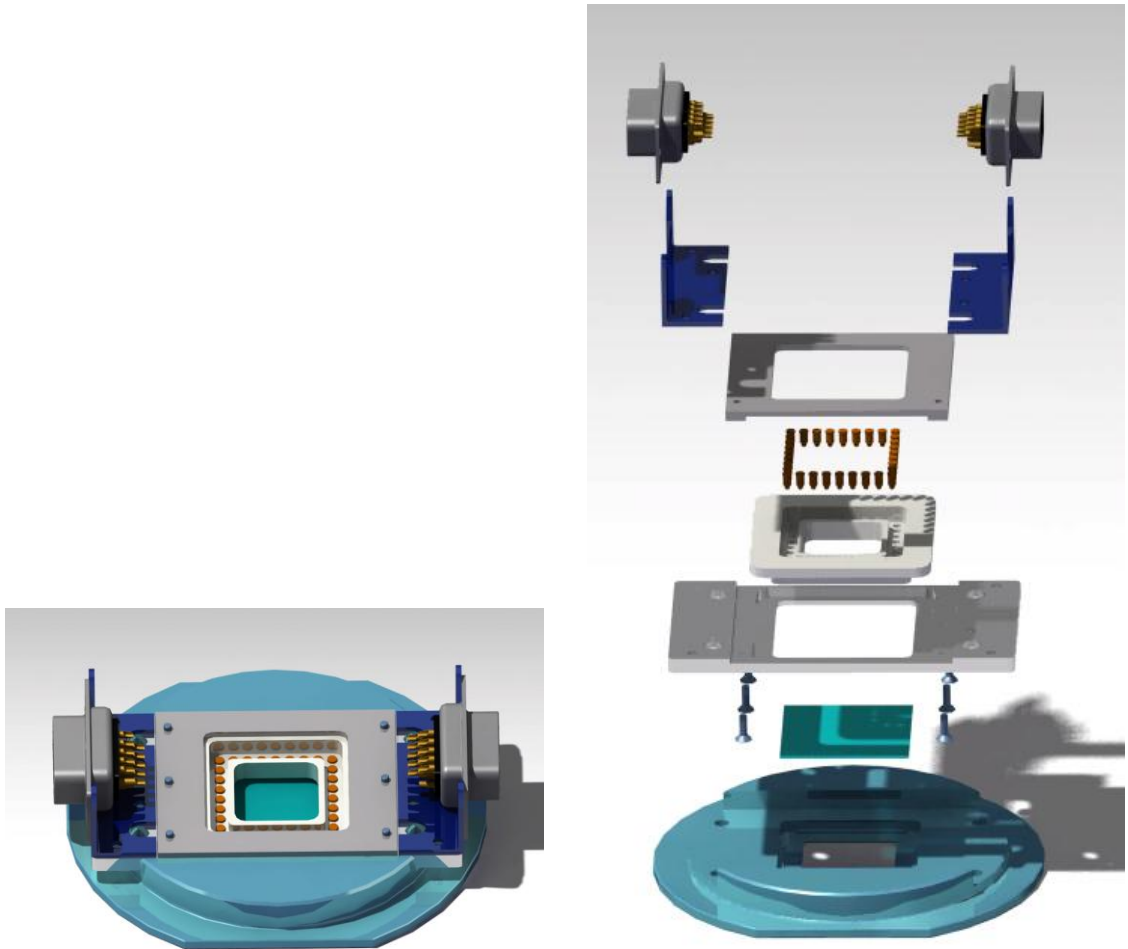


**Figure D.1 : Left: Ensemble view of the sample holder designed and fabricated compatible with inverted optical microscope setup. Right: Separated part-view.**

## D.2. SAMPLE HOLDER FOR LOW TEMPERATURE MEASUREMENTS

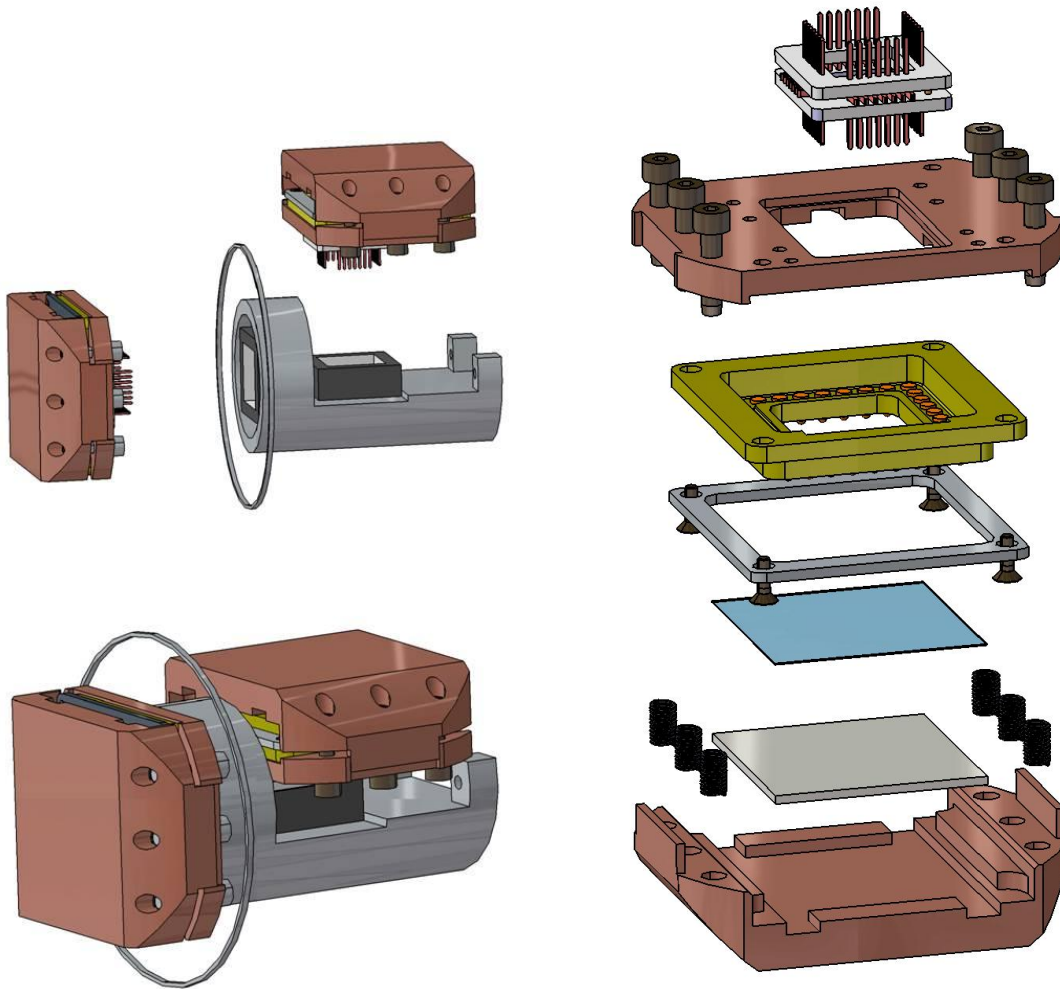


**Figure D.2 : Left: ensemble view of the sample holder designed and fabricated compatible with low temperature and magnetic field measurements, Right: parts-separated view.**